# A numerical framework for geophysical flows on logarithmic lattices

Amaury Barral

université PARIS-SACLAY

# A numerical framework for geophysical flows on logarithmic lattices

*Un environnement numérique pour des écoulements géophysiques sur grilles logarithmiques*

**Thèse de doctorat de l'université Paris-Saclay**

École doctorale n°564, Physique en Île-De-France (PIF)
Spécialité de doctorat : Physique
Graduate School : Physique. Référent : Faculté des sciences d'Orsay

Thèse préparée dans les unités de recherche **SPEC** (Université Paris-Saclay, CEA, CNRS) et **LSCE** (Université Paris-Saclay, CNRS, CEA, UVSQ), sous la direction de **Bérengère DUBRULLE**, directrice de recherche, la co-direction de **Sébastien FROMANG**, directeur de recherche

**Thèse soutenue à Paris-Saclay, le 12 octobre 2023, par**

**Amaury BARRAL**

THESE DE DOCTORAT

NNT : 2023UPASP124

## Composition du jury

Membres du jury avec voix délibérative

| | |
|---|---|
| **Sergio CHIBBARO**<br>Professeur, Institut Jean Le Rond ∂'Alembert | Président |
| **Nikki VERCAUTEREN**<br>Maître de conférences, HDR, University of Olso | Rapporteur & Examinatrice |
| **Detlef LOHSE**<br>Professeur, HDR, University of Twente | Rapporteur & Examinateur |

université PARIS-SACLAY | ÉCOLE DOCTORALE Physique en Île-de-France (PIF)

**Titre :** Un environnement numérique pour des écoulements géophysiques sur grilles logarithmiques

**Mots clés :** Turbulence, Géophysique, Grilles logarithmiques, Simulation numérique, Convection de Rayleigh-Bénard

**Résumé :** Cette thèse explore la possibilité d'utiliser des grilles logarithmiques, un nouvel outil mathématique, pour simuler des flux géophysiques et des équations de dynamique des fluides sur des grilles de Fourier clairsemées. Nous présentons d'abord les grilles logarithmiques, étudions leur interprétabilité et présentons un nouveau cadre numérique (implémenté en Python et en C) conçu pour exploiter efficacement leurs capacités. Nous appliquons ensuite ce cadre à des simulations de plusieurs équations physiques, avec un accent particulier sur trois sujets importants d'intérêt géophysique : l'équation de Rayleigh-Bénard, la formation de jets zonaux dans la turbulence quasi-géostrophique en 2D, et la turbulence rotative forcée. Dans une deuxième partie, nous présentons des contributions supplémentaires sur trois sujets distincts. Tout d'abord, le développement du blowup auto-similaire dans les équations d'Euler et de Navier-Stokes. Deuxièmement, les propriétés de l'équation de Navier-Stokes Réversible. Enfin, l'équation de Rayleigh-Bénard en rotation dans des conditions atmosphériques. Les résultats de cette recherche contribuent à l'avancement des simulations numériques sur des grilles logarithmiques, débloquant des applications potentielles dans divers domaines, y compris la modélisation climatique, la physique atmosphérique et l'océanographie.

**Title :** A numerical framework for geophysical flows on logarithmic lattices

**Keywords :** Turbulence, Geophysics, Logarithmic grids, Numerical simulation, Rayleigh-Bénard convection

**Abstract :** This thesis explores the possibility of using logarithmic grids, a new mathematical tool, to simulate geophysical flows and fluid dynamics equations on sparse Fourier grids. We first introduce logarithmic grids, study their interpretability and present a new numerical framework (implemented in Python and C) designed to efficiently exploit their capabilities. We then apply this framework to simulations of several physical equations, with particular emphasis on three important topics of geophysical interest : the Rayleigh-Bénard equation, the formation of zonal jets in 2D quasi-geostrophic turbulence, and forced rotating turbulence. In the second part, we present additional contributions on three separate topics. First, the development of the self-similar blowup in the Euler and Navier-Stokes equations. Second, the properties of the Reversible Navier-Stokes equation. Finally, the rotating Rayleigh-Bénard equation under atmospheric conditions. The results of this research contribute to the advancement of numerical simulations on logarithmic grids, unlocking potential applications in diverse fields, including climate modeling, atmospheric physics and oceanography.

# Contents

# Part I

# Introduction

## 0.1 Log-lattices

### 0.1.1 Context

In 2019, Campolina [Mar19] introduced a new mathematical framework called "log-lattices" or "logarithmic lattices" in their master's thesis, later supplemented by [CM21] and the PhD thesis [Mar22]. This innovative approach is designed to simulate and explore the equations of fluid dynamics, using a reduced number of modes.

The behavior of simple fluids can be accurately described by the incompressible Navier-Stokes equations (NSE), given as follows:

$$\partial_t \boldsymbol{u} + \boldsymbol{u} \cdot \boldsymbol{\nabla} \boldsymbol{u} = -\boldsymbol{\nabla} p + \frac{1}{\mathrm{Re}} \boldsymbol{\Delta} \boldsymbol{u}, \nabla \cdot \boldsymbol{u} = 0. \tag{1}$$

Here, $\boldsymbol{u}$ represents the fluid's velocity and $p$ denotes its pressure field. The Reynolds number $\mathrm{Re} \equiv \frac{UL}{\nu}$ depends on the characteristic velocity $U$, length scale $L$, and kinematic viscosity $\nu$ of the fluid. Campolina's original motivation was to investigate the potential blowup of the Euler equations, corresponding to the scenario of ideal turbulence where $\mathrm{Re} \to \infty$. This limit holds significant importance in turbulence, and is linked to *anomalous dissipation*, which states that the energy dissipation $\epsilon \equiv \nu |\boldsymbol{\nabla} \boldsymbol{u}|^2$ does not vanish as $\mathrm{Re} \to \infty$, which is at first surprising since smooth solutions of the Euler equations conserve energy. This discrepancy is thought to stem from singular solutions of the Euler equations [Ons49; ES06]. Numerical simulations are indispensable for exploring such claims since analytical solutions are difficult to attain due to the complexity and nonlinearity of the equations, especially in three dimensions.

In the context of the 3D Euler equations, the singularity necessarily manifests itself by a blow-up of vorticity (possibly in finite time), starting from regular initial conditions. However, classical simulations (Direct Numerical Simulations, DNS) become prohibitively expensive as $\mathrm{Re} \to \infty$ due to the substantial size requirements of the numerical domain. Earlier DNS studies [Gib08; GMG98; Ker93; PS92; Gra+08; HL07; Hou09] could not definitively establish or refute the existence of the blowup due to limited resolution ($k_{\max}/k_{\min} \approx 4 \times 10^3$ in Fourier space (figure 1a). To overcome those numerical challenges, previous works have used simplified models[UE97; Mai12], such as shell models. However, those one-dimentional models are too simple and fail to recover the basic features of the Euler blowup. Hence the need for an intermediate complexity model that combines the low degrees of freedom of shell models with the multidimensionality of DNS, without losing the properties of the original equation. This is where Campolina's log-lattice construction comes into play.

### 0.1.2 Construction of a log-lattice

Conceptually, log-lattices fit into the more general framework of REduced Wavenumber set Approximation (REWA) [Gro+94]) or fractal decimated models [Fri+12; Lan+15]. The spirit of these methods is to use a reduced subset of modes obeying a well-defined hierarchy, to stick closer to the observed organized nature of turbulence. In the original REWA models [Gro+94], non-linear-interactions are progressively decreased, either randomly or such that they are distributed over a fractal set [Fri+12; Lan+15]. In log-lattice models, the mode reduction is achieved by keeping modes following a geometric progression, thereby allowing to reach very small scales with a very small number of modes.

The log-lattice construction is based on a discrete grid in Fourier space. We write the wavevectors $\boldsymbol{k} = (k_1, \ldots, k_D)$ in a $D$-dimensional space. In contrast to the regular grid used

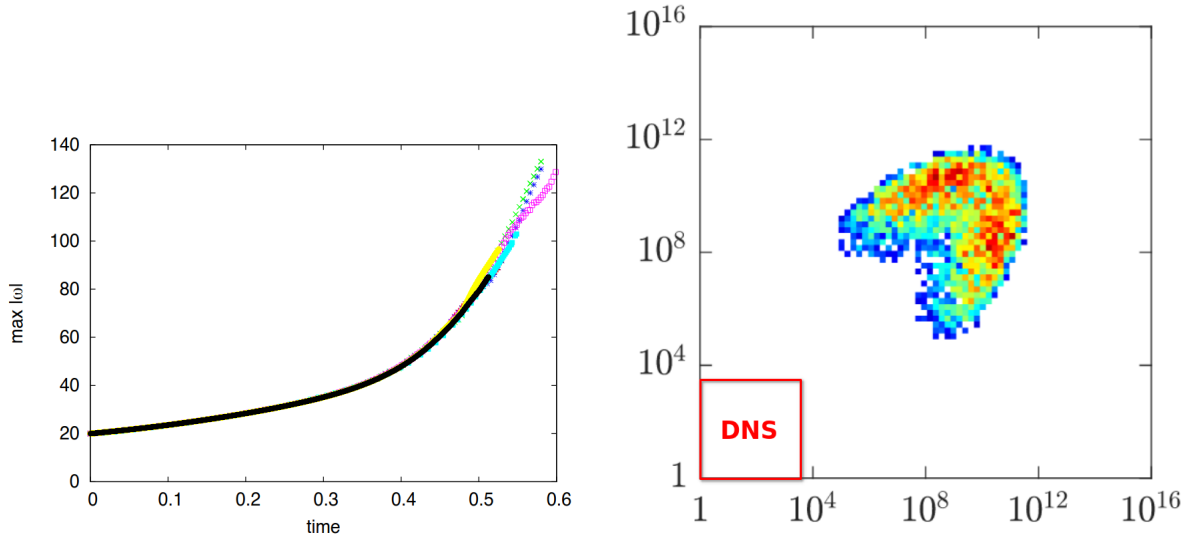


**Figure 1:** (figure 1a) Growth of maximum vorticity for different numerical schemes in 3D Euler. No DNS can reasonably conclude on the blowup of the Euler equations. (adapted from figure 1 in [Gra+08]) (figure 1b) Chaotic attractor in the 3D Euler blowup on log-lattices in function of two positive wavenumbers, in log scale. The color indicates the third component of renormalized vorticity, increasing from blue to red. The red box bounds the square region $|k_{1,2}| \leq 4096$, which would be accessible for the high-accuracy DNS with resolution $8192^3$. (adapted from figure 6.2 in [Mar19])

in DNS, where grid points are defined as $k_i = k_{\min}\lambda n$ for some integer $n$ and a constant $\lambda > 0$, log-lattice employs exponentially spaced grid points defined as $k_i = \pm k_{\min}\lambda^n$ for integers $n$ and a scaling factor $\lambda > 1$ (see figure 2). This arrangement leads to points being regularly spaced in log-space, hence the name "log-lattice".[1] This construction possesses two significant properties: sparsity, which helps to maintain a low number of degrees of freedom (to a regular discrete Fourier lattice containing $N^D$ points corresponds a log-lattice with $\sim (\log_\lambda N)^D$ points), and scale-invariance, a fundamental statistical property of turbulence. However, is it not closed under addition, making triadic interactions $k = p + q$ require special consideration. In particular, for almost any grid spacing $\lambda > 1$, the set of interacting points $\{p, q \mid k = p + q\}$ in the log-lattice is empty for all $k$. We therefore restrict our attention to values of $\lambda$ which admit triadic interactions. Moreover, we are not interested in *reducible* lattices, i.e. lattices that can be decomposed into two disconnected (non mutually interacting) lattices. This leads to three families of admissible values for $\lambda$ in log-lattices, two of which are singular.

Writing $z$ as the number of triadic interactions for each point in one dimension (leading to $z^D$ interactions in $D$ dimensions), the admissible values of $\lambda$ that result in interacting, irreducible lattices are as follows:

- $\lambda = 2$, corresponding to $z = 3$ triadic interactions,
- $\lambda$ such that $\exists b, a \in \mathbb{N}^*, \lambda^b - \lambda^a = 1$ where $b > a$, $\gcd(a, b) = 1$ and $(a, b) \notin \{(1, 3), (4, 5)\}$, corresponding to $z = 6$ triadic interactions, and

[1] Note that unlike shell models, log-lattices are truly multidimensional, and unlike the original REWA model, the decimation does not have a fixed number of points per shell.

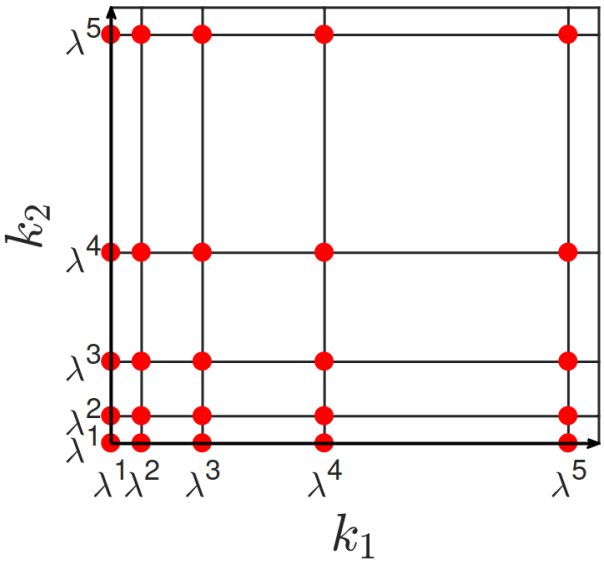


**Figure 2:** A two-dimensional logarithmic lattice with spacing $\lambda$, shown for $k_{1,2} > 0$ (adapted from figure 2.2 in [Mar19])

- $\lambda$ satisfying $\lambda^3 - \lambda^1 = 1$ (the "plastic number", also denoted as $\sigma \approx 1.3$), leading to $z = 12$. Note that this solution also satisfies $\lambda^5 - \lambda^4 = 1$.

The second family of $\lambda$ values has its greatest value when $a = 1, b = 2$, resulting in the golden number $\lambda = \phi \approx 1.6$. This particular value is especially interesting as it spans the largest range of wavenumbers for a given number of grid points[2]. For practical usage, it is useful to remember log-lattices as having three possible configurations: $\lambda = 2, \lambda = \phi, \lambda = \sigma$ (figure 3), written in order of increasing complexity. This complexity stems from both the refinement of grid spacing (coarse for $\lambda = 2$, fine for $\lambda = \sigma$) and the number of interactions $z$.

In [Mar22], *generalized* lattices add the $k_i = 0$ modes to log-lattices.

### 0.1.3 Equations on a log-lattice

In DNS, translating equations from their continuous form onto the regular numerical grid goes through a discretization process. On regular grids, we can define a maximum grid spacing $\epsilon \equiv \inf_{i,j \text{ neighbours}} x_i - x_j$, and then define discrete operators (e.g. through finite elements) that converge to the continuous operators as $\epsilon \to 0$. For instance, in 1D, we can define $\partial_k^{DNS} u = \frac{u(k+\epsilon) - u(k)}{\epsilon} \to_{\epsilon \to 0} \partial_k u$. In the case of log-lattices, the discretization sets a unique challenge because they do not have a well-defined "maximum grid spacing" due to the logarithmic spacing of grid points. The distance between two successive points $\lambda^n, \lambda^{n+1}$ is $\lambda^n(\lambda - 1)$, which is unbounded for $n \in \mathbb{Z}$. Consequently, there is no straightforward way to translate equations onto log-lattices.

Dealing with linear operators is relatively simple: defining $\partial_x u \equiv ik_x u$ is straightforward[3]. The complexity arises when dealing with non-linear operators, particularly convolution, which represents products in real space. One could take inspiration from shell models, and simply construct a bilinear operator that conserves a given quantity such as energy, but this method

[2] Another more technical reason has to do with the minimum spread of the triadic interactions, which roughly scales as $\lambda^b$, and is therefore minimal for $\lambda = \phi$.

[3] though non canonical: why $ik_x$ rather than $ik_x(1 + \lambda/2)$ for instance ?

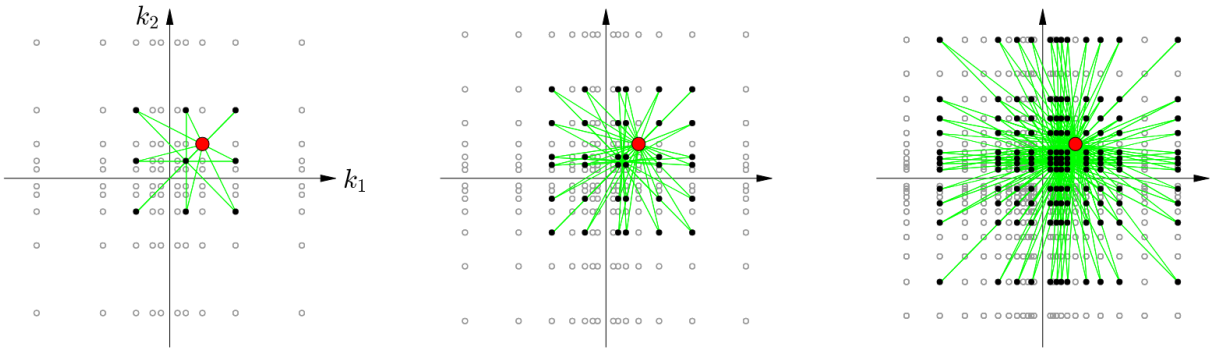


**Figure 3:** Triad interactions on two-dimensional logarithmic lattices for different spacing factors: (left) $\lambda = 2$; (middle) $\lambda = \phi$, the golden mean; (c) $\lambda = \sigma$, the plastic number. The red node $k$ can be decomposed into sums $k = p + q$ where all possible nodes $p$ and $q$ are indicated by the green lines. All figures are given in the same scale. From left to right, both the density of nodes and the number of triads per each node increase. (adapted from figure 2.2 in [Mar22])

often involves adjusting free parameters, leading to debates about their physical interpretation. In contract, log-lattices chose a different approach: rather than constructing an operator that conserves *a quantity of interest*, they build an operator that conserves *the mathematical properties of the continuous operator*[4]. Note that the symmetries naturally conserved by this process imply that quantities conserved in the original equations, such as energy, are also conserved on log-lattices.

The two operators introduced this way in [Mar19] are the inner (scalar) product

$$(f, g) = \sum_k |k|^\alpha f(k)\overline{g(k)}, \tag{2}$$

and the convolution

$$(f * g)(k) = \sum_k |k|^\alpha c_{\frac{p}{k},\frac{q}{k}} f(p)g(q), \tag{3}$$

where the *scaling exponent* $\alpha$ is linked to the measure of the log-lattice space, and where the $c_{i,j}$ are coefficients of known value.

Later in their PhD [Mar22], Campolina expanded this construction to

$$(f, g) = \sum_k |k|^\alpha f(k)\overline{g(k)}, \tag{4}$$

$$(f * g)(k) = |k|^\beta \sum_k \left|\frac{pq}{k^2}\right|^{\frac{\alpha+\beta}{3}} f(p)g(q), \tag{5}$$

where $|k|$ acts as the "volume of a lattice cell", and $\alpha, \beta$ "can be manipulated to change dimensionality and the scaling of terms"[5].

Having established how to express linear operators, scalar products, and convolutions on log-lattices is enough to simulate a wide range of equations.

[4]Obviously, not *all* the symmetries can be perfectly conserved (e.g. continuous translation)

[5]Those definitions are copied as-is from [Mar22] chapter 4, as they are provided with very little explanation, and can be interpreted in different ways.

### 0.1.4 Singularities of Euler Flow

Using those log-lattices, [Mar19] investigated the blowup of the Euler equations. They started by examining the 1D Euler and Navier-Stokes (Burgers) equations, where rigorous mathematical results are available. Additionally, in 1D, well-known shell models like the Sabra and DN shell models correspond to special cases within the log-lattice framework for specific parameters. Campolina et al. observed a finite-time blowup with a power law $|u|(k) \sim |k|^{-\xi}, \xi = 1.19$, close to the expected $\xi = 4/3$ theoretical blowup asymptotics. By introducing a small viscosity for regularization, the blowup disappeared, and the power law transitioned towards $\xi = 1$, indicating a shock solution.

Next, Campolina simulated the 3D Euler equation and observed a finite-time chaotic blowup with diverging maximum of the vorticity, linked to a chaotic traveling attractor on the Fourier grid (figure 1b). Around the blowup time $t_b$, the scaling of the location $k_{\max}$ of the maximum vorticity was found to be $k_{\max} \sim (t_b - t)^{-\gamma}, \gamma = 2.70$, corresponding to an energy spectrum $E(k) \sim k^{-\xi}, \xi = 3 - 2/\gamma \approx 2.26$.

The blowup of the 3D Euler equations serves as a compelling demonstration of the inherent advantage of log-lattices over DNS. The chaotic attractor spans approximately six decades of wavenumbers (figure 1b), where state-of-the-art DNS struggle to simulate five. Only at scales significantly beyond the reach of DNS, do we observe the more-than-double-exponential growth of vorticity, a critical feature of the blowup and a topic of much debate in DNS results.

In a subsequent work [CM21], they reinforced their findings by testing additional grid spacing ($\lambda = \phi, \sigma$) and conducting larger simulations (up to $k_{\max}/k_{\min} = 10^{14}$). While the blowup times and prefactors of the scaling laws varied, the exponents of the blowup remained consistent, and the chaotic attractors showed remarkable similarity despite the different resolutions.

### 0.1.5 Navier-Stokes equations

Following their investigation of the Euler equations, Campolina delved into the study of the Navier-Stokes equations (NSE) in [CM21], focusing on anomalous dissipation within the context of log-lattices. In large Reynolds number Re flows, where energy is injected at large scales, a characteristic feature of this anomaly is the emergence of a significant inertial zone or, equivalently, a substantial region of constant mean energy flux from large to small scales. By varying the viscosity from $\nu = 10^{-13}$ to $10^{-16}$ (which are ranges widely unreachable using DNS !), they observe that the energy flux converged to a well-defined value, and its range expanded as the viscosity decreased, indicating the development of a dissipation anomaly.

To explore the statistics further, they examined the probability distribution functions (PDFs) of $u_1(k)$ for several values of $k$, and surprisingly, they found the statistics to be Gaussian. This finding stands in contrast to other simplified models that often exhibit intermittency, reflected in non-Gaussian statistics. Campolina et al. suggested a possible explanation for this difference, hypothesizing that the relatively large number of triad interactions in log-lattices might weaken intermittency. However, reaching a definitive conclusion proved elusive, and they hinted at the need to develop appropriate tools, like structure functions on log-lattices, to thoroughly investigate intermittency in this framework.

### 0.1.6 Boundaries and log-lattices

Closely related to anomalous dissipation is the possible convergence of NSE solutions to Euler solutions as $\mathrm{Re} \to \infty$. In this context, the addition of boundaries introduces a significant change. Indeed, the boundary conditions are different for the two equations: no-slip $\boldsymbol{u} = \mathbf{0}$ for NSE,

and no penetration $\boldsymbol{u} \cdot \boldsymbol{n} = 0$ for Euler, making the convergence between the two impossible without forming a singularity. The logical continuation of the work presented above is therefore to add boundaries to log-lattices[Mar22]. In particular, this work focuses on the discontinuous formulation of the Navier-Stokes equations [GHS93].

In simple form, the discontinuous NSE write

$$\partial_t \boldsymbol{u} + \boldsymbol{u} \cdot \boldsymbol{\nabla} \boldsymbol{u} = -\boldsymbol{\nabla} p + \nu \boldsymbol{\Delta} \boldsymbol{u} + [\boldsymbol{\sigma} \cdot \boldsymbol{n}]\, \delta_{\mathcal{S}}, \nabla \cdot \boldsymbol{u} = 0, \tag{6}$$

where $[\boldsymbol{\sigma} \cdot \boldsymbol{n}]\, \delta_{\mathcal{S}}$ represents the jump of the stress tensor $\boldsymbol{\sigma}$ across the surface $\mathcal{S}$.

By reflecting the flow across the surface to obtain a flow field in the whole 3D space, this reduces to

$$\partial_t \boldsymbol{u} + \boldsymbol{u} \cdot \boldsymbol{\nabla} \boldsymbol{u} = -\boldsymbol{\nabla} p + \nu \boldsymbol{\Delta} \boldsymbol{u} - \nu \boldsymbol{J}(x, z, t)\delta(y), \nabla \cdot \boldsymbol{u} = 0, \tag{7}$$

for $y \neq 0$ and assuming that the surface is defined by $y = 0$, where the shear action exerted by the surface on the fluid $\boldsymbol{J}$ writes

$$J_x = \left[\partial_y u_x\right], J_y = 0, J_z = \left[\partial_y u_z\right]. \tag{8}$$

In order to compute $\boldsymbol{J}$, a new method is proposed, which consists in approximating $\delta_y$ in equation (7) by $\delta^\epsilon(y) \equiv \frac{1}{\epsilon\sqrt{\pi}} e^{-y^2/\epsilon^2}$, which yields

$$\boldsymbol{J}^\epsilon(x, z, t) = \frac{1}{\nu(\delta^\epsilon, \delta^\epsilon)_y}(-\boldsymbol{u} \cdot \boldsymbol{\nabla} \boldsymbol{u} - \boldsymbol{\nabla} p + \nu \Delta \boldsymbol{u}, \delta^\epsilon)_y, \tag{9}$$

where $(f, g)_y \equiv \int f g \, \mathrm{d}y$. An analogous approximation in Fourier space gives an equivalent formulation for the jump $\boldsymbol{J}$ on log-lattices.

Using this formula, [Mar22] investigate a Couette flow and a decaying shear flow. In both cases, they observe in the velocity spectra a plateau (corresponding to the inertial range in homogeneous turbulence) followed by a $k^{-2}$ tail (corresponding to the dissipative range in HT), which grows towards small wavelengths as time progresses. Comparing the results of the decaying shear flow with a corresponding DNS shows qualitatively similar features, with in particular a very good agreement in the behavior of $|J|(t)$. This result is a first step towards applying log-lattices to flows with boundaries.

### 0.1.7 Existing numerical framework

The numerical framework used in [Mar19; CM21; Mar22] is detailed in [Cam20]. This framework is written for Matlab, and although it provides a set of functions to perform some simulations on logarithmic lattices, it remains fairly simple. In particular, the following aspects are missing or lacking, in no particular order:

- proper support for $k_i = 0$ modes,
- multithreading, and optimized single-threaded performance,
- support for long simulations, which may be interrupted and resumed,
- long-term result storage,
- visualization and treatment tools for fields on log-lattices,

- access to the inner workings of the solver.

Moreover, the reliance on a proprietary software (Matlab) makes the wide diffusion of this framework difficult. There is therefore a need for a numerical framework that is adapted to Open Science requirements.

### 0.1.8 Log-lattices for geophysical flows

When I started my PhD, the only applications of log-lattices were therefore about academic problems in fluid dynamics, mainly connected to singularities and their consequences. There is however a completely different and more practical field of application of log-lattices, connected to geophysical flows. Indeed, geophysical flows are characterized by high Reynolds numbers, that are out of reach of classical DNS. For example, a rough order of magnitude of a DNS simulation of oceans on Earth (radius $R \approx 6 \cdot 10^3 km$, dissipative scale $\eta \approx 1mm$) requires $N \approx \left(\frac{R}{\eta}\right)^3 = (6 \cdot 10^9)^3 \approx 10^{29}$ degrees of freedom.

Current numerical simulations of geophysical flows, for instance in weather forecasting and climate change research, therefore rely on simplified models, such as Large Eddy Simulations (LES) and Reynolds-averaged Navier-Stokes (RANS), which aim to capture the dominant large-scale turbulent structures while modeling the smaller, unresolved scales. However, the accuracy of such methods heavily relies on the underlying turbulence model and the chosen closure assumptions that often require free adjustable parameters. There is however an alternative way to deal with this closure problem, linked with downscaling procedures, in which one injects in the large scale equations the characteristic transport laws derived by DNS or experiments. This procedure is popular in internal geophysics, where it is used to deduce conditions for dynamo onset, or for the intensity of heat transfers. The disadvantage of this procedure is that the derivation of the general scaling laws is often done in a range of parameter space that is far from real conditions, and some extrapolation is needed to obtain values relevant for Earth or other planets. Log-lattices could offer a cheap way ($N_{loglatt} \approx \left(\log_{1.6} \frac{R}{\eta}\right)^3 \approx 47^3 \approx 10^5$) to investigate relevant scaling laws at an affordable numerical cost. Given the log-lattice approximation, there is no hope to obtain exactly the correct scaling laws. However, since log-lattices respect the symmetries and conservation laws of the initial equations, we could be in a favorable situation where the exponents of the scaling laws are correct, and only the prefactors are wrong. In this case, it would take only one experiment or DNS to calibrate this constant, and we could get an efficient and reliable downscaling at a cheap cost.

To check this possibility, one needs to use log-lattices in conditions appropriate for geophysical applications, i.e. consider all sorts of additional forces such as rotation and stratification, compute the scaling laws of the corresponding transport quantities, and compare with some existing numerical or experimental data, to check both the exponent and the prefactors of the law. This thesis presents the first step towards such procedure.

## 0.2 Objectives and scope of the PhD

The central aim of this PhD research is to create a comprehensive suite of numerical tools that enable the efficient utilization of log-lattices across various scenarios. These tools are then applied to investigate several geophysical equations of interest using log-lattices. As our understanding of the practical capabilities and limitations of log-lattices was at the time very limited, this was by nature a fairly exploratory endeavor.

### 0.2.1 Development of a comprehensive numerical framework

The primary goal is to create an all-encompassing numerical framework for log-lattices. This involves the development of code for simulating equations on log-lattices and analyzing the simulation results. The framework should be user-friendly for physicists, optimized for speed, thoroughly documented, and built from open-source software.

### 0.2.2 Application to specific turbulence scenarios

The focus of the research will be on applying log-lattices to investigate geophysical turbulence scenarios of interest. Building on the existing Navier-Stokes results of Campolina, we investigate the influence of temperature and rotation on the flow. By exploring these scenarios, we aim to ascertain the applicability of log-lattices in geophysical contexts.

### 0.2.3 Identifying advantages and limitations of log-lattices

Log-lattices are a very young field of research. One lesser objective of this PhD is to gather information on the extent to which turbulence characteristics can be effectively captured on log-lattices. The research will also address potential limitations and challenges that must be tackled for broader adoption of log-lattice methods. Another crucial point is to understand the physical meaning of the log-lattice fields, particularly for performing Inverse Fourier Transforms.

# Part II

# The framework

# Chapter 1

# Mathematical framework

## Generic notation

We use $\equiv$ in place of $=$ to define new quantities: "Let $a \equiv \dots$" means "We define $a$ as being $\dots$".

$\delta_x \equiv \delta(x)$ denotes the Dirac delta distribution.

$\delta_{p,q}$ denotes the Kronecker delta function, equal to 1 if $p = q$ and 0 otherwise.

The complex conjugate of $z \in \mathbb{C}$ is $\overline{z}$.

Since we mostly work with functions in Fourier space, we write them without a hat $f \equiv \hat{f}$. Functions in real space are therefore written with a double hat: $\mathrm{TF}^{-1} f(k) \equiv \hat{\hat{f}}(x)$.

We use Einstein summation conventions $a_n b_n \equiv \sum_n a_n b_n$ whenever the set over which the sum is performed is clear from the context.

The complex number $\boldsymbol{i} \equiv \sqrt{-1}$ is always in bold, as opposed to the index $i$. In any other case, bold mathematical elements represent vectors: $\boldsymbol{x} = (x_1, \dots, x_n)$.

## 1.1 Log-lattices

### Takeaways

Logarithmic lattices, also known as "log-lattices", present a novel mathematical framework for examining equations on a spatial grid that is highly decimated and exponentially spaced. This framework proves to be highly advantageous when investigating scenarios where traditional simulations cannot handle the computational burden effectively. Log-lattices possess true multidimensionality, unlike shell models, and retain most of the symmetries found in the original equations without any additional parameters.

The spacing parameter $\lambda$ can take three main values $\lambda = 2$, $\lambda = \phi \approx 1.6$ and $\lambda = \sigma \approx 1.3$. These values are listed in ascending order of the number of interactions.

We advise against using $\lambda = 2$ for incompressible simulations.

### 1.1.1 Definition

The construction of log-lattices is detailed in section 0.1.2, then section 0.1.3 details how to write equations on log-lattices.

### 1.1.2 Remarks

There are some mathematical drawbacks to the log-lattice construction. Since log-lattices are nowhere associative, the convolution product also cannot be associative. Instead, it verifies a weaker property of associativity in average $(f * g, h) = (f, g * h)$ where $(\cdot, \cdot)$ is the inner (scalar) product. In particular, this only works for *three* functions, but is not defined for *four*. While this is not a problem for writing most fluid dynamics equations, it becomes an issue when thinking, for instance, about structure functions.

The second main drawback of this very "mathematical" formulation is that there is no canonical way (no way at all for now, actually) to go back to direct space, as discussed in section 1.2. This is an obvious obstacle when trying to compare log-lattice results and DNS results.

Nevertheless, log-lattices in their current form are already very capable. [CM21] show that it retain classical and basic properties of the Navier-Stokes equation, such as constancy of energy flux in the inertial range, over an unprecedented wide range of scales. They are used to track the blowup of the Euler equation [Mar19] or the hypoviscous Navier-Stokes equations [Pik+23], a well-known theoretical problem that DNS have not been able to provide an answer to.

Another interesting feature of log-lattices is that in 1D, they encompass classical shell models of turbulence for special values of the log-lattice spacing [CM21], such as the Sabra shell model and the Desnyansky-Novikov (dyadic) model of turbulence [Glo+85; Bif03].

### 1.1.3 Against using $\lambda = 2$ for divergence-free equations

This subsection explains why the log-lattice parameter $\lambda = 2$ is ill-suited to simulating divergence-free equations. This issue was first raised in our article [BD23].

$\lambda = 2$ is the biggest grid parameter that can be accommodated on a log-lattice. For a fixed grid size $N$ in dimension $D$, it is therefore very tempting to use $\lambda = 2$, since among all the $\lambda$s it spans the greatest range of wavenumbers (the convolution complexity rises as $O(N^D)$). However, $\lambda = 2$ misrepresents the convection term $u_j \partial_j u_i$.

The heart of the problem is easily understood through a simple 2D example. Consider the convection term $u_x \partial_x \omega + u_y \partial_y \omega$ of a divergence-free flow, with a large-scale initialization $u(k > k_0) = \omega(k > k_0) = 0$ for some $k_0$. From a physical point of view, we expect convection to populate the $k \geq k_0$ region as time advances. However, with $\lambda = 2$, this does not happen, as is demonstrated below.

In a divergence-free flow, $u_x * \partial_x \omega = -i \left( \frac{\omega k_y}{k^2} * k_x \omega \right), u_y * \partial_y \omega = i \left( \frac{\omega k_x}{k^2} * k_y \omega \right)$ where $*$ denotes a convolution. In a $\lambda = 2$ log-lattice, convolutions are defined as[1] $f * g(\lambda^n, \lambda^m) = f(\lambda^{n-1}, \lambda^{m-1}) \cdot g(\lambda^{n-1}, \lambda^{m-1})$. Due to the initial conditions, this yields:

$$\left(u_x * \partial_x \omega + u_y * \partial_y \omega\right)(k \approx k_0) = 0$$

.

There is no forward convection at all, therefore there can be no forward cascade in such case.

This does not happen for other values of $\lambda$, for which the convolution is evaluated at asymmetric positions. We therefore advise against using $\lambda = 2$ in divergence-free fluids, and suggest to rather use $\lambda = \phi$ (the second-biggest grid parameter).

Note that this issue does not arise in REWA systems, where the lack of symmetry in the interactions enables a net flux of momentum.

[1] excluding the $k = 0$ mode, which is not used in this paper

*Note: the same conclusion was reached independently and around the same time by Campolina, as written in [CM21] section 5.3: "We remark that the spacing factor $\lambda = 2$ does not provide a reliable model for the blowup study in the Euler equations. Indeed, the product on this lattice does not couple large to small scales except through diagonals, but the latter is prohibited by incompressibility."*

## 1.2 On Fourier Lattices: Towards a Physical Interpretation

*Special thanks to Germain Poullot for discussions on the constraints of $\zeta$ in the sparse case.*

### Takeaways

**There is no canonical interpretation of the fields that live on a log-lattice.** Several decompositions on Fourier lattices yield a mathematical structure that can be compared to that of log-lattices, each with their own approximations and hypothesis. Among those are Multiresolution Analysis (or wavelet decomposition), Littlewood-Paley decomposition and sparse decompositions.

Sparse decomposition (i.e. the idea that "log-lattices are a projection of the equations onto a grid of diracs") may seem like a simple idea, but it hides several non-trivial mathematical constrains.

The "best" candidates among sparse decompositions seem to be those in which we can decouple the true data ($\widetilde{f}(k) \propto f(k)$) from the "intrinsic scaling" ($\widetilde{f}(k)/f(k) \propto k^a$) such that there is a $k$-independant proportionality (up to projection approximations) between $\widetilde{f^2}$ and $(\widetilde{f})^2$.

Understanding this subject is crucial for developing techniques to connect direct space and log-lattices, performing inverse Fourier transforms of log-lattice fields, computing structure functions, etc.

### 1.2.1 Introduction

In [Mar19], operators on log-lattices are introduced with a $|k|^\alpha$ prefactor (equations (2) and (3)), where $\alpha \in \{0, 1\}$ is a "scaling exponent". This exponent is related to an "interpretation" of fields on log-lattices

$$f(k) \approx \frac{1}{|\lambda k - k|^\alpha} \int_k^{\lambda k} F(k')\,\mathrm{d}k', \tag{1.1}$$

where $F$ represents the continuous Fourier transform of some variable and $f$ is the discrete value on the log-lattice. Later works [CM21] however do not mention this exponent at all, and all equations are done as if $\alpha = 0$. Only in a small section[2] of [Mar22] does it come back as equations (4) and (5), where $|k|$ acts as the "volume of a lattice cell", and $\alpha, \beta$ "can be manipulated to change dimensionality and the scaling of terms". Note that this formulation is very vague, and unlike equation (1.1) does not give a concrete link between log-lattice fields and physical fields. Indeed, equation (1.1) is inherently flawed. In this representation, $f \sim k^{1-\alpha}$ but $f * g \sim k$ which only leaves $\alpha = 1/2 \notin \{0, 1\}$ as a possible value.

There is therefore a lack of interpretability of the physical meaning of fields on log-lattices, i.e. the relation between $f$ and $F$, and as presented thus far, log-lattices exist as a purely

[2] this generalized version is not explicitly used anywhere in the PhD of Campolina

mathematical construct. Although this is not necessarily an issue for many simulations where we look at aggregated observables such as energy, it is crucial for processes like performing an inverse Fourier transform on log-lattices.

In this chapter, we explore several ways to make sense of those quantities. Although none of those ways give a definitive answer, they offer some useful insight. The generic line of thought is to investigate several formulas for $f$ by decomposing and projecting $F$ along different basis, and comparing the resulting operators to those of log-lattices. We first investigate standard basis (sections 1.2.2 and 1.2.3), and in a second time turn our attention to projections on a family of distributions (section 1.2.4).

### 1.2.2 Generic Fourier lattices

We start by looking at the problem with an angle much broader than that of log-lattices. Given a generic Fourier lattice, we want to be able to project any function on this lattice, while retaining a mathematically consistent picture in the projected space.

Let $\mathbb{\Lambda}$ be a discrete lattice[3] of points in Fourier space in $D$ dimensions. Let $\mathbb{F} \equiv \mathbb{C}^{\mathbb{R}^D}$ be the space of functions from $\mathbb{R}^D$ to $\mathbb{C}$. Let

$$\mathcal{F} \equiv \left\{ f \in \mathbb{F} \mid \forall k \in \mathbb{F}, f(-k) = \overline{f(k)} \right\}, \tag{1.2}$$

be the space of Fourier functions. Let $(\psi_k)_{k\in\mathbb{\Lambda}}$ be a family of *real* functions of $\mathbb{F}$.

We endow $\mathbb{F}$ with its canonical scalar product $(f,g) \equiv \int \mathrm{d}k\, f(k)\overline{g(k)}$ and define the matrix

$$G_{m,n} \equiv (\psi_m, \psi_n), \tag{1.3}$$

which we assume is invertible.

Let $p$ be the projector from $\mathbb{F}$ to the space generated by the $\psi_m$, defined by[4]

$$p(f) \equiv \widetilde{f} \equiv \sum_{m\in\mathbb{\Lambda}} \psi_m \widetilde{f_m}, \tag{1.4}$$

$$\widetilde{f_m} \equiv \sum_{n\in\mathbb{\Lambda}} G^{-1}_{m,n}(\psi_n, f). \tag{1.5}$$

Using Einstein summation conventions, it is straightforward to show that $p$ is indeed a projector:

$$\begin{aligned} p^2 &= \psi_m G^{-1}_{m,n}(\psi_n, \psi_k G^{-1}_{k,q}(\psi_q, \cdot)), \\ &= \psi_m (G^{-1} G G^{-1})_{m,q}(\psi_q, \cdot), \\ &= p. \end{aligned} \tag{1.6}$$

We want $p$ to also be a projector on $\mathcal{F}$, which restricts the function space of $\psi_k$ to $\mathbb{F}_\psi$, defined as

$$\mathbb{F}_\psi \equiv \left\{ \psi \in \mathbb{F} \mid \forall k \in \mathbb{F}, \psi_p(-k) = \psi_{-p}(k) \right\}. \tag{1.7}$$

Indeed,

$$\begin{aligned} \overline{\widetilde{f}(k)} &= \psi_m(k)\overline{\widetilde{f_m}} = \psi_{-m}(k)\overline{\widetilde{f}_{-m}}, \\ \overline{\widetilde{f}_{-m}} &= G^{-1}_{-m,n}(\psi_m, \overline{f}) = G^{-1}_{-m,-n}(\psi_{-m}(k), f(-k)), \\ G^{-1}_{-m,-n} &= (\psi_{-m}, \psi_{-n}), \end{aligned} \tag{1.8}$$

[3] i.e. a countable ensemble

[4] In later sections, we may without justification generalize a result from 1D to higher dimensions, for instance by chosing $\psi_m \equiv \prod_{i=1}^{d} \psi_{m_i}$ where $m = (m_1, \ldots, m_D) \in \mathbb{R}^D$.

and thus $\overline{\widetilde{f}(k)} = \widetilde{f}(-k)$ iff equation (1.7) holds.

Note that in general $\mathbb{F}_\psi \neq \mathcal{F}$: $\psi_k$ is not a Fourier function, e.g. it can be localized around $k_0 > 0$ while being zero on $k < 0$.

#### 1.2.2.1 Scalar product, product and convolution

The scalar product of two projected functions $\widetilde{f}, \widetilde{g}$ writes

$$(\widetilde{f}, \widetilde{g}) = \widetilde{f}_p \overline{\widetilde{g}_q} G_{p,q}. \tag{1.9}$$

For a given bilinear form $B(f, g)$, the partially-projected form $B(\widetilde{f}, \widetilde{g}) = \widetilde{f}_k \widetilde{g}_q B(\psi_k, \psi_q)$ is in general *not* in the image of $p$, and thus we introduce the projected bilinear form

$$\widetilde{B}(\widetilde{f}, \widetilde{g}) \equiv \widetilde{\overline{B(\widetilde{f}, \widetilde{g})}} = \psi_k \widetilde{f}_p \widetilde{g}_q G^{-1}_{k,n} (\psi_n, B(\psi_p, \psi_q)). \tag{1.10}$$

In particular for the product we write

$$(\widetilde{\widetilde{f}\widetilde{g}})_k = \widetilde{f}_p \widetilde{g}_q G^{-1}_{k,n} (\psi_n, \psi_p \psi_q), \tag{1.11}$$

and for the convolution

$$(\widetilde{\widetilde{f} * \widetilde{g}})_k = \widetilde{f}_p \widetilde{g}_q \Gamma^k_{p,q}, \tag{1.12}$$

$$\Gamma^k_{p,q} \equiv G^{-1}_{k,n} (\psi_n, \psi_p * \psi_q). \tag{1.13}$$

Note that using equation (1.7) we have associativity in average

$$\forall f, g, h \in \mathcal{F}, (\widetilde{\widetilde{f} * \widetilde{g}}, \widetilde{h}) = (\widetilde{f}, \widetilde{\widetilde{g} * \widetilde{h}}). \tag{1.14}$$

This is due to the property $\forall \psi_p, \psi_n, \psi_q \in \mathcal{F}_\psi, (\psi_p, \psi_n * \psi_q) = (\psi_n, \psi_p * \psi_{-q})$, which is not the same as $\forall f, g, h \in \mathcal{F}, (f, g * h) = (g, f * h)$.

### 1.2.3 Complete, orthogonal and fully orthogonal Fourier lattices

So far, we have made almost no assumption on the $\psi_p$, which only verify equation (1.7) and $\det G_{m,n} \neq 0$. In this section, we gradually add more constrains to go towards cases that are more practical, and we illustrate with some concrete examples.

#### 1.2.3.1 Complete Fourier lattices

We call the lattice *complete*[5] when the $\psi_p$ form a basis of $\mathcal{F}_\psi$, i.e. $\sum_{p \in \mathbb{\Lambda}} \psi_p = 1$.

[5]We use a slight abuse of language where we associate the lattice $\mathbb{\Lambda}$ and the family of functions $\psi_p$. A more rigorous approach would be to consider $(\mathbb{\Lambda}, \psi_{p, p \in \mathbb{\Lambda}})$.

#### 1.2.3.2 Complete orthogonal Fourier lattices: the case of Multi-Scale Resolution

**Definition** We call the lattice *orthogonal* when $G_{m,n} = \delta_{m,n} G_{m,m}$. In an orthogonal lattice $G^{-1}_{m,n} = \frac{\delta_{m,n}}{G_{m,n}}$, and therefore generic equations take a simplified form:

$$\widetilde{f} = \sum_{m \in \mathbb{\Lambda}} \psi_m \frac{(\psi_m, f)}{G_{m,m}}, \tag{1.15}$$

$$(\widetilde{f}, \widetilde{g}) = \sum_{p \in \mathbb{\Lambda}} \widetilde{f_p} \widetilde{g_p} G_{p,p}, \tag{1.16}$$

$$\widetilde{B}(\widetilde{f}, \widetilde{g}) = \sum_{k \in \mathbb{\Lambda}} \psi_k \widetilde{f_p} \widetilde{g_q} \frac{(\psi_k, B(\psi_p, \psi_q))}{G_{k,k}}. \tag{1.17}$$

**Multiresolution Analysis** Multiresolution analysis (MRA) is a powerful tool for analyzing signals at different scales and resolutions, and was introduced by Stéphane Mallat'[Mal89] in the early 1990s. The basic idea behind multi-resolution analysis is to decompose a signal into multiple subbands of increasing frequency using a wavelet transform, allowing us to analyze the signal structure at different scales. Our goal here is not to go into the details of MRA, but to sketch a mathematical correspondence with the framework we have described so far.

Starting from a function $\hat{\hat{f}} : [0, 1] \to \mathbb{C}$, one can decompose it as

$$\hat{\hat{f}}(x) = \hat{\hat{f}}_0 \hat{\hat{\phi}}_0(x) + \sum_{j=1}^{N-1} \sum_{i=0}^{2^j - 1} (\hat{\hat{f}} * \overline{\hat{\hat{\psi}}_j})(b_i^{(j)}) \hat{\hat{\psi}}_j(x - b_i^{(j)}), \tag{1.18}$$

where $N \in \mathbb{N}$, $b_i^{(j)} \equiv i 2^{-j}$ and $\hat{\hat{\psi}}_j$ is a localizing function around $k = 2^j$ (i.e. "at scale $2^{-j}$").

Taking the Fourier transform and using a slight approximation[6] $\psi_j(k) \propto \delta_{k,2^j}$, we get

$$\widetilde{f}(k = 2^j) = \sum_{i=0}^{2^j - 1} (\hat{\hat{f}} * \overline{\hat{\hat{\psi}}_j})(b_i^{(j)}) e^{i 2^j b_i^{(j)}} = TF_{2^j}\left(\hat{\hat{f}} * \overline{\hat{\hat{\psi}}_j}\right), \tag{1.19}$$

where $TF_s$ represents the Fourier transform "at scale $s$".

By construction, the wavelet decomposition is a complete lattice, and by design the $\psi_j(k)$ form an orthonormal basis, and therefore this describes a complete orthogonal Fourier lattices.

There is however no easy way to simplify equations (1.15)–(1.17) with this formalism, which only leads to more complicated formulas when expanded using equation (1.18). Although we did not find the time to do it, to properly compare MRA and log-lattices, one then needs to compute (numerically if necessary) $G_{p,q}$ and $\Gamma^k_{p,q}$, and compare them to the log-lattice formulas (equations (2) and (3)), as we do in the following section with the Littlewood-Paley decomposition.

#### 1.2.3.3 Complete fully orthogonal Fourier Lattices: the case of the Littlewood-Paley decomposition

**Definition** We call the lattice fully orthogonal when $\psi_p \psi_q = \delta_{p,q} \psi_p^2$. If the lattice is also complete, it follows that $\psi_p(k) \in \{0, 1\}$. In other words, the $\psi_p$ pave the space $\mathbb{R}^D$ into disjoint

[6] This corresponds to the projection $f \to \widetilde{f}$

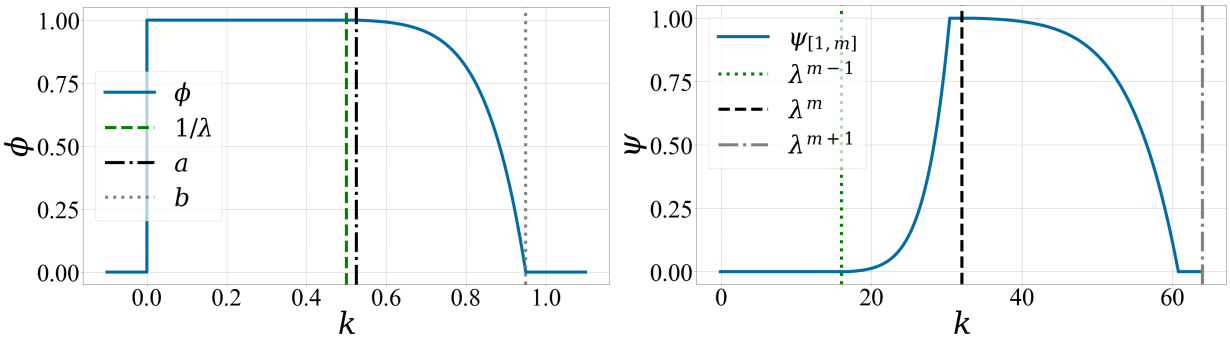


**Figure 1.1:** (1.1a) A possible shape for $\phi(k)$ given $\lambda = \frac{1+\sqrt{5}}{2}$ and an arbitrary choice of $a, b$. (1.1b) $\psi_{[\lambda^n]}$ with $n = 5$ for the same parameters as 1.1a.

intervals. In a complete fully orthogonal lattice, orthogonal equations take a simplified form:

$$\widetilde{f}(k) = \mathbb{1}_{k\in I_p} \langle f \rangle_{I_p}, \tag{1.20}$$

$$G_{p,q} = |I_p| \delta_{p,q}, \tag{1.21}$$

$$(\widetilde{f}, \widetilde{g}) = |I_p| \langle f \rangle_{I_p} \langle g \rangle_{I_p}, \tag{1.22}$$

$$\widetilde{\widetilde{f}\widetilde{g}} = \mathbb{1}_{k\in I_p} \langle f \rangle_{I_p} \langle g \rangle_{I_p}, \tag{1.23}$$

$$\Gamma^n_{p,q} = \left\langle \mathbb{1}_{k\in I_p} * \mathbb{1}_{k\in I_q} \right\rangle_{I_n}, \tag{1.24}$$

where $I_p \equiv \left\{k \in \mathbb{R}^D | \psi_p(k) \neq 0\right\}$ is the interval covered by $\psi_p$, $\langle f \rangle_{I_p} \equiv \frac{1}{|I_p|} \int_{I_p} \mathrm{d}k f(k)$ is the average value of $f$ over $I_p$ and $|I_p| \equiv \int_{I_p} \mathrm{d}k$ is the length of $I_p$.

### The Littlewood-Paley decomposition

**Introduction** Traditional Littlewood-Paley theory introduces a partition of Fourier space into "dyadic" blocs of exponentially increasing width $2^j, j \in \mathbb{Z}$. It is very well described in [Bah17] (in French; see [Bah19] for a shorter English version), and is widely used in mathematics to characterize regularity properties through the behavior of the dyadic blocs.

We hereafter use a slightly more generic approach, where the grid step $\lambda$ can be different from $\lambda = 2$. We introduce the basics in 1D, and then generalize to higher dimensions.

The partition is defined as follows. Let $\lambda > 1$ and $\mathbb{\Lambda} \equiv \lambda^{\mathbb{Z}}$. Let $\phi(k) : \mathbb{\Lambda} \to \mathbb{R}_+$ be a non-negative, non-increasing function such that $\phi(0 \leq k \leq a) = 1$ and $\phi(x < 0 | x \geq b) = 0$ where $a, b \in \mathbb{R}_+$ verify $a < b < 1 < \lambda a$ (figure 1.1a). We then introduce $\psi_{k_0}$ as

$$\psi_{k_0}(k) \equiv \phi\left(\frac{k}{\lambda k_0}\right) - \phi\left(\frac{k}{k_0}\right), k_0 \in \mathbb{\Lambda}, \tag{1.25}$$

and write $\psi \equiv \psi_1$. By definition $\psi_{k_0}$ is non-negative, equals one on the interval $k \in [k_0 b, k_0 \lambda a]$, and vanishes to 0 outside (figure 1.1b); it "localizes" information around $k = k_0$.

By construction, $\phi$ and $\psi$ form a partition of unity (figure 1.2)

$$\forall k_0 \in \mathbb{\Lambda}, \phi\left(\frac{|k|}{k_0}\right) + \sum_{p\in\mathbb{\Lambda}, |p|>|k_0|}^{\infty} \psi_p(k) = 1, \tag{1.26}$$

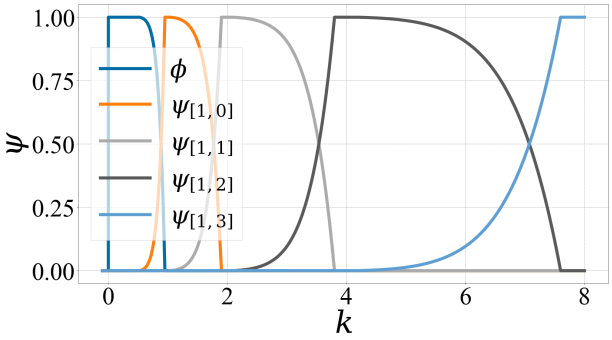


**Figure 1.2:** $\phi$ and $\psi$ partition the space in the Littlewood-Paley decomposition.

which is quasi-orthogonal

$$\begin{aligned} &\forall p, q \in \mathbb{\Lambda}, \psi_p(q) = \delta_{p,q}, \\ &\qquad \psi_p \psi_q = 0 \text{ if } |\log_\lambda(p) - \log_\lambda(q)| > 1 \text{ or } \operatorname{sign}(p) \neq \operatorname{sign}(q). \end{aligned} \tag{1.27}$$

In the context of log-lattices, we would rather have $\phi$ represent only the $k = 0$ mode, and $\psi$ all the other modes. We can therefore rewrite (1.26) as

$$\phi(0)\,\delta_0 + \sum_{k \in \mathbb{\Lambda}^*} \psi_k = 1. \tag{1.28}$$

which further simplifies to

$$\sum_{k \in \mathbb{\Lambda}} \psi_k = 1, \tag{1.29}$$

by taking the notation $\psi_0 \equiv \delta_0$.

We now make a "localization approximation":

$$f(k) = \sum_{p \in \mathbb{\Lambda}} \psi_p(k) f(k) \approx \sum_{p \in \mathbb{\Lambda}} \psi_p(k) f_p \equiv f^{\mathrm{loc}}(k), \tag{1.30}$$

where $f_p \equiv \langle f \rangle_{I_p}$.

Note that thus far, we have *not* created a Fourier lattice as defined in the above sections. Indeed, $f^{\mathrm{loc}} \neq \widetilde{f} = \sum_{p \in \mathbb{\Lambda}} \psi_p G^{-1}_{p,q}(\psi_q, f)$. However, in the limit $a = b$ which we will explore later, the lattice becomes fully orthogonal, and we recover $f^{\mathrm{loc}} = \widetilde{f}$.

**Operations on localized functions** We have $(f^{\mathrm{loc}}, g^{\mathrm{loc}}) = f_p \overline{g_q} G_{p,q}$ where

$$G_{p,q} = \int dk \psi_p(k) \overline{\psi_q}(k) = |p| \int \mathrm{d}k \psi(k) \psi(\frac{kp}{q}). \tag{1.31}$$

Likewise,

$$(f^{\mathrm{loc}} * g^{\mathrm{loc}})^{\mathrm{loc}}(k) = \psi_k f_p g_q \Gamma^k_{p,q}, \tag{1.32}$$

$$\Gamma^k_{p,q} = \left\langle |p| \int \mathrm{d}x \psi(x) \psi(\frac{k' - px}{q}) \right\rangle_{I_k}. \tag{1.33}$$

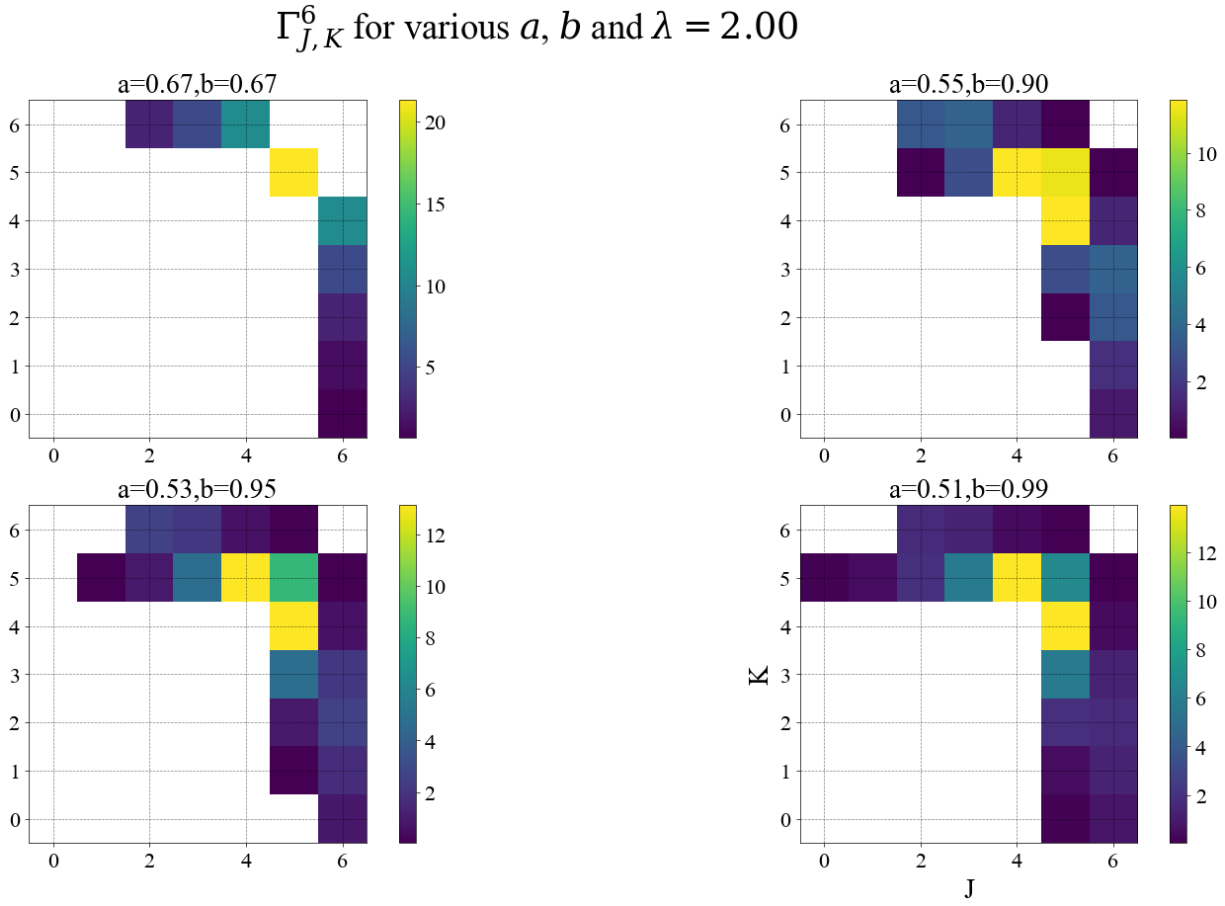


**Figure 1.3:** Absolute value of $\Gamma^k_{k-i,k-j}$ in the Littlewood-Paley decomposition for different choices of parameters $a, b$ for $k = 6, \lambda = 2$. The log-lattice behavior corresponds to $\Gamma_{5,5} \neq 0$ as the only nonzero value, which is closest to the top-left picture corresponding to $a = b$. The apparent lack of symmetry is due to floating point errors.

**Correspondence with log-lattices** In order to recover formulas coherent with log-lattices, we want that

$$G_{p,q} \propto \delta_{p,q}, \tag{1.34}$$

$$\Gamma^k_{p,q} \propto \delta_{p+q,k}. \tag{1.35}$$

As illustrated[7] in figures 1.3 and 1.4, the closest approximation we can get happens in the limit $a = b$ (which trivially satisfies equation (1.34)). This limit corresponds to a fully orthogonal (complete) lattice.

However, even in that limit, there remain irreducible differences, which by construction indicate a loss of symmetry in the projection's operators compared to those of the log-lattice, and thus in the next subsection we look at a different kind of decomposition.

### 1.2.4 Sparse Fourier lattices

Up to now, we have investigated the case where we project our physical quantities onto a mathematically "simple" basis, where the $\psi_p$ have been defined as "standard" functions. How-

[7]The python script used to compute those results can be found in the additional resources, in `Examples/LittlewoodPaley`

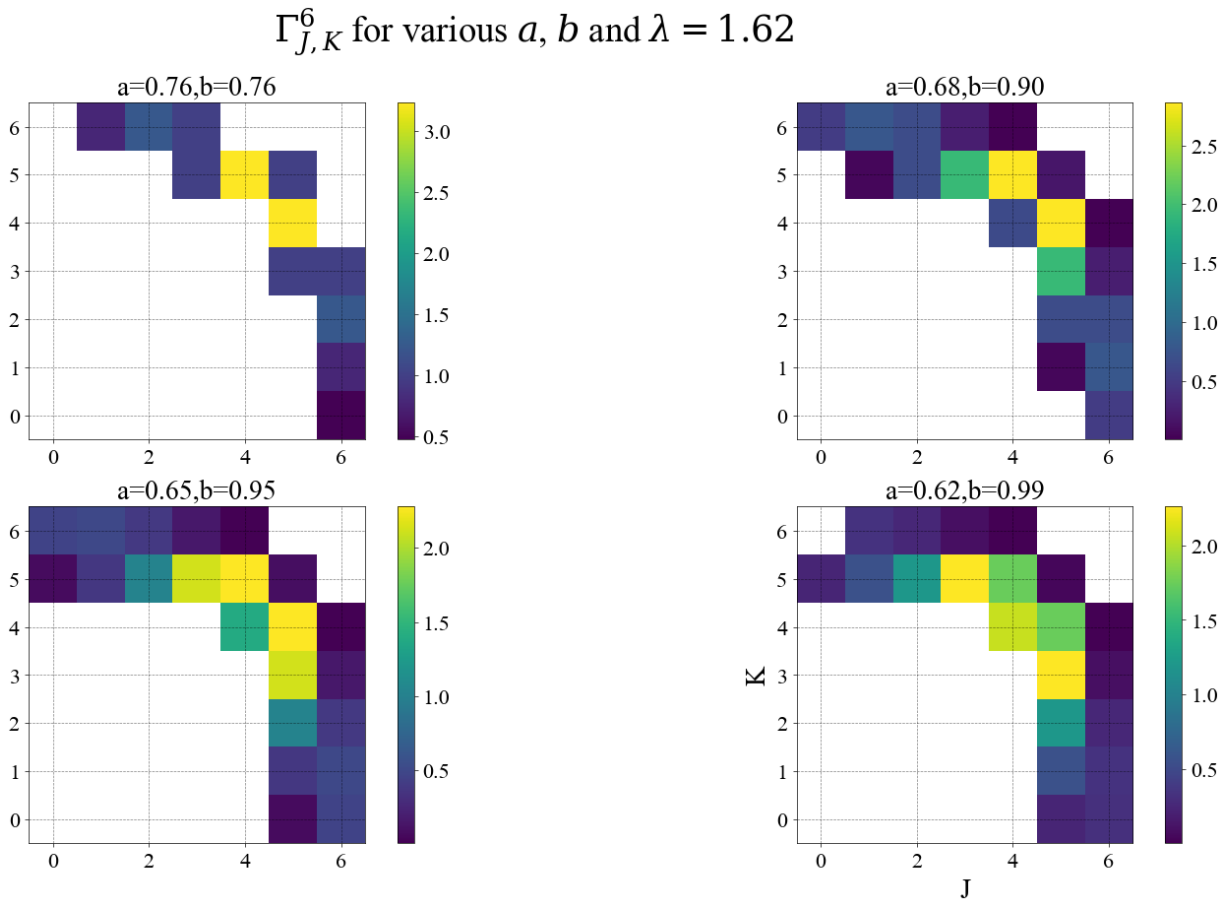


**Figure 1.4:** Absolute value of $\Gamma^k_{k-i,k-j}$ in the Littlewood-Paley decomposition for different choices of parameters $a, b$ for $k = 6, \lambda = \phi$. The log-lattice behavior corresponds to $\Gamma_{4,5} = \Gamma_{5,4} \neq 0$ as the only nonzero values, which is closest to the top-left picture corresponding to $a = b$. The apparent lack of symmetry is due to floating point errors.

ever, one way to make a correspondence between log-lattices and continuous space is to instead assume that log-lattices represent a *sparse* sampling of continuous space, i.e. for instance $\psi_p(k \neq p) = 0, \left\|\psi_p\right\|_2 > 0$, which naturally brings us into a realm other than that of functions. This new representation is not a mere extension of section 1.2.3, but another kind of decomposition altogether, and the examples outlined above (MRA, Littlewood-Paley) cannot be expressed in this new formalism.

In this section, we consider generalized functions[8] $\psi_p \equiv \lim_{\epsilon\to 0} \psi_p^\epsilon$ that are the "limit" of functions $\psi_p^\epsilon$ each supported on an interval of size $O(\epsilon)$, i.e. $\left\|\{k|\psi_p^\epsilon(k) > 0\}\right\|_1 = O(\epsilon)$. In other words, they are nonzero only at one point $[p]$: $\psi_p(k \neq [p]) = 0$. Up to a reordering of the $\psi_p$, we chose $[p] = p$.

This means that any property or expression $P(f \in \mathbb{F})$ defined on functions can be used as $P(\psi_m) \equiv \lim_{\epsilon\to 0} P(\psi_m^\epsilon)$, and likewise if several such objects appear, we have $P(\psi_m, \dots, \psi_n) \equiv \lim_{\epsilon\to 0} P(\psi_m^\epsilon, \dots, \psi_n^\epsilon)$.[9]

#### 1.2.4.1 Why we need a new formalism

The transition from "standard" functions to $\psi_p$-like objects requires some changes in the formalism used in Generic Fourier lattices. This is due to elementary metric issues.

Indeed, from the Cauchy-Schwarz inequality one gets

$$\left\|\psi_p^\epsilon\right\|_1 \leq \left\|\psi_p^\epsilon\right\|_2 O(\epsilon), \tag{1.36}$$

which implies that for $\left\|\psi_p\right\|_2 < \infty$ we need $\left\|\psi_p\right\|_1 = 0$. Since the $\psi_p$ are sparse, we can assume without loss of generality[10] that they are fully orthogonal, and using equation (1.15) we get $\widetilde{f_m} \propto \frac{\|\psi_m\|_1}{\|\psi_m\|_2} = 0$: the projector is always zero.

Another way to look at the same issue is to realize that "projector" $\widetilde{\cdot}$ now exists in a space different from $\mathcal{F}$ and $\mathcal{F}_\psi$, since the $\psi_p$ are not functions, and therefore is not a projector anymore on $\mathcal{F}$.

#### 1.2.4.2 Generic sparse Fourier lattices

We now expand part of the formalism developed in earlier sections to sparse Fourier lattices.

Let $\widetilde{\mathcal{F}}$ be the space of countable sums of $\psi$-like[11] objects with zero 1-norm and nonzero 2-norm. For sparse Fourier lattices, we define the projector $\widetilde{\cdot}$ in two ways:

$$\forall f \in \mathcal{F}, \widetilde{f} \equiv \psi_m \frac{(\psi_m, f)}{(\psi_m, 1)} \equiv \psi_m f([m]), \tag{1.37}$$

$$\forall f \in \widetilde{\mathcal{F}}, \widetilde{f} \equiv \psi_m \frac{(\psi_m, f)}{G_{m,m}}, \tag{1.38}$$

where $f_{[m]} \equiv f([m]) = f(x)|_{\psi_m(x)\neq 0}$.

This new projector on $\mathcal{F} \cup \widetilde{\mathcal{F}}$ projects functions onto $\widetilde{\mathcal{F}}$.

[8] There might be a prettier way to do the same thing with a distribution formalism, but I am unsure it would clarify anything.

[9] Note that this requires a certain care in writing expressions, as we cannot freely move limits around. For instance, if $\|\psi_m\|_2 > 0$, we can have both $\|\psi_m\|_1 = 0$ and $\|\psi_m\|_1 / \|\psi_m\|_1 = 1$ !

[10] up to collinear members

[11] i.e. the limit of a sequence of functions, as defined above, but without the $\epsilon$ constraint

For two functions $f, g \in \mathcal{F}$, we then have

$$(\widetilde{f}, \widetilde{g}) = f_{[p]} g_{[p]} \left\|\psi_p\right\|_2^2, \tag{1.39}$$

$$\widetilde{B}(\widetilde{f}, \widetilde{g}) = \psi_p f_{[m]} g_{[n]} B(\psi_m, \psi_n)_{[p]}, \tag{1.40}$$

$$\widetilde{\widetilde{f}\widetilde{g}} = \psi_p f_{[p]} g_{[p]} \left\|\psi_p\right\|_2^2, \tag{1.41}$$

$$\Gamma_{p,q}^k = (\psi_p, \psi_q)_{[k]} = \delta_{[k],[p]+[q]} \int \mathrm{d}x \psi_m(x) \psi_n([p] - x). \tag{1.42}$$

#### 1.2.4.3 Constraining $\psi$

**The $\alpha = \beta = 1$ case** We are searching for functions $\psi_p$ such that equations (1.39) and (1.42) correspond to their formulation on generalized log-lattices (equations (4) and (5)) for $\alpha = \beta = 1$:

$$(\widetilde{f}, \widetilde{g}) = f_{[p]} g_{[p]} |p|, \tag{1.43}$$

$$\Gamma_{p,q}^k = |k| |\frac{pq}{k^2}|^{2/3}. \tag{1.44}$$

We also want the $\psi$ to be scale-invariant, such that

$$\psi_p(k) = \psi_1(k/p) \equiv \psi(k/p). \tag{1.45}$$

From equations (1.43)–(1.45) we deduce

$$\|\psi\|_2 = 1, \tag{1.46}$$

$$\Gamma_{p,q}^{p+q} = |p| \int \mathrm{d}x \zeta(x) \zeta\left(-\frac{p}{q} x\right), \tag{1.47}$$

where $\zeta(x) \equiv \psi(1 + x)$.

Looking at a few special cases, we see several kinds of behaviors.[12] If $\zeta$ is a rectangle $\zeta^\epsilon(|k| < \epsilon) = \sqrt{2\epsilon}$ we get $\Gamma_{p,q}^{p+q} = \min(p, q)$. If $\zeta$ is exponential $\zeta^\epsilon(|k| < \epsilon) \propto \exp(-k^{2n}/(2\epsilon^{4n}))$ then $\Gamma_{p,q}^{p+q} = \frac{\sqrt[n]{2}|pq|}{\sqrt[n]{|p|^n + |q|^n}}$. However, most of those functions are not interesting choices, because they do not allow associativity in average for the convolution.

**Associativity in average** In sparse Fourier lattices, associativity in average (equation (1.14)) is no longer guaranteed. After some computation, one can rewrite equation (1.14) as

$$\forall a \in \mathbb{R}, \mathring{\Gamma}_a = \mathring{\Gamma}_{-a-1}, \tag{1.48}$$

where $\mathring{\Gamma}_{p/q} \equiv \frac{\Gamma_{p,q}^{p+q}}{|p|} = \int \mathrm{d}x \zeta(x) \zeta\left(-\frac{p}{q} x\right)$. The existence of solutions $\psi$ to equation (1.48) is nontrivial. However, we can make a few simple observations that show that if such solutions exist, they are very constrained.

Differentiating with respect to $a$, we obtain

$$\forall i \geq 3, \int \mathrm{d}x x^i \zeta(x) \zeta^{(i)}(-ax) = 0, \tag{1.49}$$

[12] The Mathematica notebook used to derive those results for arbitrary functions can be found in the additional resources, in `Examples/LittlewoodPaley`

where $\zeta^{(i)}$ is the $i$-th derivative of $\zeta$.

A natural space of solutions to consider is $\mathring{\Gamma}_a = G(a(1+a))$ for some function $G$, which always satisfies equation (1.48).

Under this assumption, however, $\zeta$ cannot be even. If it were, then $\mathring{\Gamma}_a = \mathring{\Gamma}_{-1-a} = \mathring{\Gamma}_{1+a} = \cdots = \mathring{\Gamma}_{1+na}, n \in \mathbb{Z}$ which is incompatible with the compact support hypothesis on $\psi^\epsilon$.

Moreover, under this same assumption, we can write $\int \mathrm{d}x\zeta(x)\,(\zeta((1+a)x) - \zeta(-ax)) = 0$ which after setting $a \equiv h - 1/2$ and taking the limit $h \to 0$ yields

$$\int \mathrm{d}x\zeta(x)\zeta^{(1)}(\frac{x}{2}) = 0. \tag{1.50}$$

**The $\alpha \neq 1$ case** We assume that we have found solutions to equations (1.43) and (1.44) for $\alpha = \beta = 1$.

By introducing $f^{(\alpha)} \equiv |k|^{(1-\alpha)/2} f$ we can establish a correspondence with log-lattice formulas for $\alpha \neq 1$. Indeed,

$$(f,g) = |k|^\alpha f_k^{(\alpha)} \overline{g_k^{(\alpha)}}, \tag{1.51}$$

$$(f*g)^{(\alpha)}(k) = \sum_{p+q=k} \left|\frac{pq}{k}\right|^{(1-\alpha)/2} f_p^{(\alpha)} g_q^{(\alpha)} |k| \left|\frac{pq}{k^2}\right|^{2/3} \tag{1.52}$$

which we can rewrite

$$(f*g)^{(\alpha)}(k) = |k|^\beta \sum_{p+q=k} f_p^{(\alpha)} g_q^{(\alpha)} \left|\frac{pq}{k}\right|^{(\alpha+\beta)/3}, \tag{1.53}$$

where $\beta = (\alpha+1)/2$.

**General case** Starting from solutions to equations (1.43) and (1.44) for given $\alpha, \beta$ and defining $f^{(\alpha',\alpha)} \equiv |k|^{(\alpha-\alpha')/2} f$, we can likewise write

$$(f,g) = |k|^{\alpha'} f_k^{(\alpha',\alpha)} \overline{g_k^{(\alpha',\alpha)}}, \tag{1.54}$$

$$(f*g)^{(\alpha',\alpha)}(k) = |k|^{\beta'} \sum_{p+q=k} f_p^{(\alpha',\alpha)} g_q^{(\alpha',\alpha)} \left|\frac{pq}{k^2}\right|^{(\alpha'+\beta')/3}, \tag{1.55}$$

where $\beta' = \beta + (\alpha' - \alpha)/2$.

## 1.2.5 Discussion

In the previous section, we have introduced several ways of projecting Fourier functions onto different kinds of lattices, with concrete examples. Each of the examples studied give an insight onto a possible interpretation of log-lattices from a physical point of view.

### 1.2.5.1 Non-sparse lattices

In non-sparse lattices, and in particular complete orthogonal lattices, we never recover the exact formalism used in log-lattices. However, we can interpret log-lattices as an approximation of each example in the $\alpha = 0$ case. This parallel is particularly easy to see in the Littlewood-Paley case, where the scaling of the convolution operator is easy to derive.

**Table 1.1:** Correspondence between log-lattices and sparse lattices for $\beta' = \beta + (\alpha' - \alpha)/2$. As outlined in the text, this correspondence is ill-suited for practical applications.

| Log-lattice | Sparse Fourier lattice |
|---|---|
| $(f, g)$ | $(f, g)$ |
| $f * g$ | $(f * g)^{(\alpha', \alpha)}$ |
| $f_k$ | $f^{(\alpha', \alpha)} \equiv \lvert k \rvert^{(\alpha - \alpha')/2} f$ |

One interesting difference between MRA and Littlewood-Paley lies in the inverse Fourier process. To perform an inverse Fourier transform (IFT) in the Littlewood-Paley case, we first create a regular Fourier grid at the smallest resolution $k_{\min}$ available on the lattice, fill it with the lattice's data, then we apply the IFT to this grid

$$IFT(u)(x) = \sum_k u_k e^{ikx}. \tag{1.56}$$

In MRA however, the wavelet decomposition implies another behavior. Indeed, each point $k$ of the grid is associated with an operator at scale $S_k$. To perform an IFT, instead of performing a "regular" IFT on a grid filled with data at the smallest scale $S_{k_{\min}}$, we perform the IFT at scale $S_k$ for each $k$:

$$IFT(u)(x) = \sum_{S_k} \sum_{k' | S'_k = S_k} u_{k'} e^{ik'x}. \tag{1.57}$$

#### 1.2.5.2 Sparse lattices

In sparse lattices, the exact form of the convolution operator greatly depends on the shape of the basis. However, assuming that one basis exists such that we match the $\alpha, \beta$ case, we find that we can find a meaning to any $\alpha', \beta'$ case, provided that $\beta' = \beta + (\alpha' - \alpha)/2$.

We then have the correspondence outlined in table 1.1.

Note however that setting $\alpha' = 0$ imposes $\beta' = 1/2$, which does not correspond to $\alpha' = \beta' = 0$ which we have taken so far in our simulations ! Indeed, this interpretation has a major flaw. When rescaling $u^{(\alpha)} = |k|^{(1-\alpha)/2} u$, we get ${u^{(\alpha)}}^2 = |k|^{1-\alpha} u^2 \neq u^{2(\alpha)}$ ! This is not an acceptable behavior, since we deal with nonlinear terms all the time. The only case that escapes this issue is, without surprise, the $\alpha = \beta = 0$ case.

#### 1.2.5.3 Leveraging equipartition in the log-lattice $\alpha = \beta = 0$ case

In the log-lattice $\alpha = \beta = 0$ case, for an energy $E \equiv (u, u)$, equipartition trivially yields $u(k) = constant$ (i.e. $E(k) \propto 1/k$). This is indeed what we observe by doing truncated Euler simulations (figure 1.5).

This simple observation gives us some additional clues to think about log-lattices. For instance, equations (3.4) and (3.5) of [Mar19] suggest an interpretation of functions on log-lattices. However, for $\alpha = \beta = 0$[13], this interpretation $\widetilde{u}(k) \approx \int_{k \leq k < \lambda k} \mathrm{d}k' u(k')$ is *not* coherent with a $\widetilde{u}(k) = constant$ equipartition on log-lattices[14].

One interpretation that *is* coherent with equipartition is a REWA-like projection. REWA [EG91; GL92; GL94] consists in taking a regular Fourier grid, pruning some components at random around $k_{\min}$, and replicating that random pattern by a scaling argument for greater wavenumbers.

[13] The $\beta$ had not been introduced yet in this paper, see (4.2) in [Mar22].

[14] Likewise, the $\alpha = \beta = 1$ case suffers from the same issue.

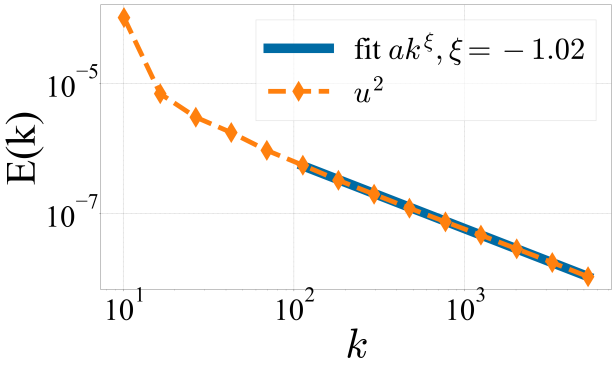


**Figure 1.5:** Energy spectrum for the Euler equations on a fixed size grid. The blue dashed line fits a $1/k$ slope.

In the same spirit, given the smallest scale of the grid $k_{\text{min}}$, one can interpret a log-lattice as a simulation on a regular grid whose only active[15] modes are pixels of size $k_{\text{min}}$ centered around $k \in \mathbb{\Lambda}$. Note that this process corresponds to a non-complete fully orthogonal lattice. Under this hypothesis, it is clear that the simulation is *extremely* sparse. This interpretation however not fully satisfying, as it relies on $k_{\text{min}}$, which may be redefined as the grid size evolves. This issue can be solved by transitioning from a basis of constant size $k_{\text{min}}$ to a sparse Fourier lattice, as outlined in the previous sections.

[15] meaning that all other modes are set to 0

# Chapter 2

# Numerical framework

---

*Special thanks to Hadrien for helping optimize the convolution code.*

A significant portion of the time of this PhD was spent on building a numerical framework to efficiently perform simulations on log-lattices. This framework went through many iterations and experimentation, most of which are documented in the code's changelog. **The goal of this section is not to go through the minute details of the framework**, but rather to concisely expose to physicists the main driving ideas of its development, its generic characteristics, and a minimal working example. Some technical details, such as precise numerical optimizations, are discussed in the appendix (appendix A). Many additional pieces of documentation can be found in the source code itself.

The code is available on Github, and on Pypi via `pip install pyloggrid`. A documentation is hosted here.

## 2.1 Key features

**Open-source** The entire numerical framework is built from scratch using Python 3.11 for the most part, with two optimized sections in Cython and C. Unlike the original Matlab framework of [Cam20], the code is thus open-source and non-proprietary[1].

**Designed for physicists** The framework provides an intuitive and user-friendly interface for simulating and analyzing complex systems, to minimize the time spent coding rather than researching. A minimal example of such code is given in section 2.2. The two main aspects of this feature are the readability of the written equations in the code, and the vast number of tools to easily analyze results on log-lattices. Having worked with this framework for over three years, and having collected the feedback of my collaborators and colleagues, many quality-of-life features and tweaks have been added.

**Adaptive grids** Highly intermittent flows may require punctually high grid sizes. To optimize numerical resources, the grid size can be automatically adapted using a user-based criterion, such as the fraction of the energy in the outer shells.

[1] The current license is CC BY-NC-SA 4.0

**Documented, typed and tested** The code is inline-documented and extensively tested using a battery of unitary and functional automated tests. An online documentation is also available[2], but is still incomplete. Taking advantage of recent Python updates, the code is also typed.

**Flexibility and high performance** The framework combines the ease of use and readability of Python with the speed and performance of compiled C. As Python is a very user-friendly programming language, the code can easily be modified to accommodate any specific needs, such as custom solvers in RNS (section 5.3). Moreover, the code is by nature modular, and allows new components to be added without changing the existing structure. Performance-wise, two processes have been specifically optimized: the computation of the interaction kernel at the start of the simulation, in Cython, and the convolution itself, in C. Those optimizations, coupled with intelligent multithreading, provide a very significant speed boost compared to a naïve implementation (and a noticeable speed boost compared to [Cam20]).

**Adapted to batches and remote sessions** Given the low computational cost of log-lattice simulations, it is common to launch several dozens at once, for extended periods of time. This requires simulations to be fail-safe, interruptible and resumable, and aware of their maximum CPU usage.

**New log-lattice features** Several physical features, such as the $k_i = 0$ modes and rectified spectra, have been implemented.

**Easy to install** Automated installation scripts, coupled with virtualization, ensured that the installation process requires no technical knowledge and does not clash with existing frameworks. In particular, this allows one to use several different versions of the framework on a single computer, for instance to work on older simulations.

## 2.2 Example code

### 2.2.1 Simulation

Below is a simplified code to simulate the 3D Navier-Stokes equations on log-lattices with our framework using an adaptive grid. For readability, we have removed imports, typing, and some minor functions. The full code can be found in `Simulations/NS3D.py`.

For numerical reasons, the equation is split into a linear part (in which goes the viscous term) and nonlinear part. Notice how the code doesn't explicitly use many features specific to log-lattices (those are handled transparently by functions such as `grid.physics.energy` or `grid.maths.laplacian`), and how the equations are easily readable.

```
"""3D Navier Stokes"""
def equation_nonlinear(_t, grid, _simu_params):
    M = grid.maths
    ux, uy, uz = grid.field("ux", "uy", "uz")

    # Forcing
    fx, fy, fz = get_forcing(grid)
```

[2] See the README

```
    # Pre-compute terms
    uxdxux, uydyux, uxdxuy, uydyuy, uzdzux, uzdzuy, uxdxuz, uydyuz, uzdzuz = \
        M.convolve_batch((
            (ux, M.dx * ux), (uy, M.dy * ux), (ux, M.dx * uy), (uy, M.dy * uy),
            (uz, M.dz * ux), (uz, M.dz * uy), (ux, M.dx * uz), (uy, M.dy * uz),
            (uz, M.dz * uz),
    ))

    # Evolution w/o pressure
    dux_dt = -uxdxux - uydyux - uzdzux + fx
    duy_dt = -uxdxuy - uydyuy - uzdzuy + fy
    duz_dt = -uxdxuz - uydyuz - uzdzuz + fz

    # Add pressure
    dux_dt, duy_dt, duz_dt = grid.maths.P_projector([dux_dt, duy_dt, duz_dt])

    return {"ux": dux_dt, "uy": duy_dt, "uz": duz_dt}

def equation_linear(_t, grid, simu_params):
    nu = np.sqrt(f0) * grid.L**1.5 / Re_F

    visc = grid.maths.laplacian * nu

    return {"ux": visc, "uy": visc, "uz": visc}

def initial_conditions(fields, grid, _simu_params):
    grid = grid.to_new_size_empty(N_points)
    u = get_forcing(grid)

    fields["ux"] = u[0]
    fields["uy"] = u[1]
    fields["uz"] = u[2]
    return fields

def update_gridsize(grid):
    """update the grid size based on the fraction of energy
    contained in the outermost layers"""
    E = grid.physics.energy()
    ux, uy, uz = grid.field("ux", "uy", "uz")
    mask = grid.ks_modulus > grid.k_min * grid.l ** (grid.N_points - 1)
    # grid
    comp = np.max(np.abs(ux[mask]) + np.abs(uy[mask]) + np.abs(uz[mask]))
    if comp / np.sqrt(E) > 1e-100:
        return grid.N_points + 1
    if comp / np.sqrt(E) < 1e-170 and grid.N_points > 5:
        return grid.N_points - 1
```

```
# Simulation's parameters
fields = ["ux", "uy", "uz"]  # the scalar fields to simulate
D = 3  # the dimension of the space
l_params = {"plastic": False, "a": 1, "b": 2}  # the grid spacing's parameters
Re_F = 1e3
simu_params = {"Re_F": Re_F}  # scalar parameter passed to the equation

rtol = 1e-4  # relative tolerance of the solver
n_threads_convolution = 4  # parallelization
N_points = 6  # initial size of the grid

save_path = f"results/save_3D_f0{f0:.2e}_ReF{Re_F:.2e}"  # save path
end_simulation = {"t": 2000, "ode_step": 1e10}  # when to end the simulation
save_one_in = 50  # save one step every N real steps

# Launching the simulation
Solver(simulation_parameters).solve()
```

### 2.2.2 Treatment

The above simulation can then be analyzed using the following simplified code, inspired by `Simulations/treat_3D.py`.

```
"""Analyze NS3D results"""

# Spectrum and Energy
def get_spectrum_and_energy(grid, _t, _simu_params):
    """LHS: spectrum vs ks
    RHS: energy vs time
    slider: time"""

    def spectrum_kinetic(fields, k):
        """Kinetic energy"""
        ux, uy, uz = fields["ux"], fields["uy"], fields["uz"]
        return np.real(ux[k] * np.conj(ux[k]) + uy[k] * np.conj(uy[k]) + \
            uz[k] * np.conj(uz[k]))
    return {"E_k": grid.physics.spectrum(spectrum_kinetic),
        "E": grid.physics.energy(), "ks": grid.ks_1D}


def plot_spectrum_and_energy(drawables):
    """Plot spectra and energy"""
    ts, E_k, E_kx, E_ky, E_kz, E, ks = drawables("t", "E_k", "E_kx",
        "E_ky", "E_kz", "E", "ks")
    _ = interactive_spectrum(ts, ks, {"$E_k$": E_k, "$E_{kx}$": E_kx,
        "$E_{ky}$": E_ky, "$E_{kz}$": E_kz}, {"$E$": E})
    pltshowm(legend=False, compact=False)

# Analysis parameters
```

```
draw_funcs = {
    "spectrum_and_energy": {"get": get_spectrum_and_energy,
        "plot": plot_spectrum_and_energy},
}

f0 = 1
Re_F = 1e3

save_path = f"results/save_3D_f0{f0:.2e}_ReF{Re_F:.2e}"
N_points = 500  # how many time points max to load
n_jobs = 3  # parallelization
loadfromsave = False  # load already computed results

# Launch analysis
DataExplorer(analysis_parameters).display()
```

# Part III

# The physics

# Chapter 3

# Asymptotic Ultimate Regime of Homogeneous Rayleigh-Bénard

In this chapter, we investigate the so-called "Asymptotic Ultimate regime of Rayleigh-Bénard convection" using log-lattices.

*Most, but not all, of the content in this chapter comes from our article [BD23].*

## Takeaways

We investigate the Homogeneous Rayleigh-Bénard equations on log-lattices.

By adding a large-scale friction, we alleviate the runaway exponential instabilities that otherwise plague the simulations, even in DNS.

We recover scalings for Nu, Re and dissipation as a function of Ra, Pr predicted by Grossman & Lohse.

At very high Re, we observe a transition from a "stable" regime to an "intermittent" regime with ill-defined statistics.

## 3.1 Introduction

Convection is a dynamical process that governs heat transport and mixing in a variety of systems, ranging from planetary and astrophysical flows to industrial devices. In that respect, a crucial question is how the heat flux in the system is connected with the temperature gradient. Near equilibrium, where both quantities are small, Fourier laws apply, and the heat flux is simply proportional to the temperature gradient. For larger values, the system enters a non-linear then turbulent regime, where thermal energy in converted into mechanical energy, and the relation becomes nonlinear. The deviations from linearity are quantified by the relation between the Nusselt number, Nu, the ratio between the heat flux and its laminar value, and the Rayleigh number Ra, the non-dimensional temperature gradient.

In fluid mechanics, the paradigmatic system describing convection is a fluid enclosed in a volume, in which thermal energy is injected at the bottom via imposed heat flux or temperature gradient (figure 3.1). Its dynamics is described by the Rayleigh-Bénard (RB) equations. Despite decades of theoretical, experimental and numerical developments, the scaling of the heat transfer in RB remains a subject of discussion and active research. In bounded domains at low Ra, a simple argument by [MC54] based on the criticality of the thermal boundary layer gives $\mathrm{Nu} \sim \mathrm{Ra}^{1/3}$,

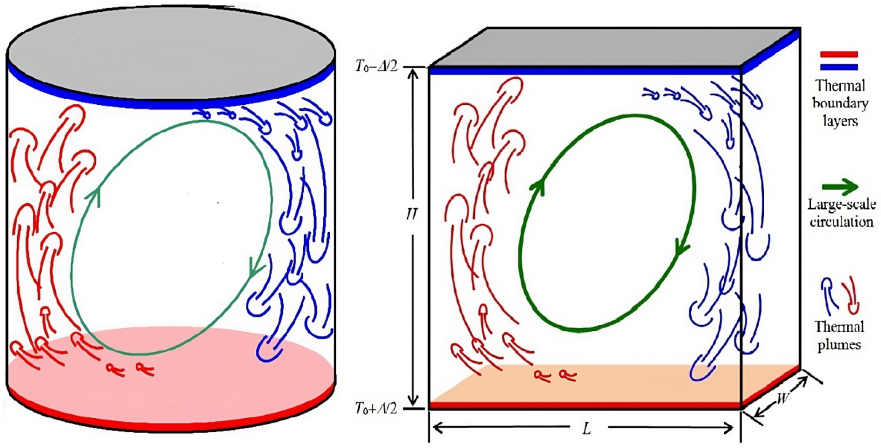


**Figure 3.1:** Figure 1.2 from [For15], illustrating turbulent thermal convection within different geometries. This represents a classical Rayleigh-Bénard setup.

**Table 3.1:** Scaling predictions for HRB observables in the turbulent regime with and without friction. The observables are given by table 3.2. DNS stands for Direct Numerical Simulation using regular Fourier modes [Cal+05] while LL refers to simulations using Fourier modes on a log-lattice. $U_{ls}^2$ and $\Theta_{ls}^2$ are large scale kinetic and thermal energy. Exponents are computed by fitting over $\mathrm{Ra} > 10^7$ (resp. $1 < \mathrm{Pr} < 50$) for varying Ra (resp. Pr). Errors represent std of fit parameters.

| | GL Theory $f = 0$ | DNS $f = 0$ | LL $f = 1$ |
|---|---|---|---|
| $\mathrm{Nu} \sim$ | $\sqrt{\mathrm{Ra}\,\mathrm{Pr}}$ | $\mathrm{Pr}^{0.43}\,\mathrm{Ra}^{0.50}$ | $\mathrm{Pr}^{0.51\pm0.01}\,\mathrm{Ra}^{0.53\pm0.03}$ |
| $\mathrm{Re} \sim$ | $\sqrt{\mathrm{Ra}/\mathrm{Pr}}$ | $\mathrm{Pr}^{-0.55}\,\mathrm{Ra}^{0.5}$ | $\mathrm{Pr}^{-0.54\pm0.01}\,\mathrm{Ra}^{0.54\pm0.01}$ |
| $\epsilon_\theta \sim$ | $c_1\sqrt{\mathrm{Re}/\mathrm{Ra}} + c_2\,\mathrm{Re}\,\sqrt{\mathrm{Pr}/\mathrm{Ra}}$ | $(\mathrm{Re}\,\mathrm{Pr})^{-0.17}$ | $\mathrm{Re}^x\,\mathrm{Pr}^{x-0.5}/\sqrt{\mathrm{Ra}},\ 1 \lessapprox x \lessapprox 1.2$ |
| $\epsilon_u \sim$ | $\mathrm{Re}^3(\mathrm{Pr}/\mathrm{Ra})^{3/2}$ | $\mathrm{Re}^{2.77}(\mathrm{Pr}/\mathrm{Ra})^{3/2}$ | $\mathrm{Re}^{2.88\pm0.03}(\mathrm{Pr}^{0.95\pm0.01}/\mathrm{Ra})^{3/2}$ |

observed in many experiments (see [AGL09] for review). As we increase $\mathrm{Ra} \to \infty$, viscous processes (and their associated boundary layers) are believed to become irrelevant, resulting in an "ultimate regime of convection", where $\mathrm{Nu} \sim \mathrm{Ra}^{1/2}$ (hereafter called "asymptotic ultimate regime") [Spi63; GL00], with possible logarithmic corrections [Kra62; GL11] (hereafter called "ultimate regime"). Experimental or numerical observations of the (asymptotic) ultimate regime prove to be very difficult, and no final consensus has been reached so far about its existence in a pure RB setting [Cha+97; Urb+19; DC96; Zhu+18; Zhu+19b; Roc20] (see [AGL09] for a less recent but more synthetic review). When the gravity is artificially increased using centrifugal force, one can indeed observe hints of an ultimate regime [Jia+22]. On the other hand, various modifications of the RB geometry aiming at modifying the influence of the boundary layers result in experimental observation of a regime where $\mathrm{Nu} \sim \mathrm{Ra}^{1/2}$: using highly elongated cells [Gib+06; Cas+17; PA16], using rough [CL99; Rus+18; Zhu+19a; Kaw+21] or porous [ZY21; MKS22] boundaries, or radiatively heating the flow [LAG18; Bou+19].

From a numerical point of view, a simple way to remove boundary layers is to consider a triply periodic geometry, and heat the flow via an applied temperature gradient. This setting was first explored by [BO97; GL00; GL01; LT03; Cal+05; CLT07] and called Homogeneous Rayleigh-Bénard (HRB) convection. The corresponding scalings and predictions are summarized in table 3.1. Although the results of those simulations are consistent with the predictions of [GL00]

(hereafter called "GL theory"), they are undermined by several drawbacks: statistics polluted by the growth of uncontrolled exponential instabilities [Cal+06] of unclear physical relevance, a small Ra and Pr range, sparse data points due to difficulties in running numerically challenging simulations. Indeed, pushing the Rayleigh number to large values increases the numerical burden beyond the capacity of present computers, as the number of grid points needed to describe the flow usually scales like $\mathrm{Re}^3$ with $\mathrm{Re} \sim \mathrm{Ra}^{1/2}$.

1D shell models of turbulence were used previously in the context of HRB [CK08] in an effort to increase the Ra and Pr range of results. They successfully display the asymptotic ultimate regime of convection, at the price of tuning several parameters of the model to get rid of the uncontrolled exponential instabilities. This, combined with the 1D nature of the model, renders the informative and conclusive nature of the observations questionable. The goal of the present chapter is therefore to re-explore the HRB equation using the log-lattice framework, that allows both the exploration of a wide range of parameters on a large array of wavenumbers, and a flexibility of dimensionality from 1D to 3D, at low numerical cost, and without additional empirical parameters. Given that they preserve all main conservation laws and symmetry of the original HRB equation, many features of the original equation are still valid, like the exact conservation laws of table 3.1. Whether the GL theory still applies, and what are the modifications of the asymptotic ultimate regime implied by the log-lattice geometry, are interesting open questions that we investigate here. In that respect, the present paper offers an exploration of the analogy and differences between log-lattices and classical fluid dynamics in a more complex case (HRB) than previous examples [CM18; CM21].

## 3.2 Numerical simulations

### 3.2.1 Generalities

The dynamics of a homogeneous fluid, with coefficient of thermal dilation $\alpha$, viscosity $\nu$ and diffusivity $\kappa$, subject to a temperature gradient $\Delta T$ over a length $H$ and vertical gravity $g$ is given by the HRB set of equations [LT03; Cal+05; Cal+06; CLT07],

$$\begin{aligned} \partial_t u + u \cdot \nabla u + \frac{1}{\rho_0}\nabla p &= \nu \nabla^2 u + \alpha g \theta \vec{z}, \\ \partial_t \theta + u \cdot \nabla \theta &= \kappa \nabla^2 \theta + u_z \frac{\Delta T}{H}, \\ \nabla \cdot u &= 0, \end{aligned} \tag{3.1}$$

where $u$ is the velocity, $\theta$ the temperature fluctuation, $\rho_0$ is the (constant) reference density and $p$ is the pressure. Here, the mean temperature gradient $\Delta T$ acts as a forcing term. This gradient is non-dimensionalized into the Rayleigh number $\mathrm{Ra} = \alpha g H^3 \Delta T/(\nu\kappa)$. The Prandtl number $\mathrm{Pr} = \nu/\kappa$ is the ratio of the fluid viscosity to its thermal diffusivity. The mean total heat flux is the $z$ direction is $J = \langle u_z \theta \rangle - \kappa \Delta T$ which is adimensionalized into $\mathrm{Nu} = JH/\kappa\Delta T$.

Taking global space and time average of equation (3.1), one can derive [LT03; Cal+05] two exact relation for the volume averaged kinetic and thermal dissipation, which respectively scale as

$$\nu \left\langle (\partial_i u_j)^2 \right\rangle_V = \nu^3 H^{-4} \,\mathrm{Nu}\,\mathrm{Ra}\,\mathrm{Pr}^{-2}, \tag{3.2}$$

$$\kappa \left\langle (\partial_i \theta)^2 \right\rangle_V = \kappa H^{-2} (\Delta T)^2 \,\mathrm{Nu}\,. \tag{3.3}$$

Additionally, to get rid of the pressure term, we take the rotational of the above equation ($\omega = \mathrm{rot} u = ik \times u$).

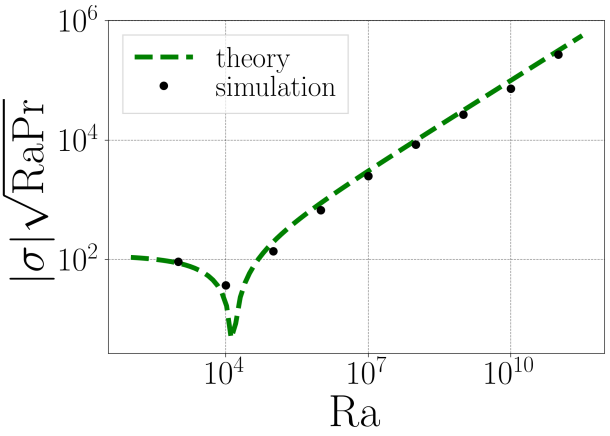


**Figure 3.2:** Absolute value of the rate of growth of instability $\sigma = d\log X/d\log t$ where $X = \langle u\theta \rangle$ without large-scale friction ($f = 0$), vs. Rayleigh number. The green dashed line is the theoretical growth rate for $k = k_c = 2\pi\sqrt{3}$, corresponding to equation (3.4). The interval $k < k_c$ corresponds to negative values of $\sigma$.

### 3.2.2 Adaptation on log-lattices: HRB with friction

#### 3.2.2.1 Exponential instabilities in HRB

As first shown by [Cal+06], HRB equations are prone to exponential instabilities, due to the conservation of the total energy. In the absence of large-scale friction, we also observe those instabilities in our log-lattice simulations (figure 3.3a). As shown in figure 3.2, the growth rate of the instability in the log-lattice simulations matches the theoretical growth rate given by [Cal+06; Sch+12]:

$$\sigma\sqrt{\mathrm{Ra\,Pr}} = \frac{1}{2}\left[\sqrt{\left((\mathrm{Pr}+1)k^2\right)^2 + 4\,\mathrm{Pr}(\mathrm{Ra}-k^4)} - (\mathrm{Pr}+1)k^2\right] \sim \sqrt{\mathrm{Ra}}, \tag{3.4}$$

for $\theta, u \sim e^{\sigma t + i\vec{k}\cdot\vec{x}}$. This expression yields unstable solutions for $\mathrm{Ra} > \mathrm{Ra}_c = k_{\mathrm{min}}^4$ where $k_{\mathrm{min}}$ is the modulus of the smallest mode on the grid, which is $2\pi\sqrt{3}$ in our case.

However, the non-linear behavior of the instability in the log-lattice case is quite different from the one reported by Calzavarini: instabilities tend to extend significantly further and for longer times. Our interpretation is that in our log-lattice model, the modes are not coupled enough to develop the nonlinear saturation. The instabilities widely interfere with the statistical stability of observables and need to be removed for a meaningful analysis. Physically, these exponential ramps originate for a lack of energy sink to absorb the constant energy injection in the bulk by the (fixed) temperature gradient. Previous works on 1D simulations [CK08] have shown that without a large-scale sink to counteract this source, energy diverges at large scales and scaling laws become incorrect. Therefore, to get rid of the exponential instabilities, we include a large-scale friction $f$ on both $u$ and $\theta$. By doing so, the instability saturates, and we achieve a statistically stationary state for the heat transfer, as displayed in figure 3.3. Note however that the fluctuations of Nu around the stationary value are very broad, and extend over one or two orders of magnitudes. The same phenomenon was observed in the DNS of HRB [Cal+05; Cal+06] and mentioned to be a source of difficulty to achieve reliable results [BO97]. For this reason, very long simulations are necessary to get steady averages [PS95; Cal+06]. In DNS, this cannot be achieved without cutting down the resolution, which may impact the reliability of dissipation estimates [YSP18]. In the log-lattice framework, we do not have this problem, and we performed

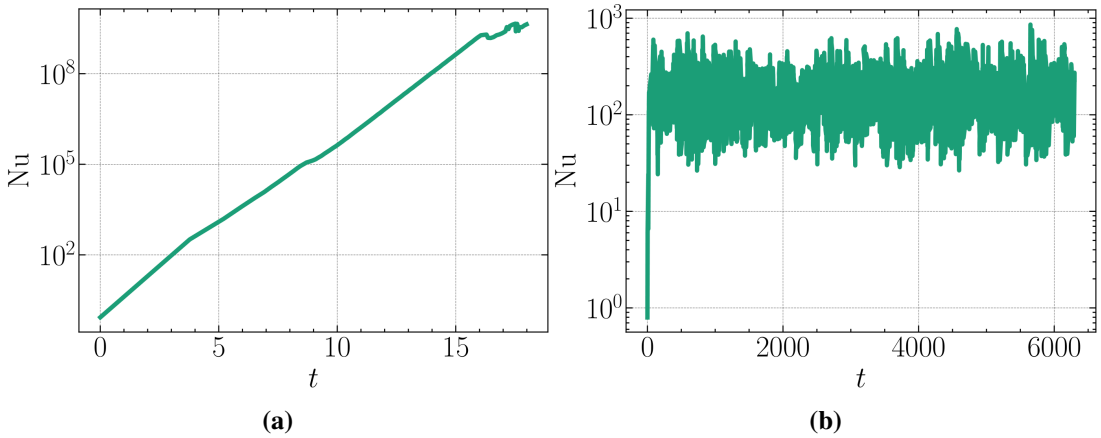


**(a)** **(b)**

**Figure 3.3:** Influence of the large-scale friction on the time behavior of the Nusselt number Nu in 3D HRB. (figure 3.3a) Without friction: we observe the growth of an exponential instability. (figure 3.3b) With friction: the instability saturates and the dynamics become statistically convergent. Parameters: $\mathrm{Ra} = 10^6, \mathrm{Pr} = 1, N = 13$.

high resolution very long time averages on the log of Nu, and represent all quantities in log-log variables.

#### 3.2.2.2 Equations

To investigate the ultimate regime, it is natural to adimensionalize the equation in terms of "inertial quantities", i.e. using the vertical width $H$ as a unit of length, the free fall velocity $U_{\mathrm{ff}} = \alpha g \Delta T H$ as a unit of velocity, and $\Delta T$ as a unit of temperature. table 3.2 indicates the form taken by observables after rescaling as indicated. The equations including the temperature gradient and the friction can then be written in terms of velocity as (with the Einstein convention on summed repeated indices):

$$\begin{aligned} \partial_t u_i &= \mathbb{P}\left[-u_j \partial_j u_i + \theta \delta_{i=z} + \sqrt{\frac{\mathrm{Pr}}{\mathrm{Ra}}}\nabla^2 u_i - f u_i \delta_{k\approx k_{min}}\right]_i, \\ \partial_t \theta &= -u_i \partial_i \theta + u_z + \frac{\nabla^2 \theta}{\sqrt{\mathrm{Ra}\,\mathrm{Pr}}} - f\theta\delta_{k\approx k_{min}}, \end{aligned} \tag{3.5}$$

where the Dirac $\delta_{k\approx k_{\mathrm{min}}}$ filters out the small scales, and the projector, given in the Fourier space by $\mathbb{P}(A) = A - \frac{k_i}{k^2} k_j A_j$, accounts for the pressure term under the divergence-free condition. We also looked at those equations expressed in terms of the vorticity $\omega = \nabla \times u$:

$$\begin{aligned} \partial_t \omega_i &= -\omega_j \partial_j u_i - u_j \partial_j \omega_i + \theta[\nabla \times z]_i + \sqrt{\frac{\mathrm{Pr}}{\mathrm{Ra}}}\nabla^2 \omega_i - f\omega_i \delta_{k\approx k_{min}}, \\ \partial_t \theta &= -u_i \partial_i \theta + u_z + \frac{\nabla^2 \theta}{\sqrt{\mathrm{Ra}\,\mathrm{Pr}}} - f\theta\delta_{k\approx k_{min}}. \end{aligned} \tag{3.6}$$

Adding a large-scale friction to damp the inverse cascade is a classical trick-it is e.g. routinely used in numerical simulations of 2D turbulence to avoid Bose condensation at $k = 0$ and enable stationarity [SGC99]. The present case is 3D, but we interpret the formation of exponential ramps

**Table 3.2:** Physical quantities expressed as a function of the non-dimensional variables of equation (3.5) . $\langle\cdot\rangle$ denotes the temporal and spatial average.

$$\mathrm{Nu} = \frac{JH}{\kappa\Delta T} - 1 \rightarrow \sqrt{\mathrm{Ra}\,\mathrm{Pr}}\cdot\langle u_z\theta\rangle - 1$$

$$\mathrm{Re} = \frac{\sqrt{\langle U_i U_i\rangle}H}{\nu} \rightarrow \sqrt{\frac{\mathrm{Ra}}{\mathrm{Pr}}}\cdot\sqrt{\langle u_i u_i\rangle}$$

$$\epsilon_\theta = \kappa\left\langle(\partial_i\Theta)^2\right\rangle \rightarrow \frac{\left\langle(\partial_i\theta)^2\right\rangle}{\sqrt{\mathrm{Ra}\,\mathrm{Pr}}}$$

$$\epsilon_u = \nu\left\langle(\partial_i U_j)^2\right\rangle \rightarrow \sqrt{\frac{\mathrm{Pr}}{\mathrm{Ra}}}\cdot\left\langle(\partial_i u_j)^2\right\rangle$$

as a signature of back-scattering of energy, a feature that was already mentioned previously in shell models of Rayleigh-Bénard convection [CK08]. The addition of the friction is therefore a convenient way to damp the large-scale modes that are generated by the large-scale instability. Such friction is also added in many models of climate, as a subgrid model to account for the friction at the boundary layer that cannot be resolved in the stratified case. The hand waving argument is that, within boundary layers, a shear profile develops, with extraction of energy at the boundaries, which is proportional to the square of the shear. Assuming the shear to be constant in the boundary layer, we can then estimate it by the difference between the velocity at the top of the layer, minus the velocity at the boundary which is zero. In total, the energy pumped by friction is proportional to the square of the velocity, which is exactly the law we have implemented. Such friction is termed Rayleigh friction in the climate community [Ste+02] and can actually be seen as a way to take into account the boundary conditions that we have removed in the HRB setting.

#### 3.2.2.3 Conservation laws for HRB with and without friction

In the absence of friction, the conservation laws for HRB are given by equations (3.2) and (3.3). The presence of the friction just adds a supplementary term proportional to $f$ in each equation. The result can be made non-dimensional using $U_{\mathrm{ff}}$, $H$ and $\Delta T$ as units of velocity, length and temperature, resulting in :

$$f\left\langle u^2\delta_{k\approx k_{min}}\right\rangle + \epsilon_u = \frac{\mathrm{Nu}+1}{\sqrt{\mathrm{Ra}\,\mathrm{Pr}}}, \tag{3.7}$$

$$f\left\langle \theta^2\delta_{k\approx k_{min}}\right\rangle + \epsilon_\theta = \frac{\mathrm{Nu}+1}{\sqrt{\mathrm{Ra}\,\mathrm{Pr}}}, \tag{3.8}$$

From now on, we define $U_{ls}^2 = \left\langle u^2\delta_{k\approx k_{\min}}\right\rangle$ and $\Theta_{ls}^2 = \left\langle \theta^2\delta_{k\approx k_{\min}}\right\rangle$.

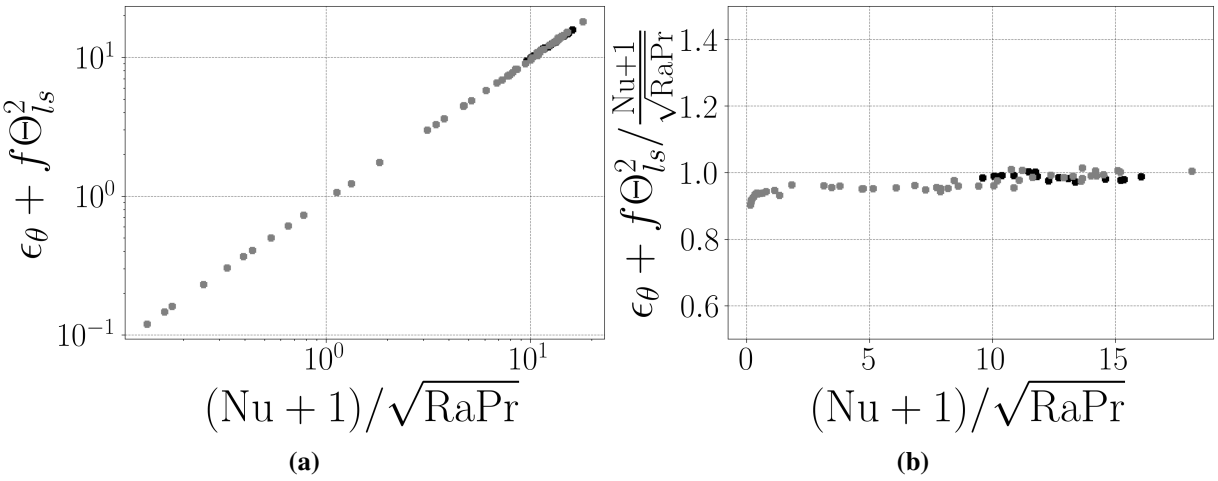


**Figure 3.4:** Exact conservation laws for $\epsilon_\theta$ in 3D results. Black points correspond to varying Ra, gray points correspond to varying Pr. (figure 3.4a) $\epsilon_\theta + f\Theta_{ls}^2$ vs $(\mathrm{Nu}+1)/\sqrt{\mathrm{Ra}\,\mathrm{Pr}}$. (figure 3.4b) Compensated plot $(\epsilon_\theta + f\Theta_{ls}^2)/\left((\mathrm{Nu}+1)/\sqrt{\mathrm{Ra}\,\mathrm{Pr}}\right)$ vs $(\mathrm{Nu}+1)/\sqrt{\mathrm{Ra}\,\mathrm{Pr}}$.

## 3.2.3 Numerical details

### 3.2.3.1 Configuration

We perform all our simulations with $\lambda = \phi$ (see in section 1.1.3 why we do not chose $\lambda = 2$), which is the second-biggest value of $\lambda$, and has the second least number of interactions per grid point. The minimum wave vector of the grid is set to $k_{\min} = 2\pi$ to match a simulation on a box of size $\tilde{L} = 1$. The grid size $N$ is then set to reach the dissipative scale both for velocity and temperature. We alternate between several initial condition (IC) choices for our simulations: large-scale initialization, Kolmogorov spectrum, flat-spectrum. All those choices are modulated by a weak multiplicative complex noise. We find no significant influence of those initial conditions on the scaling laws. As Ra or Pr increase, the simulations become slower and slower. This sets the upper bound on the range of parameters we can integrate while retaining statistically relevant observables in a reasonable simulation time (one CPU days at most). In 3D, this yields $\mathrm{Ra}_{\max} \approx 10^{10}$ for $\mathrm{Pr} = 1$ and $\mathrm{Pr}_{\max} \approx 5 \cdot 10^4$ for $\mathrm{Ra} = 10^8$. The lower bound is set by the value of the Nusselt number, which must obey $\mathrm{Nu} \gg 1$, the value $\mathrm{Nu} \approx 1$ corresponding to the laminar regime with trivial scaling laws. Finally, integrating equations on log-lattices yields interesting and new numerical challenges. We built our own ODE integrator to solve them, as detailed in Supplementary Materials. Once we have run a simulation for a long enough time, we compute Nu, $\epsilon_\theta$, $\epsilon_u$ by taking long time and space averages (with $\langle ab \rangle = \frac{1}{T}\int_t \mathrm{dt}(a,b)$) according to table 3.2. The accuracy of our results is controlled by checking that we recover the exact laws of HRB convection equations (3.7) and (3.8). This is shown in figures 3.4 and 3.5, for all 3D data sets used in the present paper (see table 3.3). Furthermore, the ratio between the friction term and the dissipation is shown in figure 3.6.

### 3.2.3.2 Simulation sets

The results we obtained come from seven types of simulation that are described in the table 3.3. For comparison, we also included in some graphs the results by [Cal+05], obtained using DNS of the same equations, but at $f = 0$.

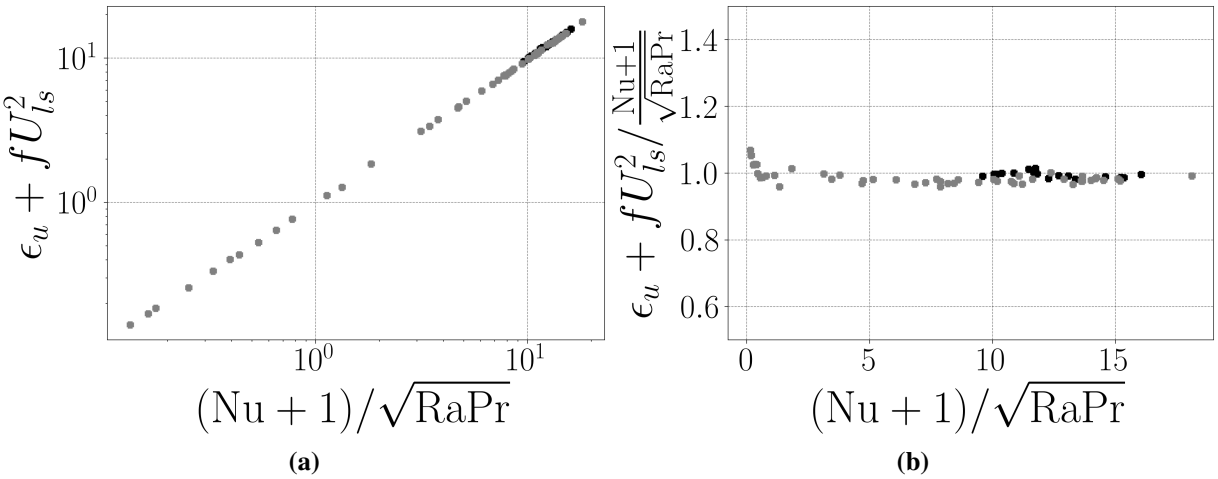


**(a)** **(b)**

**Figure 3.5:** Exact conservation laws for $\epsilon_u$ in 3D results. Black points correspond to varying Ra, gray points correspond to varying Pr. (figure 3.5a) $\epsilon_u + fU_{ls}^2$ vs $(\mathrm{Nu}+1)/\sqrt{\mathrm{Ra}\,\mathrm{Pr}}$. (figure 3.5b) Compensated plot $(\epsilon_u + fU_{ls}^2)/\left((\mathrm{Nu}+1)/\sqrt{\mathrm{Ra}\,\mathrm{Pr}}\right)$ vs $(\mathrm{Nu}+1)/\sqrt{\mathrm{Ra}\,\mathrm{Pr}}$.

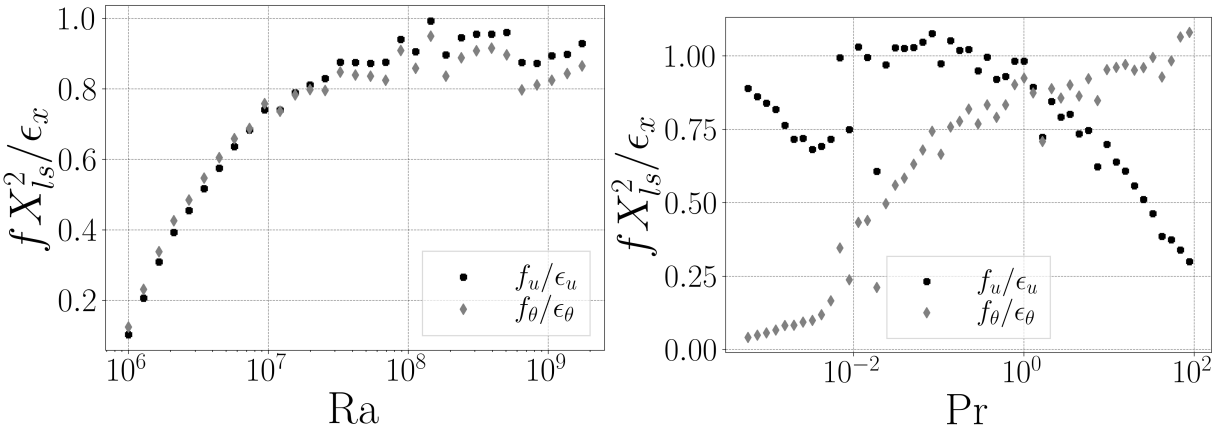


**(a)** **(b)**

**Figure 3.6:** Ratio between friction $f_x = fX_{ls}^2$ and dissipation $\epsilon_x$ for $x = u, \theta$ (figure 3.6a) versus Ra at Pr = 1 and (figure 3.6b) versus Pr at Ra = $10^8$.

**Table 3.3:** Parameters of the data sets used in the present paper. $D$ is the dimension. The "velocity" datasets are obtained by integration of equation (3.5), while the "vorticity" datasets are obtained by integration of equation (3.6). *DNS* refers to direct simulations of [Cal+05], using a classical spectral Fourier code (on a regular grid). The ++ label refers to an integration using an improved integrator, using a reshuffling of variable matrices that allows faster simulations. The Ra and Pr column provides the Rayleigh and Prandtl number range of the simulations. $f$ is the large scale friction, $N = 1 + \log k_{\max}/\log(\phi)$, where $k_{\max}$ is the maximal wavenumber of the simulation and $\phi$, the golden mean, is a measure of the spatial resolution. For log-lattices, it corresponds to the number of modes in each direction. $N_{av}$ is the length of the simulation, divided by the large eddy turnover time. It provides the number of decorrelated frames that can be used to estimate statistical averages. The tolerance refers to the absolute and relative tolerances that are fixed equal in all the simulations.

| Name | D | Type | Ra | Pr | $f$ | $N$ | $N_{av}$ | Tolerance | Symbol |
|---|---|---|---|---|---|---|---|---|---|
| (I) | 1D | Velocity | $[10^5, 10^{50}]$ | 1 | 1 | 120 | - | $10^{-3}$ | ● |
| (II) | 2D | Vorticity | $[10^5, 10^{50}]$ | 1 | 1 | 20 | - | $10^{-3}$ | ◆ |
| (III) | 3D | Velocity | $[1, 10^{10}]$ | 1 | 1 | 13 | $> 480$ | $10^{-6}$ | ● |
| (IV) | 3D | Vorticity | $[1, 10^{10}]$ | 1 | 1 | 13 | $> 480$ | $10^{-6}$ | ■ |
| (V) | 3D | Velocity | $10^8$ | $[5 \cdot 10^{-4}, 10^2]$ | 1 | 13 | $> 50$ | $10^{-6}$ | ● |
| (VI) | 3D | Vorticity | $10^8$ | $[5 \cdot 10^{-4}, 10^2]$ | 1 | 13 | $> 50$ | $10^{-6}$ | ■ |
| (VII) | 3D | ++Velocity | $\{10^9, 10^{10}, 10^{11}\}$ | $[5 \cdot 10^{-4}, 10^2]$ | 1 | 13 | $> 80$ | $10^{-6}$ | - |
| (VIII) | 3D | Velocity | $[10^6, 10^{10}]$ | 1 | 1 | 13 | $> 50$ | $10^{-6}$ | ● |
| Calzavarini | 3D | DNS | $[10^5, 10^8]$ | $[10^{-1}, 10]$ | 0 | - | $> 64$ | - | ◆● |

Historically, we performed first vorticity simulations, then velocity simulations, improving the integrator scheme in between to be able to better handle various numerical challenges raised by simulating wavenumbers as high as $k \sim 10^5$ in 3D. For transparency reasons, we decided to include all datasets we had at our disposal, but we believe that the velocity simulations are the more faithful ones, in the sense that they deal better with the small scales at large Rayleigh or Reynolds number. This sensitivity to small scale modeling (and resolution) is also a well-known feature of direct numerical simulations, especially when it comes to statistics of gradients or energy dissipation [YSP18].

We have verified that the size of the grid for 3D simulations ($N = 13$) does not affect the mean value of the observables Nu, Re, ..., which is already converged for grids of size $N \geq 6$. However, the tail of the pdfs does depend on $N$. Another 3D simulation set at $N = 20$ (not shown here, both vs Ra and Pr) displays the same scaling laws as the $N = 13$ case, confirming this analysis.

#### 3.2.3.3 Zero-divergence problem in 1D

In the 1D case, we cannot impose the zero-divergence condition, so that quantities like $u_x \partial_x \theta$ and $\partial_x(u_x \theta)$ are not equivalent. Here, we have followed the same choice as [CK08], and wrote the equation as:

$$\begin{aligned} \partial_t u &= -u\partial_x u + \theta + \sqrt{\frac{\mathrm{Pr}}{\mathrm{Ra}}}\nabla^2 u - f u \delta_{k \approx k_{min}}, \\ \partial_t \theta &= -u\partial_x \theta + u + \frac{\nabla^2 \theta}{\sqrt{\mathrm{Ra}\,\mathrm{Pr}}} - f \theta \delta_{k \approx k_{min}}. \end{aligned} \tag{3.9}$$

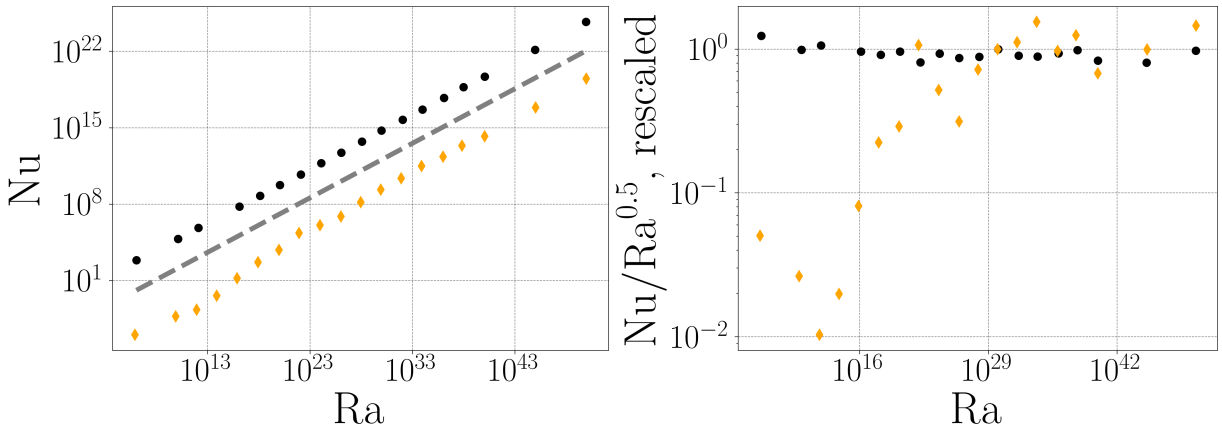


**Figure 3.7:** Non-dimensional heat transfer Nu vs Rayleigh number Ra in 1D and 2D. Correspondence between symbols and datasets are given in table 3.3. (figure 3.7a) Nu vs Ra. The gray dashed line corresponds to $\mathrm{Nu} \sim \sqrt{\mathrm{Ra}}$, corresponding to ultimate regime scaling. (figure 3.7b) Compensated plot $A\,\mathrm{Nu}/\sqrt{\mathrm{Ra}}$ vs Ra., where $A$ is adjusted to collapse the 1D and 2D data in the ultimate regime.

## 3.3 Results and Discussion

### 3.3.1 One and two-dimensional cases

Figure 3.7 presents the Nu vs Ra scaling in 1D and 2D. The 1D Nu scaling law extends over 50 orders of magnitude in Ra (figure 3.7a), and follows closely the law $\mathrm{Nu} \sim \mathrm{Ra}^{1/2}$, as can be checked by the compensated plot in Fig. (figure 3.7b), in agreement with [CK08]. In 2D, the scaling also extends approximately over 30 orders of magnitudes for $\mathrm{Ra} > 10^{23}$. Moreover, the compensated plot highlights small fluctuations around this law, see figure 3.7b, due to statistical noise.

### 3.3.2 In 3D

In 3D, the simulations get significantly more turbulent and results are subject to more statistical fluctuations. Another source of fluctuations comes from a physical phenomenon, associated with the existence of friction. To showcase this effect, we plot in figures 3.6a and 3.6b the ratio between the energy dissipated by friction and the energy dissipated by viscosity or diffusivity for both the kinetic energy and the thermal energy.

Fixing $\mathrm{Pr} = 1$ and varying Ra between $10^3$ and $10^8$, we observe in figure 3.6a that both $f_u = fU_{ls}^2/\epsilon_u$ or $f_\theta = f\Theta_{ls}^2/\epsilon_\theta$ behave in the same way as a function of Ra at low Ra, the dissipation due to friction is small, and gradually increases towards reaching a plateau around $\mathrm{Ra} \sim 10^7$, where energy dissipated by frictions reach about 90% of the energy dissipated by viscosity or diffusivity. We can thus define a "non-universal" regime where $f/\epsilon$ depends on Ra, Pr and a "universal" regime where $f/\epsilon$ does not depend on Ra, Pr.

The critical Rayleigh number where the plateau occurs is likely to depend on the Prandtl number. To check this; we now fix $\mathrm{Ra} = 10^8$ and vary Pr from several order of magnitude. In figure 3.6b, we then observe an interesting symmetrical behavior, with respect to $\mathrm{Pr} = 1$: decreasing Pr, we observe that the energy dissipated by the velocity friction remains of the same order of magnitude than the dissipation by viscosity, while the energy dissipated by

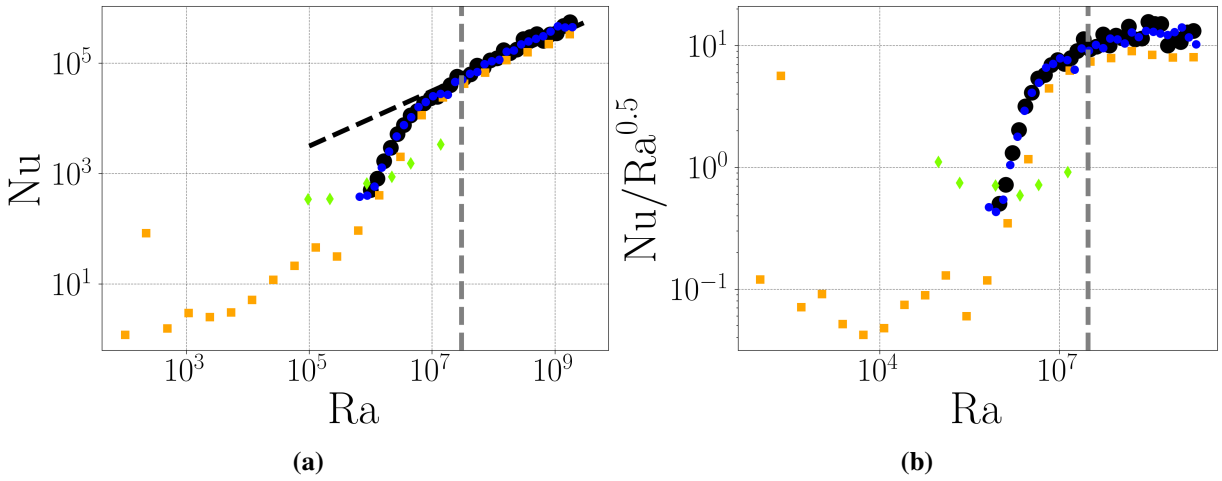


(a) (b)

**Figure 3.8:** Non-dimensional heat transfer Nu vs Rayleigh number Ra in 3D for Pr = 1. Correspondence between symbols and datasets are given in table 3.3. The gray dashed line separates the non-universal (left) and the universal (right) friction dominated regimes for data corresponding to figure 3.6. (figure 3.8a) Nu vs Ra. The black dashed line corresponds to Nu $\sim \sqrt{\text{Ra}}$, corresponding to asymptotic ultimate regime scaling. (figure 3.8b) Compensated plot $\text{Nu}/\sqrt{\text{Ra}}$ vs Ra.

thermal friction strongly decays and become negligible. As Pr shifts away from 1, we observe the symmetrical behavior, with velocity friction becoming negligible, while thermal friction remains of the same order of magnitude than the thermal energy dissipation. As we will see, this will have an impact on the thermal transport. Note that at small (resp. large) Pr, all the thermal (resp. velocity) modes become concentrated at large scale, where the friction occurs. Therefore, in the large Pr regime, the kinetic friction and viscous dissipation compete, while at small Pr the same remark holds for the thermal friction and diffusive dissipation. This may then explain the vanishing of the friction in those regimes.

We now focus on the regimes where the ratio of friction to dissipation is approximately constant. These regimes are friction dominated, but, as we will see, are characterized by interesting universal scaling regimes.

Figures 3.8 and 3.9 presents the 3D Nu vs Ra, Pr scalings. Figures 3.10 and 3.11 presents the 3D Re vs Ra, Pr scalings. Scaling are always displayed both directly and in compensated form.

At low Ra, we first observe a transition from a laminar regime, where Nu = 1 up to a turbulent regime starting around Ra $\sim 10^7$ at Pr = 1. In this transition regime, the Nusselt number varies approximately like Nu $\sim \text{Ra}^{2/3}$, while the Reynolds number remains less than $10^4$, but follows approximates laws Re $\sim \text{Ra}^{1/2}$. In this regime, the friction is negligible, as we saw, so that it corresponds to a laminar, frictionless regime.

After this laminar regime, we obtain a turbulent regime around $10^7 <$ Ra for Pr = 1 in which Nu $\sim \text{Ra}^{1/2}$ and Re $\sim \text{Ra}^{1/2}$, like GL theory. The exact value of the exponent is provided in table 3.1. In this regime, the friction is non-negligible, so that it is a "turbulent friction dominated regime" However, as both ratio $f_u = fU_{ls}^2/\epsilon_u$ or $f_\theta = f\Theta_{ls}^2/\epsilon_\theta$ remain independent of Ra, they do not change the scaling of the total kinetic and thermal energy dissipation. Therefore, the argument developed by GL theory should still apply in this situation, as is indeed observed, with minor corrections due to the small variations of the ratios.

In that respect, it is not surprising that the extent of this regime varies with Pr, as is shown in figure 3.12 for various Ra. At $Ra = 10^8$, the "universal GL" regime stops for Pr $<\sim 10^{-1}$. In this range of parameters, Re is still large, so that the flow is turbulent. However, Nu drops quicker

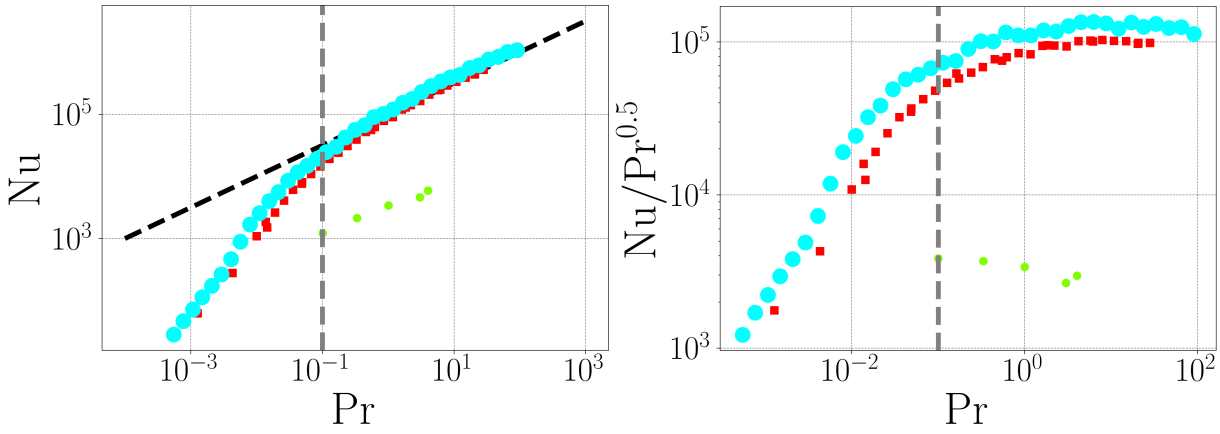


**(a)** **(b)**

**Figure 3.9:** Scaling of non-dimensional heat transfer Nu as a function of Prandtl number Pr in 3D for Ra = $10^8$. Correspondence between symbols and datasets are given in table 3.3. The gray dashed line separates the non-universal (left) and the universal (right) friction dominated regimes for data corresponding to figure 3.6. (figure 3.9a) Nu vs Pr. The black dashed line corresponds to Nu $\sim \sqrt{\mathrm{Pr}}$, corresponding to asymptotic ultimate regime scaling. (figure 3.9b) Compensated plot Nu/$\sqrt{\mathrm{Pr}}$ vs Pr.

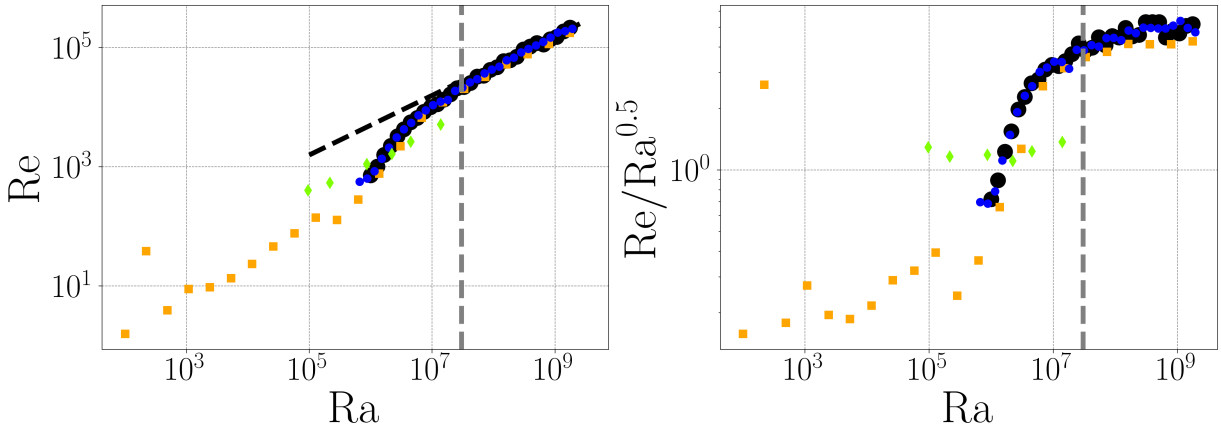


**(a)** **(b)**

**Figure 3.10:** Scaling of Reynolds number Re as a function of Rayleigh number Ra in 3D for Pr = 1. Correspondence between symbols and datasets are given in table 3.3. The gray dashed line separates the non-universal (left) and the universal (right) friction dominated regimes for data corresponding to figure 3.6. (figure 3.10a) Re vs Ra. The black dashed line corresponds to Re $\sim \sqrt{\mathrm{Ra}}$, corresponding to asymptotic ultimate regime scaling. (figure 3.10b) Compensated plot Re/$\sqrt{\mathrm{Ra}}$ vs Ra.

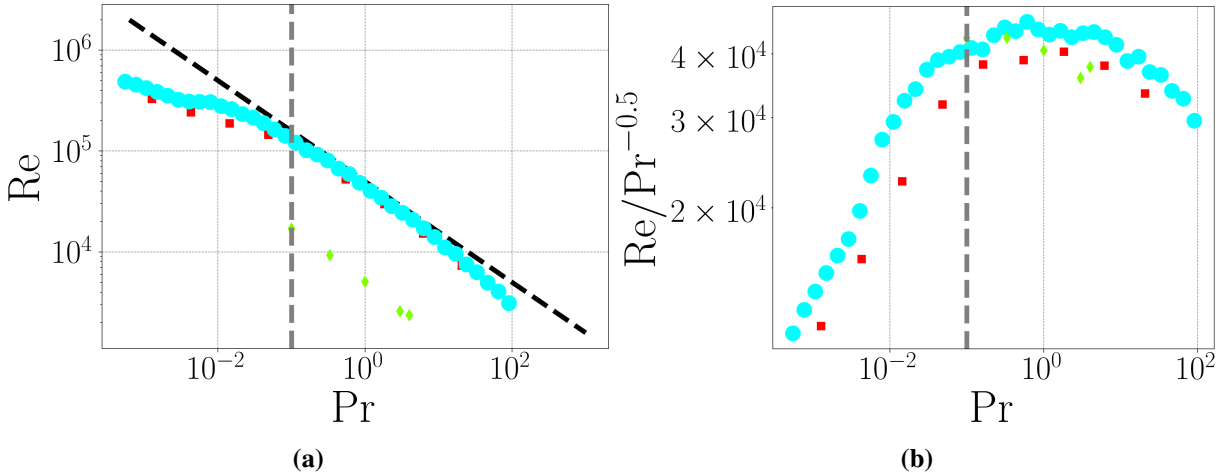


(a) (b)

**Figure 3.11:** Scaling of Reynolds number Re as a function of Prandtl number Pr in 3D for Ra = $10^8$. Correspondence between symbols and datasets are given in table 3.3. The gray dashed line separates the non-universal (left) and the universal (right) friction dominated regimes for data corresponding to figure 3.6. (figure 3.11a) Re vs Pr. The black dashed line corresponds to Re $\sim 1/\sqrt{\text{Pr}}$, corresponding to ultimate regime scaling. (figure 3.11b) Compensated plot Re$/\left(1/\sqrt{\text{Pr}}\right)$ vs Pr.

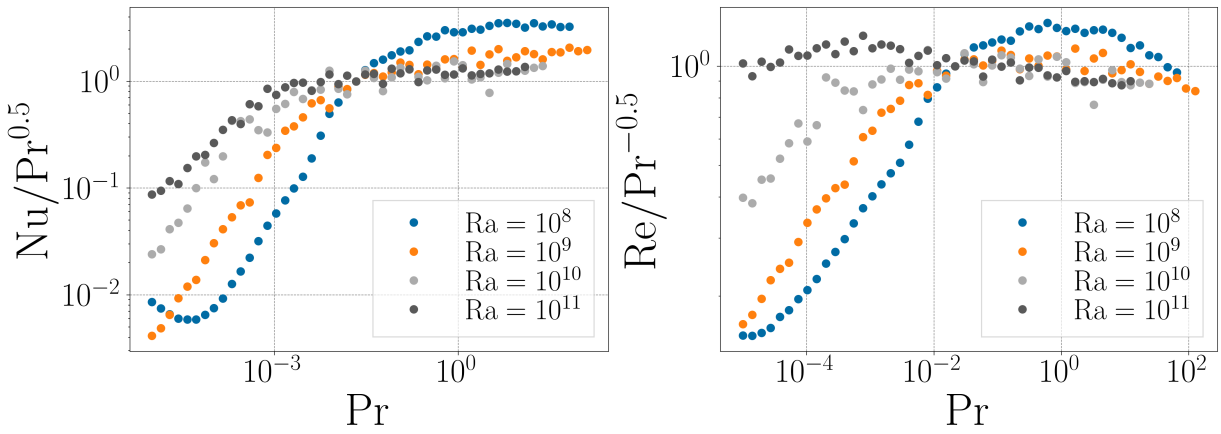


(a) (b)

**Figure 3.12:** Scaling of heat transfer Nu as a function of Prandtl number Pr in 3D results at fixed Ra, dataset VII (table 3.3) (figure 3.12a) Nu$/\sqrt{\text{Pr}}$ vs Pr for various Ra. (figure 3.12b) Re$/\left(1/\sqrt{\text{Pr}}\right)$ vs Pr for various Ra.

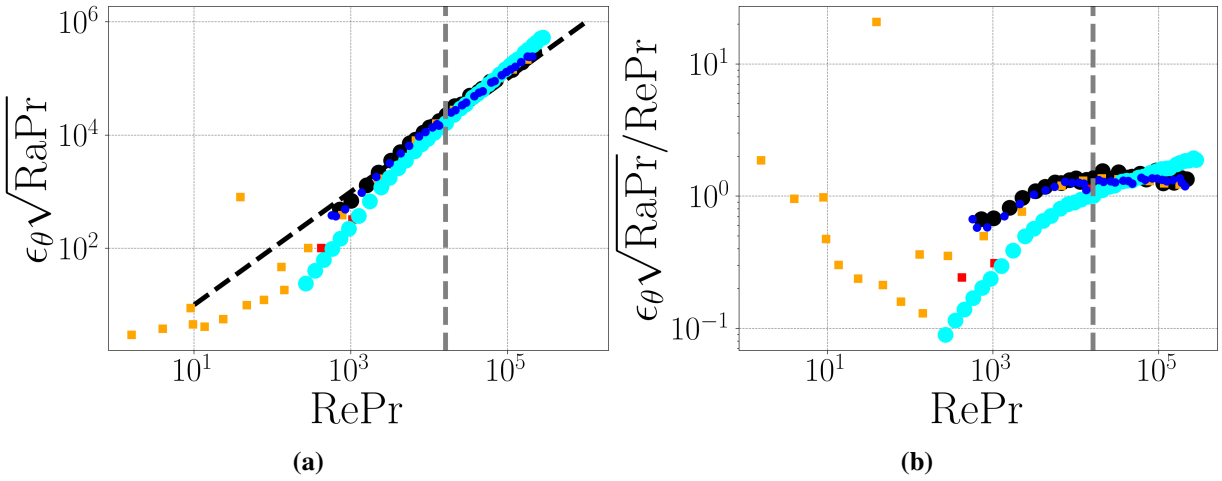


**Figure 3.13:** Scaling of thermal dissipation rate $\epsilon_\theta$ compared to the GL prediction $\mathrm{Re}\sqrt{\mathrm{Pr}/\mathrm{Ra}}$ in 3D results. Correspondence between symbols and datasets are given in table 3.3). The gray dashed line separates the non-universal (left) and the universal (right) friction dominated regimes for data corresponding to figure 3.6. (figure 3.13a) $\epsilon_\theta\sqrt{\mathrm{Ra}\,\mathrm{Pr}}$ vs $\mathrm{Re}\,\mathrm{Pr}$. The black dashed line corresponds to the GL prediction $\epsilon_\theta \sim \mathrm{Re}(\mathrm{Pr}/\mathrm{Ra})^{1/2}$. (figure 3.13b) Compensated plot $\epsilon_\theta\sqrt{\mathrm{Ra}\,\mathrm{Pr}}/\sqrt{\mathrm{Re}\,\mathrm{Pr}}$ vs $\sqrt{\mathrm{Re}\,\mathrm{Pr}}$.

with decreasing Pr than in the universal GL regime, as can be seen from the filled data points in figure 3.9, in parallel with a similar drop for the thermal friction observed in figure 3.6b. This regime seems therefore dependent on the variation on the friction, and is non-universal. In this regime, the Reynolds number variation with Pr is milder than in the universal regime, as can be seen in figure 3.11.

As the Rayleigh number increases, we nevertheless observe in figure 3.12 that the extent of the universal turbulent regime extends towards smaller and smaller values of Pr, so that the universal scaling regime corresponds to an "asymptotic scaling regime" at low value of $\mathrm{Pr} < 1$, valid in the limit of infinite Ra.

Figures 3.13 and 3.14 plot the kinetic and thermal dissipation rates $\epsilon_u, \epsilon_\theta$ against GL predictions. In agreement with what has been observed previously, we observe agreement with GL theory in the range of parameters where the friction ratios are approximately constant with the parameters, i.e. at large values of $\mathrm{Re}\,\mathrm{Pr}$. Overall, it is interesting to note that even when the friction is dominant, we can recover the ultimate regime scaling, as long as the velocity friction ratio remain relatively constant as a function of the parameters and neither there is not too big an asymmetry between the two frictions. In regimes where the asymmetry prevails, there are no clear scaling laws that emerge, meaning that the scalings are probably not universal in Ra and Pr only, and that friction-dependent corrections need to be implemented.

## 3.4 Going further: new regimes at very high Ra

So far we have focused on the $\mathrm{Ra} \leq 10^{10}$ range, for two reasons. The initial reason is that as Ra increases, the time step of the simulations decrease, leading to increasingly long simulations. The more complex reason, as we will see in this section, is that at $\mathrm{Ra} \gtrsim 10^{11}$, a transition occurs towards an ill-behaved regime. We put this section separate from the previous results, as it is more exploratory in nature and not as in-depth. We set $\mathrm{Pr} = 1$ for this whole section.

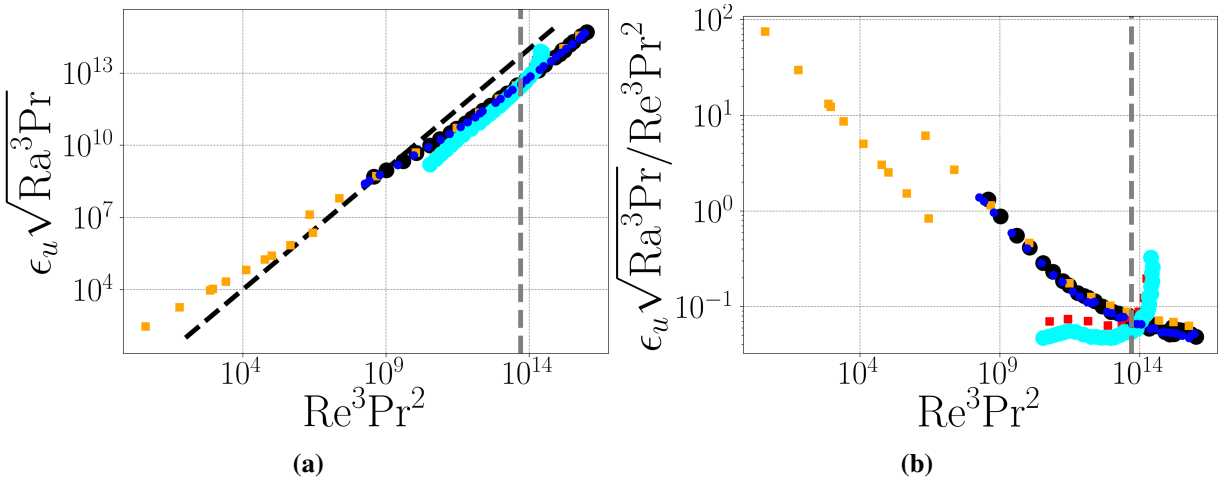


**Figure 3.14:** Scaling of kinetic dissipation rate $\epsilon_u$ compared to the GL prediction $\mathrm{Re}^3(\mathrm{Pr}/\mathrm{Ra})^{3/2}$ in 3D results. Correspondence between symbols and datasets are given in table 3.3). The gray dashed line separates the non-universal (left) and the universal (right) friction dominated regimes for data corresponding to figure 3.6. (figure 3.14a) $\epsilon_u \sqrt{\mathrm{Ra}^3\,\mathrm{Pr}}$ vs $\mathrm{Re}^3\,\mathrm{Pr}^2$. The black dashed line corresponds to the GL prediction $\epsilon_u \sim \mathrm{Re}^3(\mathrm{Pr}/\mathrm{Ra})^{3/2}$. (figure 3.14b) Compensated plot $\epsilon_u \sqrt{\mathrm{Ra}^3\,\mathrm{Pr}}/\mathrm{Re}^3\,\mathrm{Pr}^2$ vs $\mathrm{Re}^3\,\mathrm{Pr}^2$.

### 3.4.1 Stable and intermittent regimes

Figure 3.15 exhibits the compensated Nu vs Ra scaling for a very large range of Ra up to $10^{20}$. We observe three separate behaviors. At "low" Ra up to $\mathrm{Ra} \approx 10^{11}$, we recover our usual asymptotic ultimate regime, as in the previous sections. At $\mathrm{Ra} \approx 10^{11}$, we observe a very abrupt transition towards a new highly-fluctuating regime, which still exhibits a $\mathrm{Nu} \sim \mathrm{Ra}^{0.5}$ scaling. At very high Ra, the simulations become too slow and temporally under-resolved, and the results become irrelevant.

This new highly fluctuating regime, which we will refer to as the "intermittent" regime (as opposed to the "stable" regime), is a lot less stable numerically, and thus requires significantly longer simulations.

### 3.4.2 Instabilities in the intermittent regimes

Looking at Nu as a function of time in this regime in figure 3.16, we observe that the simulation first follows a rather long evolution along the stable regime, before suddenly transitioning towards the intermittent regime as an instability develops, increasing its energy by several orders of magnitude in the process.

A first insight into what is happening comes from looking at the energy spectra. Before the instability develops (figure 3.17a), we have standard stable regime spectra with $E(k) \sim k^{-5/3}$. In the intermittent regime, we observe a very singular point in the spectrum that peaks above the others (figure 3.17b). This behavior, and the location of the singular point, do not depend on the relative tolerance nor on the adaptive cutoff of the solver.

We track the location $k_{\mathrm{peak}}$ of this point with respect to Ra in figure 3.18, and observes that $k_{\mathrm{peak}} \propto \mathrm{Ra}^{1/4}$. This corresponds to the scaling of the critical wavenumber $k_c$ above which the instability growth rate $\sigma$ defined in section 3.2.2.1 becomes positive.

We do not have a clear explanation for this instability. Although it seems linked to equation (3.4), its evolution is counterintuitive. We can qualitatively explain *why* an instability of

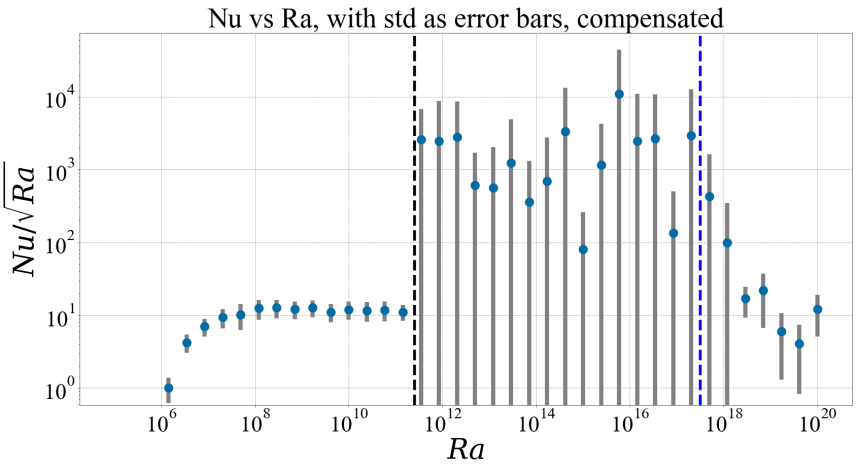


**Figure 3.15:** $\mathrm{Nu}/\sqrt{\mathrm{Ra}}$ vs Ra on a very big range of Ra. Grey lines represent the standard deviation of Nu. Up to $\mathrm{Ra} \approx 10^{11}$ (dashed black line) we observe an asymptotic ultimate regime with low fluctuations. At $\mathrm{Ra} \approx 10^{11}$ there is a very abrupt change of regime into a much more volatile behavior, which still exhibits ultimate regime scalings. Simulations at $\mathrm{Ra} \gtrsim 10^{17}$ (dashed blue line) are under-resolved in time and are far from statistical equilibrium.

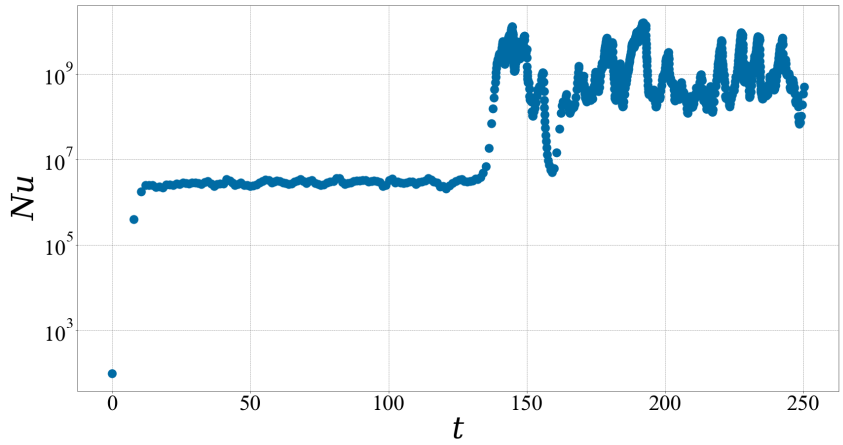


**Figure 3.16:** Nu vs time for $\mathrm{Ra} = 3.46 \cdot 10^{11}$. The first half of the simulation follows the stable regime, before transitioning onto the intermittent regime.

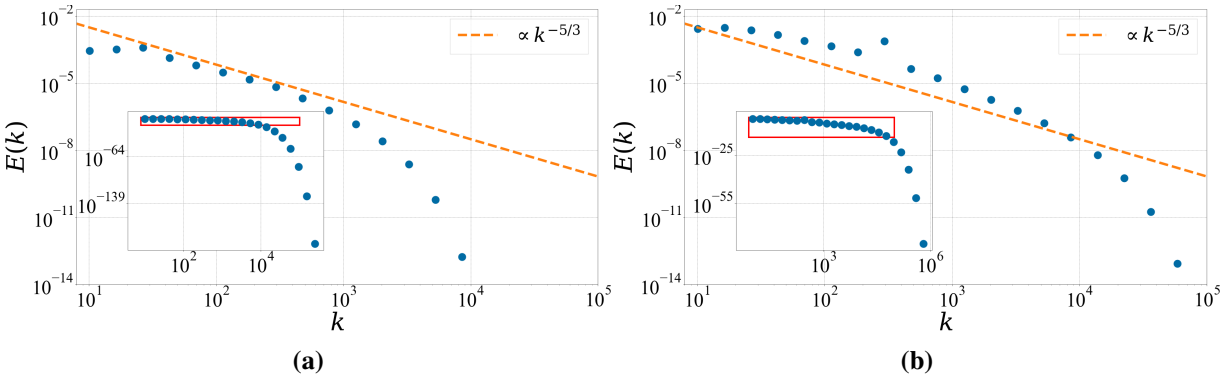


**Figure 3.17:** Energy spectra $E(k)$ before and after the instability for Ra = $3.46 \cdot 10^{11}$, zoomed in on the inertial regime. The insert shows the full spectrum, with a red border indicating the zoomed region. (figure 3.17a) Before the instability, in the stable regime, we observe a standard $E(k) \propto k^{-5/3}$ spectrum. (figure 3.17b) After the instability, in the intermittent regime, we observe a very singular peak around $k = 300$.

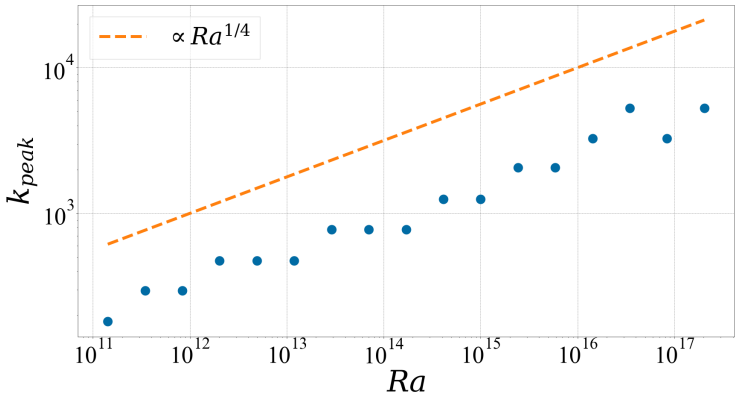


**Figure 3.18:** Location $k_{\text{peak}}$ of the peak in the $E(k)$ spectrum versus Ra. We observe that $k_{\text{peak}} \propto k_c \propto \text{Ra}^{1/4}$ where $k_c$ is the wavevector at which the instability growth rate $\sigma$ (defined in section 3.2.2.1) becomes positive for a given Ra.

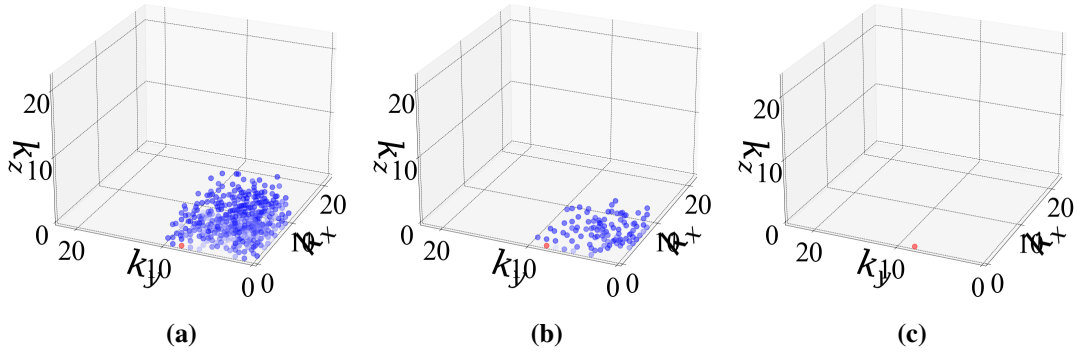


**Figure 3.19:** Evolution of the points with an energy $E(k) \geq \max E(k)/5$ during the growth of the instability. Axis ticks represent the indice $n$ of the point $k_n = k_{\min}\lambda^n$. Color represents the value of the energy (normalized per frame), increasing from blue ($E(k) = \max E(k)/5$) to red ($E(k) = \max E(k)$). Figure 3.19a is during the stable regime, figure 3.19b is during the transition and figure 3.19c is during the intermittent regime. We see that the instability is already very visible in the stable regime, and eventually becomes the main component of the simulation, while remaining extremely singular.

the sort develops after a certain Ra. We have added a large-scale friction to counteract the instabilities. However, this friction only acts on a portion of the spectrum, and as Ra increases and the spectrum subsequently becomes bigger and bigger, it is only expected that far enough from the large-scale friction we eventually see the instabilities develop again. Nevertheless, $\sigma(k)$ is a decreasing function $k$, and by this logic we would thus expect $k_{\text{peak}}$ to remain roughly constant, not increase. The second intriguing part concerns the extremely localized nature of the instability. The spectra indicate that it is localized on a single shell, but looking at individual points (figure 3.19) reveals that it is localized on a single *point* ! Moreover, this point is not even in a corner of the grid. Figure 3.19a also tells us that although the transition between the regimes happens late in the simulation, its traces are already visible much earlier on. The last characteristic is that it always happens at an (inner) edge of the grid.

### 3.4.3 Adding an edge friction

In the same way we have added a large-scale friction to counteract instabilities at small $|k|$, we can add an "edge friction" to counteract instabilities at the inner edges of the grid, i.e. at small $|k_{x,y,z}|$. However, although this edge friction counteracts the instability *for some time*, it eventually resurfaces at slightly higher wavenumbers. As seen in figure 3.20, the qualitative behavior of Nu vs Ra is the same as in the common case, with a stable and an intermittent regime. However, as expected, the fluctuations of the intermittent regime are lower (compared to the stable baseline) when we add the edge friction.

## 3.5 Conclusion

In this chapter, we investigated scaling laws in the Homogeneous Rayleigh Bénard (HRB) equations using log-lattices, which enables us to explore a range of parameters and wave-numbers way beyond what is accessible in direct numerical simulations of the equations. By adding a large-scale friction to the HRB equations, we are able to solve the issue of exponentially diverging solutions in a bounded range of Ra. This large scale friction become non-negligible when the fluid become turbulent enough, so that total energy balance depart from the energy balance

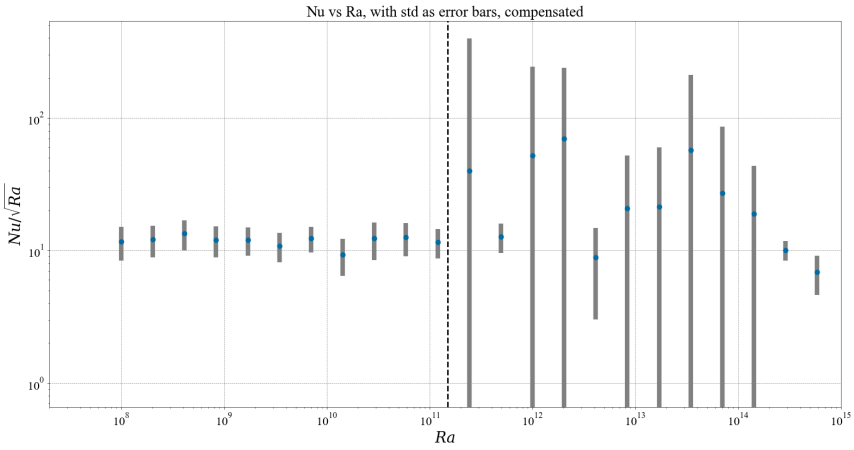


**Figure 3.20:** $\mathrm{Nu}/\sqrt{\mathrm{Ra}}$ vs Ra with an edge friction equal to $10^{-3} * f$. Grey lines represent the standard deviation of Nu. We observe the same qualitative behavior as in figure 3.15.

considered in GL theory, where no friction is present. Despite this, we still observe scaling law for Nu and Pr that are very close to the universal turbulent predictions of Grossmann-Lohse (GL) theory: $\mathrm{Nu} \sim \mathrm{Ra}^{1/2}\,\mathrm{Pr}^{1/2}$, $\mathrm{Re} \sim \mathrm{Ra}^{1/2}\,\mathrm{Pr}^{-1/2}$, $\epsilon_\theta \sim \mathrm{Re}(\mathrm{Pr}/\mathrm{Ra})^{1/2}$, $\epsilon_u \sim \mathrm{Re}^3(\mathrm{Pr}/\mathrm{Ra})^{3/2}$ for an important range of parameters, corresponding to situations where the thermal friction is non-negligible and the kinetic friction does not vary significantly as a function of the parameters. This is obtained at large enough Ra and for Pr depending on the value of Ra.

In addition to this regime, we also observe another turbulent, friction dominated regime at $\mathrm{Pr} \ll 1$. This regime has no simple and universal dependence with the parameter, and depends on the variations of the kinetic friction with the parameters.

Our observation show that the inclusion of friction, which is necessary to obtain well-behaved stationary regimes in the HRB framework, complexifies the phase space but nevertheless allows for the existence of a universal turbulent regime, where scaling laws are very close to the GL friction-less theoretical laws. In some geophysical or astrophysical situations, large scale friction arises due to rotation (Ekman friction), stratification (Rayleigh friction) or magnetic field (Hartman friction), and the two scaling regimes we find (one universal, and one non-universal) may be relevant and could be explored within the log-lattice framework.

It is not yet clear how the decimation of nonlinear interaction that takes place in log-lattice influences the prefactors of the scaling law. The comparison with DNS data shown on figure 3.8a for example, indicate that the log-lattice model with friction is more efficient to transport heat than the DNS without friction. Whether this difference is due to friction, or to the decimation is still an open question, and the topic of ongoing work.

# Chapter 4

# Rotating fluids

Our long-term vision is to employ log-lattices in the study of concrete geophysical flows. In the preceding chapter, we examined a fundamental aspect of geophysical flows, namely, temperature variations within the flow In this chapter, we delve into another significant component of geophysical flows, rotation. We first employ log-lattices to investigate simple 2D beta-plane flows, and subsequently transition to studying fully rotating 3D turbulence.

## Takeaways

We have not succeeded in reproducing the dynamics of quasi-geostrophic beta-plane (QGBP) flows on log-lattices.

The raw 2-layer QGBP equations pose mathematical challenges when treated on Fourier grids.

The 1-layer QGBP do not pose such issues. However, the emergence of zonal jets, despite the apparent satisfactory behavior of Rossby waves, is not visible.

This could be due to the impossibility to observe exact Rossby wave resonance on log-lattices due to geometrical constrains. Further investigations are required to determine whether this could also be due to problems with the inverse cascade in 2D log-lattices, the absence of nonlocal interactions, the sparse nature of local interactions, or the mathematical implementation of the $k_i = 0$ modes.

We then simulate the 3D rotating NSE, without $k_i = 0$ modes, which prevents condensation to a quasi2D flow. We recover the same scaling laws as in DNS [Ale15] for all regimes that do not involve condensation.

## 4.1 2D beta-plane flows

Most of the endeavors in this section ended up in failure. However, there is much to learn from those attempts. Those simulations are the first in-depth 2D simulations on log-lattices, and the first to use the $k_i = 0 \mid_{i=x,y,z}$ modes.

### 4.1.1 Introduction

When simulating fluid dynamics in the Earth's rotating frame of reference, a new force due to the Earth's rotation intervenes, called the Coriolis force $F = -2m\Omega \times u$ (responsible for the "Coriolis

effect"). The corresponding parameter $f = 2\Omega \sin \phi$ depends on the latitude $\phi$, and therefore varies at the surface of the globe. A number of common approximations can be made to simplify those equations. Due to the small aspect ratio of the considered geometry, it is standard to consider the flow quasi-2D. The quasi-geostrophic (QG) approximation assumes a near-balance between the Coriolis force and the pressure forces. On top of the 2D QG approximation, the "beta-plane" model consists in working around a fixed $\phi = \phi_0$ and doing a first-order Taylor expansion, leading to $f = f_0 + \beta y$ where $y$ is the meridional distance from $\phi_0$. This approximation greatly simplifies the dynamics of the system, while retaining interesting features such as Rossby waves. For those reasons, this model is widely used as a toy model in geophysical fluid dynamics [Ped13].

### 4.1.2 Issues with 2-layer flows on log-lattices

A common setting for the 2D QG beta-plane (simply referred to as "beta-plane" hereafter) equations is a 2-layer flow with an "upper" and a "lower" layer. Our original goal was to replicate on log-lattices some features of this model observed in DNS, such as the growth of a linear baroclinic wave, the crossing of a baroclinic jet by a vortex, the variability of a forced zonally uniform zonal jet, based on DNS code by Sebastien Fromang `https://github.com/sfromang/QGbeta`. Unfortunately, the 2-layer nature of the equation poses a critical difficulty on log-lattices.

#### 4.1.2.1 2D quasi-geostrophic beta-plane equations

Let the subscript 1 represent the upper layer, and 2 represent the lower layer. The zonal velocity $u$ and the meridional velocity $v$ can then be expressed by their streamfunction

$$\begin{aligned} u_i(x, y) &= -\partial_y \psi_i, \\ v_i(x, y) &= \partial_x \psi_i, \end{aligned} \tag{4.1}$$

where $x$ (resp. $y$) represents the zonal (resp. meridional) position.

The potential vorticity $q$ is then defined as

$$q_i(x, y) = \partial^2_{xx} \psi_i + \partial^2_{yy} \psi_i + \frac{\psi_j - \psi_i}{\lambda_R}, \tag{4.2}$$

where $j = \delta_{i,2} + 2\delta_{i,1}$ and $\lambda_R$ is the Rossby deformation radius. It follows that

$$\partial_t q_i + \partial_x (u_i q_i) + \partial_y (v_i q_i) + \beta v_i = 0. \tag{4.3}$$

#### 4.1.2.2 Linear instabilities in the Eady model

A simple feature of this system is the growth of a linear baroclinic instability when $\beta = 0$ ("Eady model"[1]), whose growth rate can be exactly computed. This happens with the following initial conditions:

$$\begin{aligned} \overline{u_1}(x, y) &= U, \\ \overline{u_2}(x, y) &= 0, \end{aligned} \tag{4.4}$$

[1]The Eady model also includes some additional hypothesis, among which the Boussinesq approximation and a constant static stability parameter

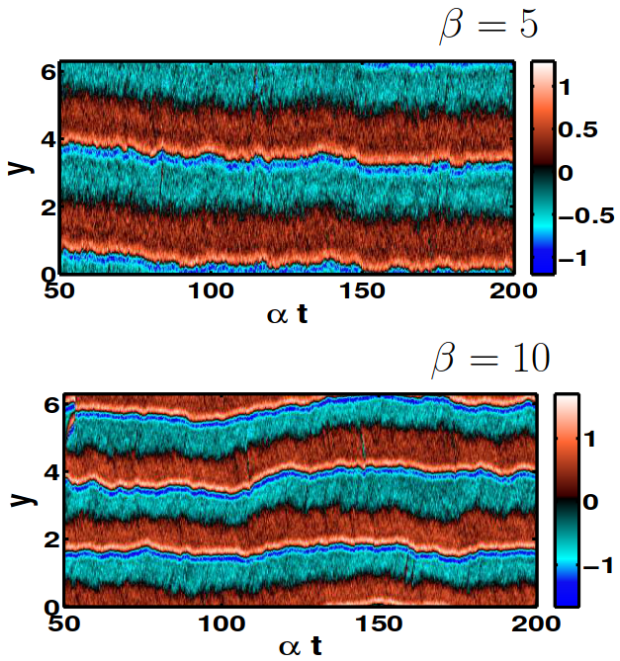


**Figure 4.1:** Extract of figure 2 from [SRB21]: Hovmöller diagrams of the vorticity $\omega$ for different $\beta$ (the color represents the value of the zonally averaged vorticity as a function of time and latitude). We observe that the number of jets increases with $\beta$.

where we have decomposed the fields into a time-independent "background" flow $\bar{\cdot}$ and a "perturbed" flow $\cdot'$:

$$u_i(x, y, t) = \overline{u_i}(x, y) + u_i'(x, y, t). \tag{4.5}$$

Plugging this back into equation (4.2) requires computing $\psi_i$. This is trivial in direct space. However, in Fourier space, $\psi_1(x, y) = -Uy$ is not a periodic function, and in particular in very sparse spaces such as log-lattices it cannot be represented at all !

Note that this incompatibility is *only* raised by the layer interaction term $\frac{\psi_i - \psi_j}{\lambda_R}$, which is the very reason why we cannot practically work directly with $u, v$ instead of $\psi$.

### 4.1.3 1-layer flows: the case of zonal jets

The easiest way to overcome the mathematical issue raised in the previous paragraph is to work with a single layer of fluid. Despite its simplicity, this model still exhibits numerous physical phenomena and bifurcations [LB15].

#### 4.1.3.1 A simple model of zonal jets

In order to compare log-lattice and DNS results, we focus on a simple application of 2D QG beta-plane 1-layer flows, in which we look at the formation of zonal jets, following [SRB21] (figure 4.1). Mid-latitude zonal jets naturally form in the atmosphere of many planets. In their paper, Simmonet et al. investigate spontaneous transitions between different numbers of jets under random forcing.

The non-dimentional equation describing our 2D QG beta-plane flow is the following[2]

$$\partial_t \omega + u \cdot \nabla \omega + \beta u_y = -\alpha\omega - \nu\Delta\omega + \sqrt{2\alpha}\eta, \tag{4.6}$$

[2]Note that since we use log-lattices, we do not need to use hyperviscosity as in the original paper

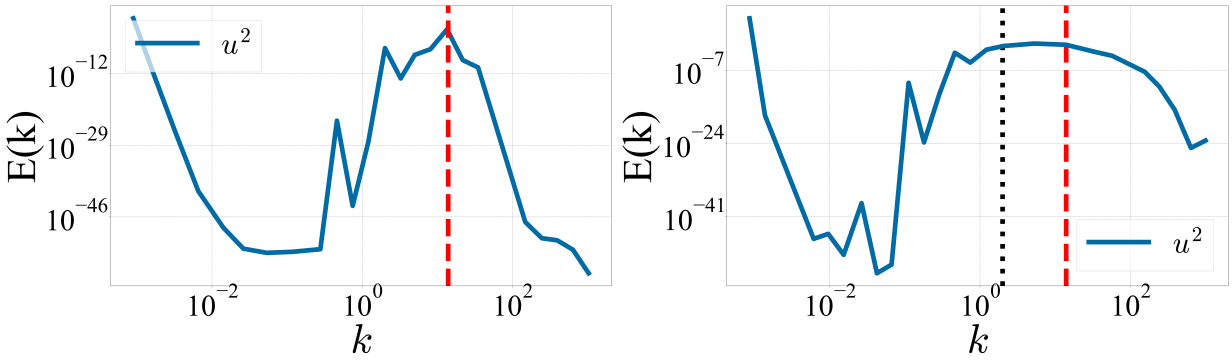


**(a)** **(b)**

**Figure 4.2:** Energy spectra at different times for a 2D QG beta-plane 1-layer forced flow. (figure 4.2a) In the transient state, (figure 4.2b) in the stationary state. The dashed red line indicates the scale $k_f$ at which the energy is injected, and the dotted black line in figure 4.2b indicates the approximates Rhines scale $k_R$. We observe no noticeable peak around the Rhines scale.

where $\omega$ is the non-dimentional vorticity, $u$ is the non-dimentional non-divergent velocity, $\beta$ is the non-dimentional gradient of the Coriolis parameter, $\alpha$ is the ratio of the shear timescale over the dissipative timescale, $\nu$ is the non-dimentional viscosity, and $\eta$ is a random noise, white in time and space, confined around a given wavenumber $k_f$.

In this setting, it is believed that the number of zonal jets $N_j$ scales as $N_j \sim \beta^{1/2}$. A slightly more complex version of this equation shows great agreement with experimental results [LFB21].

#### 4.1.3.2 Results

Our original goal was to observe the evolution of $N_j$ with $\beta$ on log-lattices. However, we never managed to observe zonal jets on log-lattices. In this section, we explain the results we obtained, the steps we took to better understand what went wrong, and our conclusions.

**Expectations** Counting the number of zonal jets in DNS (Direct Numerical Simulation) can be a straightforward task. A commonly employed approach involves looking at temporal averages of the zonally averaged vorticity as a function of latitude. By examining the number of sign changes in the magnitudes of order 1, one can determine the count of zonal jets. However, in Fourier space, this simple technique cannot be applied. Instead, a possible indication of the formation of zonal jets is observed as a bump in the energy spectrum at a wavenumber that corresponds to the periodicity of the jets in space. Unfortunately, employing this method in DNS [Che+96; DG02; SDG07] has yielded relatively weak results, as the peaks in the energy spectrum are not very pronounced.

To get a hint of the rough wavenumber at which we expect to see the peak, one can look around the Rhines scale $L_R$ and its associated wavenumber $k_R \approx \sqrt{\frac{\beta}{2U}}$ [SDG07], where $U$ is the RMS of $u$.

We expect to see a strong energy condensation around large scales in our simulations due to the inverse cascade. In order to decouple the condensation scale and the Rhines scale, we chose a low $k_{\text{min}}$.

**Energy spectra** Figure 4.2 shows the energy spectra in the transient and stationary state.

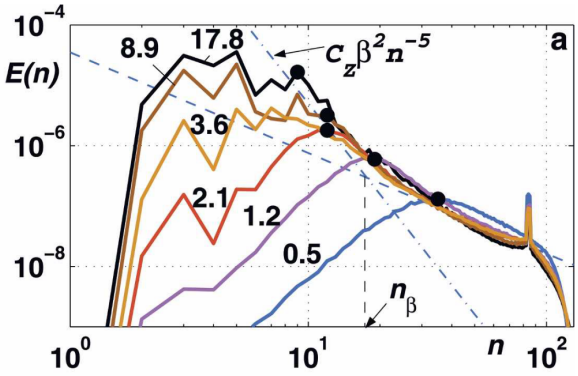


**Figure 4.3:** Figure 3a from [SDG07]: total energy spectra at different times of unsteady DNS simulations of two-dimensional turbulent flows on the surface of a rotating sphere. Note the marked injection peak around $k \approx 80$. The spectra are marked by the total energy ($\times 10^5$) accumulated in the flow field from the beginning of simulations. Black dots show the location of the energy front. Dashed blue lines mark the $-5$ and $-5/3$ slopes.

We observe no noticeable peaks around the Rhines scale in figure 4.2b. Although there are other peaks present in the spectrum at larger scales, we believe those to be artifacts of the initial conditions, and totally unrelated to hypothetical zonal jets.

Looking at the difference between the transient and the stationary state, and comparing the stationary state to DNS results of figure 4.3, we observe a striking difference.

Although the injection scale $k_f$ corresponds to a clear injection peak in the transient state (figure 4.2a, $k \approx 14$), energy accumulation eventually smooths out this peak in the stationary state, (figure 4.2b) where no injection peak is visible. In contrast, DNS results show a very sharp injection peak that remains throughout the simulation (figure 4.3, around $k = 80$). The absence of a marked injection peak in log-lattice is not a feature specific to beta-plane flows, and has been observed in our other simulations. It is, however, hard to quantify the extent of its impacts on the dynamics of the system.

**Rossby waves in the formation of zonal jets** To explain the absence of zonal jets on log-lattices, one must first understand how zonal jets are formed. The exact process is very complex, and involves a combination of fast and slow, small-scale and large-scale processes, characterized by nonlinear and nonlocal interactions. However, a very simplified but still informative picture can be drawn.

When starting from a state of rest, the application of a random forcing at scales smaller than the Rhines scale leads to the development of a 2D inverse energy cascade during an initial phase. However, this cascade is halted at a scale comparable to the Rhines scale, where the influence of Rossby waves becomes crucial and restricts energy transfer. It is widely acknowledged that this barrier has an anisotropic nature and promotes the formation of zonal structures. As a result, zonal jets emerge, exhibiting a typical width on the order of the Rhines scale.

Based on this simplified understanding, a hypothesis can be put forward, suggesting that the absence of zonal jets on log-lattices comes from a defect related to Rossby waves.

Section 4.1.3.2 shows the 2D observed maxima of the temporal Fourier peaks against the theoretical dispersion relation of Rossby waves. We observe a perfect agreement between the two, without any adjustable parameter.

This indicates that a priori, the lack of zonal jets on log-lattices cannot be attributed to the presence not to the temporal dynamics of Rossby waves.

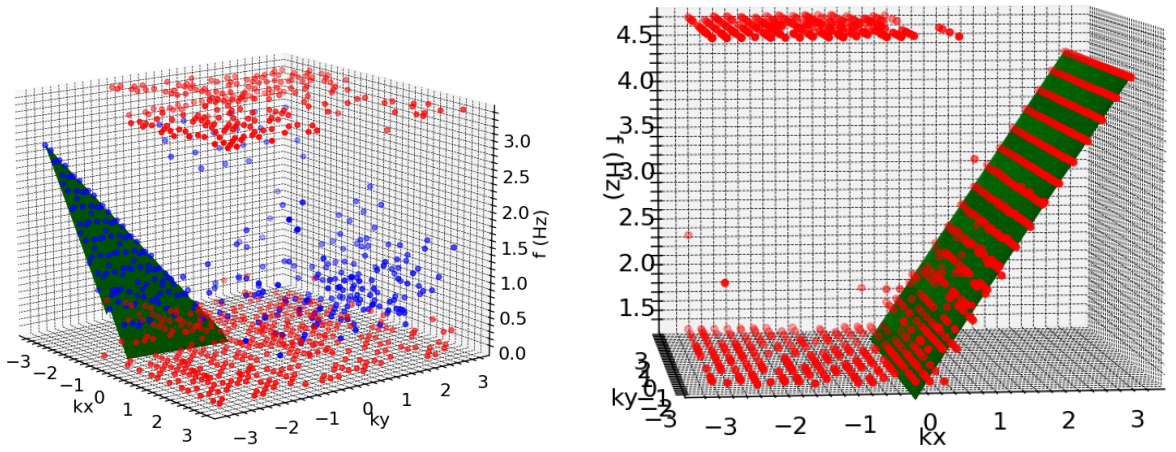


**(a)** **(b)**

**Figure 4.4:** Temporal Fourier peaks $\omega(k_x, k_y)$ and theoretical dispersion relation of Rossby waves (figure 4.4a) for $\omega > 0$ and (figure 4.4b) for $\omega < 0$. The green surface represents the theoretical dispersion relation of Rossby waves. The blue and red points represent the peaks of the temporal Fourier transform of $\omega$ for each point $(k_x, k_y)$. In the $\omega > 0$ figure only, the red points indicate extremal points where we likely do not have enough sampling to compute the peaks accurately. All axes are in log scale from an arbitrary reference, such that $k_x = 2$ indicates $k_x = k_0 \cdot 10^2$ and $f = 0.5$ indicates $f = f_0 \cdot 10^{0.5}$. We observe a very good agreement, without adjustable parameters.

**Energy transfers** The next aspect to look at is energy transfers in the inverse energy cascade. Indeed, the spectral energy transfer in DNS [SDG07] shows clear anisotropic peaks conducting energy from high wavenumbers to low wavenumbers. However, we do not observe those behaviors in our log-lattice simulations. We can think of several reasons why this could be the case, but did not have enough time to extensively test any of them.

Firstly, we have no clear analysis of 2D-NSE on log-lattices. Therefore, it is possible that the inverse cascade itself manifests in an unexpected way even without beta-plane equations. Second, some key process of the formation of zonal jets involve nonlocal interactions, which should be noticeably weakened on log-lattices due to the mathematical form of the convolution. Third, the anisotropic transfers that lead to the formation of zonal jets occur on a restricted range of scales, and involve precise local triadic interactions, which might be absent or not enough represented on our sparse grids. Finally, as expanded below, the log-lattice structure hinders the resonance of Rossby waves.

**Rossby wave resonance on log-lattices** By construction, log-lattices are intrinsically constrained, as only some values of $\lambda$ allow triadic interactions $k = k_1 + k_2$. However, the resonance of two waves $u_1(k_1, \omega_1), u_2(k_2, \omega_2)$ into $u(k, \omega)$ requires both the wavevector and the pulsation to match:

$$k = k_1 + k_2, \tag{4.7}$$

$$\omega = \omega_1 + \omega_2. \tag{4.8}$$

It is therefore non-trivial that despite existing on the log-lattice, the Rossby waves can enter into resonance with one another.

The dispersion relation for Rossby waves with zero background flow is

$$\omega = -\beta \frac{k_x}{k^2}. \tag{4.9}$$

Let's consider a generic 2D log-lattice, in which $k_1 = k_x\lambda^a + k_y\lambda^c$, $k_2 = \sigma_x k_x \lambda^b + \sigma_y k_y \lambda^d$ where $a, b, c, d \in \mathbb{Z}$ and $\sigma_{x,y} = \pm 1$.

The resonance condition then writes

$$\frac{\omega_1 + \omega_2}{\omega} = 1 = \frac{k^2\lambda^a}{\lambda^{2a}k_x^2 + \lambda^{2c}k_y^2} + \sigma_x \frac{k^2\lambda^b}{\lambda^{2b}k_x^2 + \lambda^{2d}k_y^2}. \tag{4.10}$$

This can easily be solved for $k_x^2$, $k_y^2$, and upon removing trivial solutions, there remains a unique possibility

$$k_y^2 = H^2 k_x^2, \tag{4.11}$$

$$H^2 = \frac{\lambda^{b+a}}{\lambda^{a+2d} - \lambda^{b+2c}}, \tag{4.12}$$

$$\sigma_x = -1. \tag{4.13}$$

Equation (4.11) only works on a log-lattice if $\log_\lambda H \in \mathbb{Z}$, which admits no solutions[3].

Therefore, there can be no strict resonance of Rossby waves on log-lattices, which in itself could explain the absence of zonal jets.

**Other potential sources of divergence** There is a final, more technical source of divergence between our results and DNS outputs, which is due to the implementation of the $k_i = 0$ modes. This chapter is the only one in which we have used them, and as such we have a weak understanding of the quantitative changes they bring to the log-lattice dynamics. Moreover, several questions, such as the influence of the prefactors of the $k_i = 0$ modes in the convolution, remain open.

## 4.2 Rotating homogeneous turbulence

As written in the previous section, a difficulty in evaluating the failures of the 2D QG beta-plane model is the lack of perspective and hindsight on generic 2D log-lattice simulations, such as 2D NSE. However, we have accumulated more experience in the 3D case [CM18; Mar19; CM21; Mar22; BD23; Pik+23] where we recover many known properties of the original equations. It is therefore natural to look at rotating turbulence through a new angle, in 3D.

### 4.2.1 Introduction

The inclusion of uniaxial rotation in the Navier-Stokes Equations (referred to as "rotating turbulence") introduces a wide range of fascinating characteristics that are absent in the original equations. Among these, two prominent mechanisms emerge: the emergence of inertial waves, and the transition to quasi-2D flow as the rotation rate intensifies, causing the gradual disappearance of vertical velocity gradients. These two features interact in intriguing and complex ways, leading to a diverse set of phenomena. Although the quasi-2D behavior is theoretically well understood, the transition from the 3D and the quasi-2D flows, which involves nonlinear processes, is more elusive.

Rotating turbulence is characterized by two control parameters in a system of length $L$, rotation rate $\Omega$, velocity $U$ and kinematic viscosity $\nu$. The first one, as in non-rotating turbulence, is the usual Reynolds number $\mathrm{Re} \equiv \frac{Ul}{\nu}$. The second one, the Rossby number, quantifies the ratio

[3] For $\lambda = 2$ this is trivial. For $\lambda \neq \sigma \approx 1.3$ we have $a - b > 2(c - d)$ from $H^2 > 0$, which implies $a = c - d$, $b = -d$, and the condition becomes $\log_\lambda(\lambda^d - \lambda^{c-d}) \in 2\mathbb{Z}$, QED. For $\lambda = \sigma$ a similar argument can be drawn.

between linear and nonlinear time scales $Ro \equiv \frac{U}{2\Omega L}$. In the limit of low rotation (Ro $\gg$ 1), the flow essentially follows the characteristics of homogeneous isotropic turbulence (HIT). When Ro $\approx$ 1, cyclonic vortices manifest themselves on large scales, resulting in a quasi-2D flow. Further increasing the rotation (Ro $\ll$ 1) introduces both cyclonic and anticyclonic vortices, leading to a nearly complete two-dimensionalization of the flow fields. Moreover, rotation has a major impact on viscous dissipation, with inertial waves giving rise to [Gal03; CRG04] an anisotropic energy spectrum $E(k) \sim k_\perp^{-7/2} k_\parallel^{-1/2}$ in the fast rotating limit, where $\perp, \parallel$ are relative to the rotation axis. As a result, the viscous dissipation is reduced by a factor equal to Rossby $\epsilon_{rot} \sim \text{Ro}\, \epsilon_{\Omega=0}$.

Because the Coriolis force does not do any work and therefore does not alter the energy budget, it is necessary to add an external forcing to counteract the viscous dissipation in order to reach a statistical steady state. However, the details of this forcing, as well as the choice of control parameters, greatly influence the resulting regime of the simulation or experiment. This very large parameter space has led to difficulties in comparing results across publications.

Additionally, from a numerical perspective, thoroughly investigating a broad range of the Ro, Re parameter space is difficult. The combination of low viscosity values and high rotation rates necessitates simulations with high resolution, while reaching steady states demands extended integration times.

Recent numerical work by Alexakis [Ale15] attempts to alleviate most of those hurdles and investigate forced turbulence on a wide range of Ro, Re using many pseudo-spectral DNS. Each simulation is forced with a normalized Taylor-Green (TG) vortex.

This paper is particularly well suited to serve as a reference to compare log-lattice results: it covers a wide range of control parameters, requires many simulations, uses equations that translate well to Fourier space, and investigates scaling laws of aggregated observables such as dissipation.

While [Ale15] does not specifically examine the anisotropic distribution of velocity, a subsequent study by Yokoyama and Takaoka [YT17] addresses this aspect. They observe hysteresis in the anisotropy tensor $b_{zz} \equiv 1/3 - \left\langle u_z^2 \right\rangle / \left\langle |u|^2 \right\rangle$.

### 4.2.2 Equations and parameters

We restrict ourselves to rotating *homogeneous* turbulence, in periodic space without boundaries, of size $L$.

The rotating NSE then write

$$\partial_t u + u \cdot \nabla u + 2\Omega e_z \times u = -\nabla P + \nu \Delta u + F_0 f, \tag{4.14}$$

where $P$ is the pressure, $e_z$ is the rotation axis, and $F_0 f$ is the forcing.

The forcing is taken as a TG vortex localized around a scale $k_f$:

$$\begin{aligned} f_x &= A \sin(k_f x) \cos(k_f y) \sin(k_f z), \\ f_y &= A \cos(k_f x) \sin(k_f y) \sin(k_f z), \\ f_z &= 0, \end{aligned} \tag{4.15}$$

where $A$ is chosen such that[4] $\left\langle f^2 \right\rangle^{1/2} = 1$.

[4]In a DNS we can choose a single $k_f$ and set $A = 1/2$. On log-lattices however, we need to force on several neighboring $k_f$ because of the convolution's width, which also changes $A$ after normalization.

The fields are initialized from a random vorticity field, and the size of the grid is dynamically adjusted by looking at the energy fraction in the outermost layers[5].

Two control parameters $\mathrm{Re}_F, \mathrm{Ro}_F$ are derived based on the forcing amplitude as in [Ale15]:

$$\begin{aligned} \mathrm{Re}_F &\equiv \frac{\sqrt{F_0 L}}{\nu}, \\ \mathrm{Ro}_F &\equiv \frac{F_0}{2\Omega\sqrt{L}}. \end{aligned} \tag{4.16}$$

By non-dimensionalizing with respect to the RMS velocity $U$, we obtain another useful set of *computed* (a posteriori) parameters:

$$\begin{aligned} \mathrm{Re}_U &\equiv \mathrm{Re}_F\, U, \\ \mathrm{Ro}_U &\equiv \mathrm{Ro}_F\, U. \end{aligned} \tag{4.17}$$

**Lack of a $k_i = 0$ mode** In appendix A, we acknowledge our limited understanding of the impact of enabling the $k_i = 0$ modes on log-lattices, which may be connected to the failures observed in previous sections. To address this, we opt to simulate using a "classical" log-lattice configuration that excludes the $k_i = 0$ modes.

However, this choice is far from being transparent. Indeed, one of the major features of highly rotating turbulence is a quasi-2D behavior, which entails a condensation towards $k_z = 0$ modes. By using a classical log-lattice, we by design block this condensation. Therefore, this section should not be seen as an attempt to simulate *true* rotating homogeneous turbulence (RHT) on log-lattices, but rather as a first step in this direction, in which we investigate which features of RHT can be recovered in this setting, and which widely differ. In particular, there are two different ways in which a flow can become "quasi-2D". From a mathematical perspective, the Taylor-Proudman theorem only states that the vertical gradient of velocity in a highly rotating body of fluid tends to zero (nor observable on a classical log-lattice). This, in itself, does not have any implication on the anisotropy of the flow, which is free to have arbitrarily large (constant) vertical velocity. However, numerical experiments [YT17] indicate that the anisotropy tensor $b_{zz}$ goes to $1/3$ as rotation increases, indicating that not only $\partial_z u$ but also $u_z/u_{RMS}$ go to zero. To our knowledge, no study has explored the evolution of anisotropy in a flow where transfers towards $k_i = 0$ modes are impeded, and there are no theoretical predictions available regarding its progression.

### 4.2.3 Results

Figure 4.5 shows the two major regimes observed in our simulations: a laminar regime (figure 4.5a) and a turbulent, weakly rotating regime (figure 4.5b).

Figure 4.6 show the square of the RMS velocity $U^2$ as a function of $\mathrm{Re}_F, \mathrm{Ro}_F$ for 64 simulations spanning a large range of $\mathrm{Re}_F, \mathrm{Ro}_F$ (figure 4.6a), and the corresponding DNS results from [Ale15] (figure 4.6b). The log-lattice results display a $Ro_F^2$ slope up to $\mathrm{Ro}_F \approx 50$, followed by a plateau for $\mathrm{Ro}_F \gtrapprox 50$.

Figure 4.7 show the viscous dissipation $\epsilon$ as a function of $\mathrm{Re}_F, \mathrm{Ro}_F$ for those same simulations (figure 4.7a), the corresponding DNS results from [Ale15] (figure 4.7b), and figure 4.7c shows the same data as figure 4.7a but rescaled by $\mathrm{Re}_F$. In figure 4.7a, we observe a $\mathrm{Re}_F$-dependent

[5]We increase the grid size whenever $u_{rms,outer}/u_{rms} > 10^{-200}$.

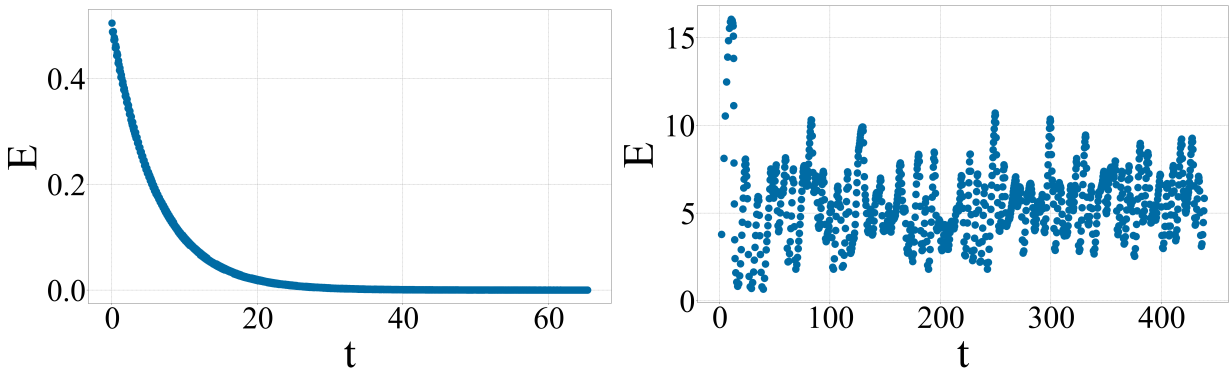


(a) (b)

**Figure 4.5:** Energy as a function of time for (figure 4.5a) $\mathrm{Re}_F = 3.73 \cdot 10^3, \mathrm{Ro}_F = 3.6 \cdot 10^{-3}$ and (figure 4.5b) $\mathrm{Re}_F = 3.73 \cdot 10^3, \mathrm{Ro}_F = 2.55$. We observe two main regimes in our simulations, either (figure 4.5a) laminar or (figure 4.5b) turbulent and weakly rotating.

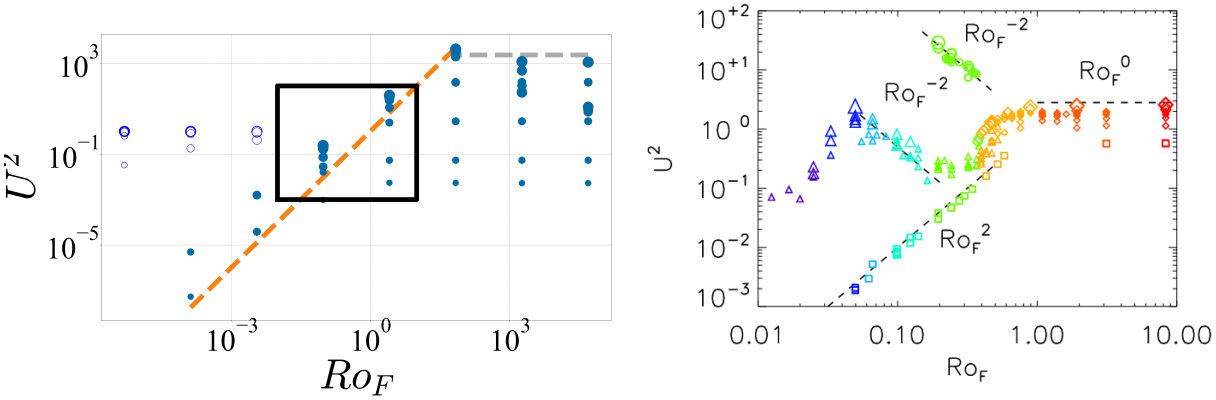


(a) (b)

**Figure 4.6:** Square of the velocityRMS$U^2$ as a function of $\mathrm{Ro}_F$. (figure 4.6a) Our log-lattice results. Dot sizes (from small to big) represent increasing $\mathrm{Re}_F$ (from $10^1$ to $10^7$ , in log scale). Empty dots indicate simulations that are have not reached a statistical steady state and should be disregarded. The black box indicates the range of parameters obtained in [Ale15]. The orange line draws a $\mathrm{Ro}_F^2$ power law, and the gray line draws a $\mathrm{Ro}_F^0$ power law. (figure 4.6b) Figure 14a from [Ale15] showing corresponding DNS results. We recover the same scaling law for the laminar and weakly rotating regimes.

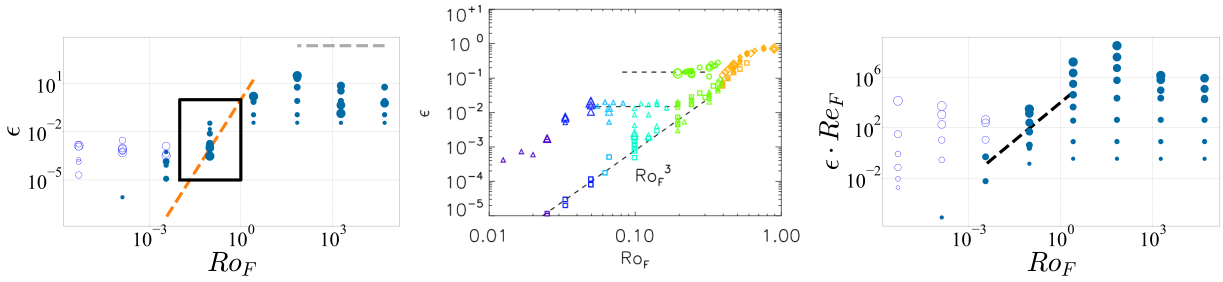


(a) (b) (c)

**Figure 4.7:** Viscous dissipation $\epsilon$ as a function of $\mathrm{Ro}_F$. (figure 4.7a) Our log-lattice results. Dot sizes and filling are the same as in figure 4.6. The black box indicates the range of parameters obtained in [Ale15]. The orange line draws a $\mathrm{Ro}_F^3$ power law, and the gray line draws a $\mathrm{Ro}_F^0$ power law. (figure 4.7b) Figure 14b from [Ale15] showing corresponding DNS results. (figure 4.7c) Same as figure 4.7a but plotting $\epsilon \cdot \mathrm{Re}_F$ instead of $\epsilon$. The black dashed line draws a $\mathrm{Ro}_F^2$ power law. Comparing figures 4.7a and 4.7b shows that, as expected, we do not recover the scalings of the quasi-2D condensates and the intermittent bursts. Due to numerical choices (see section 4.2.4), it is not relevant to compare the $\mathrm{Ro}_F^3$ law in those two figures; the corresponding law in our simulations is $\epsilon\,\mathrm{Re}_F \sim \mathrm{Ro}_F^2$, which we observe in figure 4.7b.

slope, and then a plateau for $\mathrm{Ro}_F \gtrapprox 50$. By rescaling in figure 4.7c, we observe a corresponding well-defined $\mathrm{Ro}_F^2$ slope, followed by a plateau.

Figure 4.8 shows the results of later simulations, which combine the 64-points parameter space previously studied with an additional 64 simulations around the parameter space of [Ale15] but focuses on the anisotropy tensor $b_{zz}$ (figure 4.8a), and related results from [YT17] (figure 4.8b). We observe that $b_{zz}$ decreases from $b_{zz} > 0$ to $b_{zz} < 0$ as $Ro_F$ decreases.

Finally, figure 4.9 shows the viscous dissipation $\epsilon$ versus $\mathrm{Re}_F$, $\mathrm{Ro}_F$ for a new set of simulations (figure 4.9a), as well as its rescaled counterpart $\epsilon_U$ as a function of $\mathrm{Re}_U$, $\mathrm{Ro}_U$ (figure 4.9b), and the corresponding DNS results from [Ale15] (figure 4.9c). Although the non-rescaled log-lattice results seem to exhibit a rich evolution with several bifurcations depending on both $\mathrm{Re}_F$ and $\mathrm{Ro}_F$, which we did not have time to study in detail, the rescaled results nicely collapse onto two branches, one following $\epsilon_U \sim \mathrm{Re}_U^{-1}$, and the other seemingly reaching a plateau at high $\mathrm{Re}_U$.

### 4.2.4 Discussion

[Ale15] identifies four major behaviors[6] in its simulations, represented by different symbols in figures 4.6b, 4.7b and 4.9c: laminar flows (squares) for small $\mathrm{Ro}_F$ along $\mathrm{Ro}_F \sim \mathrm{Re}_F^{-1}$, intermittent bursts (triangles) at high $\mathrm{Re}_F$ and low $\mathrm{Ro}_F$, quasi-2D condensates (circles) at high $\mathrm{Re}_F$ and moderate $\mathrm{Ro}_F$, and weakly rotating flows (diamonds) at high $\mathrm{Re}_F$ and high $\mathrm{Ro}_F$.

As shown in figure 4.5, we only observe the laminar and weakly rotating regimes on log-lattices. This is expected, as the two other regimes [Ale15] exhibit properties of a 2D3C flow, which is by construction not possible without the $k_i = 0$ modes.

Overall, the lack of a perfect agreement between DNS and log-lattice results is not surprising, as previous log-lattice experience suggests that scaling laws differ in their prefactors. What we are rather looking for is a qualitative matching, and relevant scaling laws.

In figure 4.6, we recover the same scaling laws as in DNS for the intermittent and weakly rotating regimes: a $U^2 \sim \mathrm{Ro}_F^2$ slope followed by a saturation at high $\mathrm{Ro}_F$. The saturation at high $\mathrm{Ro}_F$ is fairly trivial, as the effects of the rotation become negligible. The $U^2 \sim \mathrm{Ro}_F^2$ slope is a

[6] This is a simplified picture, see figure 1 in [Ale15].

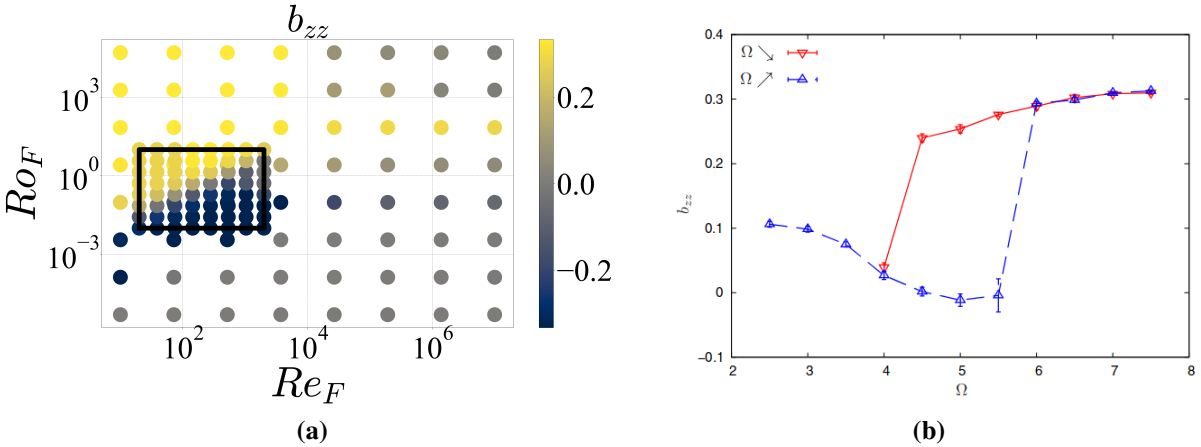


**Figure 4.8:** Anisotropy tensor $b_{zz}$ as a function of $\mathrm{Re}_F, \mathrm{Ro}_F$. (figure 4.8a) Our log-lattice results. The black box indicates the range of parameters used in [Ale15]. The gray points at low $\mathrm{Ro}_F$ are likely not converged. (figure 4.8b) Figure 1 from [YT17] showing $b_{zz}$ versus $\Omega$ for $\mathrm{Re}_F \approx 200$, in DNS. Surprisingly, we observe the *inverse* behavior of DNS, namely that $b_{zz}$ decreases with increased rotation on log-lattices.

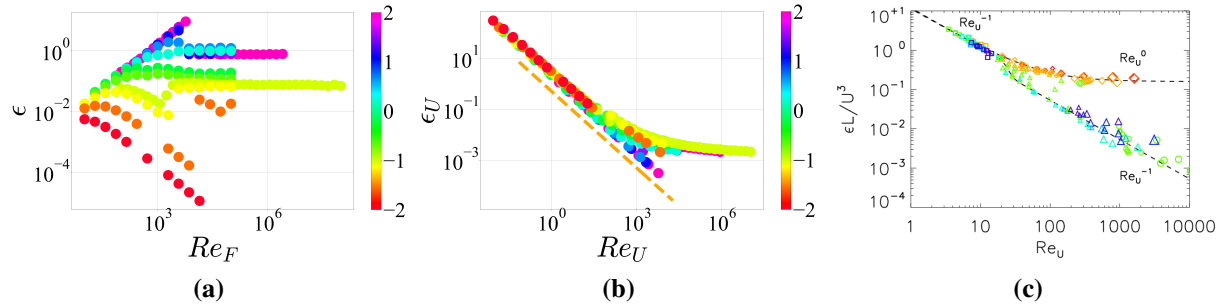


**Figure 4.9:** (figure 4.9a) Viscous dissipation $\epsilon$ as a function of $\mathrm{Re}_F$, color-coded by $\mathrm{Ro}_F$. The colorbar is in log scale, i.e. "2" corresponds to $\mathrm{Ro}_F = 10^2$. Visible gaps indicate non-converged points that were removed. (figure 4.9b) Rescaled viscous dissipation $\epsilon_U$ as a function of rescaled Reynolds number $\mathrm{Re}_U$, color-coded by $\mathrm{Ro}_F$ as in the previous figure. The orange dashed line corresponds to $\mathrm{Re}_U^{-1}$. (figure 4.9c) Figure 15a from [Ale15] showing $\epsilon_U$ as a function of $\mathrm{Re}_U$ in DNS.

signature of the laminar regime for non-negligible rotations. Indeed, balancing the forcing and the Coriolis force in equation (4.14) yields $u \sim \frac{F_0}{\Omega}$ and thus $U \sim \mathrm{Ro}_F$. The branches in $\mathrm{Ro}_F^{-2}$, which correspond to the "quasi-2D condensates" and "intermittent bursts", are as expected not found on log-lattices.

Likewise, in figure 4.7, we do not recover the $\mathrm{Ro}_F^0$ branches of those two regimes. In the laminar regime, it would not make sense to observe the $\epsilon \sim \mathrm{Ro}_F^3$ observed in DNS in our log-lattice results. Indeed, from $U \sim \mathrm{Re}_F$ we deduce $\epsilon \sim U^3/\mathrm{Re}_U \sim \mathrm{Ro}_F^2/\mathrm{Re}_F$. However, in [Ale15], for technical numerical reasons, the laminar simulations are located along $\mathrm{Re}_F \sim \mathrm{Ro}_F^{-1}$, giving rise to an apparent $\epsilon \sim \mathrm{Ro}_F^{-3}$ scaling. In our case, since our $\mathrm{Re}_F, \mathrm{Ro}_F$ are uniformly (in log space) distributed, we have no reason to observe this specific scaling. In figure 4.7c we plot $\epsilon\,\mathrm{Re}_F$ as a function of $\mathrm{Ro}_F$, in which we recover the $\mathrm{Ro}_F^2$ law predicted by the laminar balance.

The DNS results from [YT17] (figure 4.8b) indicate that $b_{zz} \approx 0$ at high $\mathrm{Ro}_F$ and $b_{zz} \approx 1/3$ at low $\mathrm{Ro}_F$, with $b_{zz}$ never taking significant negative values during the transition. However, we find the opposite in our log-lattice simulations: as $\mathrm{Ro}_F$ decreases, $b_{zz}$ decrease to approximately $-1/3$. This corresponds to a flow whose energy is mainly contained in the vertical components. This difference is most likely the result of the lack of $k_i = 0$ modes, which hinders condensation.

Figure 4.9a displays a rich evolution with several bifurcations depending on both $\mathrm{Re}_F$ and $\mathrm{Ro}_F$, which we did not have time to study in detail. Rescaling $\epsilon$ and $\mathrm{Re}_F$ through $\epsilon_U \equiv \epsilon L/U^3$ and $\mathrm{Re}_U$, we obtain in figure 4.9b a much simpler picture, which we can compare to DNS results in figure 4.9c. We recover the same quantitative behavior, with a branch following $\mathrm{Re}_U^{-1}$ and a branch seemingly[7] reaching a state in which dissipation decay is very slow at high $\mathrm{Re}_U$.

Overall, we therefore have a strong agreement between log-lattice scaling laws and DNS results, except for the regimes that we do not observe due to the lack of $k_i = 0$ modes.

[7]Further analysis is necessary to determine whether we eventually reach a true plateau, or whether log-lattices exhibit a dissipation decaying very slowly (logarithmically) with $\mathrm{Re}_U$. This behavior is not specific to rotating turbulence.

# Chapter 5

# Other contributions

In the previous chapters, I discussed the research endeavors that primarily centered around my own work. However, science is a collaborative pursuit that thrives on the collective efforts and insights of researchers from diverse backgrounds. In this new chapter, I shift the focus to scientific articles in which I have contributed as a collaborator, but not as the primary author.

The articles presented in this section are the result of collaborative work with fellow PhD students who joined our log-lattice research group one or two years after I started my own research. Although I did not take on the role of the primary author, I actively participated in shaping the research direction, enhancing the numerical framework to suit their specific requirements, and engaging in intellectual discussions within the respective research groups.

The first article, "Log-lattices for atmospheric flows", combines chapter 3 and section 4.2 to investigate flows under both rotation and temperature gradients.

The second article, titled "Tracking complex singularities of fluids on log-lattices", builds upon the work of [CM21]. It investigates signatures of singularities in 1D viscous and non-viscous Burgers, 3D Euler and 3D Navier-Stokes equations, with hyper-, normal, and hypo-viscosity, using the singularity strip method.

The third article, "Reversible Navier-Stokes equation on logarithmic lattices", focuses on phase transitions within the Reversible Navier-Stokes equation and attempts to clarify an old conjecture by G. Galavotti.

Those articles are very good examples of numerically very intensive DNS that highly benefit from the log-lattice approach.

As they are self-contained, further introduction is unnecessary, and I present them in their original format[1] below.

## 5.1 Log-lattices for atmospheric flows

[1] "Tracking complex singularities of fluids on log-lattices" [Pik+23] is about to be submitted to Nonlinearity, while "Reversible Navier-Stokes equation on logarithmic lattices" [CBD23] has been accepted in PRE. "Log-lattices for atmospheric flows" is in a fairly advanced draft state.

MDPI

*Article*

# Log-lattices for atmospheric flows

**Quentin Pikeroen [1], Amaury Barral [1], Guillaume Costa [1] and Bérengère Dubrulle[1]***

[1] University Paris-Saclay, CEA, CNRS, SPEC, 91191, Gif-sur-Yvette, France
* Correspondence: berengere.dubrulle@cea.fr

**Abstract:** We discuss how projection of geophysical equations of motion onto an exponential grid allows to achieve realistic values of parameters, at a moderate cost. This allows to perform many simulations over a wide range of parameters, thereby leading to general scaling laws of transport efficiency that can then be used to parametrize the turbulent transport in general climate models for Earth or other planets. We illustrate this process using the equation describing the heat transport in a dry atmosphere, to obtain the scaling laws for onset of convection as a function of rotation. We confirm the theoretical scaling of the critical Rayleigh number $\mathrm{Ra}_c \sim E^{-4/3}$ over a wide range of parameter. We have also demonstrate the existence of two regimes of convection, one laminar extending near the convection onset, and one turbulent, occurring as soon as the vertical Reynolds number reaches a value of $10^4$. We derive general scaling laws for these two regimes, both for transport of heat, dissipation of kinetic energy, and value of the anisotropy and temperature fluctuations.

**Keywords:** keyword 1; keyword 2; keyword 3 (List three to ten pertinent keywords specific to the article; yet reasonably common within the subject discipline.)

**Citation:** Pikeroen,Q.; Barral, A.,Costa, G.,Dubrulle, B. Log-lattices for atmospheric flows. *Atmosphere* **2023**, *1*, 0. https://doi.org/

Received:
Revised:
Accepted:
Published:



## 1. Forewords by B. Dubrulle

I met Jack in 1999, when I came to the MMM division of NCAR for a one-year sabbatical. I had been attracted there by Jack's reputation, from conversation with Annick Pouquet, Uriel Frisch and Maurice Meneguzzi. Being a theoretician of turbulence, interested in geophysical application, I then knew that I would find in Jack a very good interlocutor, and benefit greatly of his physical insight, his broad knowledge about turbulence and geophysical flows, and his open mind. I met Jack regularly during my stay, and we spoke of all sorts of topics. It was after a discussion with him that I started to investigate Rayleigh Bénard flows and heat transfer properties-I published two papers on that topic that year. About Jack, I keep the memory of a true "gentleman of science", very kind to junior scientist (as I still was at that time), with a great sense of humor and an immense knowledge that he was keen to share. It is certainly thanks to Jack that I jumped into the modeling of geophysical flows, and I will always be grateful to him for this.

## 2. Introduction

Ultra-high Reynolds number flows are ubiquitous in geosciences, due to small viscosity, large dimensions or velocity. They are described by the Navier-Stokes Equations (NSE). A natural control parameter of NSE is the Reynolds number $Re = LU/\nu$ built using the viscosity $\nu$ and characteristic length $L$ and velocity $U$. Classical turbulent flows are thought to be described by NSE, with $Re \gg 1$. In 1941, Kolmogorov [K41] used such equations to predict the shape of the energy spectrum $E(k)$ derived from the Fourier transform of the velocity correlation function for isotropic and homogeneous turbulence stirred at a constant rate $\epsilon$. He found that it should scale like $E(k) \sim \epsilon^{2/3}k^{-5/3}$ in the range $1/L \ll k \ll \nu^{-3/4}\epsilon^{1/4}$ where $k$ is the wave-number. This prediction was verified in 1962 on data from a turbulent flow in Seymour Narrows [1] and appears to be one of the most robust laws of turbulence [2,3] being independent of the boundaries or on the stirring process. At large wave-numbers, viscous processes take over, and the spectrum decays

very fast, so that the energy contained in wave-numbers greater than $k_d = \nu^{-3/4}\epsilon^{1/4}$ is negligible. The overall behavior of $E(k)$ can be used to infer the typical number of dynamically active modes as $N = (k_d L)^3$. In geophysical flows such number can be quite large: for example, the atmosphere has $L = 10^3 km$ (the size of the large typhoons or cyclones), while $k_d^{-1}$ is smaller than 10 mm, resulting in $k_d L > 10^8$. Direct numerical simulations of the Navier-Stokes equations for such flows are thus impossible, as the total computational cost of reading-in/writing-out and coupling all these modes exceeds by many orders of magnitude the capability of the present most powerful computers.

If one wishes to simulate ultra-large Reynolds numbers like the atmosphere, one has no other way out than to empirically decimate modes via a clever selection of grid points or modes. Simulating viscous flows with just as many scales as needed to "get the physics right" has been and still is the holy grail of all researchers in the computational fluid community. If a well-established theory of turbulence were available, including a deep understanding of all interactions between scales, the quest would probably be over by now. In the absence of such complete theory, we need empirical yet clever strategies for mode number reduction. Jack Herring worked many years on such issue, using e.g. two-point closure (see e.g. [4]).

Nowadays, the most popular approach is to use a Large Eddy simulation strategy, in which only the large scales are simulated: present climate models have a grid size of 10 km, allowing to handle the data volume in 2 CPU seconds per time step. However, there is no free lunch: the price to pay for such a mode reduction is the addition of a (sometime very large) damping, to avoid accumulation of energy at the smallest simulated scale. In LES type climate simulations, the damping is the same as if the atmosphere were made of peanut butter and the ocean of honey, so that no fluctuations can develop. This is problematic to capture possible bifurcations, such as those observed in von Karman flows [5].

In this paper, we consider another class of model in which the modes reduction is achieved by keeping modes following a geometric progression. Such approximation leaves out a lot of possible interactions, as we shall see. However, it allows reaching very small scales with a very small number of modes. In the atmosphere, for example, only 27 modes are necessary to go from $k_0 = 1/L$ to $10^8/L$ by a geometrical progression of step 2 (38 with a step being the golden number). This means, that we can perform a "resolved" 3D simulation of an atmospheric flow with less than $2 \times 10^4$ modes (resp. less than $6 \times 10^4$), corresponding to the number of modes involved in a LES simulation at a resolution of 37km. The corresponding models correspond to Fluid dynamics on Log-Lattices, the properties of which were detailed in [6]. For example, they respect classical and basic properties of Navier-Stokes equation, such as constancy of energy flux in the inertial range. Given the potential of such models to describe ultra-high Reynolds number flow at a cheap prize, we investigate here further properties of such models with respect to one important open problems of atmospheric flows, which was dear to Jack, namely the influence of rotation on convection.

## 3. Log-Lattices framework

Consider a velocity field that obeys Navier-Stokes equation (NSE), with viscosity $\nu$ and forcing. Its Fourier transform, noted $u(t,k)$ is a complex field that obeys the equation:

$$\begin{aligned} \mathbf{i}k_j u_j &= 0, \\ \partial_t u_i + \mathbf{i}k_j u_i * u_j &= -\mathbf{i}k_i p - \nu k^2 u_i + f_i, \\ u(k,t) &= u^*(-k,t). \end{aligned} \tag{1}$$

where $*$ denotes the traditional convolution product, that involves for each $k$, coupling of modes $u(t,p)$ and $u(t,q)$, such that $k_i = p_i + q_i$ for any $i^{th}$ component. The (constant) density has been set to 1 for convenience, and thus disappears in front of the pressure term in Eq. (1).

In traditional spectral simulation of NSE, the wave-numbers are discretized on a linear grid, and can be written as $k = (m_1, \dots m_3)$ with $m_i \in \mathbb{Z}^3\}$. The convolution being ensured by the condition $m = n + q$ for any $(m, n, q) \in \mathbb{Z}^3$, it allows a lot of interactions between Fourier modes.

In the log-lattice framework, we now impose that the wave-numbers follow a geometric progression as

$$k = (\lambda_1^m, \dots \lambda_3^m), \tag{2}$$

with $m_i \in \mathbb{Z}^3\}$, where $\lambda$ is a parameter yet to be defined. It is imposed by the condition that the convolution product appearing in Eq. (1) has some non-zero solution, which is only possible if the equation:

$$\lambda^m = \lambda^p + \lambda^q, \tag{3}$$

has some solutions for any $m, p, q \in \mathbb{Z}^3$. As discussed by [6], Eq. (3) can only be achieved provided $\lambda$ takes some specific values, among which $\lambda = 2$, $\lambda \equiv \phi = (1 + \sqrt{5})/2 \approx 1.618$, the golden mean and $\lambda \equiv \sigma =\approx 1.325$ , the plastic number[1]. Different values of $\lambda$ correspond to different number of coupling between modes: they become more and more numerous and less and less local as $\lambda \to 1$ [6]. In this sense, log-lattices can be seen as a special case of the REWA model [7] or fractal decimated models [8,9], in which the non-linear interactions of NSE is projectively decreased randomly or in a scale invariant manner.

### *3.1. Energy spectra*

It is possible to write the mean energy, that measures the scaling properties of the mode at $k = \lambda^n$ as:

$$E_m(n) =< ||u(k^{[M]})||^2 >_{S_n}, \tag{4}$$

where the average is taken over wave numbers in the shell delimited by spheres with radii $\lambda^{n-1}$ and $\lambda^n$. Specifically:

$$< ||u(k^{[M]})||^2 >_{S_n} = \frac{1}{N_k} \sum_{\lambda^{n-1} \le ||k^{[M]}|| < \lambda^n} \sum_{\alpha=1}^{d} |u_\alpha(k^{[M]})|^2, \tag{5}$$

where $d$ is the space dimension and $N_k \sim (\log(k))^{d-1}$ is the number of wave-numbers in the shell $S_n$.

From this quantity, one can define a pseudo-energy spectrum as:

$$E(k) = \frac{\lambda^{-n}}{\lambda - 1} < ||u(k^{[M]})||^2 >_{S_n}, \tag{6}$$

Examples of such spectrum in $d = 3$ are shown in fig. 1 for $\lambda = 2$. One sees that it is self-similar and display a very clear $k^{-5/3}$ law. This spectrum has been obtained by simulating eq. (1) with $20^3$ modes, which can easily be done on a PC. Due to the exponential spacing, it enables to reach resolutions and inertial range even larger than what is achieved by oceanic measurements, a performance which is out-of-reach of DNS simulations of NSE. This shows the interest of FDLL in geophysics.

### *3.2. Generalizations*

The equations (1), (2) and (3) define Navier-Stokes equation on log-lattice. By extension, any equation of fluid dynamics on log-lattice can be defined by performing the two steps [6]: (i) write the equation in the Fourier-space. (ii) replace any convolution product by the convolution on log-lattice. This construction guarantees that the resulting equation obeys all the conservation laws and symmetries of the original equations [6].

[1] $\sigma$ is defined as the common real root to $\sigma^3 - \sigma - 1 = 0$ and $\sigma^5 - \sigma^4 - 1 = 0$

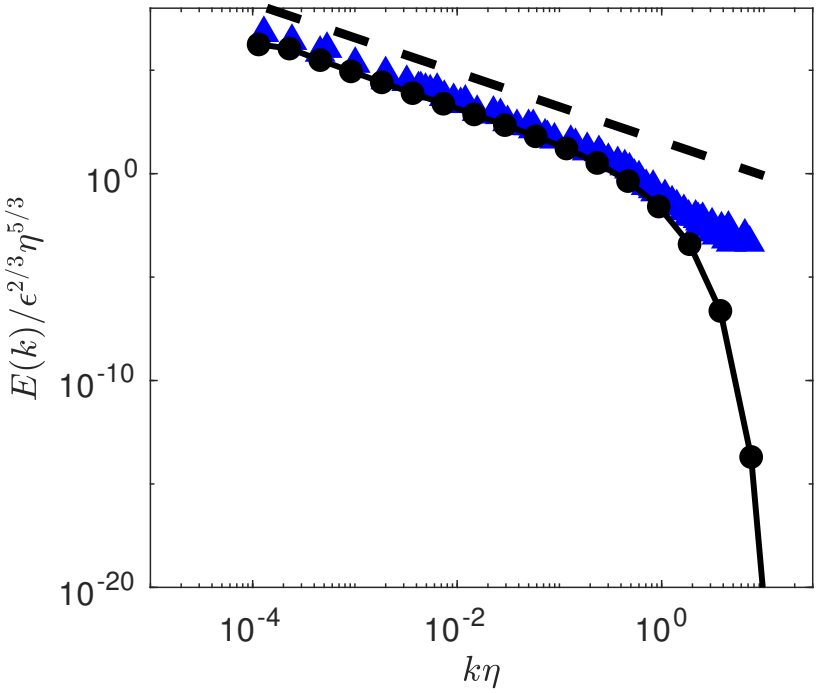


**Figure 1.** Renormalized energy spectrum $E(k)/\epsilon^{2/3}\eta^{5/3}$ as a function of renormalized wavenumber $k\eta$ for a simulation of Navier-Stokes on a $20^3$ log-lattice (black dotted line) and for a turbulent flow in Seymour Narrows (Ocean) [1] (blue squares).

Due to the spectral nature of the construction, it may appear that the log-lattice framework is only appropriate for homogeneous flows, i.e. far from boundaries. In a recent work, [10] have however shown that the extension to flow with boundaries is possible, via lattice symmetrization around the boundary and careful treatment of the resulting discontinuity. Despite the high relevance of this situation for geophysical flow, we here concentrate on the simpler case of homogenous flow.

## 4. Homogeneous rotating convection on log-lattices

### *4.1. Definitions*

We now consider a rotating homogeneous fluid, with coefficient of thermal dilation $\alpha$, viscosity $\nu$ and diffusivity $\kappa$, subject to a temperature gradient $\Delta T$ over a length $H$ and vertical gravity $g$. Its dynamic is given by the HRB set of equations [11–14],

$$\partial_t \boldsymbol{u} + \boldsymbol{u}\cdot\nabla\boldsymbol{u} + \frac{1}{\rho_0}\boldsymbol{\nabla} p + 2\boldsymbol{\Omega}\times\boldsymbol{u} = \nu\nabla^2\boldsymbol{u} + \alpha g\theta\vec{\boldsymbol{z}} - f\boldsymbol{u}, \tag{7}$$

$$\partial_t\theta + \boldsymbol{u}\cdot\boldsymbol{\nabla}\theta = \kappa\nabla^2\theta + u_z\frac{\Delta T}{H} - f\theta, \tag{8}$$

$$\nabla\cdot\boldsymbol{u} = 0, \tag{9}$$

where $\boldsymbol{u}$ is the velocity, $\theta$ the temperature deviation from the equilibrium profile $T = -\Delta T z/H + \theta$, $\boldsymbol{\Omega}$ the rotation vector, $\rho_0$ is the (constant) reference density, $p$ is the pressure and $f$ is a (Rayleigh) friction term, accounting for the friction at the boundary layer that cannot be resolved by the present framework. In the sequel, we will assume that this friction is concentrated only on large scale. As proved in [14], this term is mandatory to allow the system to reach well-defined stationary states. This set of equation has to be completed with boundary conditions. In this paper, we consider periodic boundary conditions and focus on the case when rotation is aligned with the $z$-axis, $\boldsymbol{\Omega} = \Omega e_z$.

### 4.2. Non-dimensional numbers

We can build 5 independent non-dimensional numbers to characterize the system:

the Rayleigh number $\mathrm{Ra} = \alpha g H^3 \Delta T/(\nu\kappa)$, that characterizes the forcing by the temperature gradient.

the Prandtl number $\mathrm{Pr} = \nu/\kappa$, which is the ratio of the fluid viscosity to its thermal diffusivity.

the Nusselt number $\mathrm{Nu} = JH/\kappa\Delta T$. that characterizes the mean total heat flux is the $z$ direction is $J = \partial_z < u_z\theta > -\kappa\Delta T$.

the Ekman number $\mathrm{E} = \nu/(2\Omega H^2)$, measuring the importance of the rotation with respect to diffusive process.

the Rossby number $\mathrm{Ro} = \sqrt{\alpha g \Delta T}/(2\Omega\sqrt{H})$, measuring the importance of the rotation with respect to buoyancy. In terms of other variables, we have $\mathrm{Ro} = \mathrm{E}\sqrt{\mathrm{Ra}}/(\sqrt{Pr})$.

the friction coefficient $F = f\sqrt{H}/\sqrt{\alpha g \Delta T}$, that provides the intensity of the Rayleigh damping.

### 4.3. Equations on log-lattice

The regimes we want to explore are very turbulent regimes where the viscosity and diffusivity do not play any role anymore. Therefore, it is natural to adimensionalize the equation in terms of "inertial quantities", i.e. using the vertical width $H$ as a unit of length, the free fall velocity $U = \sqrt{\alpha g \Delta T H}$ as a unit of velocity, and $\Delta T$ as a unit of temperature.

Then, to define the Rotating Homogeneous Rayleigh-Benard (RHRB) equations on log-lattice, we take the Fourier transform of Eq. (7) that can be written in non-dimensional form as (with the Einstein convention on summed repeated indices):

$$\mathbf{i}k_j u_j = 0, \tag{10}$$

$$\begin{aligned}\partial_t u_i + \mathbf{i}k_j u_i * u_j = & -\mathbf{i}k_i p + \theta\delta_{i3} - F u_i \delta_{k\approx k_{min}} \\ & - \sqrt{\frac{\mathrm{Pr}}{\mathrm{Ra}}} k^2 u_i - \frac{1}{\mathrm{Ro}}\epsilon_{i3k}u_k\end{aligned} \tag{11}$$

$$\partial_t\theta + \mathbf{i}k_j\theta * u_j = u_z - \frac{k^2\theta}{\sqrt{\mathrm{Ra}\,\mathrm{Pr}}} - F\theta\delta_{k\approx k_{min}}, \tag{12}$$

$$u(k,t) = u^*(-k,t), \tag{13}$$

$$\theta(k,t) = \theta^*(-k,t). \tag{14}$$

where the Dirac $\delta_{k\approx k_{\min}}$ filters out the small scales.

In these equations, the convolution product is taken over the log-lattice, see Eq. 3.

### 4.4. Convection onset

Convection is an instability, so it sets-up at a certain critical value of the parameter $\mathrm{Ra}_c$. To estimate the convection threshold, we set $F = 0$ (it only acts at $k = k_{\min}$) and assume that we are very near the threshold, so that deviations from the "equilibrium state" $u = \theta = 0$ are small. This will allow us to neglect all non-linear terms in the equations 14. Then, we look for solutions behaving like:

$$\begin{aligned}\mathbf{u}(k,t) &= (u(k), v(k), w(k))e^{\sigma t}, \\ p(k,t) &= p(k)e^{\sigma t}, \\ \theta(k,t) &= \theta(k)e^{\sigma t},\end{aligned} \tag{15}$$

where $\sigma$ is the growth rate of the instability: if $\sigma$ has a negative real part, then all perturbation decay, while the instability develop when the real part of $\sigma > 0$. Plugging this decomposition into eq. (14) and neglecting non-linear terms, we get:

$$\begin{aligned} ik_x u + ik_y v + ik_z w &= 0, \\ \sigma u - \frac{v}{Ro} &= -ik_x p - \sqrt{\frac{\mathrm{Pr}}{\mathrm{Ra}}} k^2 u, \\ \sigma v + \frac{u}{Ro} &= -ik_y p - \sqrt{\frac{\mathrm{Pr}}{\mathrm{Ra}}} k^2 v, \\ \sigma w &= -ik_z p - \sqrt{\frac{\mathrm{Pr}}{\mathrm{Ra}}} k^2 w + \theta, \\ \sigma \theta &= w - \frac{1}{\sqrt{\mathrm{Ra}\,\mathrm{Pr}}} k^2 \theta. \end{aligned} \tag{16}$$

This represents a linear, homogeneous system of equations in the variable $(u, v, w, p, \theta)$. If we want this system to have other solutions than $(0, 0, 0, 0, 0)$, we must impose the determinant of the system to be zero, which provides us with an expression linking $\sigma$, $k$ and the parameters of the system. Taking $Pr = 1$ for simplicity [2], we get:

$$\sigma^2 + 2k^2\,\mathrm{Ra}^{-1/2}\,\sigma + \frac{k^4}{\mathrm{Ra}} + (1+\mu^2)^{-1}\left(\frac{\mu^2}{\mathrm{Ro}^2} - 1\right) = 0, \tag{17}$$

where $\mu^2 = k_z^2/(k_x^2 + k_y^2)$. This is a second order equation for $\sigma$, there are therefore two solutions. Since the prefactor of $\sigma$ is positive, it means that the sum of the two solution is negative. To ensure that there exist at least one solution with a positive real part, we must then ensure that the product of the solution, given by term independent of $\sigma$ is negative. To study the consequences of this condition, we consider two limiting cases.

#### 4.4.1. Onset at zero rotation

We first consider the case with no rotation, $\mathrm{Ro} \to \infty$. Then, the condition for instability is: $\frac{(1+\mu^2)k^4}{\mathrm{Ra}} - 1 < 0$. Since $(1+\mu^2)k^4$ is minimum when $k = (k_{\min}, k_{\min}, k_{\min})$, where $k_{\min}$ is the minimal wavenumber, this is achieved whenever $Ra > \frac{3}{2}k_{\min}^4$. In our simulations, $k_{\min} \sim 2\pi\sqrt{3}$, this gives $Ra_c \sim 2.1\ 10^4$.

### *4.5. Onset at large rotation*

In the limit of large rotation, $Ro \to 0$ and the condition for instability now reads: $\frac{\mu^2}{\mathrm{Ro}^2} - 1 < 0$. The minimal value of $\mu^2$ is obtained when $k_z$ takes its smallest possible value $k_z = 2\pi$, while $k_x^2 + k_y^2$ takes its largest possible value, i.e. $k_x^2 + k_y^2 \sim \sqrt{\mathrm{Ra}}$ (above that, all is dissipated by viscosity, which means that $k^4/Ra$ becomes non negligible in the equation 17.). Taking into account that $\mathrm{Ro}^2 \sim \mathrm{Ra}\,\mathrm{E}^2/2$ we then get $\mathrm{Ra}^{3/2} > 16\pi^2\,\mathrm{E}^{-2}$, giving a critical Rayleigh number

$$\mathrm{Ra}_c = 12\,\mathrm{E}^{-4/3}. \tag{18}$$

This means that the larger the rotation (the smaller E), the more difficult it is to get convection: rotation stabilizes the flow.

### *4.6. Phenomenology when $F = 0$*

In the case $F = 0$, there are a number of simple physical argument that provide scaling laws relation between the non-dimensional numbers.

[2] The general case leads to the same conclusions

#### 4.6.1. Non-rotating case

We first consider the non-rotating case, $\mathrm{E} = \infty$. In this case, the phenomenology of homogeneous convection distinguishes 3 regimes for the behavior of the heat flux, as a function of the forcing [11,14]:

(I): when $\mathrm{Ra} \leq \mathrm{Ra}_c$, we are in the laminar case. The fluid is at rest, $< u_z\theta >= 0$ and the heat flux is only piloted by the Fourier law, so that $J = \kappa\Delta T/H$ and $Nu = 1$.

(II) : above the critical threshold for instability, when $\mathrm{Ra} >\sim \mathrm{Ra}_c$, convection sets in, $< u_z\theta >$ starts becoming positive, and we have $\mathrm{Nu} \sim (\mathrm{Ra} - \mathrm{Ra}_c)^\chi$, where $\chi$ is an exponent characterizing the (super)-critical transition to convection.

(III) : when $\mathrm{Ra} \gg \mathrm{Ra}_c$, the turbulence become fully developed, and we are entering an "ultimate" regime (also called Spiegel regime), in which the heat flux does not depend anymore on the viscosity or the diffusivity. In that case, we have $\mathrm{Nu} \sim (\mathrm{Ra}\,\mathrm{Pr})^{1/2}$ [15–17]. This regime is very difficult to observe in DNS, because of the need for high resolutions, to be able to cope with $\mathrm{Ra} \gg \mathrm{Ra}_c$. In the atmosphere Ra is typically of the order of $\mathrm{Ra} \sim 10^{18-22}$ so we expect the atmosphere to be in this ultimate regime.

Note that in the case where boundaries are present, there is the possibility of an intermediate regime (the Malkus regime), where the heat flux is piloted by the boundary layers and $\mathrm{Nu} \sim \mathrm{Ra}^\gamma$, $\gamma \sim 1/3$. This regime is frequently observed in laboratory experiments, but it does not apply to homogeneous turbulence, because of the absence of boundaries.

#### 4.6.2. Rotating case

Let us consider the case with rotation. As shown by many studies, the rotation has a stabilizing influence on the flow, so that the threshold for instability now increases with increasing rotation. Detailed studies show that $\mathrm{Ra}_c \sim \mathrm{E}^{-4/3}$ [18]. In addition, the rotation modifies the structure of the convective cells, that become aligned with the vertical axis in the case of strong rotation. This changes profoundly the heat transfer. To account for this effect, [19] suggest performing the same phenomenology as in the non-rotating case, using $\mathrm{Ra}\,E^{4/3}$ instead of Ra. The two turbulent regimes in the presence of rotation are now:

(R1) in the presence of boundaries, a rotating Malkus regime, where the heat flux is independent of the height of the cell, and in which $\mathrm{Nu} \sim \mathrm{Ra}^3\,\mathrm{E}^4$. This regime cannot be present in HRB.

(R2) at Reynolds number larger than the threshold for onset of turbulence in the boundary layers, or when boundaries do not limit the heat flux, like in HRB, a rotating ultimate regime, also called Quasi-Geostrophic (QG) regime. This regime is then found by stating that the relation between Nu and $\mathrm{Ra}\,\mathrm{E}^{4/3}$ and Pr should be such that the energy flux $J$ is independent of $\kappa$ and $\nu$, resulting in [19].

$$\mathrm{Nu} \sim \mathrm{Ra}^{3/2}\,\mathrm{E}^2\,\mathrm{Pr}^{-1/2}\,. \tag{19}$$

An interesting property of the geostrophic turbulent regime is that it can be expressed as a universal law, independent of the rotation and the Prandtl number, using the "turbulent" coordinates [19]:

$$\begin{aligned} \mathrm{Nu}_* &= \frac{\mathrm{Nu}\,\mathrm{E}}{\mathrm{Pr}}, \\ \mathrm{Ra}_* &= \frac{\mathrm{Ra}\,\mathrm{E}^2}{\mathrm{Pr}}. \end{aligned} \tag{20}$$

In that case, the relation (19) becomes:

$$\mathrm{Nu}_* \sim \mathrm{Ra}_*^{3/2}\,. \tag{21}$$

#### 4.6.3. Log-lattice simulation details

To simulate these equations, we can perform log-lattice simulations. The minimum wave vector of the grid is set to $k_{\min} = 2\pi$ to match a simulation on a box of size $\tilde{L} = 1$.

The grid size $N$ is then set to reach the dissipative scale for both velocity and temperature. We have verified that the size of the grid for 3D simulations ($N \geq 13$) does not affect the mean value of the observables Nu, Re, ..., which are already converged for grids of size $N \geq 6$. However, the tail of the pdfs does depend on $N$. Another 3D simulation set at $N = 20$ (not shown here, both vs Ra and Pr) displays the same scaling laws as the $N = 13$ case, confirming this analysis.

## 5. Results

### *5.1. Non-rotating case*

As reference, we have performed simulations without rotation, for various Ra up to $10^{25}$ at Pr $= 1$ and Pr $= 0.7$. Note that present direct numerical simulation for these Prandtl number are limited to Ra $\approx 10^{15}$ [20]. The resulting heat transfer Nu as a function of Rayleigh-number Ra is shown in fig. 2. As predicted by the linear theory, the convection starts as $\mathrm{Ra}_c = 10^4$, with a near onset regime $\mathrm{Nu} \sim (\mathrm{Ra} - \mathrm{Ra}_c)^{3/2}$, then turning into an asymptotic regime where $\mathrm{Nu} \sim \sqrt{(}\,\mathrm{Ra})$. This regime itself splits in two distinct regimes, characterized by the same scaling law $\mathrm{Nu} \sim \mathrm{Ra}^{1/2}$, but with very different amplitude: (i) a *laminar regime*, characterized by low fluctuations of the heat transfer. This laminar regime is well-fitted by an empirical law

$$\mathrm{Nu} = A(\mathrm{Ra} - \mathrm{Ra}_c)^{3/2}/(\mathrm{Ra} \,/\, \mathrm{Ra}_t + 1), \tag{22}$$

where $A = 7$, $\mathrm{Ra}_c = 10^4$ is the critical number for convection onset and $\mathrm{Ra}_t = 5 \times 10^6$ is the transition number from near-onset to asymptotic regime. This laminar regime is followed by (ii) a *turbulent regime*, with much larger fluctuations. Typical time behavior of the heat transfer in the two regimes is displayed in fig. 3 which showcases both regimes. The laminar regime is stable up to Ra $\approx 10^{12}$, and unstable above: if we wait long enough, the solution jumps from the laminar regime to the turbulent regime, as illustrated in fig. 3. Looking at Nu as a function of time in this regime in fig. 3, we observe that the simulation first follows a rather long evolution along the laminar regime, before suddenly transitioning towards the turbulent regime as an instability develops, increasing its energy by several orders of magnitude in the process.

### *5.2. Rotating case*

#### 5.2.1. Parameter space and critical Rayleigh number

We turn now to the case with rotation. Figure 4 shows the parameter space we have explored, with E ranging from $10^{-9}$ to $10^{-1}$ and Ra up to $10^{14}$. In this range of parameters, we observe typically three types of behaviors: (i) conductive behaviors, where both velocity and temperature fluctuations are zero, and Nu $= 1$. These cases are reported as white symbols on fig. 4; (ii) transitional regimes, where velocity and temperature fluctuations are decaying very slowly but steadily, along with Nu over the time of simulation, so that asymptotically, they are likely to converge to the conductive limit. The typical timescale to reach this limit increases as $E$ decays, and $Ra$ increases. To save computational time, we have stopped the simulation before reaching the limit for E $\geq 10^{-6}$, but have reported this points as yellow points on fig. 4; (iii) convective regimes, where both velocity and RMS velocities reach a stationary state; these points are reported as black points in fig. 4. This representation allows seeing clearly the stabilizing influence of rotation on the convection threshold. In the asymptotic regime of large rotation, E $\ll 1$, such influence is very-well described by the prediction of the linear theory Eq. 18, which is reported as a red line on the diagram.

#### 5.2.2. Laminar vs turbulent regime

Figure 5 reports the heat transport Nu as a function of Rayleigh Ra and Ekman number E. One sees that larger Ekman numbers correspond to smaller heat transport, at a given Ra. However, the rotation does not suppress the existence of the laminar to turbulent transition,

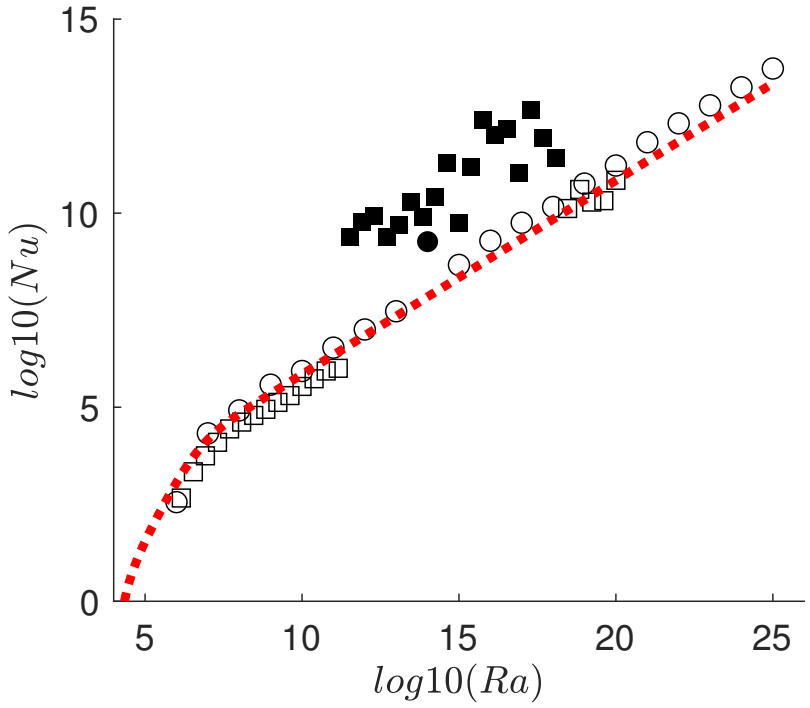


**Figure 2.** Non-dimensional heat transfer Nu vs Rayleigh number Ra in 3D for Pr $=$ 0.7 (circle) and Pr $=$ 1 (squares). The dotted line corresponds to the empirical law: Nu $=$ $7(\mathrm{Ra}-\mathrm{Ra}_c)^{3/2}/(\mathrm{Ra}\,/\,\mathrm{Ra}_t+1)$, with $\mathrm{Ra}_c = 10^4$ and $\mathrm{Ra}_t = 5\times10^6$ that connects the near-convection onset regime to the asymptotic law Nu $\sim 20\sqrt{\mathrm{Ra}}$ for large Ra, corresponding to asymptotic non-rotating ultimate regime scaling. This regime is itself split into a laminar regime (open symbols) and a turbulent regime (filled symbols).

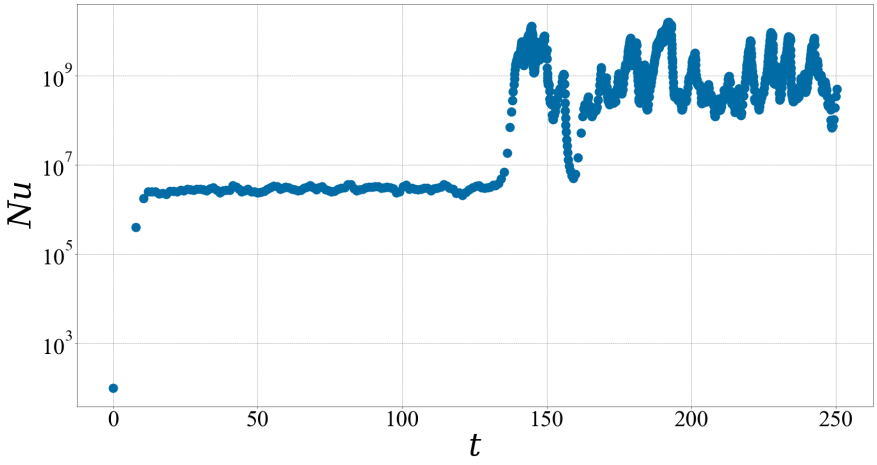


**Figure 3.** Non-dimensional heat transfer Nu versus time $t$ for $\mathrm{Ra} = 3.46\cdot10^{11}$. The flow starts in a laminar regime, then abruptly transitions to a turbulent regime.

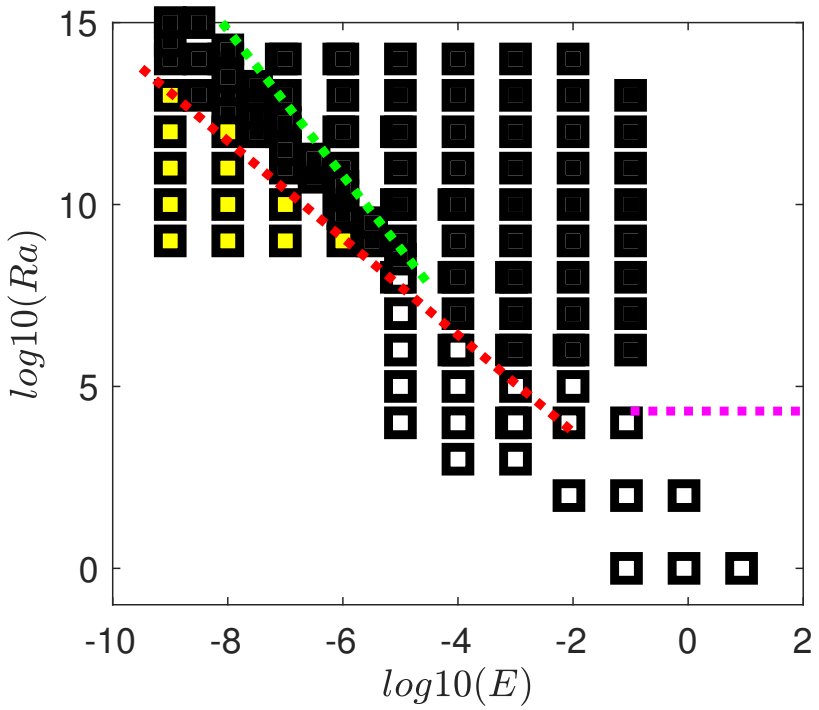


**Figure 4.** Parameter space covered by our log-lattices simulations at Pr $= 0.7$. The color of the symbols codes the 3 possible regimes: conductive (white), transitional (yellow) and convective (black). The red line is the theoretical asymptotic prediction given by Eq. (18). The magenta line is the theoretical convection threshold in the absence of rotation $Ra = 2.1 \times 10^4$. The green line has equation $Ra = 0.03E^{-2}$ and delineates regions of the parameter space where turbulent is influenced by rotation (below the line) or not influenced by rotation (above the line), as diagnosed by the behavior of the kinetic energy dissipation, see fig. 7. The quasi-geostrophic regime is observed in between the red and the green-line.

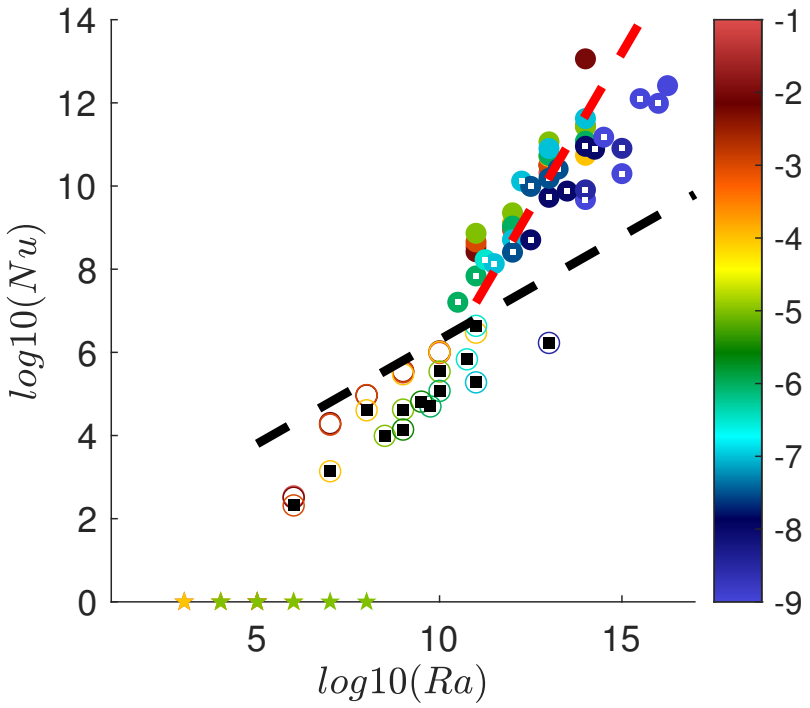


**Figure 5.** Non-dimensional heat transfer Nu vs Rayleigh number Ra in 3D for Pr $= 0.7$ for simulations of rotating HRB simulations on log-lattice. The symbols are colored according to their Ekman number E. The stars traces the conductive regime. The open symbols trace the laminar regime, while the filled symbol trace the turbulent regime. The rotation dominated regimes are tagged by a black (resp. white) square for the laminar (resp. turbulent) regime. The black dashed line is Nu $= 20\sqrt{\text{Ra}}$, corresponding to asymptotic non-rotating ultimate regime scaling. The red dotted line is Nu $\sim \text{Ra}^{3/2}$ corresponding to the QG regime, see fig. 12 for an exact representation of the corresponding scaling law.

already present in the non-rotating case. Like in the non-rotating case, it is happening when the vertical Reynolds number exceeds $u_z^{rms} L/\nu = \text{Re}_c = 10^4$, corresponding to Ra $\sim 10^{12}$, with a bi-stability occurring around Ra $= 10^{11}$, see fig. 6.

#### 5.2.3. Influence of rotation and onset of rotation dominated regimes

The influence of rotation onto the turbulence is well documented (see e.g. [21,22]), and is characterized by a *decrease* of the efficiency of the transport properties with respect to the non-rotating case. For the case of the heat transport, this is already clear from fig. 2, as already discussed. In the case of the turbulent kinetic energy dissipation $\nu < (\nabla u)^2 >$, it is known that the decrease is proportional to the vertical Rossby number, $\text{Ro}_z = u_z/2H\Omega$ [22]. We indeed observe this effect in our simulations, as illustrated in fig. 7, where the non-dimensional turbulent kinetic energy dissipation $\epsilon_u = \nu < (\nabla u)^2 > H/U^3$ is shown, as a function of the vertical Rossby number. We see that in both the laminar and turbulent regime, the energy dissipation indeed decreases for sufficiently low-vertical Rossby number. In the turbulent regime, the decrease is indeed proportional to $\text{Ro}_z$, indicated by the black dotted line. In the laminar regime, however, the decrease is milder, going like $\text{Ro}_z^{1/2}$. In the turbulent case, the rotation dominated regime starts below $\text{Ro}_z \sim 0.1$, while in the laminar case, it starts at $\text{Ro}_z \sim 0.03$. We can use this change of regime to tag the simulations that are or are not influenced by the rotation. In the sequel, we denote them by a white dot inside the filled symbol, for the turbulent regime, and a black dot inside an open symbol, for the laminar regime. Reporting this on figs. 5 and 6, we see that this regime corresponds to lower heat transport, and smaller Reynolds number, in agreement with the general

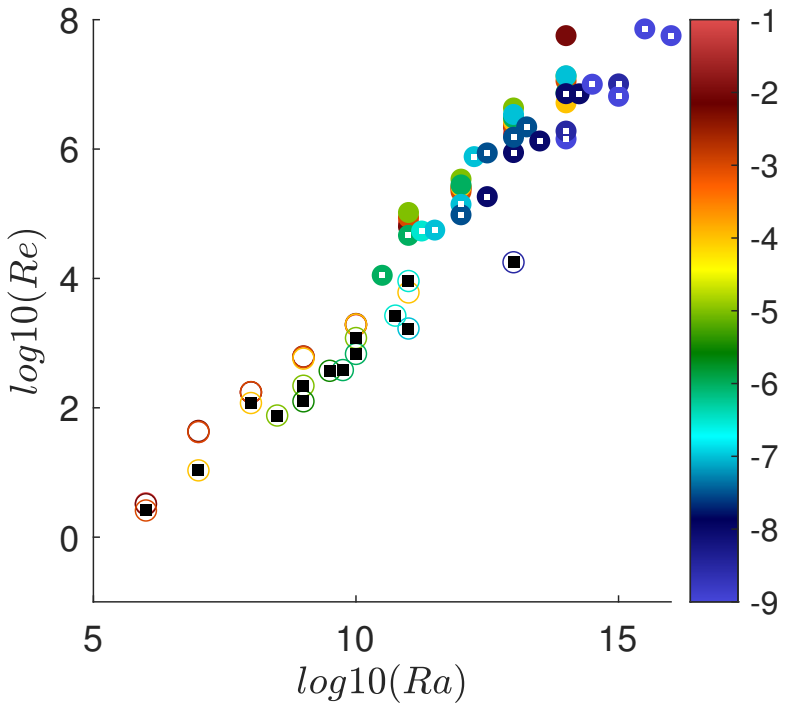


**Figure 6.** Vertical Reynolds number $\mathrm{Re} = \sqrt{< u_z^2 >} H/\nu$ as a function of Rayleigh number Ra in 3D for $\mathrm{Pr} = 0.7$ for simulations of rotating HRB simulations on log-lattice. The symbols are colored according to their Ekman number E. The open symbols trace the laminar regime, while the filled symbol trace the turbulent regime. The rotation dominated regimes are tagged by a black (resp. white) square for the laminar (resp. turbulent) regime.

findings that rotation impedes heat transport and vertical velocities. Note that the vertical Rossby number scales like the global Rossby number, following $\mathrm{Ro}_z \sim (\mathrm{Ra}\,\mathrm{E})^{1/2}$ in both the laminar and the turbulent regime, see fig. 8.

#### 5.2.4. Temperature fluctuation and anisotropy

Another interesting indicator of the influence of rotation on convection is given by the behavior of the temperature fluctuations, displayed in fig. 9. In the laminar case, they are plateauing at a low value (less than 0.01) as Ra increases, showing that the dynamic is indeed laminar. The rotation tends to even decrease the size of the fluctuations. In the laminar case, the temperature fluctuations are increasing with Ra, showing that convection is more and more vigorous, even so large rotation tends to somehow impede the development of too large fluctuations. The rotation also influences the anisotropy of the turbulence, as seen in fig. 10. Both in the laminar and turbulent case, the anisotropy is well above the value 1/2, that would correspond to a situation where kinetic energy is split evenly between motions along and perpendicular to the rotation axis. Due to the special nature of our projection, we cannot get a meaningful representation of what this result means in the physical space. It might however be interpreted as the influence of strong up (resp. down)-drafts that are observed in direct numerical simulations to carry the heat from bottom to top (resp. the cold fluid from top to bottom). The values we obtain here for the anisotropy are much larger to what is usually observed in simulation or experiment of RB convection with boundaries, but they are compatible with observation of radiative convection [23] or convection with no-slip boundary conditions [19], that observe the formation of very extended plumes extending towards the whole bulk of the flow. The decrease of anisotropy observed at decreasing E can be connected with the stabilizing influence of rotation, that impedes vertical fluctuations [21].

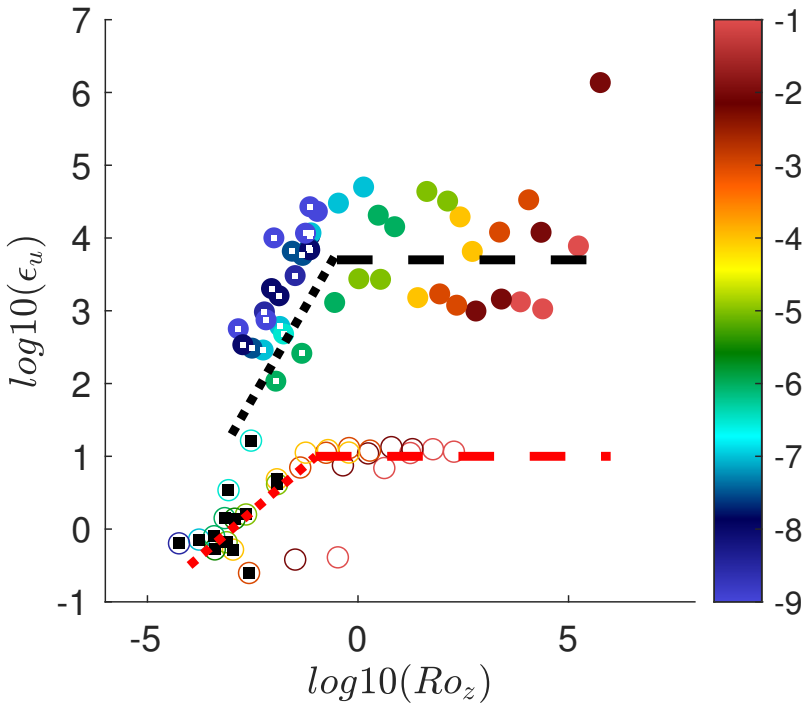


**Figure 7.** Non-dimensional energy dissipation $\epsilon_u = \nu < (\nabla u)^2 > H/U^3 = \mathrm{Ra}\,\mathrm{Nu}\,\mathrm{Pr}^{-2}/(\mathrm{Ra}\,\mathrm{Pr})^{3/2}$ vs vertical Rossby number $\mathrm{Ro}_z$ in 3D for $\mathrm{Pr} = 0.7$ for simulations of rotating HRB simulations on log-lattice. The symbols are colored according to their Ekman number E. The open symbols trace the laminar regime, while the filled symbol trace the turbulent regime. The rotation dominated regimes are tagged by a black (resp. white) square for the laminar (resp. turbulent) regime. . The black (resp. red) dotted line corresponds to $\epsilon_u \sim \mathrm{Ro}_z$ (resp. $\epsilon_u \sim \mathrm{Ro}_z^{1/2}$), while the black (resp. red) dashed line correspond to $\epsilon_u = 3.7$ (resp. $\epsilon_u = 1$).

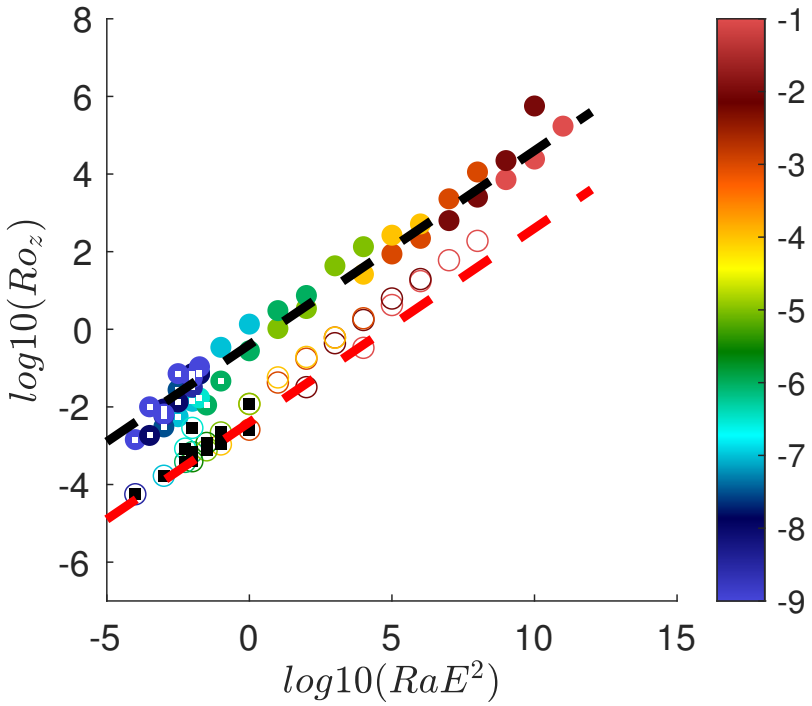


**Figure 8.** Vertical Rossby number $\mathrm{Ro}_z$ vs "turbulent" Rayleigh number $\mathrm{Ra}\,E^2$ in 3D for $\mathrm{Pr} = 0.7$ for simulations of rotating HRB simulations on log-lattice. The symbols are colored according to their Ekman number E. The open symbols trace the laminar regime, while the filled symbol trace the turbulent regime. The rotation dominated regimes are tagged by a black (resp. white) square for the laminar (resp. turbulent) regime. The black (resp. red) dashed line follows $0.4\,\mathrm{Ra}^{1/2}\,E$ (resp. $0.04\,\mathrm{Ra}^{1/2}\,E$).

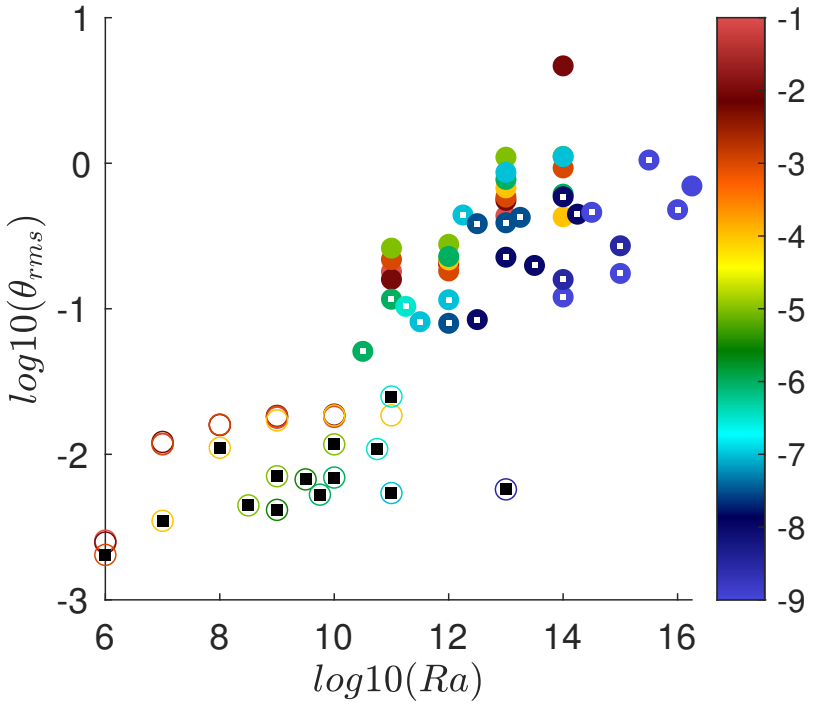


**Figure 9.** Temperature fluctuations $\theta_{rms} = \sqrt{< \theta^2 >}$ vs Rayleigh number Ra in 3D for Pr $= 0.7$ for simulations of rotating HRB simulations on log-lattice. The symbols are colored according to their Ekman number E. The open symbols trace the laminar regime, while the filled symbol trace the turbulent regime. The rotation dominated regimes are tagged by a black (resp. white) square for the laminar (resp. turbulent) regime.

#### 5.2.5. Laminar and turbulent scaling laws and QG regimes

The laminar regime starts from the convection onset. It is therefore likely that it is influenced by near onset dynamics. A natural idea is then to try to see whether it also follows the near-onset scaling law of the non-rotating case, Eq. (22), albeit with $\mathrm{Ra}_c$ being replaced by its rotating value $30\,\mathrm{E}^{-4/3}$ and $\mathrm{Ra}_t$ being replaced by $B\,\mathrm{E}^{-4/3}$, where the constant $B$ needs to be determined. With this hypothesis, we then find that in the laminar regime, Nu $E^{2/3}$ should be a function of $\mathrm{Ra}\,\mathrm{E}^{4/3}$, where the function satisfies Eq. (22), with $A = 7$, $\mathrm{Ra}_c = 30$ and $\mathrm{Ra}_t = 5 \times 10^2$, see fig. 11. The turbulent regime corresponds to large Reynolds number, in which viscosity and diffusivity should not play a role anymore. It is then natural to represent it in the turbulent variable Nu E and $\mathrm{Ra}\,\mathrm{E}^2$, which is done in fig. 12. This representation indeed collapses the data on two different scaling laws: one with exponent $3/2$ for regimes influenced by rotation -this is the QG regime- and one with exponent $1/2$ corresponding to the turbulent regime not influenced by rotation. The precise location in parameter space where the QG regime occurs can be computed using the fit of the vertical Rossby number as a function of Ra E, see fig. 8. The condition $\mathrm{Ro}_z < 0.1$ then translates into the condition $\mathrm{Ra} \leq 1/(16E^2)$, which is the green line reported on fig. 4. The QG regime is then to be found in-between the blue and the green line, which is the region where we concentrate additional numerical simulations.

## 6. Discussion

We have shown that projection of geophysical equations of motion allow achieving realistic values of parameters, at a moderate cost. This allows to perform many simulations over a wide range of parameters, thereby leading to general scaling laws of transport efficiency that can then be used to parametrize the turbulent transport in general climate models for Earth or other planets. We have illustrated this process using the equation

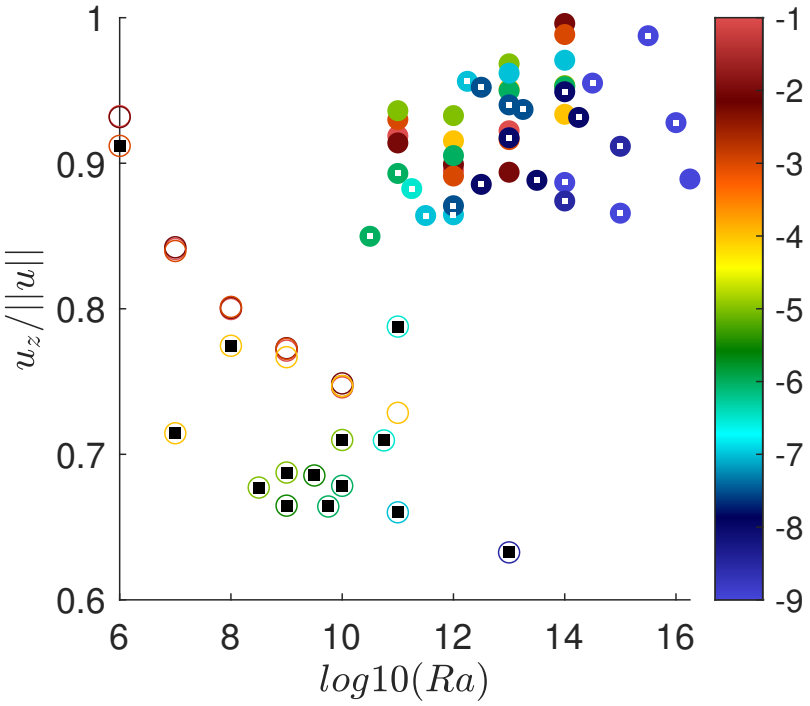


**Figure 10.** Velocity anisotropy $\sqrt{< u_z^2 >}/\sqrt{< u^2 >}$ vs Rayleigh number Ra in 3D for Pr $= 0.7$ for simulations of rotating HRB simulations on log-lattice. The symbols are colored according to their Ekman number E. The open symbols trace the laminar regime, while the filled symbol trace the turbulent regime. The rotation dominated regimes are tagged by a black (resp. white) square for the laminar (resp. turbulent) regime.

describing the heat transport in a dry atmosphere, to obtain the scaling laws for onset of convection as a function of rotation, and confirmed the theoretical results $\mathrm{Ra}_c \sim E^{-4/3}$ over a wide range of parameters. We have also demonstrated the existence of two regimes of convection, one laminar extending near the convection onset, and one turbulent, occurring as soon as the vertical Reynolds number reaches a value of $10^4$. We have derived general scaling laws for these two regimes, both for transport of heat, dissipation of kinetic energy, and value of the anisotropy and temperature fluctuations. The set-up we have used here is far from reproducing the full complexity of the atmosphere, as it models the friction at the bottom with a simple law, and ignores the moist dynamics. We plan to include these features in a future work. Finally, it is not clear how the projection of the dynamics on log-lattice influences the results we are deriving. It is quite remarkable that the procedure is able to capture the scaling laws, since we recover here some results already obtained in experiments [23] numerical simulations [19] of convection without boundary layers, albeit with different prefactors. This of course has some important implications when translating these scaling laws as parametrization in models. However, if we believe that the scaling laws themselves are robust, it only takes comparison with a few direct numerical simulation to recalibrate the constants and turn our laws into useful parametrization.

**Author Contributions:** Conceptualization, all authors; methodology, all authors; software, A.B. , G.C; and Q.P.; validation, all authors; formal analysis, B.D.; investigation, Q.P.; resources, A.B.; data curation, all authors; writing—original draft preparation, B.D.; writing—review and editing, all authors.; visualization, B.D.; supervision, B.D.; project administration, B.D..; funding acquisition, B.D. All authors have read and agreed to the published version of the manuscript.

**Funding:** This work received funding through the PhD fellowship programs of the Ecole Polytechnique and Ecole Normale Superieure Paris-Saclay, and through the ANR, via the grants ANR TILT grant agreement no. ANR-20-CE30-0035 and ANR BANG grant agreement no. ANR-22-CE30-0025.

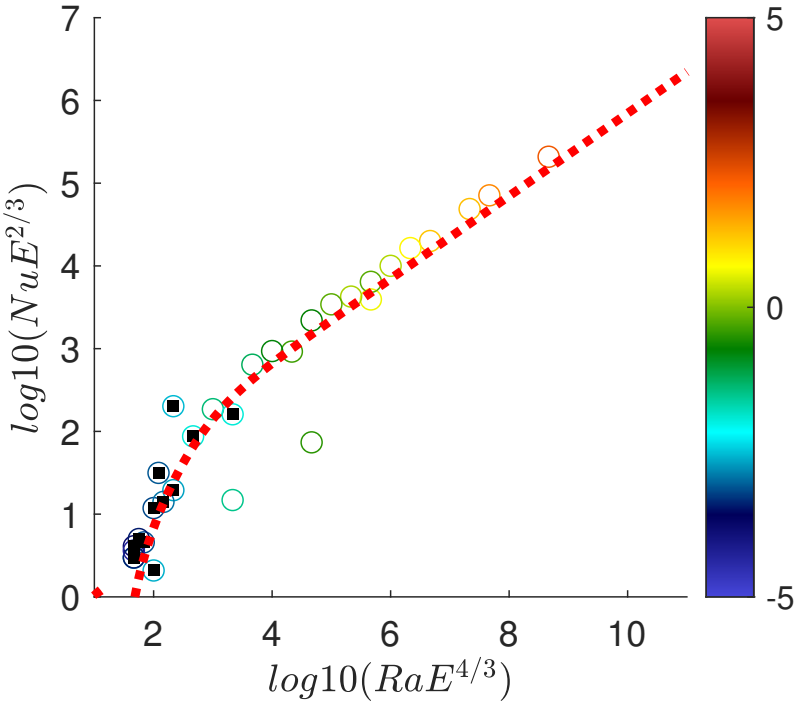


**Figure 11.** Universal law governing the heat transfer in the laminar regime $\mathrm{Nu}\,\mathrm{E}^{2/3}$ as a function of $\mathrm{Ra}\,\mathrm{E}^{4/3}$ in 3D for $\mathrm{Pr} = 0.7$ for simulations of rotating HRB simulations on log-lattice. The symbols are colored according to their Ekman number E. The open symbols tagged by a black square trace the rotation dominated regime, while the open symbols trace the rotation independent regime. The red dotted line follows Eq. 22, whith $A = 7$, $\mathrm{Ra}_c = 30$ and $\mathrm{Ra}_t = 5 \times 10^2$.

**Data Availability Statement:** Data are available upon request to the author.

**Acknowledgments:** In this section you can acknowledge any support given which is not covered by the author contribution or funding sections. This may include administrative and technical support, or donations in kind (e.g., materials used for experiments).

**Conflicts of Interest:** Declare conflicts of interest or state "The authors declare no conflict of interest." Authors must identify and declare any personal circumstances or interest that may be perceived as inappropriately influencing the representation or interpretation of reported research results. Any role of the funders in the design of the study; in the collection, analyses or interpretation of data; in the writing of the manuscript; or in the decision to publish the results must be declared in this section. If there is no role, please state "The funders had no role in the design of the study; in the collection, analyses, or interpretation of data; in the writing of the manuscript; or in the decision to publish the results".

## References

1. Grant, H.L.; Stewart, R.W.; Moilliet, A. Turbulence spectra from a tidal channel. *Journal of Fluid Mechanics* **1962**, *12*, 241–268. https://doi.org/10.1017/S002211206200018X.
2. Frisch, U. . In *Turbulence, the legacy of A. N. Kolmogorov*; Cambridge University Press, 1996.
3. Dubrulle, B. Beyond Kolmogorov cascades. *Journal of Fluid Mechanics* **2019**, *867*, P1. https://doi.org/10.1017/jfm.2019.98.
4. Herring, J.R. Some Contributions of Two-Point Closure to Turbulence. In Proceedings of the Frontiers in Fluid Mechanics; Davis, S.H.; Lumley, J.L., Eds., Berlin, Heidelberg, 1985; pp. 68–87.
5. Dubrulle, B.; Daviaud, F.; Faranda, D.; Marié, L.; Saint-Michel, B. How many modes are needed to predict climate bifurcations? Lessons from an experiment. *Nonlinear Processes in Geophysics* **2022**, *29*, 17–35. https://doi.org/10.5194/npg-29-17-2022.
6. Campolina, C.S.; Mailybaev, A.A. Fluid dynamics on logarithmic lattices. *Nonlinearity* **2021**, *34*, 4684–4715. https://doi.org/10.1088/1361-6544/abef73.
7. Grossmann, S.; Lohse, D.; L'vov, V.; Procaccia, I. Finite size corrections to scaling in high Reynolds number turbulence. *Phys. Rev. Lett.* **1994**, *73*, 432–435. https://doi.org/10.1103/PhysRevLett.73.432.

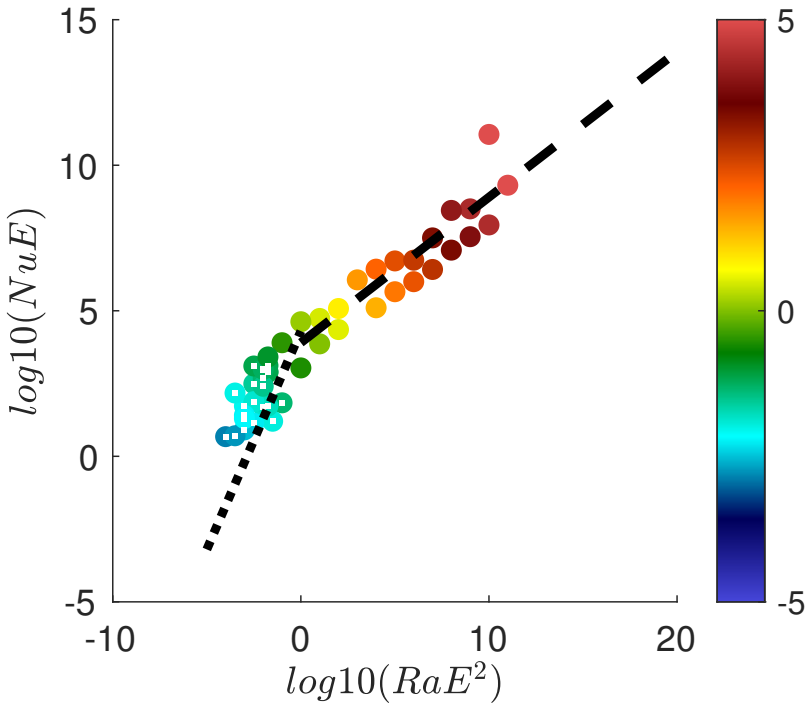


**Figure 12.** Universal law governing the heat transfer in the turbulent regime Nu E as a function of Ra $E^2$ in 3D for Pr = 0.7 for simulations of rotating HRB simulations on log-lattice. The symbols are colored according to their Ekman number E. The symbols tagged by a white square trace the rotation dominated regime, while the filled symbols trace the rotation independent regime. The black dotted (resp. dashed) line follows the equation $y \sim x^{3/2}$ (resp. $y \sim x^{1/2}$).


8. Frisch, U.; Pomyalov, A.; Procaccia, I.; Ray, S.S. Turbulence in Noninteger Dimensions by Fractal Fourier Decimation. *Phys. Rev. Lett.* **2012**, *108*, 074501. https://doi.org/10.1103/PhysRevLett.108.074501.
9. Lanotte, A.S.; Benzi, R.; Malapaka, S.K.; Toschi, F.; Biferale, L. Turbulence on a Fractal Fourier Set. *Phys. Rev. Lett.* **2015**, *115*, 264502. https://doi.org/10.1103/PhysRevLett.115.264502.
10. Campolina, C.S. Fluid dynamics on logarithmic lattices. PhD thesis, IMPA, 2022.
11. Calzavarini, E.; Lohse, D.; Toschi, F.; Tripiccione, R. Rayleigh and Prandtl number scaling in the bulk of Rayleigh-Bénard turbulence. *Physics of Fluids* **2005**, *17*, 055107, [https://doi.org/10.1063/1.1884165]. https://doi.org/10.1063/1.1884165.
12. Calzavarini, E.; Doering, C.R.; Gibbon, J.D.; Lohse, D.; Tanabe, A.; Toschi, F. Exponentially growing solutions in homogeneous Rayleigh-Bénard convection. *Phys. Rev. E* **2006**, *73*, 035301. https://doi.org/10.1103/PhysRevE.73.035301.
13. Calzavarini, E.; Lohse, D.; Toschi, F. Homogeneous Rayleigh-Bénard Convection. In Proceedings of the Progress in Turbulence II; Oberlack, M.; Khujadze, G.; Günther, S.; Weller, T.; Frewer, M.; Peinke, J.; Barth, S., Eds., Berlin, Heidelberg, 2007; pp. 181–184.
14. Barral, A.; Dubrulle, B. Asymptotic ultimate regime of homogeneous Rayleigh-Bénard convection on logarithmic lattices. *Journal of Fluid Mechanics* **2023**, *962*, A2. https://doi.org/10.1017/jfm.2023.204.
15. Spiegel, E.A. A Generalization of the Mixing-Length Theory of Turbulent Convection. *The Astrophysical Journal* **1963**, *138*, 216.
16. Kraichnan, R.H. Turbulent Thermal Convection at Arbitrary Prandtl Number. *The Physics of Fluids* **1962**, *5*, 1374–1389, [https://aip.scitation.org/doi/pdf/10.1063/1.1706533]. https://doi.org/10.1063/1.1706533.
17. Grossmann, S.; Lohse, D. Scaling in thermal convection: a unifying theory. *Journal of Fluid Mechanics* **2000**, *407*, 27–56. https://doi.org/10.1017/S0022112099007545.
18. Cheng, J.S.; Stellmach, S.; Ribeiro, A.; Grannan, A.; King, E.M.; Aurnou, J.M. Laboratory-numerical models of rapidly rotating convection in planetary cores. *Geophysical Journal International* **2015**, *201*, 1–17, [https://academic.oup.com/gji/article-pdf/201/1/1/2149282/ggu480.pdf]. https://doi.org/10.1093/gji/ggu480.
19. Plumley, M.; Julien, K. Scaling Laws in Rayleigh-Bénard Convection. *Earth and Space Science* **2019**, *6*, 1580–1592, [https://agupubs.onlinelibrary.wiley.com/doi/pdf/10.1029/2019EA000583]. https://doi.org/https://doi.org/10.1029/2019EA000583.
20. Iyer, K.P.; Scheel, J.D.; Schumacher, J.; Sreenivasan, K.R. Classical 1/3 scaling of convection holds up to Ra = 10<sup>15</sup>. *Proceedings of the National Academy of Sciences* **2020**, *117*, 7594–7598, [https://www.pnas.org/doi/pdf/10.1073/pnas.1922794117]. https://doi.org/10.1073/pnas.1922794117.
21. Dubrulle, B.; Valdettaro, L. Consequences of rotation in energetics of accretion disks. *Astronomy and Astrophysics* **1992**, *263*, 387–400.

22. Campagne, A.; Machicoane, N.; Gallet, B.; Cortet, P.P.; Moisy, F. Turbulent drag in a rotating frame. *Journal of Fluid Mechanics* **2016**, *794*, R5. https://doi.org/10.1017/jfm.2016.214.
23. Bouillaut, V.; Miquel, B.; Julien, K.; Aumaître, S.; Gallet, B. Experimental observation of the geostrophic turbulence regime of rapidly rotating convection. *Proceedings of the National Academy of Sciences* **2021**, *118*, e2105015118, [https://www.pnas.org/doi/pdf/10.1073/pnas.2105015118]. https://doi.org/10.1073/pnas.2105015118.

## 5.2 Tracking complex singularities of fluids on log-lattices

# Tracking complex singularities of fluids on log-lattices

**Quentin Pikeroen, Amaury Barral, Guillaume Costa, Ciro Campolina, Alexei Mailybaev & Berengere Dubrulle**

SPEC/IRAMIS/DSM, CEA, CNRS, University Paris-Saclay, CEA Saclay, 91191 Gif-sur-Yvette, France

E-mail: `berengere.dubrulle@cea.fr`

**Abstract.** In 1981, Frisch and Morf [1] postulated the existence of complex singularities in solutions of Navier-Stokes equations. Present progress on this conjecture is hindered by the computational burden involved in simulations of the Euler equation or the Navier-Stokes equations at high Reynolds numbers. We investigate this conjecture in the case of fluid dynamics on log-lattices, where the computational burden is logarithmic concerning ordinary fluid simulations. We analyze properties of potential complex singularities in both 1D and 3D for lattices of different spacings. Dominant complex singularities are tracked using the singularity strip method to obtain new scalings regarding the approach to the real axis and the influence of normal, hypo and hyper dissipation.

## 1. Introduction

Viscous fluids dissipate mechanical energy into heat due to the first law of thermodynamics. Observations and numerical simulations reveal that this dissipation is not homogeneous within the flow but occurs via spatially or temporally intermittent bursts, a phenomenon classically referred to as intermittency. Moreover, after spatial and temporal averaging, the mean energy dissipation becomes independent of the viscosity in the inviscid limit, according to the empirical "zeroth law of turbulence". Onsager explained these observations in 1949 [2], conjecturing that strong enough singularities in the fluid could provide a non-viscous dissipation. While this conjecture has been proven mathematically [3], its application to fluids obeying the Navier-Stokes equation is still debated, as the existence and development of singularities for these equations is still an unsolved problem belonging to the 6th Millennium problems of the Clay foundation. This debate concerns the existence of singularities in real space. In 1981, Frisch and Morf [1] paved the way to another possibility based on the existence of complex singularities. They proved on a simple one-dimensional non-linear Langevin system that the dynamics of such complex singularities could be directly connected to intermittency, as dissipation bursts occur whenever a complex singularity approaches the real axis.

Since then, this scenario was also confirmed in the 1-dimensional Burgers equation – a 1D surrogate of the Navier-Stokes equation. In this system, real singularities can be observed in the inviscid limit and manifest as shocks, i.e. finite jump in the velocity. The shocks dissipate energy in agreement with the Onsager conjecture [4]. They correspond to the collapse of two complex conjugate singularities onto the real axis [5, 6]. When a viscosity $\nu$ is added, the singularities are repelled from the real axis, the closest one being constantly at a distance greater than $O(\nu^{3/4})$ to the real axis. The complex singularities follow Calogero-Moser (CM) dynamics [7], with long-range interactions (decaying in $1/r$). There is an exact mapping between such CM dynamics and the solution of the PDE, which can be described exactly via pole decomposition coupled to the integration of the CM equations [6].

The generalization of these findings to 3D is challenging. The computational burden to resolve the Navier-Stokes equation for a fluid with typical velocity $U$ and length $L$ scales like $\mathrm{Re}^3$, where $\mathrm{Re} \sim UL/\nu$ is the Reynolds number. Most of the earlier attempts to track complex singularities in the inviscid limit were performed using the "singularity strip" method, which is based on the observation that the behaviour of the energy spectrum at large wavenumber $k$ is dominated by the position of the singularity closest to the real axis, and decays like $\exp(-2\delta k)$, where $\delta$ is the imaginary part of corresponding singularity. Fitting the large wavenumber tail of the energy spectrum as a function of time, one then gets an estimate of $\delta(t)$, and a real singularity occurs when $\delta(t) = 0$. So far, studies have only identified exponentially decaying regimes for $\delta(t)$ [8] which suggests the absence of finite time blow-up. However, we cannot guarantee that this extrapolation is correct due to numerical limitations.

New perspectives on these issues were opened recently by Campolina and Mailybaev [9], exploring fluid dynamics on log-lattices. This technique may be viewed as a generalization of the so-called "shell models" [10, 11] and solves the equations of motion in Fourier space using a sparse basis of Fourier modes. The modes are evenly spaced points in log space ("logarithmic lattices"). They interact via nonlinear equations derived from the fluid equations by substituting for the convolution product a new operator, which can be seen as a convolution on the log-lattice, while preserving most symmetries of the original equation. The model is valid for all dimensions. In 1D, it was shown to encompass [9] the Sabra shell model of turbulence [10, 11]. In 3D, its solutions have the same behaviour as the Navier-Stokes equation in Fourier space (energy spectrum, energy transfers), over an unprecedented wide range of scales [9]. In the inviscid limit, a self-similar finite time blow-up is observed [12] in connection with a stochastic attractor that propagates at a finite velocity in Fourier space like a wave. However, Campolina and Mailybaev did not attempt to track possible complex singularities in connection with such a blow-up.

This is the purpose of the present paper. In the first part, we validate the close connection between fluid dynamics on log-lattice and real fluid dynamics by focusing on the 1D Burgers equation, where dominant complex singularities are tracked using the singularity strip method. In the second part, we extend this technique to 3D to obtain new scalings regarding the approach to the real axis and the influence of normal, hypo and hyper dissipation.

## 2. Log-lattice framework

### *2.1. Definitions and notations*

We consider a $d$-dimensional complex vector fields $u(t,k) = (u_1, \dots, u_d)$ depending on time $t \in \mathbb{R}$ and on the wave vector $k = (k_1, \dots, k_d)$. We shall interpret $u$ as the Fourier components of the velocity field. For this reason, we require them to satisfy the Hermitian symmetry $u(t,-k) = \overline{u(t,k)}$ with respect to $k$, which is the Fourier property of a real-valued function in physical space. The wave vector $k$ is embedded on a *logarithmic lattice* (in short, *log-lattice*), which means that its components follow geometric progressions $k = k_0(\pm\lambda^{m_1}, \dots, \pm\lambda^{m_d})$ for integers $m_1, \dots, m_d$, where $k_0$ is a fixed‡ positive reference scale, and $\lambda$ is the spacing factor of the lattice. The dependence of $u$ on $t$ and $k$ is henceforth implicit and specified only when ambiguity prevails.

*Fluid dynamics on log-lattice* [9] is the set of vector fields $u$ which are solutions of

‡ By default $k_0 = 2\pi$

the equations

$$ik_\beta u_\beta = 0, \tag{1a}$$

$$\partial_t u_\alpha + ik_\beta (u_\alpha * u_\beta) = -ik_\alpha p - \nu k^{2\gamma} u_\alpha + f_\alpha, \tag{1b}$$

$$(u_\alpha * u_\beta)(k) = \sum_{q+r=k} u_\alpha(q) u_\beta(r), \tag{1c}$$

where $p$ is a complex field that enforces incompressibility (1a), $f$ is a vectorial forcing, and $\nu$ is a non-negative viscosity parameter. When $\nu > 0$, the exponent $\gamma$ measures the dissipation degree: we say the flow has *viscous* (or *usual*) *dissipation* if $\gamma = 1$, it has *hypo-dissipation* if $\gamma < 1$, and it has *hyper-dissipation* if $\gamma > 1$. Similarly to the dynamics of continuous media, system (1) is the *incompressible Navier-Stokes equations* on the log-lattice. When $\nu = 0$, the flow is *inviscid*, and the system reduces to the *incompressible Euler equations* on the log-lattice.

The convolution in eq. (1c) defines triadic interactions on the logarithmic lattice, which are nontrivial only if the equation $\lambda^m = \pm\lambda^q \pm \lambda^r$ has integer solutions $m, q, r$. As shown in [9], this is possible only for particular values of $\lambda$, which determine the number of possible interactions on the grid. In this paper, we consider the following three values: $\lambda = 2$, with 3 interactions per direction; $\lambda = \phi \approx 1.618$ (the golden number), with 6 interactions per direction; and $\lambda = \sigma \approx 1.325$ (the plastic number), with 12 interactions per direction. As $\lambda$ decreases from 2 to $\sigma$, the density of nodes and the number of interactions on the grid increase. We recall, however, that the interactions for these log-lattices are all local.

### *2.2. Global quantities*

By analogy with the Fourier representation of classical fluid flows, we define the global quantities representing the *total energy* $E$ and the *helicity* $H$ as

$$E = \sum_k |u|^2, \tag{2}$$

$$H = \sum_k u_\alpha \overline{\omega}_\alpha, \tag{3}$$

where $\omega_\alpha = \epsilon_{\alpha\beta\gamma} i k_\beta u_\gamma$ is the *vorticity* field; here, $\epsilon_{\alpha\beta\gamma}$ is the Levi-Civita symbol. Regular solutions of the unforced three-dimensional inviscid system (1) conserve these quantities in time [9].

Moreover, we define the energy spectrum $E(k)$ as

$$E(k) = k^{-1} \langle |u|^2 \rangle_{S_k}, \tag{4}$$

where the average $\langle \cdot \rangle_{S_k}$ is taken over the wave vectors in the shell $S_k$ delimited by spheres of radii $k$ and $\lambda k$. More explicitly,

$$\langle |u|^2 \rangle_{S_k} = \frac{1}{N_k(\lambda k - k)} \sum_{k \le |q| < \lambda k} |u(q)|^2, \tag{5}$$

where $N_k \sim (\log(k))^{d-1}$ is the number of wave vectors in the shell $S_k$.

*2.3. Regularity*

The solutions of fluid dynamics equations on log-lattices (1) share some regularity properties with the original models. The main mathematical results are for the inviscid Euler equations [9]. For this system, the local-in-time existence of strong solutions and a Beale-Kato-Majda blow-up criterion was proved. One can extend regularity properties to this setting by exploiting the conservation of enstrophy in two dimensions. In the three-dimensional case, high-resolution numerical log-lattice simulations disclosed a finite-time blow-up, characterized by a chaotic wave travelling with constant average speed along a renormalized set of variables [12]. Such blow-up scenarios were confirmed for $\lambda = \phi$ and $\lambda = \sigma$, presenting the same asymptotic blow-up scalings [9]. In the viscous case, numerical simulations suggest the expected global regularity of solutions.

*2.4. Singularity strip method for log-lattices*

If a potential singularity is due to an imaginary pole crossing the real axis, one can track its distance to the real axis via the *singularity strip method* [13]. This method considers the analytic continuation $u(z)$ of the physical-space velocity field and is based on the following property: if

$$u(z) \sim 1/(z - z_*)^{\xi}, \quad \text{for } z \to z_* \tag{6}$$

in a neighborhood of the complex singularity $z_* = a + i\delta$, then its Fourier transform $\hat{u}_k$ satisfies

$$\hat{u}_k \sim k^{-d-\xi} e^{ika} e^{-\delta k}, \quad \text{as } k \to \infty. \tag{7}$$

Asymptotics of (7) provide the corresponding exponential decay $E(k) \sim e^{-2\delta k}$ for the energy spectrum over a typical length $2\delta$. Therefore, one can measure the distance of the dominant pole to the real axis by monitoring the decay of the energy spectrum in Fourier space. A finite-time singularity at instant $t_b$ would occur if $\delta \to 0$ as $t \to t_b$.

Extension of this notion to the log-lattice framework is natural. It relies on the observation that if a flow (1) on log-lattice satisfies $u(k) \sim k^{-d-\xi} e^{-\delta k}$, then its inverse Fourier transform obeys a relation similar to (6). Therefore, we can generalize the singularity strip method to log-lattices, where $2\delta$ is estimated from the slope of $\log E(k)$ as a function of $k$.

*2.5. Numerical methods*

Equations (1) are integrated using an implicit 4th order Runge-Kutta with adaptive time-step. Starting from initial conditions $u(t)$, we first solve the inviscid equation

$$\partial_t u_\alpha = P_{\alpha\beta} \left( -\boldsymbol{i} k_\sigma u_\sigma * u_\beta + f_\alpha \right), \tag{8}$$

where $P_{\alpha\beta} = \delta_{\alpha\beta} - \frac{k_\alpha k_\beta}{k^2}$ accounts for the pressure term under hypothesis (1a), which yields $u(t+dt)_{\nu=0}$. The viscosity is then taken into account using a technique analogous to viscous splitting leading to $u(t+dt) = u(t+dt)_{\nu=0} e^{-\nu_r k^{2\gamma} dt}$ where $dt$ is the time-step.

## 3. 1D Burgers equation

Before going to the full three-dimensional Navier-Stokes system on log-lattices, we take an intermediate step by studying the more straightforward one-dimensional Burgers equation. For this system, several exact mathematical results are available. This allows us to probe the singularity strip method on log-lattices, by comparing our numerical computations with the exact expected results.

The one-dimensional Burgers equation on log-lattices is obtained from system (1) as follows. We consider a compressible pressureless flow on a one-dimensional log-lattice. Mathematically, this translates into setting $p = 0$ and dropping eq. (1a) from the system, which reduces to

$$\partial_t u + (u * \partial_x u) = -\nu k^{2\gamma} u + f, \tag{9a}$$

$$(u * \partial_x u)(k) = \sum_{q+r=k} u(q)(ir)u(r). \tag{9b}$$

It was shown [14] that, if we change the coefficient in front of the convolution (9b), the Burgers equation on log-lattices is equivalent to well-known shell models of turbulence for specific choices of parameters. Particularly, when $\lambda = 2$, system (9) (but with a factor 2 added in the convolution and restricting to imaginary solutions) is the dyadic model [15], while for $\lambda = \phi$ (but with a factor $-\phi^2$ added in the convolution) it is the Sabra model [16] in a three-dimensional parameter regime (second invariant is not sign defined). Because of this relation with shell models of turbulence, the Burgers equation on the one-dimensional log-lattice inherits several results concerning the regularity of its solutions, which we briefly review now.

For the dyadic model ($\lambda = 2$) with $\nu > 0$, there are theorems [17] for global existence of weak solutions (satisfying the energy inequality at almost all time), local regularity when $\gamma > 1/3$, global regularity when $\gamma \geq 1/2$, and finite-time blow-up when $\gamma < 1/3$. We remark that there are no rigorous statements about the parameter range $1/3 \leq \gamma < 1/2$. This means that the mathematical techniques used in the currently available theorems are not sharp enough to separate the finite-time blow-up and the global regularity regimes. The finite-time singularity in the inviscid case was also rigorously established [18].

For the viscous Sabra model ($\lambda = \phi$) with usual dissipation $\gamma = 1$, there are proofs [19] of global regularity of strong solutions. Like the Navier-Stokes equations, the dynamics of the Sabra model are developed within finite degrees of freedom. Indeed, the finite dimensionality of the global attractor and the existence of a finite-dimensional inertial manifold were proved [19]. On the other hand, the inviscid model has [20] global-in-time existence of weak solutions with finite energy, local-in-time regularity, and a Beale-Kato-Majda-like blow-up criterion. Despite the absence of rigorous proofs, it is well-known [21] that Sabra (in the three-dimensional parameter regime) develops a self-similar finite-time blow-up, characterized as a travelling wave in a renormalized system of variables (cf. [22]). Following the dynamical systems approach, such blow-up

**Table 1:** Exponents of the inviscid scalings of various quantities measured for the 1D Burgers and the 3D Euler equations within different values of the grid spacing $\lambda$. The scalings are with respect to $\tau = 1 - t/t_b$ where $t_b$ is the blow-up time. By definition, the energy spectrum scales like $E(k) \sim k^{-1-2\alpha}$, the maximum value of the vorticity scales like $\omega_{\max} \sim \tau^{-\beta}$, and the width of the singularity strip scales like $\delta \sim \tau^{\mu}$. The $^{(0)}$ superscript indicates a simulation performed with no forcing. The $^*$ superscript indicates a simulation made with a different initial condition.

| | $\lambda$ | $t_b$ | $\alpha$ | $\beta$ | $\mu$ |
|---|---|---|---|---|---|
| 1D Burgers | 2 | 0.3898 | 0.37 | 1 | 1.55 |
| | $\phi$ | 0.5193 | 0.37 | 1 | 1.55 |
| | $\sigma$ | 0.4300 | 0.37 | 1 | 1.55 |
| | $2^{(0)}$ | 0.2687 | 0.37 | 1 | 1.55 |
| | $\phi^{(0)}$ | 0.1460 | 0.37 | 1 | 1.55 |
| 3D Euler | 2 | 0.8481 | 0.67 | 1 | 2.81 |
| | $\phi$ | 5.8005 | 0.67 | 1 | 2.83 |
| | $\phi^*$ | 0.1542 | 0.67 | 1 | 2.82 |
| | $\sigma^*$ | 0.8430 | 0.67 | 1 | 2.67 |

can be seen as a fixed-point attractor of the associated Poincar map [23].

To our knowledge, there are no systematic results about the development of singularities in Sabra with general dissipation exponents $\gamma$, nor in the case of our third lattice parameter $\lambda = \sigma$.

### *3.1. Inviscid flow*

We start with the inviscid ($\nu = 0$) Burgers equation without and with forcing. When forcing, initial conditions are equal to zero, and the forcing is equal to the imaginary unit $j$ on the first mode ($k_0$) for $\lambda = 2$, the first two modes when $\lambda = \phi$, and the first three modes when $\lambda = \sigma$. Without forcing, initial conditions are taken such that total energy $E = 1$, and first mode, two first modes or three first modes have positive uniform real value, depending on $\lambda = 2$, $\phi$ or $\sigma$, while initial smaller scales are nil. We observe finite-time blow-up for all three values of $\lambda$ in the two cases. Numerical results are plotted in fig. 1, and scaling exponents are summarized in table 1.

The maximum of the gradient $\omega_{\max}(t) = \max_k |ku(k)|$ blows up in finite time, following the self-similar law

$$t_b \omega_{max} \sim \frac{1}{\tau}, \quad \tau = 1 - \frac{t}{t_b}, \tag{10}$$

displayed in fig. 1b. While the blow-up time depends on the forcing and the value of $\lambda$, the self-similar law (10) is independent of these variables. This law also holds for the original continuous model. Indeed, differentiating the classical Burgers equation $\partial_t u + u\partial_x u = 0$ with respect to $x$, we get that the space derivative $\omega = -\partial_x u$ obeys $d\omega/dt = \omega^2$, whose solution is exactly eq. (10) with $t_b = 1/\omega(t = 0)$.

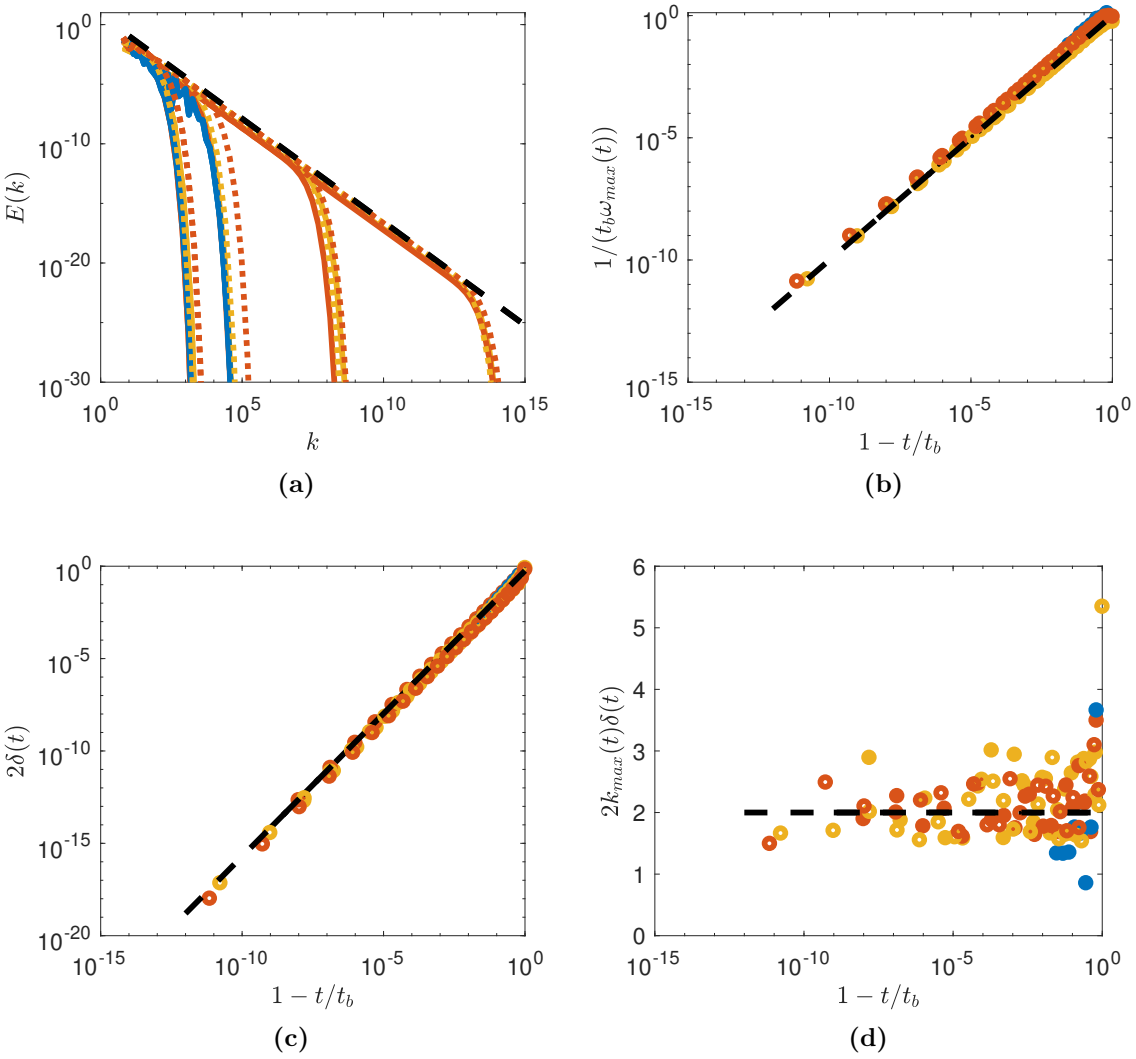


**Figure 1:** Inviscid blow-up for Burgers (1D) case for $\lambda = 2$ (yellow), $\lambda = \phi$ (red) and $\lambda = \sigma$ (blue). Continuous lines and filled symbols indicate simulations with constant forcing, while dotted lines and open symbols indicate simulations without forcing. (1a) Spectra at different renormalized relative time $\tau = 1 - t/t_b$. The black dotted line has a slope of $-1.733$. (1b) Maximum value of the derivative $1/t_b\omega_{\max}$ as a function of $\tau$; The black dotted line is the theoretical value from eq. (10). (1c) Width of the analyticity strip $\delta$ as a function of $\tau$. The black dotted line has a slope given in table 1. (1d) Renormalized width $k_{\max}\delta$ as a function of $\tau$. The black dotted line has a slope of 0.

We also check that the energy spectrum's blow-up evolution is universal in that it only depends on $\tau$. This is illustrated in fig. 1a, where spectra at different $\lambda$ but similar $\tau$ are shown to overlap. As $\tau$ approaches zero, the energy spectrum gradually widens towards larger values of $k$, developing a power-law spectrum $E(k) \sim k^{-2\alpha-1}$ with $1 + 2\alpha = 1.733$, which corresponds to the scaling law $u(k) \sim k^{-\alpha}$ with $\alpha = 0.367$. Such asymptotics agrees with exact results from the renormalization group formalism applied to the Sabra shell model [24].

Finally, we compute the analyticity strip width $\delta$ as the solutions approach the blow-up. This is done using the formula (7) with $\xi + 1 = \alpha$. The result is shown in fig. 1c. We verify that $\delta$ decays to zero in finite time, following a power law $\delta \sim \tau^\mu$, with $\mu = 1.546$. This decay is also universal and does not depend on the value of $\lambda$ or the forcing. The width of the analyticity strip is closely associated with $k_{\max}$, defined as the wavenumber at which $\omega$ attains its maximum value. Indeed, we see in fig. 1d that $k_{\max}\delta$ is approximately constant in time. This is in agreement with the asymptotic eq. (7), which implies that $\omega_{\max}$ is achieved at $k_{\max} \sim 1/\delta$.

The self-similar law (10) is valid for all $\lambda$ in average only. The figures show that the blow-up looks truly self-similar only for the values $\lambda = 2$ and $\lambda = \phi$. The oscillations in the case $\lambda = \sigma$ suggest a different blow-up scenario (e.g. quasi-periodic or chaotic). A detailed analysis of this is left for future work.

### *3.2. Viscous dissipation*

We now introduce viscous dissipation ($\gamma = 1$) and study how the dynamical behaviour depends upon the viscosity parameter $\nu$. This section restricts the analysis to the value $\lambda = 2$. We introduce a force at the large scale, whose amplitude is adapted dynamically so that the total power input is constant in time ($f_{k=k_0} = P u_{k=k_0}/|u|^2_{k=k_0}$, where $P = 1$).

In this setup, the dissipative term is strong enough to prevent the blow-up, and the solution reaches stationarity. The energy spectrum develops a power law in the intermediate scales (called the *inertial range*) followed by an exponential decay at larger $k$ – see fig. 2a. In the inertial range, $E(k) \propto k^{-5/3}$, corresponding to $u(k) \propto k^{-1/3}$.

The maximum value of the derivative $\omega_{\max}$ is inversely proportional to the viscosity, following the power law $\omega_{\max} \sim \nu^{-\beta}$ with $\beta = 0.5$, as shown in fig. 2b. This scaling law can be derived when assuming a viscosity-independent *anomalous dissipation* $\epsilon > 0$ in the inviscid limit $\nu \to 0$. Under this assumption, we have the balance $\nu\omega^2 \sim \epsilon$, which provides $\omega \sim (\epsilon/\nu)^{1/2}$.

Accordingly, the width of the analyticity strip does not decline to zero. However, it stabilizes at a finite value that depends on the viscosity – see fig. 2c – and follows the power-law scaling $\delta \sim \nu^\mu$, with exponent $\mu = 0.7067$. This is smaller than expected from a dimensional argument "a la Kolmogorov", in which $\epsilon = \nu u^2/\delta^2$, with $u \sim \delta^{1/3}$, would instead predict $\delta \sim \nu^{3/4}$. The strip width follows approximately the scaling $\delta \sim 1/k_{\max}$, as shown in fig. 2d.

### *3.3. Hyper- and hypo-dissipation*

We have also studied the influence of the dissipation degree $\gamma$ on the various scaling laws. This is summarized in fig. 2 and table 3. The slope of the spectrum is insensitive to $\gamma$ and displays a $E(k) \sim k^{-5/3}$ law with no intermittency correction. On the other hand, the slopes of both the inverse of the maximum gradient and the singularity width increase in absolute value as $\gamma$ is decreased towards 1/3. We defer the discussion about those results to section 5.1.

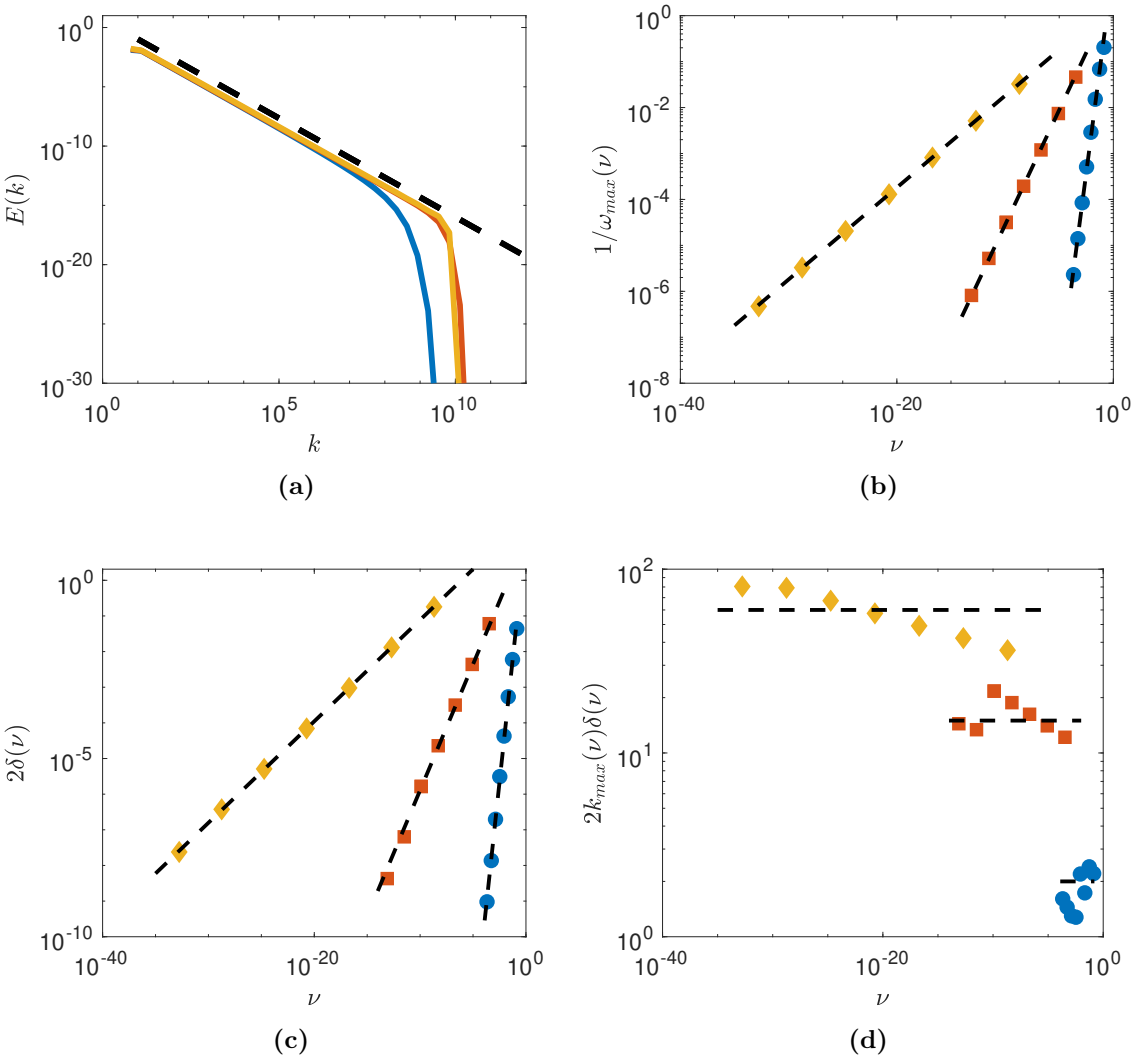


**Figure 2:** Influence of the type of viscosity on the stationary dynamics for viscous Burgers (1D) case for $\lambda = 2$ and $\gamma = 0.5$ (hypo-viscous case, blue circle), $\gamma = 1$ (viscous case, red squares) and $\gamma = 2$ (hyperviscous case, yellow diamond). (2a) Energy spectrum. The black dotted line has a slope $-5/3$; (2b) Maximum value of the derivative $1/\omega_{\max}$ as a function of viscosity. The black dotted line has a slope given in table 3 for each case. (2c) Width of the analyticity strip $\delta$ as a function of viscosity. The black dotted line has a slope given in table 3 for each case. (2d) Renormalized width $k_{\max}\delta$ as a function of viscosity.

### *3.4. Critical dissipation degree* $\gamma = 1/3$

According to [25], there are finite time blow-up solutions for the Burgers equation (9) with $\lambda = 2$ whenever $\gamma < 1/3$. However, the theorems say nothing about the limit case $\gamma = 1/3$. For this reason, we call this value as being the *critical dissipation degree*. It is natural to ask whether the blow-up might or might not occur in this specific situation. Here we consider not only $\lambda = 2$, but also extend this question to the other two lattice parameters.

**Table 2:** Exponents in the critical case $\gamma = 1/3$ of various quantities measured for different values of the grid spacing $\lambda$ and dimension $d$. The scalings are with respect to $\tau = 1 - t/t_b$ in the inviscid case, where $t_b$ is the blow-up time. By definition, the energy spectrum scales like $E(k) \sim k^{-1-2\alpha}$, the maximum value of the vorticity scales like $\omega_{\max} \sim \tau^{-\beta}$ and the width of the analyticity strip scales like $\delta \sim \tau^{\mu}$.

| | 1D Burgers | | | | 3D Navier-Stokes | | | |
|---|---|---|---|---|---|---|---|---|
| $\lambda$ | $t_b$ | $\alpha$ | $\beta$ | $\mu$ | $t_b$ | $\alpha$ | $\beta$ | $\mu$ |
| 2 | 0.8497 | 0.37 | 1 | 1.55 | 7.8194 | 2/3 | 1 | 2.81 |
| $\phi$ | 0.5193 | 0.37 | 1 | 1.55 | 6.51 | 2/3 | 1 | 2.83 |
| $\sigma$ | 0.4546 | 0.37 | 1 | 1.84 | – | – | – | – |

We initialized the flow with the same data as in the inviscid case and set the small viscosity $\nu = 10^{-7}$. We observed a finite time blow-up for all three $\lambda$, illustrated in fig. 3. The blow-up time is larger than in the inviscid case, but the scaling laws are the same – both the prefactor and the scaling exponents – than in the inviscid case. The exponents are summarized in table 2. The only exception is for the scaling law of $\delta$ in the case $\lambda = \sigma$. This might be due to the oscillations in the energy spectrum, making it harder to fit the exponential decreasing, see fig. 3a.

In this small-viscosity run, viscosity only delays the blow-up but does not influence the development of the singularity. However, we observed a surprising behaviour change when increasing the viscosity to larger values. There is a transition between a small-viscosity regime, where finite time blow-up occurs, and a large-viscosity regime, where the blow-up disappears, and the width of the analyticity strip saturates to a finite value – see insert of fig. 3c. The amplitude of $\delta$ seems to follow a critical mean-field behaviour, as it varies like $\delta \sim \sqrt{\nu - \nu_c}$, with $\nu_c \sim 0.4$. A similar transition is observed at a lower value of $\gamma$, with $\nu_c$ increasing as $\gamma$ decreases.

This transition is in contradiction with mathematical results by [25]. We have no explanation of the discrepancy so far, but we suspect it might be linked to a numerical non-linear viscosity—see [26] for a discussion. But, for $\nu > \nu_c$, the energy spectrum becomes clearly stationary and has a small inertial range, while for a blowup the inertial range becomes very large. And changing the value of the tolerance in the Runge-Kutta step doesn't change much the size of the inertial range.

## 4. 3D Euler and Navier-Stokes equations

### *4.1. Inviscid flow – Euler equations*

We now turn to the full three-dimensional incompressible fluid dynamics on log-lattices, starting with the inviscid Euler equations. We consider here the three lattice spacings $\lambda$. In order to test universality, we ran the case $\lambda = \phi$ with two different initial conditions.

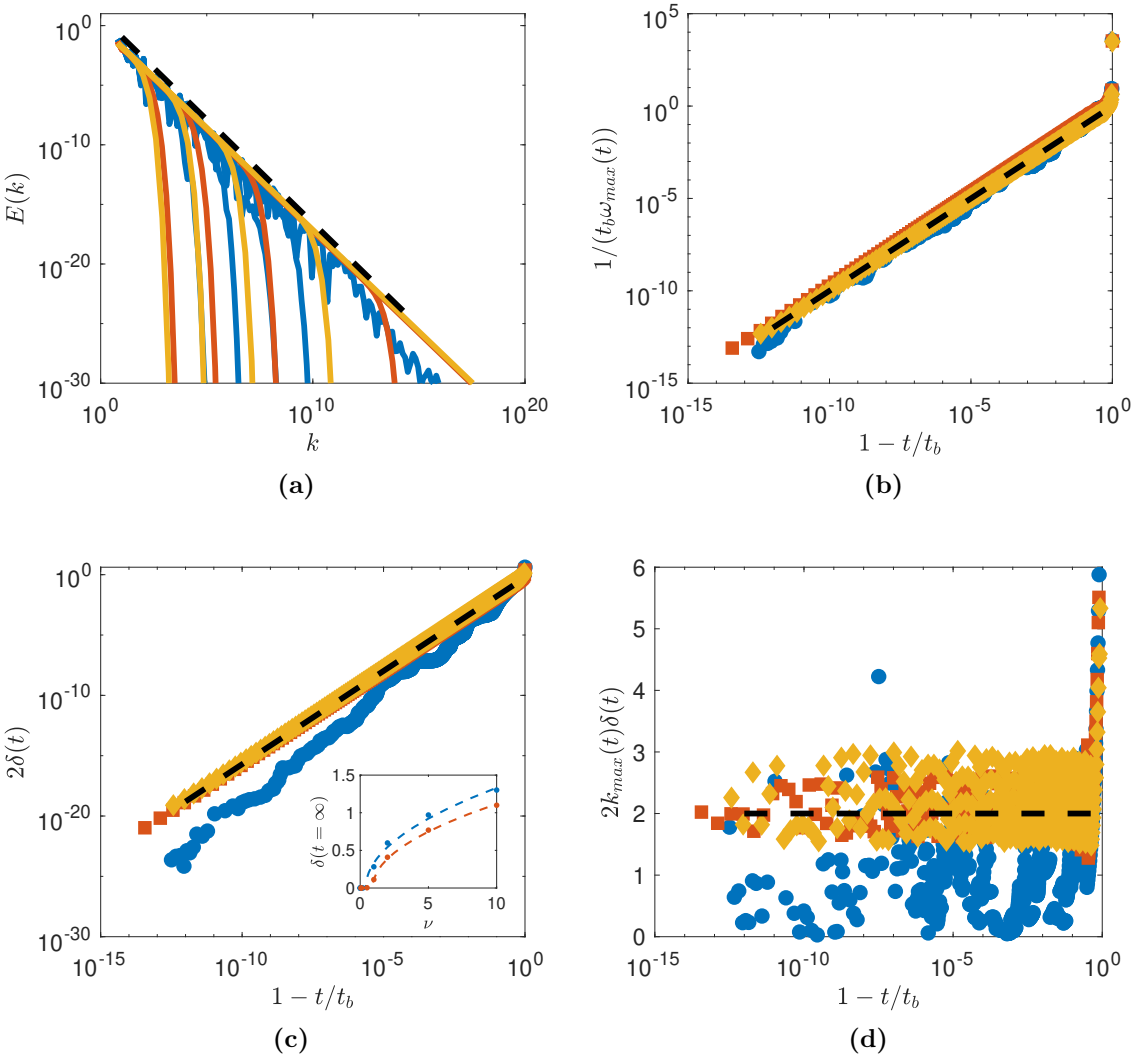


**Figure 3:** Blow-up for critical Burgers (1D) case, with $\gamma = 1/3$, $\nu = 10^{-7}$ and for $\lambda = 2$ (yellow), $\lambda = \phi$ (red) and $\lambda = \sigma$ (blue). (3a) Spectra at different renormalized relative time $\tau = 1 - t/t_b$; (3b) Maximum value of the derivative $1/t_b\omega_{\max}$ as a function of $\tau$ (3c) Width of the analyticity strip $\delta$ as a function of $\tau$. The insert shows the behaviour of the width of the analyticity strip at $t = \infty$ when the viscosity is increased, for $\gamma = 1/3$ (blue data points) (resp. $\gamma = 1/4$ (red data points)). The dotted lines are fits of the type $\sqrt{\nu - \nu_c}$, with $\nu_c = 0.4$ (resp. $\nu = 0.9$. (3d) Renormalized width $k_{\max}\delta$ as a function of $\tau$. The dotted line has the same scaling and prefactor as in the inviscid blow-up case, see fig. 1

Default initial conditions are complex random initial conditions at large scale $|k| < 3k_0$, and the other (denoted by a star $*$) are complex random initial conditions along two dimensions (the third one being determined by incompressibility), at large scale $|k| < k_0\lambda^3$. We observed a finite-time blow-up in all set-ups, in agreement with previous results documented in [12, 9]. Here, we observe that while the blow-up time depends on the initial conditions, the dynamics become universal when plotted in relevant non-dimensional variables, as illustrated in fig. 4. The spectra for distinct values of $\lambda$ overlap when plotted at the same non-dimensional times $\tau = 1 - t/t_b$, as evidenced in fig. 4a. The slope of the power law in the inertial range is steeper than in 1D Burgers, with a value very close to $-7/3$. This is the slope expected for a helicity cascade. Our exponent is slightly smaller than those found in some direct numerical simulations of the Euler equations, where a $E(k) \sim k^{-3}$ spectrum is observed [27, 28], but comparable to the value 2.33 obtained in more recent simulations [29].

The maximum value of the vorticity $\omega_{\max}$ diverges during the blow-up, as shown in fig. 4b. Its asymptotic scaling is the same as for the maximum gradient in the 1D Burgers equation, given by eq. (10). However, contrarily to the 1D case, the constant in front of the power law varies as a function of $\lambda$ and is not simply given by $1/t_b$. This is not too surprising given the 3D nature of the flow, which prevents the application of the simple blow-up argument used for 1D Burgers. However, as $\lambda$ is decreased towards 1, the non-dimensional curve becomes closer to the exact asymptotic law.

Approaching the blow-up, the width of the analyticity strip decays to zero with a power law $\delta \sim \tau^\mu$ with exponent $\mu \approx 2.81$ – see fig. 4c. This is larger than in 1D Burgers. This decay is also universal, as it does not depend on $\lambda$. However, it does not show a simple dependence with $k_{\max}$ as seen in fig. 4d. This might be related to the chaotic nature of the blow-up attractor [9].

### *4.2. Viscous dissipation – Navier-Stokes equations*

We now add the viscous term with $\gamma = 1$ and a constant-power forcing. The solutions achieve a statistically stationary state in this framework, whose average scalings are depicted in fig. 5. Like in 1D Burgers, the energy spectra display a power law until the solution reaches the viscous scale, with an inertial range widening as $\nu$ decreases. The slope of the energy spectrum is slightly steeper than Kolmogorov's $-5/3$, with an intermittency correction of around 0.13. Accordingly, the scaling exponent $\alpha$ for $u(k) \sim k^{-\alpha}$ is $\alpha = 0.40$, slightly larger than $1/3$. The maximum vorticity $\omega_{\max}$ increases with decreasing viscosity, following the power law $\omega_{\max} \sim \nu^{-\beta}$ with an exponent $\beta = 0.39$ lower than Kolmogorov's $1/2$.

The width of the analyticity strip decays with viscosity as $\delta \sim \nu^\mu$ with an exponent $\mu = 0.65$ – see fig. 5c. Such decay is less intense than in the 1D Burgers equation. Nevertheless, the dependence of $\delta$ on $1/k_{\max}$ in the Navier-Stokes case is sharper, as one verifies by comparing fig. 5d with fig. 2d.

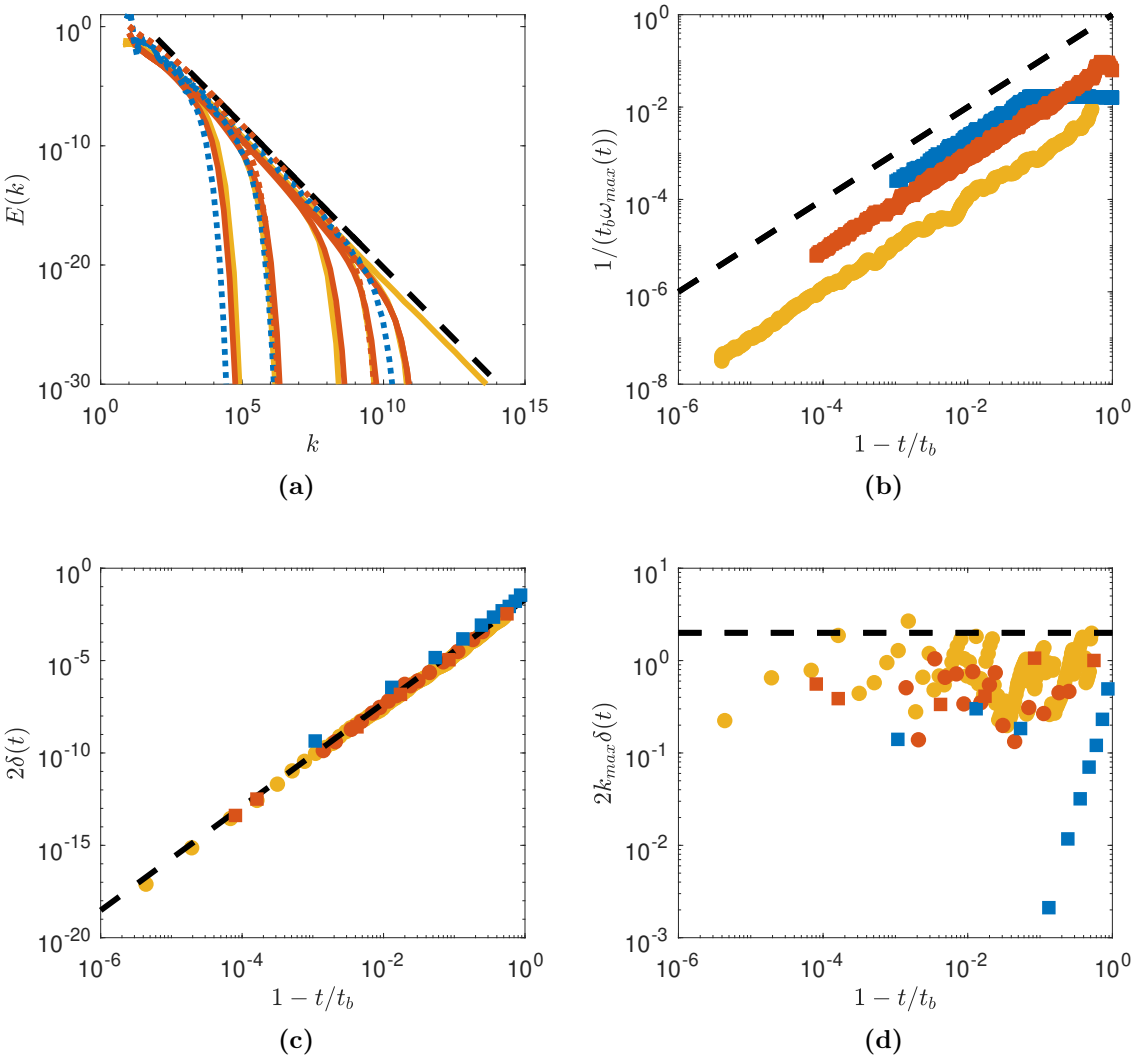


**Figure 4:** Inviscid blow-up for the Euler (3D) case for $\lambda = 2$ (yellow), $\lambda = \phi$ (red) and $\lambda = \sigma$ (blue). (4a) Spectra at different renormalized relative time $\tau = 1 - t/t_b$, from 0.2542 to 0.00001 from left to right. Spectra with continuous lines and dotted lines correspond to different initial conditions. The black dotted line has a slope of $-7/3$; (4b) Maximum value of derivative $1/t_b\omega_{\max}$ as a function of $\tau$. The black dotted line has a slope of 1; (4c) Width of analyticity strip $\delta$ as a function of $\tau$; The black dotted line has a slope 2.805. (4d) Renormalized width $k_{\max}\delta$ as a function of $\tau$. In panels 4b, 4c and 4d, we used different symbols for different initial conditions: circles, and squares.

### *4.3. Hyperviscous dissipation*

We now consider what happens in the hyperviscous case $\gamma > 1$. We keep the constant-power forcing to reach stationary states.

For $\gamma = 2$, we still observe a power-law energy spectrum followed by an exponential cut-off at the viscous scales – see fig. 5a. The inertial range keeps widening as $\nu$ is decreased. The slope of the energy spectrum is very close to $-5/3$, being slightly steeper with an intermittency correction around 0.07, corresponding to $\alpha = 0.37$. The

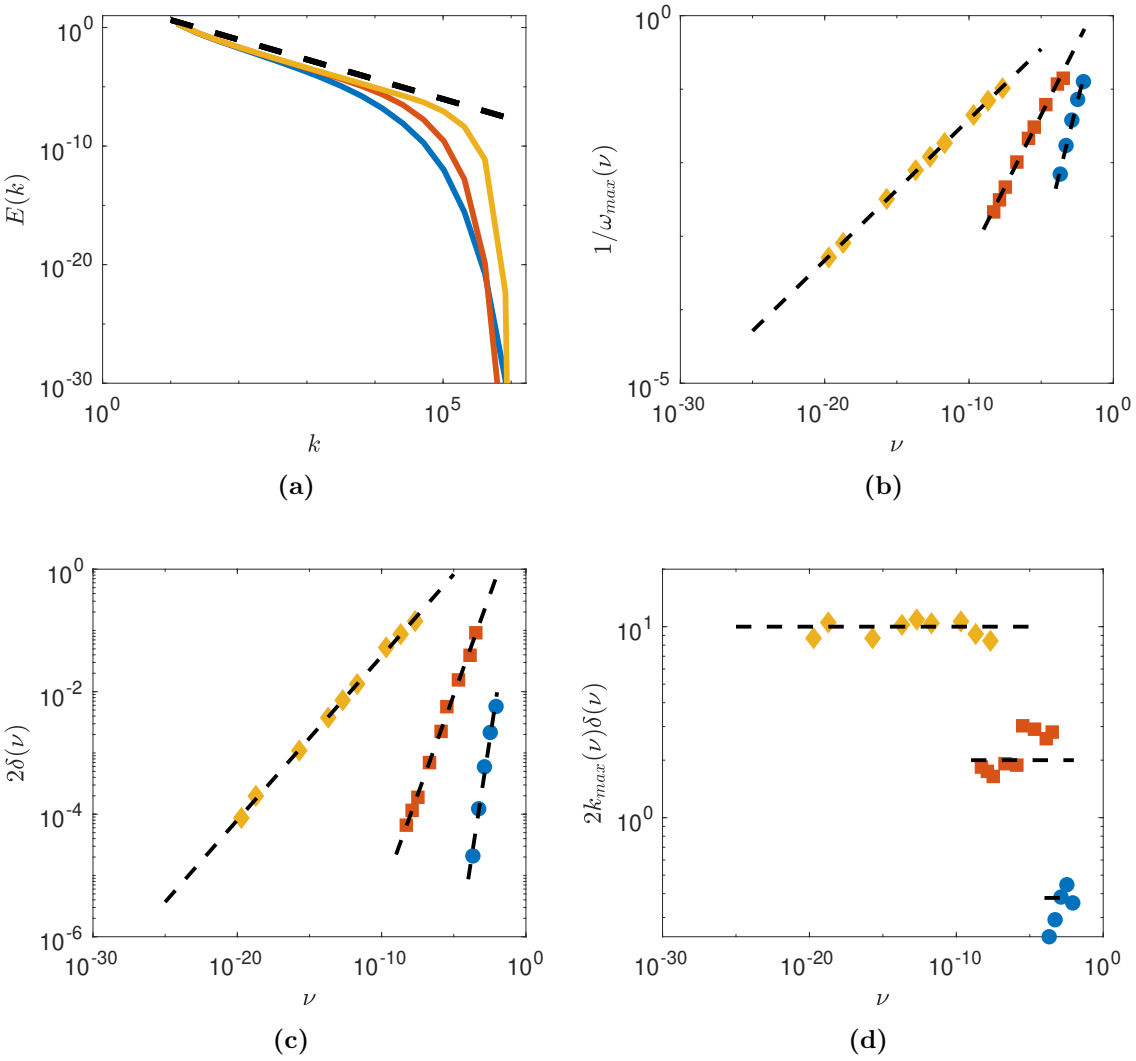


**Figure 5:** Stationary dynamics for the Navier-Stokes (3D, viscous) case for $\lambda = 2$ and $\gamma = 0.5$ (hypo-viscous case, blue circle), $\gamma = 1$ (viscous case, red squares) and $\gamma = 2$ (hyperviscous case, yellow diamond ). (5a) Energy spectrum. The black dotted line has a slope $-5/3$; (5b) Maximum value of the derivative $1/\omega_{\max}$ as a function of viscosity. The black dotted line has a slope given in table 3 for each case. (5c) Width of the analyticity strip $\delta$ as a function of viscosity. The black dotted line has a slope given in table 3 for each case. (5d) Renormalized width $k_{\max}\delta$ as a function of viscosity.

maximum vorticity $\omega_{\max}$ increases with decreasing viscosity like a power law, with an exponent $\beta = 0.19$ lower than usual ($\gamma = 1$) viscous case. The width of the analyticity strip decays with viscosity with an exponent $\mu = 0.26$. Like in the viscous case, $\delta$ appears to scale simply like $1/k_{\max}$, as seen on fig. 5d.

The above results suggest that the intermittency corrections in the energy spectra are smaller for hyperdissipation. We checked that for the stronger degree $\gamma = 8$, they vanish completely, and the dependence of $\omega_{\max}$ and $\delta$ on $\nu$ become very weak. This is explained by the very sharp viscous cut-off due to the hyperviscous dissipation. Indeed,

**Table 3:** Exponents of the scaling of various quantities as a function of $\gamma$ measured for the grid spacing $\lambda = 2$ and various dimensions $d$. The scalings are with respect to the viscosity $\nu$. By definition, the energy spectrum scales like $E(k) \sim^{-1-2\alpha}$, the maximum value of the vorticity scales like $\omega_{\max} \sim \nu^{-\beta}$ and the width of the analyticity strip scales like $\delta \sim \nu^{\mu}$.

| | 1D Burgers | | | 3D Navier-Stokes | | |
|---|---|---|---|---|---|---|
| $\gamma$ | $\alpha$ | $\beta$ | $\mu$ | $\alpha$ | $\beta$ | $\mu$ |
| 1/3 | – | – | – | 2/3 | 1 | 2.81 |
| 1/2 | 1/3 | 1.80 | 2.78 | 0.5 | 0.78 | 1.53 |
| 1 | 1/3 | 0.50 | 0.71 | 0.40 | 0.39 | 0.65 |
| 2 | 1/3 | 0.20 | 0.28 | 0.37 | 0.19 | 0.27 |
| 8 | 1/3 | 0.045 | 0.06 | 1/3 | 0.05 | 0.06 |

the equivalent of the Kolmogorov scale $k_d$ in the hyperviscous case relates to $\nu$ as $k_d \sim \nu^{1/(1/3+2\gamma-1)}$, becoming independent of viscosity in the limit $\gamma \to \infty$. For $\gamma = 2$ the dependence is $\delta \sim \nu^{0.3}$, close to what is observed for the scaling of the singularity strip width.

### *4.4. Hypoviscous dissipation*

The case with hypoviscous dissipation $1/3 < \gamma < 1$ is qualitatively similar to the viscous and hypervisous cases – see fig. 5. Exponents, however, are steeper. The corresponding values are reported in table 3. The energy spectrum develops a slope corresponding to the exponent $\alpha = 0.5$, which is steeper than Kolmogorov's 1/3 but milder than Euler's 2/3 on log-lattices. The singularity width appears again to be controlled by the wave number corresponding to the maximum vorticity – see fig. 5d. On the other hand, the maximum vorticity grows much more rapidly than in the viscous case, with an exponent twice as big, as shown in fig. 5b. This may indicate that we are approaching a critical dissipation degree, below which finite-time blow-up will occur.

### *4.5. Critical dissipation degree $\gamma = 1/3$*

The asymptotics of Kolmogorov's length scale for a flow with a general dissipation degree predicts the breakdown of the viscous cut-off when $\gamma$ approaches the critical value 1/3. Indeed, the dissipation scale $k_d$ is obtained from the dimensional balance between the convective and the dissipative terms $k_d u_d^2 \sim \nu k_d^{2\gamma} u_d$. On the other hand, Kolmogorov's theory states that $u_d \sim \epsilon^{1/3} k_d^{-1/3}$ for the energy dissipation rate $\epsilon$, which has a finite positive value in the inviscid limit. Together, these expressions yield

$$k_d \sim \epsilon^{\frac{1}{6(\gamma-1/3)}} \nu^{\frac{1}{2(1/3-\gamma)}}, \tag{11}$$

which, for sufficiently small $\nu$, provides $k_d \to +\infty$ when $\gamma \searrow 1/3$. For this reason, we call $\gamma = 1/3$ the *critical dissipation exponent*, the value at which we expect that

the dissipative term is no longer strong enough to prevent a finite-time singularity. We recall this was the case for the 1D Burgers equation on log-lattices.

Motivated by the above arguments, we investigate the critical hypo-diffusive degree in the full 3D system on log-lattices. The following analysis considers the spacings $\lambda = 2$ and $\lambda = \phi$. The initial data is the same as we used in the inviscid simulations, and viscosity is the same $\nu = 10^{-7}$.

In this regime, we observed a finite time blow-up for the two values of $\lambda$, illustrated in fig. 6. Like in 1D Burgers, the blow-up time is larger than in the inviscid case, but the scaling laws are the same. This is summarized in table 2. The slope of the energy spectrum remains $-7/3$. For $\lambda = 2$ and $\nu = 10^{-3}$, the dynamics becomes stationary, meaning there is as in 1D a phase transition, but between $\nu = 10^{-3}$ and $10^{-7}$, smaller than $\nu_c \sim 0.4$ in 1D.

## 5. Discussion

### *5.1. Scaling laws*

The variations of the scaling exponents with respect to the diffusion exponent $\gamma$ are shown in fig. 7.

Predictions for the scaling laws are possible using simple dimensional arguments if we impose $\delta \sim 1/k_{\max}$, as empirically observed. Indeed, from $u \sim k^{-\alpha}$ and $\omega \sim ku$, we get $\omega_{\max} \sim k_{\max}^{1-\alpha} \sim \delta^{\alpha-1}$ so that we get:

$$\beta = \mu(1-\alpha). \tag{12}$$

This fixes a link between the 3 exponents that is well satisfied – see fig. 7b. On the other hand, one can connect $\mu$ and $\alpha$ by extending the argument fixing the Kolmogorov scale to hypo and hyper-viscous cases: we impose that $k_{\max}$ is fixed by the condition that the viscous term balances the non-linear term $\nu k_{\max}^{2\gamma} u_{\max} \sim k_{\max} u_{\max}^2$. Using $u_{\max} \sim k_{\max}^{-\alpha}$ and $\delta \sim 1/k_{\max}$ we then get:

$$\mu = -\frac{1}{1-\alpha-2\gamma}, \tag{13}$$

This prediction is tested in fig. 7c and is well satisfied. The only free parameter is (wlog) $\alpha(\gamma)$. In the limit $\gamma \to 1/3$, we can fix it by imposing that $\beta = 1$, which is the scaling corresponding to conservation of the circulation of $u$ [30]. From eqs. (12) and (13), we then get $\alpha = 1 - \gamma = 2/3$, corresponding to a helicity cascade. In all other cases, we have no clear theories to predict the variations of $\alpha$ with $\gamma$. Notably, when $\gamma \to \infty$, we recover $\alpha = 1/3$ corresponding to an energy cascade.

### *5.2. Interest of the critical case*

The critical case $\gamma = 1/3$ is more than purely academic: renormalization group (RNG) analysis of NSE in Fourier space [31] indeed shows that the fixed point of the equations corresponds to a Navier-Stokes equation with turbulent viscosity scaling like $A\epsilon^{1/3}k^{-4/3}$,

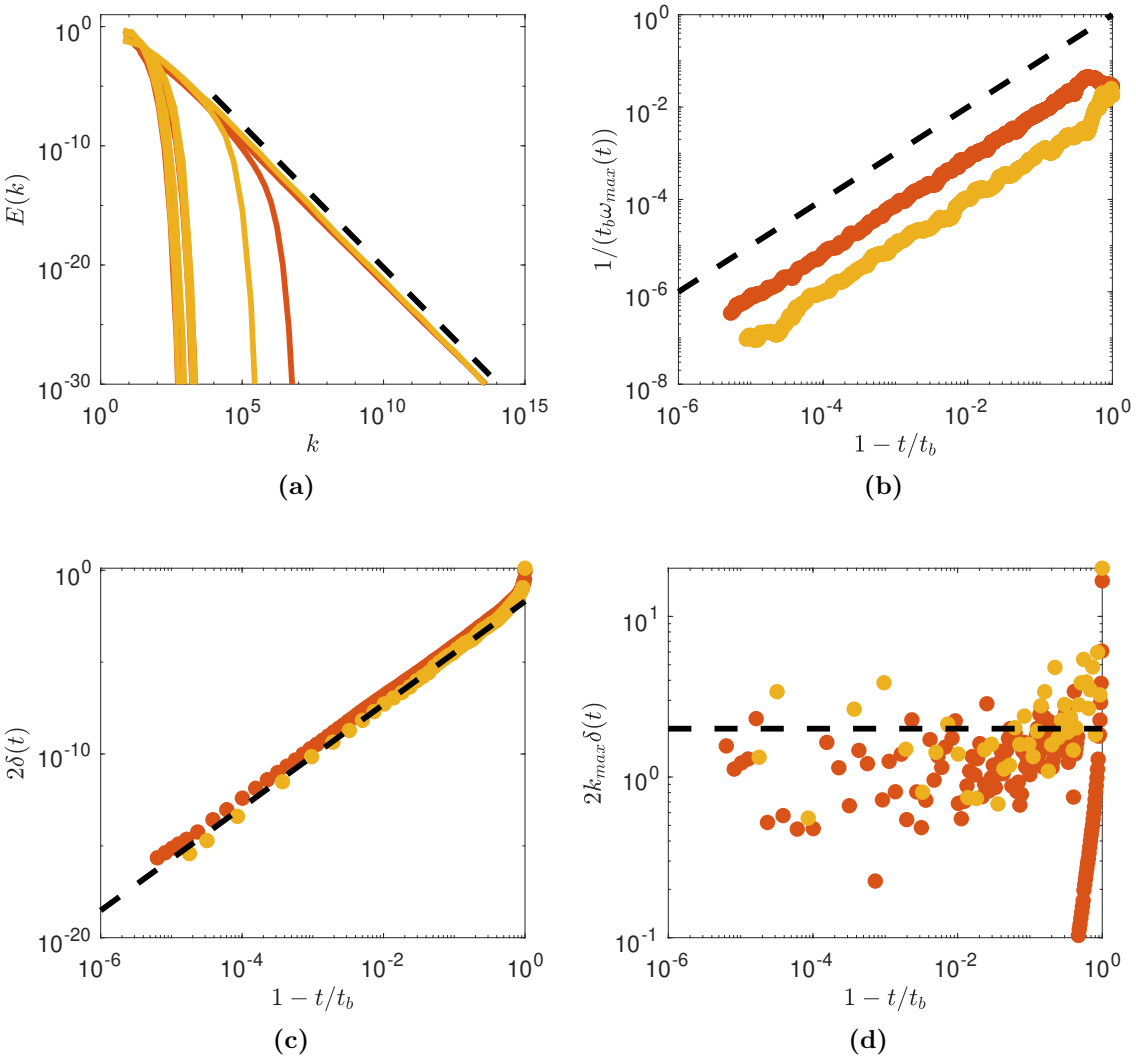


**Figure 6:** Blow-up for the critical 3D case, with $\gamma = 1/3$ and for $\lambda = 2$ (yellow) and $\lambda = \phi$ (red). (6a) Spectra at different renormalized relative time $\tau = 1 - t/t_b$; (6b) Maximum value of the derivative $1/t_b\omega_{\max}$ as a function of $\tau$ (6c) Width of the analyticity strip $\delta$ as a function of $\tau$ (6d) Renormalized width $k_{\max}\delta$ as a function of $\tau$. The dotted line has the same scaling and prefactor as in the inviscid blow-up case, see fig. 4

where $A$ is a constant with value $A = 0.1447$ in 1D and $A = 0.4926$ in 3D. This corresponds exactly to eq. (1), with $\gamma = 1/3$ and $\nu = A\epsilon^{1/3}$. This model is sometimes used as a subgrid model of turbulence [32]. In that respect, it is interesting that the transition viscosity found in sections 3.4 and 4.5 (at constant injected power, i.e. $\epsilon = 1$) is very close to the RNG value in 1D. On the one hand, this guarantees that the size of the inertial range is very wide, in agreement with the RNG picture of scale invariant solutions. On the other hand, this means that the solution is very close to a blow-up, which could have implications regarding the stability of this subgrid scheme.

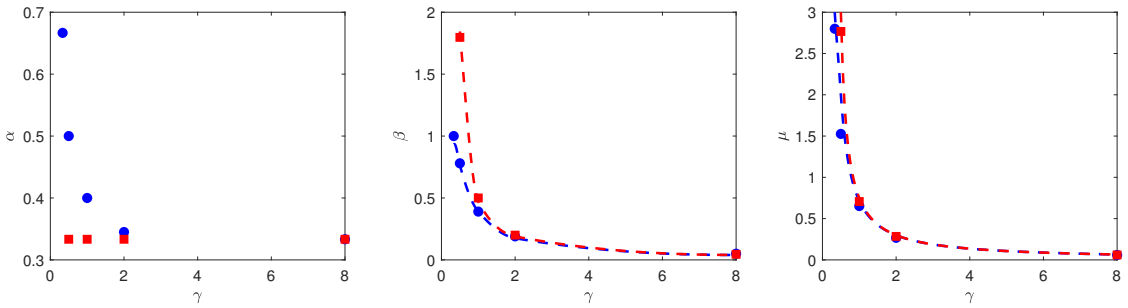


**(a)** **(b)** **(c)**

**Figure 7:** Variation of the scaling exponents as a function of the diffusive exponent $\gamma$ in $d = 1$ (blue circle) and $d = 3$ (red square) for $\lambda = 2$. (7a) For the scaling of the velocity $u \sim k^{-\alpha}$. (7b) for the scaling of the maximum vorticity $\omega_{\max} \sim \nu^{-\beta}$. The data points are reported from tables 2 and 3, while the dotted lines correspond to eq. (12); (7c) for the scaling of the singularity strip $\delta \sim \nu^{\mu}$. The data points are reported from tables 2 and 3. while the dotted lines correspond to eq. (13).

### *5.3. Implications for real Euler or Navier-Stokes?*

The log-lattices simulations we performed cannot be seen as an exact model of the Euler or Navier-Stokes equations because they remove by construction many non-linear interactions of the original equations, especially the non-local one. Nevertheless, because they obey the same conservation laws and symmetries, they may capture some scaling laws of the original equation more accurately. Comparing our findings with the few results on the topic is engaging.

Regarding the Euler equation, recent high-resolution numerical simulation in the axisymmetric case by [33] explored the scaling of the singularity strip in the blowing situation proposed by [34]. They found an exponent $\mu = 2.6 \pm 0.5$, which is compatible with the value $2.8 \pm 0.1$ that we get from table 3. Unfortunately, they do not provide an estimate of the slope of the energy spectrum. Previous older results in the Taylor-Green vortex [35, 28] found a steeper spectrum corresponding $\alpha \sim 1$. However, spectra with exponent matching our $-7/3$ value were observed in the early stage of recent simulations at larger resolution [29]. Therefore, the main characteristics of blow-up in log-lattices simulations agree with the most recent results observed in the traditional DNS of the Euler equation.

Regarding the Navier-Stokes equations, we can look at two recent results. The first one by [36] finds a value of $\mu = 0.89$ using recent DNS of NSE. This value is larger than the value we found in the present paper, corresponding to $\mu = 0.65$. Another recent result [37] estimates $\beta$ in 3D NSE. They indeed found that the tail of the PDF of enstrophy scales like $\nu^{0.77}\tau_K^{-2}$, where $\tau_K \sim \nu^{1/2}$ is the Kolmogorov time. Identifying such extreme events of enstrophy with $\omega_{\max}^2$, we thus get $\beta_{DNS} \sim 0.88$, which is also much larger than the value we observe in log-lattices $\beta_{LL} \sim 0.39$. Note, however, that both DNS values are compatible with eqs. (12) and (13), provided we choose $\alpha \sim 0$, hinting at the presence of multifractality. Log-lattices simulations

are generally much less intermittent than DNS [9], with one dominating exponent (monofractal behaviour). Some time ago, [32] linked the intermittency properties of NSE with non-local interactions, which is coherent with this observation. Therefore, the difference between log-lattices simulations and DNS could be explained by differences in the amount of non-local interactions.

## Acknowledgments

This work received funding from the Ecole Polytechnique, from ANR TILT grant agreement no. ANR-20-CE30-0035, and from ANR BANG grant agreement no. ANR-22-CE30-0025. CC is thankful for the financial support from CEA during his visit to Paris-Saclay, where this work was elaborated.

## References

[1] Uriel Frisch and Rudolf Morf. Intermittency in nonlinear dynamics and singularities at complex times. *Phys. Rev. A*, 23:2673–2705, May 1981.

[2] L. Onsager. Statistical hydrodynamics. *Il Nuovo Cimento (1943-1954)*, 6(2):279–287, 1949.

[3] Philip Isett. A proof of Onsager's conjecture. *Annals of Mathematics*, 188(3):871 – 963, 2018.

[4] G. L. Eyink. Turbulence Theory. http://www.ams.jhu.edu/ eyink/Turbulence/notes/, 2007-2008. course notes, The Johns Hopkins University,.

[5] J-D. Fournier and U. Frisch. L'équation de burgers déterministe et statistique. *Journal de Mécanique Théorique et Appliquée*, 2(5):699–750, 1983.

[6] D Senouf, R Caflisch, and N Ercolani. Pole dynamics and oscillations for the complex burgers equation in the small-dispersion limit. *Nonlinearity*, 9(6):1671–1702, nov 1996.

[7] F. Calogero. Motion of poles and zeros of special solutions of nonlinear and linear partial differential equations and related solvable many-body problems. *Il Nuovo Cimento B (1971-1996)*, 43:177–241, 1978.

[8] Michael Siegel and RE Caflisch. Calculation of complex singular solutions to the 3d incompressible euler equations. *Physica D: Nonlinear Phenomena*, 238(23-24):2368–2379, 2009.

[9] Ciro S Campolina and Alexei A Mailybaev. Fluid dynamics on logarithmic lattices. *Nonlinearity*, 34(7):4684–4715, jun 2021.

[10] C. Gloaguen, J. Léorat, A. Pouquet, and R. Grappin. A scalar model for mhd turbulence. *Physica D: Nonlinear Phenomena*, 17(2):154–182, 1985.

[11] Luca Biferale. Shell models of energy cascade in turbulence. *Annual Review of Fluid Mechanics*, 35:441–468, 2003.

[12] Ciro S. Campolina and Alexei A. Mailybaev. Chaotic blowup in the 3d incompressible euler equations on a logarithmic lattice. *Phys. Rev. Lett.*, 121:064501, Aug 2018.

[13] Catherine Sulem, Pierre-Louis Sulem, and Hélène Frisch. Tracing complex singularities with spectral methods. *Journal of Computational Physics*, 50(1):138–161, 1983.

[14] C. S. Campolina. Fluid Dynamics on Logarithmic Lattices and Singularities of Euler Flow. Master's Thesis, Instituto de Matemática Pura e Aplicada, 2019.

[15] V. N. Desnyansky and E. A. Novikov. The evolution of turbulence spectra to the similarity regime. *Izv. Akad. Nauk SSSR, Fiz. Atmos. Okeana*, 10:127–136, 1974.

[16] V. S. L'vov, E. Podivilov, A. Pomyalov, I. Procaccia, and D. Vandembroucq. Improved shell model of turbulence. *Phys. Rev. E*, 58(2):1811, 1998.

[17] Alexey Cheskidov. Blow-up in finite time for the dyadic model of the Navier-Stokes equations. *Transactions of the American Mathematical Society*, 360(10):5101–5120, 2008.

[18] Nets Katz and Nataša Pavlović. Finite time blow-up for a dyadic model of the euler equations. *Transactions of the American Mathematical Society*, 357(2):695–708, 2005.

[19] Peter Constantin, Boris Levant, and Edriss S Titi. Analytic study of shell models of turbulence. *Physica D: Nonlinear Phenomena*, 219(2):120–141, 2006.

[20] Peter Constantin, Boris Levant, and Edriss S. Titi. Regularity of inviscid shell models of turbulence. *Phys. Rev. E*, 75:016304, Jan 2007.

[21] Alexei A Mailybaev. Spontaneously stochastic solutions in one-dimensional inviscid systems. *Nonlinearity*, 29(8):2238, 2016.

[22] Thierry Dombre and Jean-Louis Gilson. Intermittency, chaos and singular fluctuations in the mixed Obukhov-Novikov shell model of turbulence. *Physica D: Nonlinear Phenomena*, 111(1-4):265–287, 1998.

[23] Alexei A Mailybaev. Bifurcations of blowup in inviscid shell models of convective turbulence. *Nonlinearity*, 26(4):1105, 2013.

[24] Côme Fontaine, Malo Tarpin, Freddy Bouchet, and Léonie Canet. Functional renormalisation group approach to shell models of turbulence, 2022.

[25] Alexey Cheskidov. Blow-up in finite time for the dyadic model of the navier-stokes equations. *Transactions of the American Mathematical Society*, 360(10):5101–5120, 2008.

[26] A. Barral and B. Dubrulle. Asymptotic ultimate regime of homogeneous rayleigh-bénard convection on logarithmic lattices. *J. Fluid Mech.*, x(xx):submitted, 2022.

[27] P. Orlandi, S. Pirozzoli, and G. F. Carnevale. Vortex events in Euler and Navier-Stokes simulations with smooth initial conditions. *Journal of Fluid Mechanics*, 690:288–320, 2012.

[28] Miguel D. Bustamante and Marc Brachet. Interplay between the beale-kato-majda theorem and the analyticity-strip method to investigate numerically the incompressible euler singularity problem. *Phys. Rev. E*, 86:066302, Dec 2012.

[29] Niklas Fehn, Martin Kronbichler, Peter Munch, and Wolfgang A. Wall. Numerical evidence of anomalous energy dissipation in incompressible Euler flows: towards grid-converged results for the inviscid Taylor-Green problem. *Journal of Fluid Mechanics*, 932:A40, 2022.

[30] Yves Pomeau. On the self-similar solution to the euler equations for an incompressible fluid in three dimensions. *Comptes Rendus Mécanique*, 346(3):184–197, 2018. The legacy of Jean-Jacques Moreau in mechanics / L'héritage de Jean-Jacques Moreau en mécanique.

[31] Victor Yakhot and Steven A. Orszag. Renormalization-group analysis of turbulence. *Phys. Rev. Lett.*, 57:1722–1724, Oct 1986.

[32] J-P. Laval, B. Dubrulle, and S. Nazarenko. Nonlocality and intermittency in three-dimensional turbulence. *Physics of Fluids*, 13(7):1995–2012, 2001.

[33] Sai Swetha Venkata Kolluru, Puneet Sharma, and Rahul Pandit. Insights from a pseudospectral study of a potentially singular solution of the three-dimensional axisymmetric incompressible euler equation. *Phys. Rev. E*, 105:065107, Jun 2022.

[34] Guo Luo and Thomas Y. Hou. Potentially singular solutions of the 3d axisymmetric euler equations. *Proceedings of the National Academy of Sciences*, 111(36):12968–12973, 2014.

[35] M. E. Brachet, M. Meneguzzi, A. Vincent, H. Politano, and P. L. Sulem. Numerical evidence of smooth self?similar dynamics and possibility of subsequent collapse for three?dimensional ideal flows. *Physics of Fluids A: Fluid Dynamics*, 4(12):2845–2854, 1992.

[36] Bérengère Dubrulle. Multi-fractality, universality and singularity in turbulence. *Fractal and Fractional*, 6(10), 2022.

[37] Dhawal Buaria, Alain Pumir, Eberhard Bodenschatz, and P K Yeung. Extreme velocity gradients in turbulent flows. *New Journal of Physics*, 21(4):043004, apr 2019.

## 5.3 Reversible Navier-Stokes equation on logarithmic lattices

# Reversible Navier-Stokes equation on logarithmic lattices

Guillaume COSTA, Amaury BARRAL, and Bérengère DUBRULLE*
*Université Paris-Saclay, CEA, CNRS, SPEC, 91191, Gif-sur-Yvette, France.*
(Dated: June 20, 2023)

The three-dimensional Reversible Navier-Stokes (RNS) equations are a modification of the dissipative Navier-Stokes (NS) equations, first introduced by [1], in which the energy or the enstrophy is kept constant by adjusting the viscosity over time. Spectral direct numerical simulations of this model were performed by [2, 3]. Here we consider a new non-linear, forced reversible system obtained by projecting RNS equations on a log-lattice rather than on a linearly spaced grid in Fourier space, as is done in regular spectral numerical simulations. We perform numerical simulations of the system at extremely large resolutions, allowing us to explore regimes of parameters that were out of reach of the direct numerical simulations of [2]. Using the non-dimensionalized forcing as a control parameter, and the square root of enstrophy as the order parameter, we confirm the existence of a second order phase transition well described by a mean field Landau theory. The log-lattice projection allows us to probe the impact of the resolution, highlighting an imperfect transition at small resolutions with exponents differing from the mean field predictions. Our findings are in qualitative agreement with predictions of a 1D non-linear diffusive model, the reversible Leith model of turbulence. We then compare the statistics of the solutions of RNS and NS, in order to shed light on an adaptation of the Gallavotti conjecture, in which there is equivalence of statistics between the reversible and irreversible models, [1] to the case where our reversible model conserves either the enstrophy or the energy. We deduce the conditions in which the two are equivalent. Our results support the validity of the conjecture and represent an instance of non-equilibrium system where ensemble equivalence holds for mean quantities.

## I. INTRODUCTION

In an out-of-equilibrium statistical mechanical system, achieving a steady state requires a balance between energy injection and energy dissipation. One practical example of such a system can be found in fluid mechanics, where a large-scale forcing drives a system out of equilibrium. To attain a steady state, the system must dissipate the excess energy. Such dissipation is ensured by a viscous term acting as a thermostat. This system is described by the Navier-Stokes equations (NSE), which are symmetric by time-reversal in the unforced, inviscid limit. However, the presence of the viscous term breaks this time-reversal symmetry of the NS equations . When the fluid is laminar, the resulting energy dissipation is proportional to the viscosity. In the turbulent case, however, the mean dissipation becomes independent of the viscosity [4–6] suggesting a spontaneous breaking of the time-reversal symmetry. To study the validity of such an assumption, one can restore time-reversal symmetry by transforming the usual viscosity, $\nu$, into a quantity that is odd under time reversal. There are numerous ways to do this, but the most interesting procedure is due to [1], who suggested to monitor $\nu$ so as to conserve at each time a macroscopic observable $\mathcal{G}$ (such as enstrophy [1, 3] or kinetic energy [2]). Besides spontaneous symmetry breaking, this procedure allows investigation of two important questions in the context of out-of-equilibrium physics: (i) to which extent can a reversible model describe the irreversible dynamics? (ii) does the statistics of the reversible model depend on the conserved quantity? This last question refers to the possible generalization of the notion of "ensemble equivalence in equilibrium statistical mechanics", by which a system is equivalently described by micro-canonical (conserved energy) or canonical (conserved temperature) ensembles. In the present case, the system is out-of-equilibrium due to the combination of forcing and dissipation. The equivalence between both constant energy and constant enstrophy ensemble would then be a natural generalization of ensemble equivalence in equilibrium statistical mechanics.

These questions have been previously investigated via direct numerical simulations (DNS) of the reversible Navier-Stokes equations (RNS). In the case of conserved energy, Shukla et al. [2] showed that the system undergoes a second order phase transition, with exponents in quantitative agreement with that of a Landau mean field theory [2]. Before the transition, the system is in a warm phase, where the system is thermalized at small scale. After the transition, the system is in a over-damped regime, where the system dynamics are dominated by viscous dissipation. At the transition, the system is in a turbulent state, that bears many similarities with the stationary state of the irreversible

*Electronic address: berengere.dubrulle@cea.fr

equation, hinting at a possible positive answer to question (i) in this case. Question (ii), which has never been investigated before, will be addressed in this article.

However, there are a number of issues that could not be addressed due to the massive numerical costs of directly simulating the NSE. For example, it was not possible to study the importance of the resolution on the transition or the convergency of the equivalence of ensemble. In addition, some scaling properties of the dynamics at the transition could not be investigated, as the inertial range was not wide enough due to the difficulty of accommodating very small values of $\nu$ with DNS.

Motivated by these observations, we decided to extend the study of Shukla et al. [2] and Margazoglou [3] to a case where the RNS equations are projected on a log-lattice rather than on a linearly spaced grid in Fourier space. The resulting equations correspond to a new non-linear, forced reversible system that we name hereafter Log-Lattice Reversible Navier-Stokes (LLRNS). We know from the work of Campolina & Mailybaev [7] that this projection allows simulations with a large resolution, at a moderate numerical cost, while the corresponding model displays most symmetries and conservation laws of the classical model on a linear grid (used for DNS with spectral methods). Moreover, the log-lattice projection makes it possible to adapt the resolution to monitor very low values of the viscosity, as already proved by [8] on the blow-up problem for the Euler equations.

The outline of the paper is as follow: we first introduce the RNS equations, followed by the projection on log-lattices that we will be using to define our LLRNS model. We display our choice regarding the numerical procedure, and briefly present the tools that will be useful to analyze our results, including the reversible Leith model, already used in [2]. We then go through the results and discuss the presence of a second order transition in LLRNS and extract critical exponents. In this section, we also study the ansatz of the structure functions of LLRNS, comparing them to the case of LLNSE (Log-Lattice Navier-Stokes Equations), where the viscosity is kept constant. We then perform a comparison between energy transfer in LLRNS and the reversible Leith model, based on a non-linear diffusion equation in Fourier space. Finally, we study to what extent the equivalence conjectures postulated by Gallavotti ([1, 3]) for RNS and NS equations hold in the framework of log-lattices for two conservation schemes: one energy conserving and one enstrophy conserving.

## II. FRAMEWORK: REVERSIBLE NAVIER-STOKES AND LOG-LATTICES PROJECTIONS

### A. Reversible Navier-Stokes

The Navier-Stokes equations describing a fluid of viscosity $\nu$, subject to a force $\boldsymbol{f}$, are given by:

$$\partial_t \boldsymbol{u} + (\boldsymbol{u}\cdot\boldsymbol{\nabla})\boldsymbol{u} = -\boldsymbol{\nabla} p + \nu\boldsymbol{\Delta}\boldsymbol{u} + \boldsymbol{f}, \tag{1}$$

where $\mathbf{u}$ is the velocity, $p$ is the pressure, and we have set the constant density equal to 1. Due to the presence of the dissipative term $\nu\boldsymbol{\Delta}\boldsymbol{u}$, the dynamics induced are clearly irreversible as (1) is not left-invariant under the time-reversal symmetry:

$$\mathcal{T} : t \to -t; \boldsymbol{u} \to -\boldsymbol{u}; p \to p. \tag{2}$$

This is true even in the presence of a force that is symmetric by time-reversal (which will be the case of every forcing used in this paper).

Following the work of Shukla et al. [2], we introduce a reversible version of the NSE by defining a (time dependent) reversible viscosity $\nu_r$, which conserves the total kinetic energy $E = \frac{1}{2}\int_{\mathcal{D}} \|\boldsymbol{u}\|_2^2 \,\mathrm{d}\boldsymbol{x}$ over our domain $\mathcal{D}$. The expression of $\nu_r$ can be derived from an energy budget under the constraint $\partial_t E = 0$:

$$\nu_r = \frac{\int_{\mathcal{D}} \boldsymbol{f}\cdot\boldsymbol{u}\ \mathrm{d}\boldsymbol{x}}{\int_{\mathcal{D}} \|\boldsymbol{\nabla}\times\boldsymbol{u}\|_2^2 \,\mathrm{d}\boldsymbol{x}}. \tag{3}$$

It is also possible to define another framework, where the viscosity is still time-dependent, but adjusted to conserve the total enstrophy $\partial_t\Omega = 0$, where $\Omega = \int_{\mathcal{D}} \|\nabla\times\boldsymbol{u}\|_2^2 \,\mathrm{d}\boldsymbol{x}$ [1]. The corresponding expression of the viscosity is obtained by taking the Fourier transform of (1), multiplying by $k^2\hat{u}_i$ and summing over $\boldsymbol{k}$, leading to :

$$\nu_r(\boldsymbol{u}) = \frac{\sum_{\boldsymbol{k}} \|\boldsymbol{k}\|_2^2\, \hat{\boldsymbol{f}}_{\boldsymbol{k}}\cdot\hat{\boldsymbol{u}}_{-\boldsymbol{k}} + \Lambda(\hat{\boldsymbol{u}})}{\sum_{\boldsymbol{k}} \|\boldsymbol{k}\|_2^4\, \|\hat{\boldsymbol{u}}_{\boldsymbol{k}}\|_2^2}, \tag{4}$$

where $\Lambda(\hat{\boldsymbol{u}})$ comes from the non-linear term of the Navier-Stokes equations. While it is yet unclear whether viscid or inviscid Navier-Stokes equations with regular initial conditions and finite energy are subject to a finite-time blow-up, it is known that controlling the enstrophy is sufficient to prevent a blow-up ([9]). Therefore, the enstrophy conserving scheme is associated with more regular solutions than the energy conserving scheme. In particular, it rules out a spontaneous breaking of the time-reversal symmetry mediated by dissipating singularities as conjectured by Onsager [4]. Therefore, it is interesting to explore the properties of both conservation schemes.

In the first part of this paper, we mainly focus on the conserved energy scheme, where an interesting phase transition takes place. In the second part, we analyze the Gallavotti conjecture using both conservation procedures.

Replacing the usual viscosity $\nu$ with its "reversible" counterpart $\nu_r$ in (1), we obtain the reversible Navier-Stokes (RNS) equations:

$$\partial_t \boldsymbol{u} + (\boldsymbol{u}\cdot\boldsymbol{\nabla})\boldsymbol{u} = -\boldsymbol{\nabla}p + \nu_r \boldsymbol{\Delta}\boldsymbol{u} + \boldsymbol{f}. \tag{5}$$

Taking into account that $\boldsymbol{f}$ is invariant by the time-reversal symmetry, it is then easy to check that the whole equation is also invariant by the symmetry (2), hence its name.

Since the viscosity is no longer a constant, the Reynolds number $\mathrm{Re} = \frac{LU}{\nu}$ is no longer as a valid control parameter. Therefore, in the fixed energy case we introduce the dimensionless control parameter $\mathcal{R}_\mathrm{r}$ [2] given by:

$$\mathcal{R}_\mathrm{r} = \frac{f_0}{E_0 k_f} \tag{6}$$

where $f_0$ is the forcing amplitude, $k_f = \frac{2\pi}{L_f}$ the wavenumber at which the forcing occurs and $E_0$ the constant, total kinetic energy.

### B. LLRNS model on log-lattices

Our LLRNS model is obtained by projecting the reversible equations (5) onto a discretized logarithmic grid, composed of exponentially spaced modes (Fig. 1):

$$k = k_0 \lambda^n,$$

where $\lambda$ is the log-lattice spacing parameter. This construction is detailed in Campolina & Mailybaev [7, 8]. We start by taking the Fourier transform of Eq. 5, to get the RNS equations in spectral space:

$$\partial_t \hat{u}_i + \boldsymbol{i} k_j \hat{u}_j * \hat{u}_i = -\boldsymbol{i} k_i \hat{p} - \nu_r k_j k_j \hat{u}_i + \hat{f}_i, \tag{7}$$

where Einstein summation over repeated indices is used, $\boldsymbol{i}$ is the square root of $-1$, $k_i$ is the $i^{th}$ component of the wavenumber $\mathbf{k} = (m,n,q)\mathbf{k}_0$ , $\hat{g}$ is the Fourier transform of $g$, and $*$ is the convolution product which couples modes in triadic interactions such that $\boldsymbol{k} = \boldsymbol{p} + \boldsymbol{q}$.

We then project this equation onto the log-lattice. For this, we consider from now on that the velocity modes $\hat{u}_i$ only depend on the wavevectors on the log-lattice. This projection is then valid provided that the convolution operator is "well-defined", i.e. that it respects the symmetries of a convolution operator and has a nonempty set of triadic interactions. We thus require that

$$\lambda^m = \lambda^n + \lambda^q,\ (\mathrm{m,n,q}) \in \mathbb{Z}^3 \tag{8}$$

admits solutions, which restricts the values of $\lambda$ to three families of solutions, each having $z$ interactions in $D$ dimensions:

- $\lambda = 2$ ($z = 3^D$).
- $\lambda = \sigma \approx 1.325$, the plastic number ($z = 12^D$)
- $\lambda$ such that $1 = \lambda^b - \lambda^a$ for some integers $0 < a < b$. $(a,b) \neq (1,3),(4,5)$ with $\gcd(a,b) = 1$ ($z = 6^D$).

Note that for the lowest possible values of $a$ and $b$, which is $(1,2)$, $\lambda$ is the golden number ($\phi \approx 1.618$). The 2D geometry of such a lattice is shown in Fig. 1.

Besides the convolution product, log-lattices are also endowed with a scalar product given by:

$$(f,g) = \Re\left(\sum_{\boldsymbol{k}} f(\boldsymbol{k})\overline{g(\boldsymbol{k})}\right). \tag{9}$$

Our LLRNS model is then defined by the set of ODE's (7), with viscosity being given by Eqs. (3) or (4), and by the choice of $\lambda$ among the possible values that follow from Eq. (8). Each configuration corresponds to a reversible non-linear out-of-equilibrium model whose conservation laws and symmetries are very close to that of the RNS equations.

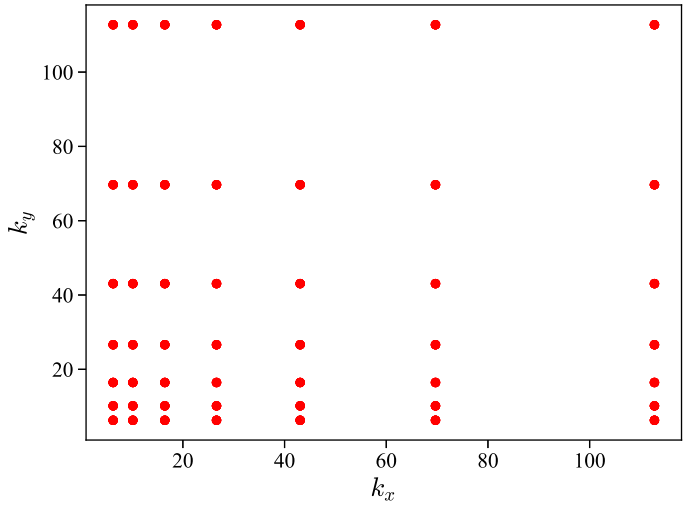


FIG. 1: **Geometry of the logarithmic lattices.** Example of modes on a 2D log-lattice with a spacing parameter $\lambda = \phi \approx 1.618$.

### C. Quantities of interest

#### 1. *Generic quantities*

In the fixed energy case, the enstrophy $\Omega$ and the reversible viscosity $\nu_r$ are good candidates for the order parameter, while $\mathcal{R}_\mathrm{r}$ (6) is a good control parameter.

Throughout our study, we can compute two large scale quantities of interest:

- The energy spectrum $E(k,t) = \dfrac{1}{(\lambda-1)kN_k} \displaystyle\sum_{k\leq|\boldsymbol{k'}|<\lambda k} \|\hat{\boldsymbol{u}}(\boldsymbol{k'},t)\|_2^2$, where $N_k$ is the number of points in the shell of radius $k$ (proportional to $\log^2(k)$).
- The total enstrophy $\Omega(t) = \displaystyle\sum_k k^2 E(k,t)$.

We also compute the mean energy transfer at scale $k$ through:

$$\Pi(k) = \langle -2\Im(\boldsymbol{u}, \boldsymbol{k}\cdot\boldsymbol{u} * \boldsymbol{u})\rangle\,, \tag{10}$$

and an ansatz of the structure functions, using the following convention:

$$F_q(k) = \langle \|\hat{\boldsymbol{u}}(\boldsymbol{k},t)\|_2^q\rangle\,, \tag{11}$$

where $\|\mathbf{k}\|_2 = k$ and $\langle\cdot\rangle$ refers to temporal averages over shells of radius $k$.

#### 2. *Leith model*

The Leith model is a toy model based on a non-linear diffusive equation, which in its inviscid description [10], approximates the dynamics of the energy spectrum of a Euler flow. it exhibits both an inertial domain with scaling $k^{-5/3}$ and a quasi-thermalization at small scales characterized by a Gibbsian equipartition with scaling $E(k,t) \propto k^2$. Such model is described by a well-chosen second order diffusive operator:

$$\begin{aligned}\partial_t E(k,t) &= -\,\partial_k \Pi(k,t) - \nu k^2 E(k,t)\\ \Pi(k,t) &= -\,C k^{11/2}\sqrt{E(k,t)}\partial_k\left(\frac{E(k,t)}{k^2}\right).\end{aligned}$$

Note that $C$ is a dimensional constant that we set to 1 in this article.

This model has been adapted by [2] to accommodate reversible viscosities by changing $\nu$ into $\nu_r$, given by Eq. 3. Its solutions confirm the existence of a mean field second order phase transition, albeit for an order parameter equal to $\sqrt{\Omega}$. Moreover, it showed that the resolution of the simulation could have a large impact on the nature of the transition, the latter becoming imperfect as the resolution is decreased. In this article, we adopt the same convention for the dimensionless number representing the influence of resolution, namely $h = k_0/k_{\max}$, where $k_0$ and $k_{\max}$ are respectively the minimum and maximum wave number in our simulation.

In our system, the thermalization is no longer associated with an energy spectrum following $E(k,t) \propto k^2$ but instead to a $k^{-1}$ behavior. It is then necessary to adapt the previous definition of the energy transfer to our system:

$$\Pi(k,t) = -Ck^{5/2}\sqrt{E(k,t)}\partial_k\left(kE(k,t)\right).$$

Solving $\partial_k\Pi(k,t) = 0$, we obtain an energy spectrum of the form $E(k,t) \propto (Ak^{-5/2} + Bk^{-3/2})^{2/3}$, where $(A,B)$ are two constants taking into account boundary conditions and governing the scale at which the thermalization occurs.

### D. Numerical framework

#### 1. *Integration scheme*

We integrate (7) using a three-step method. Starting from the initial conditions $\hat{u}(t)$, we first solve the equation without any viscosity using an explicit adaptive Runge-Kutta method of order 4–5 via the DOPRI5 solver from the python library Scipy. The equation solved is

$$\partial_t \hat{u}_i = P_{ij}\left(-\boldsymbol{i}k_q\hat{u}_q * \hat{u}_j + \hat{f}_j\right), \tag{12}$$

where $P_{ij} = \delta_{ij} - \frac{k_i k_j}{k^2}$ accounts for the pressure term under zero divergence hypothesis. This gives us $\hat{u}(t+dt)_{\nu_r=0}$ where $dt$ is the time-step. To maintain a very high degree of accuracy for our conservation laws, we do not use the expression for reversible viscosity given by Eq. 3 or 4, but instead compute in a second step the reversible viscosity $\nu_r$ by numerically solving $\mathcal{G}(\nu_r, t+dt) = \mathcal{G}_0$, where $\mathcal{G}$ stands for the conserved quantity. The final step is to apply the chosen viscosity by a technique similar to viscous splitting: $\hat{u}(t+dt) = \hat{u}(t+dt)_{\nu_r=0}e^{-\nu_r k^2 dt}$.

We provide in Appendix A a comparison between this method and direct computation using the analytical expression of $\nu_r$ Eq. 3 in the Runge-Kutta solver.

#### 2. *Numerical details*

The minimum wavenumber of the grid is set to $k_{\min} = 2\pi$. The maximum grid size $N = 20^3$ is chosen such the hydrodynamic branch is well-enough resolved. We set a maximum time-step $dt = 0.005$, in order to avoid under-resolving some very stiff moments when the viscositiy tends to zero. As a result, whenever the viscosity is not very small, the time-step is a constant equal to $dt$.

The equation $\mathcal{G}(\nu_r, t+dt) = \mathcal{G}_0$ is solved such that $\mathcal{G}$ is conserved with floating-point accuracy: $|\,\mathcal{G}(t+dt) - \mathcal{G}_0\,| < 10^{-14}\,\mathcal{G}_0$.

We use the following initial conditions, taken from [2]:

$$\begin{aligned}
\hat{u}_x(\mathbf{k}) &= U(\boldsymbol{k}),\\
\hat{u}_y(\mathbf{k}) &= -\hat{u}_x(\boldsymbol{k})\frac{k_x}{k_y},\\
\hat{u}_z(\mathbf{k}) &= 0.
\end{aligned} \tag{13}$$

where $U$ is an initial field, with initial energy centered on the large scales.

The forcing term $\boldsymbol{f}$ is a constant field of norm $f_0$, symmetric by time-reversal, with non-zero contributions for $\boldsymbol{k}$ such that $15 < \|\boldsymbol{k}\|_2 < 16$:

$$\begin{aligned}
\hat{f}_x(\mathbf{k}) &= f_0 \text{ if } 15 < \|\boldsymbol{k}\|_2 < 16 \text{ else } 0,\\
\hat{f}_y(\mathbf{k}) &= f_0 \text{ if } 15 < \|\boldsymbol{k}\|_2 < 16 \text{ else } 0,\\
\hat{f}_z(\mathbf{k}) &= 0.
\end{aligned} \tag{14}$$

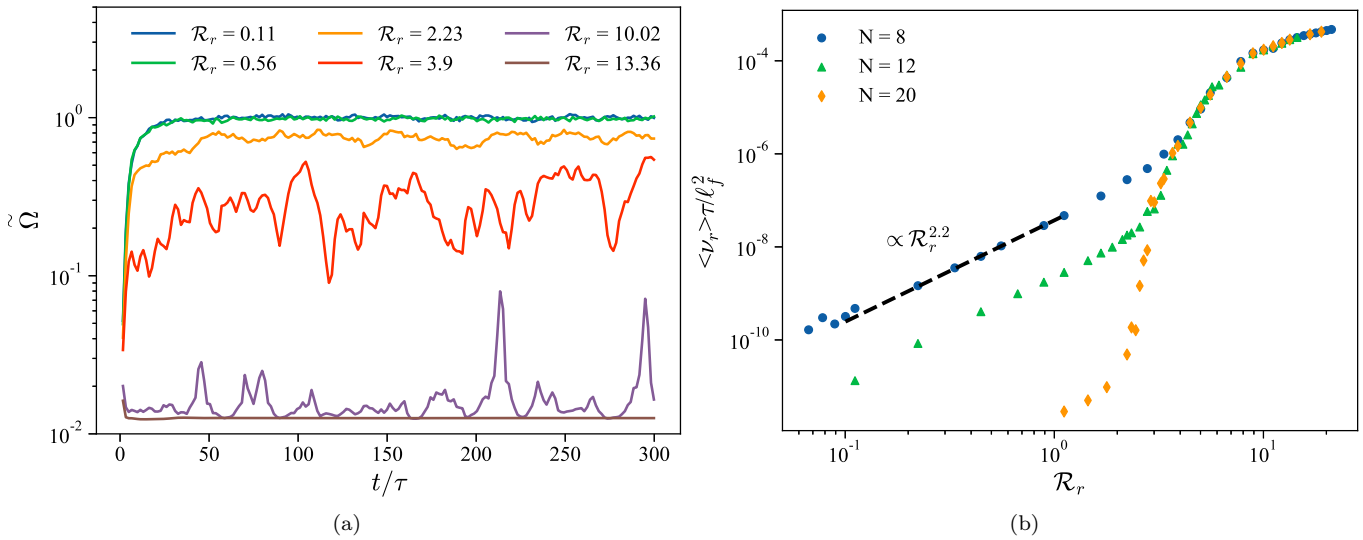


FIG. 2: **Behaviors of order parameters using $\lambda = \phi$.** (2a) Time series of the normalized enstrophy $\widetilde{\Omega}$ for different values of the control parameter $\mathcal{R}_\mathrm{r}$, with $N = 8^3$. (2b) Time averaged reversible viscosity as a function of the control parameter $\mathcal{R}_\mathrm{r}$. The dashed line represents a linear fitting in the warm regime, exhibiting a power-law behavior. The dimensionless time is $\tau = \ell_f/\sqrt{E_0}$, where $\ell_f$ is the scale at which the forcing occurs.

Unless written otherwise, the log-lattice spacing parameter is $\lambda = \phi$. The range of parameters studied is chosen such that it is possible to observe the two regimes previously observed by Shukla et al.

All the simulations ran on one core of a consumer-grade computer, for a few ($< 4$) CPU days at most.

## III. RESULTS

All the results presented in this paper before section III G are obtained in the conserved energy case, i.e. for $\mathcal{G} = E$.

### A. Dynamics

Fig. 2a illustrates the time-evolution of the normalized enstrophy $\widetilde{\Omega}$ (properly defined in Appendix. B) for many modes $N = 20^3$. As in [2], different regimes are observed. At low values of the control parameter $\mathcal{R}_\mathrm{r}$, the solutions converges to a constant mean value of $\widetilde{\Omega}$ with little to no fluctuations. This regime is associated with a lower branch of mean viscosity $\langle \nu_r \rangle$ (Fig. 2b) that develops a power-law $\langle \nu_r \rangle \propto {\mathcal{R}_\mathrm{r}}^{\alpha}$, where $\alpha \approx 2$. This result was already obtained in DNS [2], and can be justified using a Kubo fluctuation dissipation theorem, that also applies on log-lattices. As the size of the grid increases, it becomes harder to reach the limit $\mathcal{R}_\mathrm{r} \to 0$ as the low values of viscosity require smaller time-steps. This limit is associated to a thermalized steady state, as it is characterized by a vanishing energy injection and therefore, in order to conserve the energy, to a vanishing viscosity.

As $\mathcal{R}_\mathrm{r}$ increases, the system fluctuations continually increase up to a certain value of ${\mathcal{R}_\mathrm{r}}^*$ at which fluctuations reach their maximum. Beyond this critical value, fluctuations slowly decrease to zero, towards a lower branch of enstrophy (Fig. 2a). This branch corresponds to a branch of large viscosity (Fig. 2b). Before vanishing completely, the enstrophy fluctuations appear as "bursts" of enstrophy.

Note that defined in such a way, ${\mathcal{R}_\mathrm{r}}^*$ depends on the resolution N. Indeed, both the value of $\mathcal{R}_\mathrm{r}$ at which the system leaves the collapsed branch (Fig. 2b) and the location of maximum fluctuations (Fig. 3d) clearly depends on the resolution. Also note that both definition of ${\mathcal{R}_\mathrm{r}}^*$ (from fluctuations and the asymptote in Fig. 2b) and are equivalent in the limit $N \to \infty$ as the thermalized branch can never be reached.

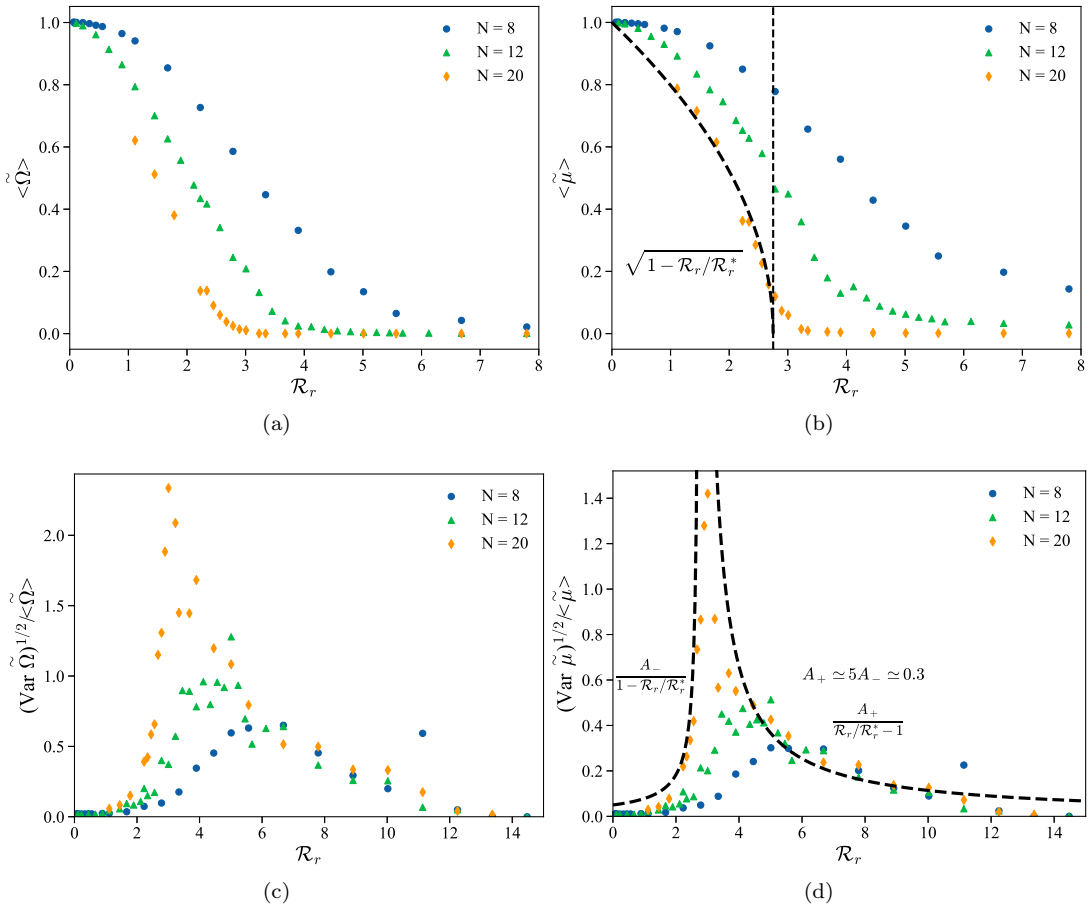


FIG. 3: **Second order transition for $\lambda = \phi$.** Evolution of (3a) the renormalized mean enstrophy and (3b) $\widetilde{\mu}$ as a function of $\mathcal{R}_\mathrm{r}$. Variance of (3c) the renormalized enstrophy and of (3d) $\widetilde{\mu}$ as a function of $\mathcal{R}_\mathrm{r}$. The dashed lines associated with the equations corresponds to a Landau mean field formulation of the phase transition.

### B. Phase transitions

In Shukla et al. [2], the various regimes of the enstrophy dynamics are associated with the existence of a second order phase transition, described by a Landau mean field theory. Specifically, the time-averaged normalized enstrophy $\left\langle \widetilde{\Omega} \right\rangle$ exhibits a power-law $\left\langle \widetilde{\Omega} \right\rangle = \left(1 - \frac{\mathcal{R}_\mathrm{r}}{{\mathcal{R}_\mathrm{r}}^*}\right)^\beta$, with $\beta \simeq 0.5$, while the normalized standard deviation of the renormalized enstrophy $\sigma_{\widetilde{\Omega}}$ presents a divergence around ${\mathcal{R}_\mathrm{r}}^*$, following a power-law $\sigma_{\widetilde{\Omega}} = \left(1 - \frac{\mathcal{R}_\mathrm{r}}{{\mathcal{R}_\mathrm{r}}^*}\right)^{-\gamma}$ with $\gamma \simeq 1$. As it is possible to observe different values of $\gamma$ on each side of the transition, we define $\gamma_l$ and $\gamma_r$ where $l$ and $r$ stand for left and right, respectively.

In our case, we also observe at $N = 20^3$ behaviors for the enstrophy that are reminiscent of a second-order phase transition, albeit with exponents that do not correspond to the mean field description (Fig. 3a & 3c and Tab. I). Indeed, we observe a power-law with exponent $\beta \simeq 1$, which is larger than its mean-field version (Fig. 3a). In the case of the variance, we observe a divergence at ${\mathcal{R}_\mathrm{r}}^*$ with a critical exponent corresponding to the mean field value $\gamma_l = 1$, like in [2].

Our results show that, while the nature of the transition is unaffected by the details of the interactions between modes, the value of the critical exponents depends on those details. One should see Tab. I for different values of $\lambda$, and recall that on log-lattices, different values of $\lambda$ correspond to different numbers of local interactions.

In that respect, it is interesting to see whether our result fits in the cruder description of the interactions provided by the Leith model. In this model, the mean-field description is found by taking the square root of the enstrophy

TABLE I: **Critical exponents of $\widetilde{\Omega}$ as a function of h.** For $\lambda = 2$, values of $\gamma_r$ were not extracted as the variance does not vanish, but converges to a constant on a domain extending quite far away from ${\mathcal{R}_\mathrm{r}}^*$.

| $\lambda$ | $N$ | $h$ | $\beta$ | $\gamma_r$ | $\gamma_l$ |
|---|---|---|---|---|---|
| 2 | $8^3$ | $7 \cdot 10^{-3}$ | - | - | - |
| | $12^3$ | $4 \cdot 10^{-4}$ | $\simeq 0.8$ | - | 1.6 |
| | $16^3$ | $3 \cdot 10^{-5}$ | $\simeq 1$ | - | 1.0 |
| $\phi$ | $8^3$ | $3 \cdot 10^{-2}$ | - | 1.0 | 2.2 |
| | $12^3$ | $5 \cdot 10^{-3}$ | $\simeq 0.5$ | 1.0 | 1.8 |
| | $20^3$ | $1 \cdot 10^{-4}$ | $\simeq 1$ | 1.0 | 1.0 |
| Shukla ([2]) | $128^3$ | $2.4 \cdot 10^{-2}$ | $\simeq 0.5$ | $\simeq 1$ | $\simeq 1$ |
| Landau Mean field | - | - | 0.5 | 1 | 1 |

TABLE II: **Critical exponents of $\widetilde{\mu}$ as a function of h.** Values of $\gamma_r$ were not extracted as the variance does not vanish, but converges to a constant on a domain extending quite far away from ${\mathcal{R}_\mathrm{r}}^*$.

| $\lambda$ | $N$ | $h$ | $\beta$ | $\gamma_r$ | $\gamma_l$ |
|---|---|---|---|---|---|
| 2 | $8^3$ | $7 \cdot 10^{-3}$ | - | - | - |
| | $12^3$ | $4 \cdot 10^{-4}$ | $\simeq 0.4$ | - | 1.6 |
| | $16^3$ | $3 \cdot 10^{-5}$ | $\simeq 0.5$ | - | 1.0 |
| $\phi$ | $8^3$ | $3 \cdot 10^{-2}$ | - | 1.0 | 1.6 |
| | $12^3$ | $5 \cdot 10^{-3}$ | $\simeq 0.27$ | 1.0 | 1.4 |
| | $20^3$ | $10^{-4}$ | $\simeq 0.5$ | 1.0 | 1.0 |

as an order parameter. In our case, upon defining $\widetilde{\mu} = \overset{\sim}{\Omega}^{1/2}$, we indeed observe a mean field behavior for $\left\langle \widetilde{\mu} \right\rangle$ in the limit of large grids $k_\mathrm{max} \to \infty$ (e.g. Fig. 3b & 3d). Its critical order parameters depend on the lattice spacing $\lambda$ as ${\mathcal{R}_\mathrm{r}}^* \approx 3.75$ for $\lambda = 2$ and ${\mathcal{R}_\mathrm{r}}^* \approx 2.75$ for $\lambda = \phi$. The computed exponents associated with this model are presented in Tab. II. Note however that the mean field description is not entirely valid in our model, as we do not observe the peculiar link between pre- and post-transitions prefactors: $A_+ = 2A_-$. Still, it seems that as the number of interactions grows (i.e. as $\lambda$ decreases), we are getting closer and closer to this description.

Finally, we stress that as soon as $\mathcal{R}_\mathrm{r} > {\mathcal{R}_\mathrm{r}}^*$, both the variance and the mean viscosity (Fig. 2b) become independent of the grid size. Therefore, only $\beta$ and $\gamma_l$ depend on $k_\mathrm{max}$.

### C. Characterizing the various phases with spectra

As shown in [2], the nature of the different phases before and after the transition can be elucidated by looking at energy spectra. Examples are provided in Fig. 4. Before the transition, we observe a spectrum that is characterized by two slopes: one at low wavenumbers, with an exponent close to $-5/3$ and one at large wavenumbers, with an exponent closer to $-1$. As already discussed in [7, 11], the $-1$ slope corresponds to thermalization on log-lattices, characterized by equipartition of energy among the modes. The $-5/3$ regime corresponds to a classical spectrum due to a positive flux of energy, as evidenced by the insert of Fig. 4b. We call this phase with a coexistence of two cascades the "warm cascade" regime. As $\mathcal{R}_\mathrm{r}$ decreases, the thermalized phase extends further towards lower $k$, and the pseudo-Kolmogorov phase disappears. Conversely, as $\mathcal{R}_\mathrm{r}$ increases, the thermalized phase progressively disappears, to leave room for an increasingly laminar state as the reversible viscosity increases. Such state is shown in Fig. 4b.

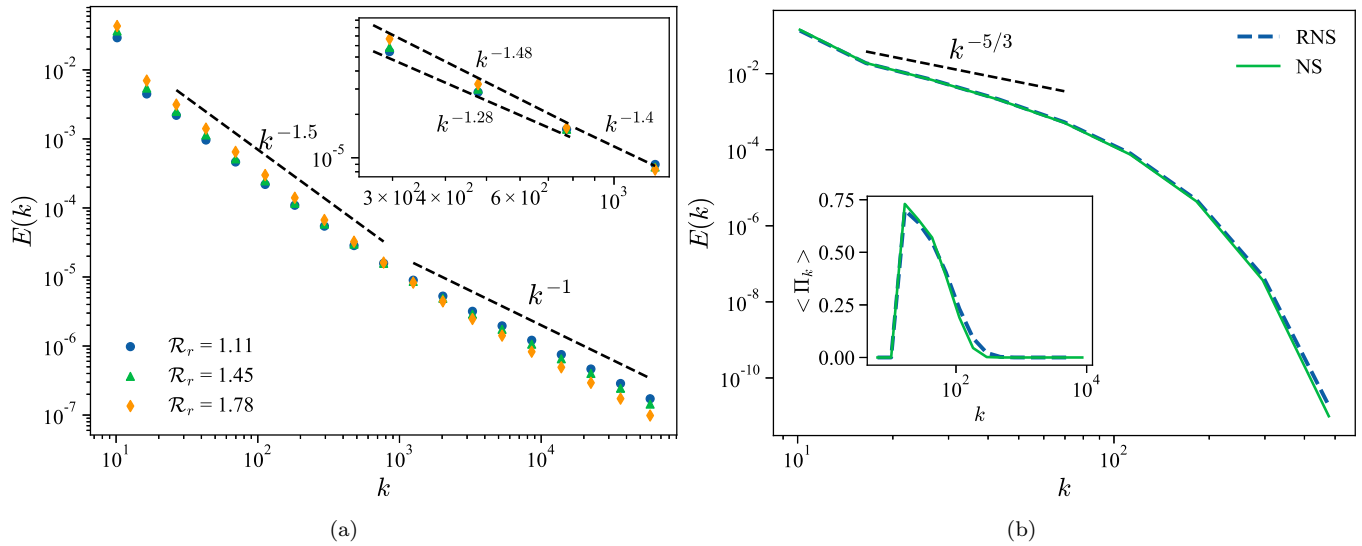


(a) (b)

FIG. 4: **Time averaged energy spectra vs $\mathcal{R}_r$, $\lambda = \phi$, $N = 20^3$ Modes**. (4a) Warm regime, with coexistence of two phases. The dotted line represents the slope of the two coexisting regime, a pseudo Kolmogorov regime at large scales and a thermalized regime at small scales exhibiting a -1 slope. The inset shows a zoom in the crossover area, highlighting the difference in slopes with respect to $\mathcal{R}_r$ associated to the contamination of the bigger scales by the thermalization. (4b) Laminar state, with dominant dissipative range, and no thermalization. The inset shows the energy transfer $\Pi_k$.

### D. Structure functions

The nature of the various phases can be further characterized using higher orders of the velocity field, via the structure functions (Eq. 11). In classical shell models, such structure functions are subject to intermittency, as they exhibit scaling laws $F_q(k) \sim k^{-\xi_q}$ that deviate from the monofractal behavior $\xi_q = q\xi_1$ [12–15].

In our case, it is difficult to measure the exponents of the structure functions for all phases: at large values of $\mathcal{R}_r$ the viscosity rises quickly, and the inertial range becomes very small. At small values of $\mathcal{R}_r$, the scaling laws are polluted by the coexistence of the pseudo-Kolmogorov regime and the thermalized state, as illustrated in Fig. 4a. This invalidates the classical method of computing exponents via extended self similarity [16] as the structure functions can present multiple slopes at different scales. We extracted exponents via the following method: we first determine the inertial range by computing the time-averaged energy transfer $\Pi_k$ through Eq. 10. Then, we define the inertial range as the range of wavenumber where it is flat. If this range is large enough (at least a decade), we fit the scaling exponents of the structure functions on this range only. This provides us with an unambiguous determination of $\xi_q$. The extracted exponents are shown in Fig. 5a, for value of $\mathcal{R}_r$ in various regimes, as illustrated in Fig. 5b.

In the limit of low $\mathcal{R}_r$, the $\xi_q$ exponents appear to be significantly lower than the usual exponents (Fig. 5, blue, green and orange curves). This phenomenon can be explained by the fact that, in such a limit, the system tends to follow equipartition, associated with an energy spectrum of $E(k) \sim k^{-1}$ (Fig. 4). This is indeed what we observe: as $\mathcal{R}_r$ gets closer to 0 a quasi-thermalized spectra appears, first at low scales, and then progresses towards the larger scales, impacting the slope even at larger scales (as illustrated in Fig. 4a and the inset of Fig. 5a). There is no intermittency in this regime, with all exponents aligning onto a perfect line. In the other limit, as $\mathcal{R}_r$ rises, the RNS exponents increase (Fig. 5). However, there is still no intermittency in this regime. To check whether it was a feature of the RNS system, we computed the same exponents from a simulation of NSE with fixed viscosity. The result is also shown in Fig. 5a (brown curve). We see that the resulting exponents are very close to the exponents we observe in RNS, reaching a quasi perfect agreement for both exponents and slope (Tab. III) located around the middle of the transition area.

This absence of intermittency is not surprising, as log-lattice models only consider local interactions. Such phenomenon was also observed in REWA models of turbulence, where intermittency decreases as the number of interactions decreases [17–19]. In contrast, intermittency has already been observed in various shell models such as SABRA or GOY models. In that case, it was observed (SABRA [20], GOY [21]) that the tuning of the free parameter controlling additional conservation can bring the system from a situation where the only fixed point is the K41 scaling (no intermittency) to a situation where the K41 scaling becomes unstable, leading to chaos and intermittency [21]. In our case, it is likely that with $\lambda = \phi$ we are in the first situation, with only one stable fixed point. It would be

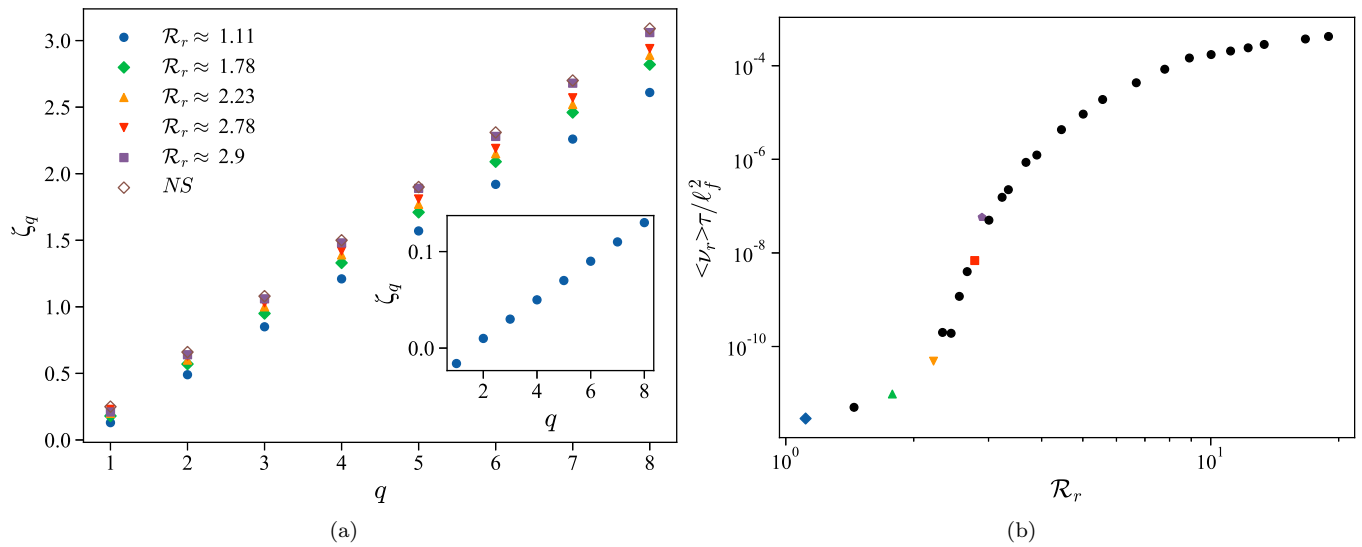


(a) (b)

FIG. 5: **Extracted exponents of the structure functions and localization in the transition for $\lambda = \phi$, $N = 20^3$ Modes.** Both figures share the same legend. (5a) Exponents of the structure function of order $q$ for various RNS simulations and comparison to a NS simulation. The inset presents the exponents, extracted at small scales, in the case of a quasi-thermalized state. (5b) Color coded version of the $\nu_r$ vs $\mathcal{R}_\mathrm{r}$ diagram, showing where the various results are located with respect to the transition. The color of the data points are the same as those from panel (a).

TABLE III: **Slopes of the exponents of the structure functions** for both RNS and NS equations. Values were extracted by fitting the structure functions in the inertial range, determined by the domain of constant energy transfer.

| Equation | RNS | | | | | NS |
|---|---|---|---|---|---|---|
| $\mathcal{R}_\mathrm{r}$ | 1.11 | 1.78 | 2.23 | 2.78 | 2.9 | - |
| Slopes | 0.36 | 0.38 | 0.4 | 0.4 | 0.42 | 0.42 |

interesting to check whether decreasing the value of $\lambda$ results in the loss of stability of the fixed point and appearance of intermittency. This is however beyond the scope of this article, and left for future work.

Note finally that in the log-lattices simulations, the usual Kolmogorov prediction $\xi_q \propto q/3$ does not hold. Indeed, even for NS equation, the slope is roughly equal to 0.42 (Tab. III).

### E. Universal and non universal laws

In previous sections, we described the dependence of $\langle\nu\rangle\,\tau/\ell_f^2$ (or $\left\langle\widetilde{\Omega}\right\rangle$) on $\mathcal{R}_\mathrm{r}$ for LLRNS models with constant energy. Surprisingly, such behavior extends to both LLRNS models with conserved enstrophy and to irreversible LL-Navier-Stokes models (Fig. 6) upon defining $\mathcal{R}_\mathrm{r} = \frac{f_0}{\langle E\rangle k_f}$. This property is interesting as it provides information on the steady state of the system, and on whether the system is well resolved. Indeed, if the system is under-resolved (i.e $k_\mathrm{max} \ll k_\eta$, $k_\eta$ being the Kolmogorov scale), it is characterized by a thermalization of the small scales, and corresponds to a state located before the transition at $\mathcal{R}_\mathrm{r} < \mathcal{R}_\mathrm{r}{}^*$, on the linear part of Fig. 6a.

However, neither the LLRNS with conserved enstrophy, nor the LL-Navier-Stokes model display the divergence of fluctuations observed in the LLRNS with fixed energy (see Fig. 3d). Indeed, the LL-Navier-Stokes model exhibits bounded values of energy and enstrophy fluctuations, as shown in Fig. 6c & 6d. The LLRNS model with constant enstrophy cannot, by construction, display any enstrophy fluctuations. However, it does not present diverging fluctuations for the energy either (see Fig. 6d). This shows that the phase transition feature observed in the LLRNS model with constant energy is non-trivial. We conjecture that these events are linked with the existence of events of quasi-blow-up in the vorticity, that are naturally present in the inviscid blow-up [22, 23]. These quasi-blow-ups can

propagate from low wavenumbers to large wavenumbers when the viscosity is low, provoking events of large vorticity. In the case where the enstrophy is fixed, such quasi blow-ups cannot exist anymore. In addition, these events are blocked by normal constant viscosity, but not by hypoviscosity [23]. A time-dependent viscosity like in the RNS case could be viewed as a hypo-viscosity, leaving room for these events to develop, in contrast with LL-Navier-Stokes. This therefore explains why we only observe these events in the LLRNS with constant energy.

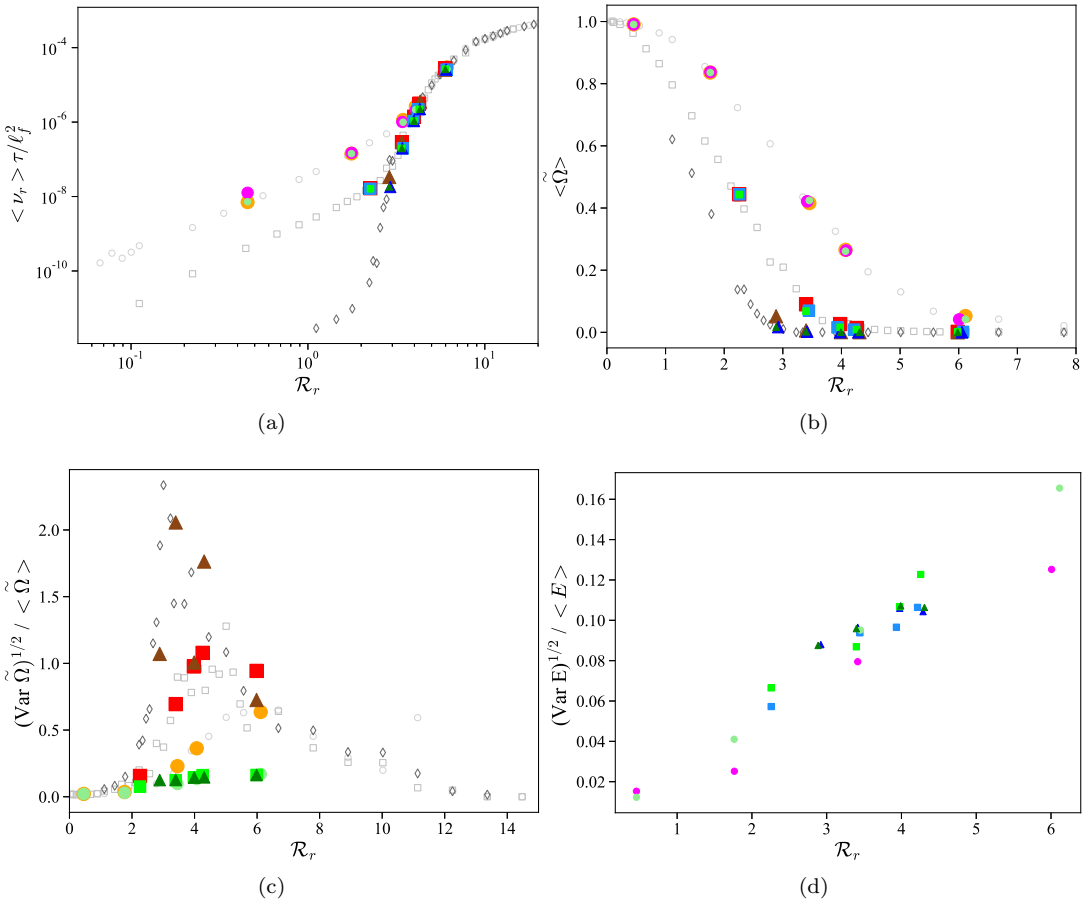


FIG. 6: **Existence of a phase transition in the different systems for different order parameter**.(6a) Renormalized viscosity function of the previously introduced control parameter $\mathcal{R}_\mathrm{r}$. (6b) Renormalized enstrophy as a function of the control parameter $\mathcal{R}_\mathrm{r}$. (6c) Rescaled variance of the normalized enstrophy as a function of $\mathcal{R}_\mathrm{r}$. (6d) Rescaled variance of the energy, as a function of $\mathcal{R}_\mathrm{r}$, for the LLRNS conserved enstrophy case and LLNS. In all four figures, the empty gray symbols are the data of Fig. 2b & 3a. Circles, squares and triangles are associated to $N = 8^3, 12^3, 16^3$, respectively. The conservation schemes are coded by color, with light green to dark green being the irreversible LL-Navier-Stokes model, purple to dark blue LLRNS model with conserved enstrophy, orange to brown LLRNS model with conserved energy. Note that in the non-conserved energy case, we define $\mathcal{R}_\mathrm{r}$ using the averaged kinetic energy. Also note that the difference between the grey and blue symbols lies in the numerical details, both are associated to conserved energy case. But, grey symbols are obtained varying the forcing amplitude $f_0$ while blue symbols are associated to a fixed $f_0$ and varying initial condition i.e varying $E_0$. Fig. 6a & 6b show that all mean viscosities and enstrophy collapse on an universal law. While Fig. 6c & 6d highlight the absence of transition for LL-Navier-Stokes and LL-RNS with conserved enstrophy.

### F. Comparison with Leith model predictions

#### 1. *Influence of the resolution*

While performing simulations on log-lattices, it is possible to reach high resolutions ($k > 10^{20}$) at a moderate numerical cost, making it possible to analyze the effect of the resolution on the transition. Such a study could not be done using DNS.

TABLE IV: **Values of various quantities around the transition area.** $\mathcal{R}^*_{r\_}$ defines the value at which the transition area starts, defined by the quick rise in viscosity. $\Delta\nu$ represents the difference in viscosity between the two asymptotic regimes separated by the transition area. $h = \frac{k_0}{k_{\max}}$ is a parameter used to quantify the influence of the resolution and $N$ is the number of spectral modes.

| $\lambda$ | $N$ | $h$ | $\Delta\nu_r$ | $\mathcal{R}^*_{r\_}$ | $\mathcal{R}^*_r$ |
|---|---|---|---|---|---|
| 2 | $8^3$ | $7 \cdot 10^{-3}$ | $10^4$ | $\approx 4.3$ | $\approx 7$ |
| | $12^3$ | $4 \cdot 10^{-4}$ | $10^6$ | $\approx 3.6$ | $\approx 5$ |
| | $16^3$ | $3 \cdot 10^{-5}$ | $10^8$ | $\approx 3.1$ | $\approx 3.75$ |
| $\phi$ | $8^3$ | $3 \cdot 10^{-2}$ | $10^2$ | $\approx 4.4$ | $\approx 5$ |
| | $12^3$ | $5 \cdot 10^{-3}$ | $10^4$ | $\approx 2.8$ | $\approx 4$ |
| | $20^3$ | $10^{-4}$ | $10^8$ | $\approx 1.8$ | $\approx 2.75$ |
| Shukla ([2]) | $128^3$ | $2.4 \cdot 10^{-2}$ | - | $\simeq 2.0$ | 2.75 |

A first influence of resolution can be obtained on the value of the mean reversible viscosity, illustrated in Fig. 2b: as $k_{\max}$ (or equivalently the number of modes, $N$) is increased, the viscosity decreases for a same value of $\mathcal{R}_{\rm r}$, as there is more room for the cascade to operate. Therefore, the time-averaged viscosity gives us some insights on the dependence of the system on the resolution. Indeed, before the transition, for $\mathcal{R}_{\rm r} < \mathcal{R}^*_{r,\_}$ (being the lower-bound of the transition) the viscosity exhibits a very large dependence on the size of the grid. As we reach the transition area, that we locate at the beginning of the quick rise of viscosity, all the data then collapses on the same universal curve, independent of $k_{\max}$. Note that $\mathcal{R}^*_{r,\_}$ shifts to lower values as the size of the grid increases (Tab. IV).

Another influence of the resolution is given by the nature of the transition, that shifts from a second-order transition to an imperfect transition as the number of modes is decreased (see Fig. 3c & 3d). This effect was a prediction of the Leith model introduced in [2], and we observe the same typical features found in this model.

Indeed, for $N < 20^3$, neither the mean enstrophy nor its square root follow a power-law. Such description is only accurate upon reaching $N = 20^3$. In the case of the variance, we observe in Fig. 3d a scenario that resembles the one predicted by the Leith model: at low resolution, the standard deviation exhibits a "bump" (Fig. 3d, circle and triangle markers). In this case, extracting a $\gamma$ exponent is questionable. Nevertheless, Tab. I gathers all the extracted critical exponents. At larger resolution, the divergence of the variance becomes more visible, with a critical exponent converging to the mean field value $\gamma_l = 1$. Note that even while using log-lattices, there are still finite size effects, as the limit $\mathcal{R}_{\rm r} \to 0$ exhibits truncated Euler dynamics, characterized by equipartition $E(k) \propto k^{-1}$ (Fig. 4).

#### *2. Further comparison with the Leith model*

It appears that, so far, our results and observations are in general agreement with the Reversible Leith model proposed in [2]. It is then interesting to compare more quantitatively those two systems. The only quantity from the RNS runs that can be compared to the Leith model is the energy transfer. Therefore, our comparison will rely on computing the Leith-like energy transfers $\Pi_{\rm Leith}$ (see section II C 2) from the RNS energy spectra and comparing it to the RNS transfers $\Pi_{\rm RNS}$.

The comparison between the two quantities is presented in Fig. 7. We see that the Leith-like transfer is able to mimic the RNS transfer in the inertial domain, but drops more quickly in the dissipative domain. This effect is probably caused by the Leith-like computation not taking into account the strong oscillations of the viscosity (and therefore of the Kolmogorov length) naturally present in RNS. Such oscillations tend to straighten the transfer a bit further outside the inertial range. Overall, it seems that the Leith models shares features with the RNS equations without completely reproducing its dynamics.

### G. Gallavotti conjecture

In this section, we now investigate how relevant the reversible models are to understand the dynamics of the irreversible LL-Navier-Stokes model. This can be done via suitable adaptation of conjectures by Gallavotti.

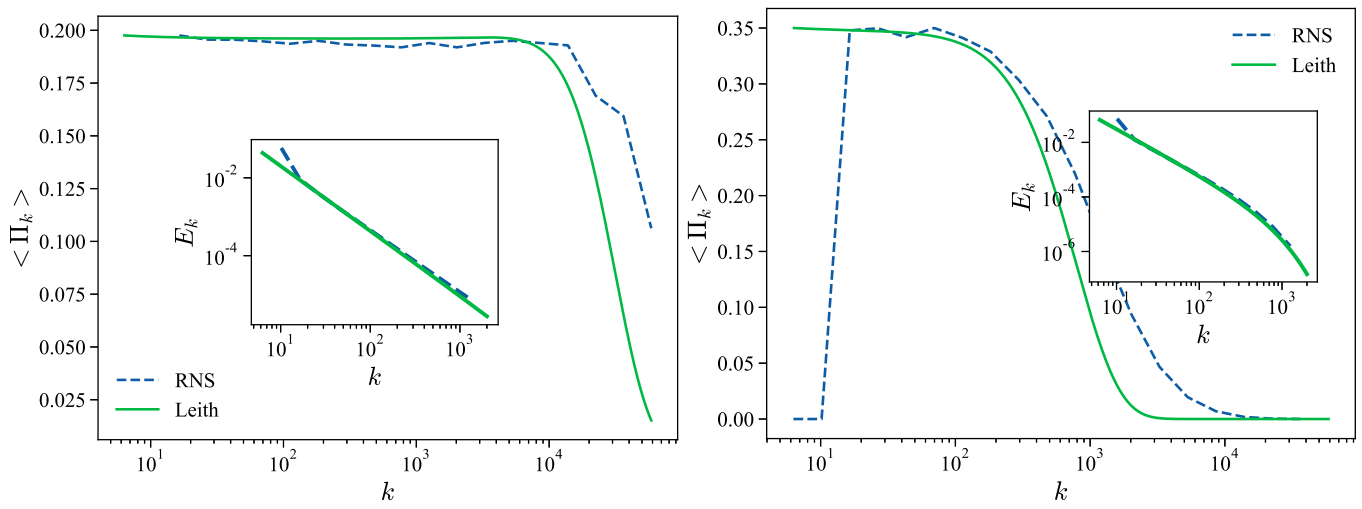


FIG. 7: **Quantitative comparison of the energy transfers** between RNS (dashed lines) and Leith-like transfers (full lines). The main figures present the two energy transfers, while the insets show the fitted energy spectra. The two figures are obtained for different values of $\mathcal{R}_r$ (7a) $\mathcal{R}_r \approx 2.23$ (7b) $\mathcal{R}_r \approx 3.34$.

### 1. *Definitions and conjectures*

Following [3], we introduce the collection $\mathcal{E}^{\mathcal{I},N}$ of the stationary distributions $\mu_\nu^{\mathcal{I},N}$, where $\mathcal{I}$ characterizes the irreversible equation (with time-independent viscosity i.e. LL-Navier-Stokes), with $N$ modes. Similarly, we define the collection $\mathcal{E}^{\mathcal{R},N}$ of the stationary distributions $\mu_G^{\mathcal{R},N}$, associated with the LLRNS model of $N$ modes, where $G$ is the conserved quantity (total enstrophy, total kinetic energy...). For any observable $\mathcal{O}$, $\langle\mathcal{O}\rangle_\nu^{\mathcal{I},N}$ and $\langle\mathcal{O}\rangle_\mathcal{G}^{\mathcal{R},N}$ denote the averages over the distributions $\mu_\nu^{\mathcal{I},N}$ and $\mu_G^{\mathcal{R},N}$, respectively.

As in [3], a set of parameters $\nu$, $G$ and $N$ will be said to be "in correspondence" if

$$\langle\mathcal{G}(\boldsymbol{u})\rangle_\nu^{\mathcal{I},N} = G \tag{15}$$

G is associated to a conserved, and therefore constant, quantity in the RNS model while $\mathcal{G}$ is its irreversible counterpart in regular NS.

The adaptation of the two Gallavotti conjectures to our models can then be formulated as:

**Conjecture 1:** *If $\nu$, $G$ and $N$ are in correspondence, then for any local observable (i.e. depending on a limited number of modes) $\mathcal{O}(\boldsymbol{u})$ one has*

$$\forall N, \lim_{\nu\to 0}\langle\mathcal{O}\rangle_\mathcal{G}^{\mathcal{R},N} = \lim_{\nu\to 0}\langle\mathcal{O}\rangle_\nu^{\mathcal{I},N} \tag{16}$$

**Conjecture 2:** *Let $\mathcal{O}(\boldsymbol{u})$ be a local observable depending on $\boldsymbol{u}(\boldsymbol{k})$ for $k < K$, then if $\nu$, $G$ and $N$ are in correspondence one has*

$$\lim_{N\to\infty}\langle\mathcal{O}\rangle_\mathcal{G}^{\mathcal{R},N} = \lim_{N\to\infty}\langle\mathcal{O}\rangle_\nu^{\mathcal{I},N} \tag{17}$$

*$\forall\nu$ and $K < c_\nu k_\eta$, $c_\nu \xrightarrow[\nu\to 0]{} c_0 < \infty$, where $k_\eta$ is the Kolmogorov scale.*

Those two conjectures are associated to different regimes. Indeed, by fixing the resolution $N$ and sending the viscosity to 0, one reaches the warm regime, characterized by thermalization (*Conjecture 1*). In contrast, by sending first the resolution $N$ to infinity, then viscosity to 0, one prevents the thermalization from occurring (as it is associated to under-resolved simulations). Therefore, *Conjecture 2* is associated to hydrodynamical regimes, and better describes turbulence in the limit of low viscosities.

### 2. Numerical procedure

In order to investigate the equivalence of ensemble, we start by running a LL-Navier-Stokes simulation, with time independent viscosity of $\nu = 10^{-4}, 10^{-5}, 5\cdot10^{-6}, 10^{-6}, 10^{-7}$ for different values of $N$. After reaching a steady state for a sufficient number of time-steps (to ensure the possibility of doing statistics), we use the LL-Navier-Stokes field as an initial condition for the LLRNS equation, in both conservation case. We then let both reversible and irreversible simulations run for $4.10^5$ time-steps.

This procedure enables us to highlight any divergence of the reversible solution from the irreversible solution, while allowing us to characterize the simulations by viscosity $\nu$ or equivalently by their Reynolds number (Re).

### 3. Using scores to compare PDFs

In the next sections, we need to compare PDFs. To quantify their similarity, we introduce a scalar parameter – a score –, defined as:

$$\mathcal{S}(\mathcal{O}) = 1 - \sum_{i=1}^{p} \frac{|\mathcal{O}_{\mathcal{R}}^{(i)} - \mathcal{O}_{\mathcal{I}}^{(i)}|}{\mathcal{O}_{\mathcal{I}}^{(i)}} \mathcal{B}^{-i+1} \tag{18}$$

where $\mathcal{O}^{(i)}$ stands for the i-th moment of the local observable $\mathcal{O}$, p for the number of moments we take into account and $\mathcal{B}$ for a decomposition basis ($\mathcal{B} = 10$, being a decimal basis in our case).

A score of one implies little errors between irreversible and reversible moments and leads to matching PDFs. We will restrict the computation of the score to the first three moments because of large statistical errors in our kurtosis. Therefore, the score should be roughly 1 whenever the 3 first moments coincide, i.e. whenever the distributions are identical around the mean value. Thus, $\mathcal{S}$ appears as a good indicator to qualify to what extent the conjecture holds.

### 4. Statistics of the reversible viscosity

Because of its presence in the limits, the viscosity plays a special role in the conjectures. However it is a non-local observable. There is therefore no reason that mean reversible viscosities should be equivalent to irreversible viscosities, even when only small values are considered. However, there are several differences between the conservation schemes that may temper this observation. First, the total kinetic energy is concentrated at the large scales whereas enstrophy is a small scale quantity, resulting in completely different statistics of the viscosity. In fact, a major difference between the two cases arises in the possible occurrence of negative viscosities. At low viscosities, there is almost no occurrence of negative viscosities in the conserved energy case, even in systems presenting a quasi-thermalized spectrum (Fig. 8a). This is no longer true for the conserved enstrophy case as we observe many occurrences of negative viscosities in well thermalized regimes (Fig. 8b).

In addition, conserving the enstrophy is a strong constraint, that implies additional equivalence for the viscosity. Indeed, if the first conjecture holds, we should observe conservation of the mean work of the forcing term $\mathcal{W} = \langle \boldsymbol{f}.\boldsymbol{u} \rangle$, because it is local at large scales (more details in section III H 1 and Tab. V & VI in section B). Using the energy budget, this yields $\langle \nu_r \rangle = \nu$ in the constant enstrophy case ([3]), even though $\nu_r$ is not a local observable. The property is not true for the conserved energy case, so that the *Conjecture 1* should not hold a priori for the viscosity.

Our measurements are generally in agreement with these theoretical predictions, with some exceptions (Fig. 9a). In the conserved enstrophy LLRNS model, we observe that the condition $\langle \nu_r \rangle = \nu$ holds for most values of $\nu$, except for very low viscosity. In the conserved energy case, the situation is opposite: the property does not hold a priori for large enough values of viscosity. However, for small enough values of $\nu$, we recover $\langle \nu_r \rangle \approx \nu$.

Note that since injection is a local observable, and since we are in a stationary state, where on average injection equals dissipation, we expect that $\nu_r\Omega$ obeys *Conjecture 1* & *2*. In the case of constant enstrophy, this condition is equivalent to $\langle \nu_r \rangle \approx \nu$, as we just saw. However, in the conserved energy case, this is not true anymore. Indeed, as we see in Fig. 9b, we have $\langle \nu_r\Omega \rangle \approx \nu \langle \Omega \rangle$ for the conserved energy case, even though the equivalence is not fulfilled for the viscosity alone.

### 5. Energy and enstrophy

The first obvious quantities to investigate are energy $E$ and enstrophy $\Omega$. Results are reported in Tab. V & VI (see section B), where we give the mean ratios between reversible and irreversible values at various $\nu$ and for the

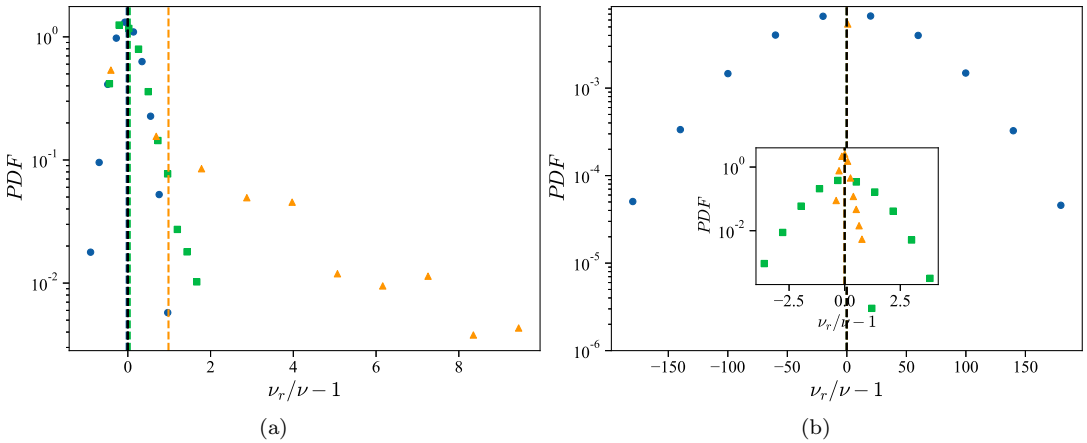


FIG. 8: **PDF of the ratio** $\nu_r \ / \ \nu - 1$ where $\nu_r$ stands for the reversible viscosity, for $N = 8^3$ (blue dots), $12^3$ (green squares), $16^3$ (orange diamonds), $\nu = 10^{-7}$. Fig. 8a shows the results associated to $\mathcal{G} = E$, while Fig. 8b is associated to $\mathcal{G} = \Omega$. Colored dashed lines represents the mean values of the PDF while the black dashed line is associated to $\langle \nu_r \rangle = \nu$.

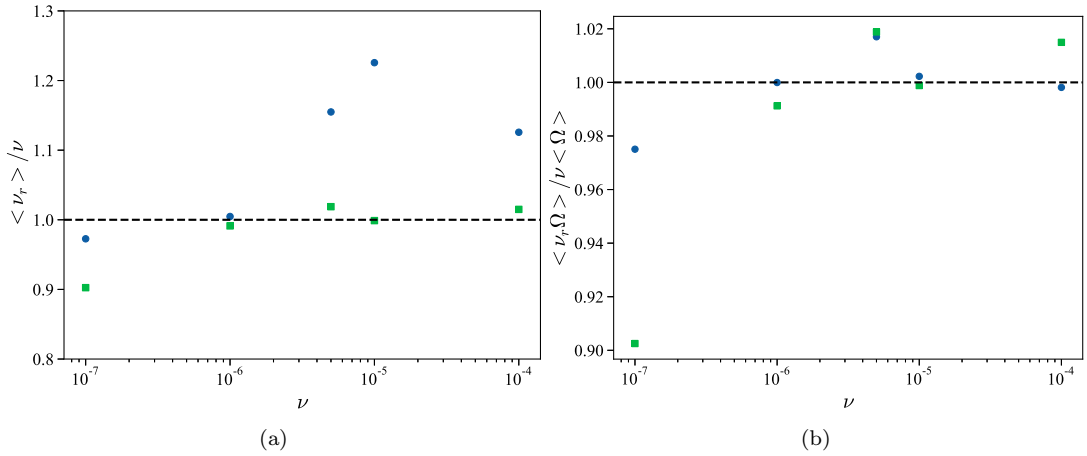


FIG. 9: **Equivalence between the viscosities**. (9a) Ratio of the mean reversible viscosity over the standard NS viscosity. (9b) Ratio of the mean dissipation $\nu\Omega$. Both figures are obtained for $N = 8^3$, blue dots correspond to conserved energy while green squares are associated with conserved enstrophy.

two conservation schemes. In all cases, the ratio of $\langle \mathcal{G} \rangle / G$ is very close to 1, showing the validity of Eq. 15 for both conservation schemes. It is interesting to note that the mean energy is well described even in the conserved enstrophy case. On the other hand, in the conserved energy case the enstrophy is correctly reproduced only in the quasi-thermalized state (Tab. V & Fig. 6a). In particular, at high resolution ($N = 16^3$), we observe enstrophy ratio above 100%.

### H. Analysis of Conjecture 1 - Warm regime

In this subsection, we focus on the *Conjecture 1*. We consider various local quantities, and analyze results at fixed number of modes $N = 8^3$ and decreasing viscosity of $\nu = 10^{-4}$, $10^{-5}$, $5 \cdot 10^{-6}$, $10^{-6}$ and $10^{-7}$.

#### 1. *Work of the forcing term*

We now consider the work $\mathcal{W} = \langle \boldsymbol{f}.\boldsymbol{u} \rangle$. This quantity appears as a good candidate for *Conjecture 1*, as the forcing term is localized around $k_f = 15$ (see Eq. 14). Tab. V & VI (see section B) summarize the ratio of mean values

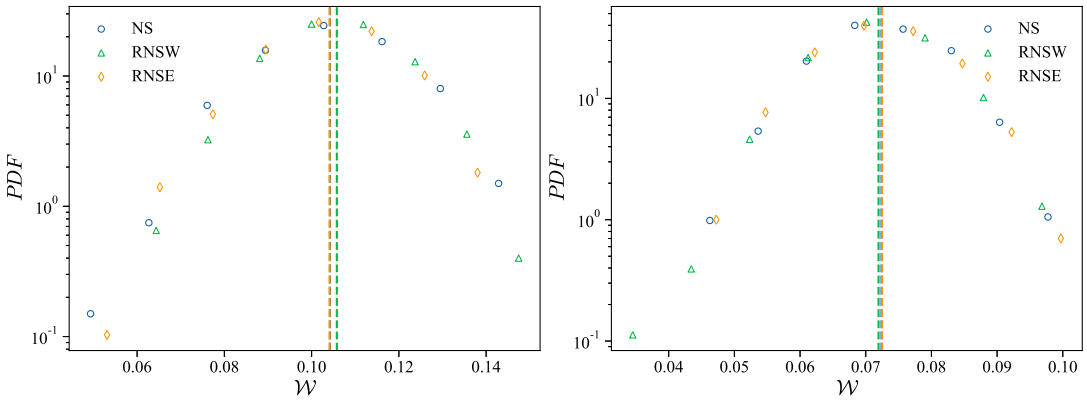


FIG. 10: **PDF of the work of the forcing term $\mathcal{W}$.** Simulations are performed with $N = 8^3$. (10a) $\nu = 10^{-4}$ (10b) $\nu = 10^{-6}$. Dashed lines represent the mean values of the PDF. Both conservation schemes show good agreement for the mean values. At higher viscosities, tails differ.

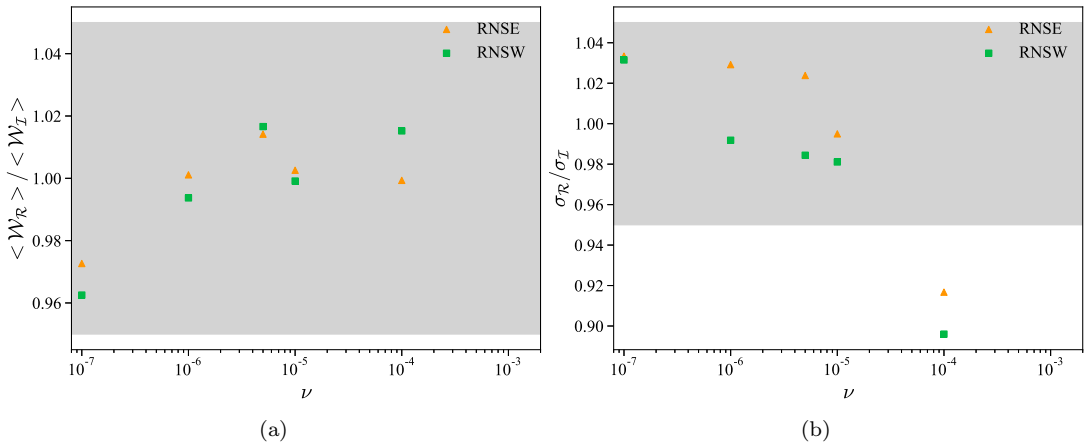


FIG. 11: **Ratios of the two first moments of $\mathcal{W}$ as a function of the viscosity $\nu$.** Simulations are performed with $N = 8^3$. (11a) Ratio $\langle \mathcal{W}_\mathcal{R} \rangle / \langle \mathcal{W}_\mathcal{I} \rangle$, (11b) Ratio $\sigma^\mathcal{W}_\mathcal{R}/\sigma^\mathcal{W}_\mathcal{I}$, where $\sigma$ stands for the standard deviation. The gray shaded area represents the 5% confidence interval.

between reversible and irreversible values, and show that almost all simulations fulfill correspondence conditions Eq. 15, with either conserved energy or conserved enstrophy. A finer understanding of this correspondence can be obtained by exploring the properties of its PDF in both the hydrodynamical case ($\nu = 10^{-4}$) and quasi-thermalized ($\nu = 1 \cdot 10^{-6}$). This is shown in Fig. 10. In both case and with both schemes, the PDF shows good agreement between the reversible and irreversible case, except for the high viscosity case, where tails are different. This difference is due to the difference in standard deviations. Nevertheless, in the quasi-thermalised regime (Fig. 10b), the PDF presents quasi perfect agreement between irreversible and reversible cases, which is a signature that *Conjecture 1* holds for the local observable $\mathcal{W}$.

To further support this claim, we analyze the ratio of the two first order moments $\frac{\langle \mathcal{W}_\mathcal{R} \rangle}{\langle \mathcal{W}_\mathcal{I} \rangle}$ and $\frac{\sigma^\mathcal{W}_\mathcal{R}}{\sigma^\mathcal{W}_\mathcal{I}}$. Fig. 11 gathers those results, obtained for $N = 8^3$. One observes that for any value of $\nu$, the mean value of $\mathcal{W}$ corresponds to the mean value of the reversible equations, within a 5% error margin (Fig. 11a). This property does not hold however for the standard deviation, where the ratios lie outside the confidence interval in the hydrodynamical case (Fig. 11b). As the viscosity decreases, both ratios enter the confidence interval, and thus both PDFs match in the inviscid limit.

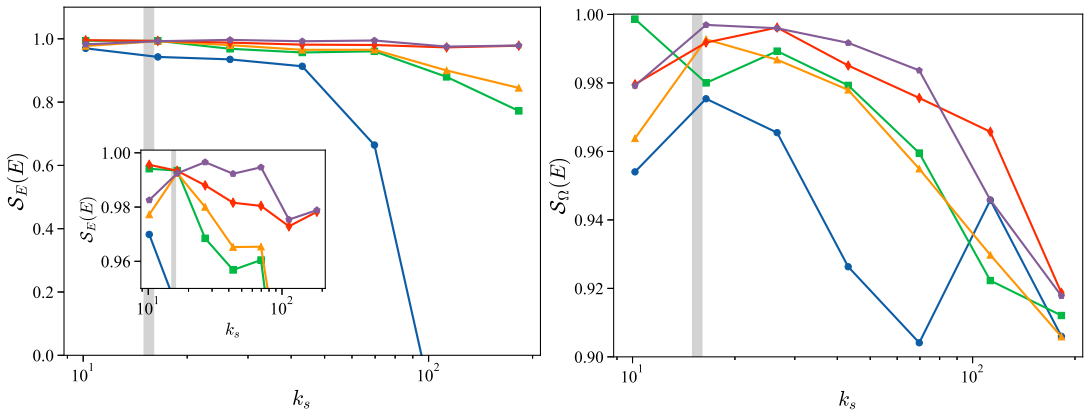


(a) (b)

FIG. 12: **Score $\mathcal{S}(E)$ of the energy in each shell** Figures (12a) corresponds to the conserved energy case while (12b) is associated to the conserved enstrophy case. The gray shaded areas show where the forcing term is localized. Figures are obtained for $N = 8^3$. Blue dots, green squares, orange triangles, red diamonds and purple pentagons are respectively associated to $\nu = 10^{-4}$, $10^{-5}$, $5 \cdot 10^{-6}$, $10^{-6}$ and $10^{-7}$.

### 2. *Energy spectra*

We now consider the equivalence for the distribution of energy in the wavenumber space, through the instantaneous energy spectra $E(\boldsymbol{k})$. As time varies, and for each given $k$, $E(k)$ fluctuates in time, and we can study its statistics through our score function. Fig. 12 gathers the different scores $\mathcal{S}(E)$, obtained for different $\nu$ at various $k_s$. In the conserved energy case (Fig. 12a), *Conjecture 1* holds quite well. Indeed, as $\nu \to 0$, the score is almost equal to one (purple pentagons) over the whole space, highlighting good moments matching. For higher viscosities (blue dots, green squares...) the score starts to drop at smaller $k$, indicating that only the first shells display equivalence. Note that the statistics around the first and last data points might be biased by side effect associated to the sampling process. The conserved enstrophy case (Fig. 12b) shares some similar features, as the score indeed appears to grow as $\nu$ decreases, progressively spanning the whole grid.

According to the score, one should observe PDF matching (outside the tails) for $\nu = 10^{-4}$ at big scales ($k_s \approx 16.5$) and PDF differences at small scales ($k_s \approx 182.6$). This is indeed what we observe in Fig. 13a & Fig. 13b. In addition, one expects near identical PDF in both conservation schemes, at all scales for $\nu = 10^{-7}$. This statement is confirmed in Fig. 13c& Fig. 13d, where the PDFs are almost indistinguishable.

## I. Analysis of Conjecture 2 - Hydrodynamical regime

In this section, we analyze the *Conjecture 2*, i.e. equivalence at fixed $\nu$ and varying $N$ in the case of the hydrodynamical regime, in the thermodynamic limit $h \to 0$ ($k_{\max} \to \infty$).

In the analysis of this conjecture, there appears a strong difference between the conserved energy case, and the conserved enstrophy case. Indeed, the former case presents a phase transition whose characteristics depend on $N$ (Fig. 6). This dependence complicates the analysis on the impact of $k_{\max} \to \infty$ ($N \to \infty$) in *Conjecture 2*. Indeed, for a given $\mathcal{R}_r$, increasing $N$ implies switching phase (Fig. 6a), going from quasi-thermalized regimes ($\mathcal{R}_\mathrm{r} < \mathcal{R}_r^*$, in which *Conjecture 1* holds) to hydrodynamical ones ($\mathcal{R}_\mathrm{r} \geq \mathcal{R}_r^*$). Therefore, one must be careful while comparing similar Re for different resolutions as the validity of the conjecture is related to the position in the transition, as will be highlighted later.

### 1. *Energy spectra*

We now focus on the statistics of the energy spectrum, at given values of $k_s$. In the hydrodynamical regime, *Conjecture 2* implies that the score of $\mathcal{E}(k)$ should be equal to 1 in the thermodynamic limit $h \to 0$ ($k_{\max} \to \infty$). In practice, we shall see that this will be true only for a given range of wavenumber $k < K_\nu$ ([3, 24]).

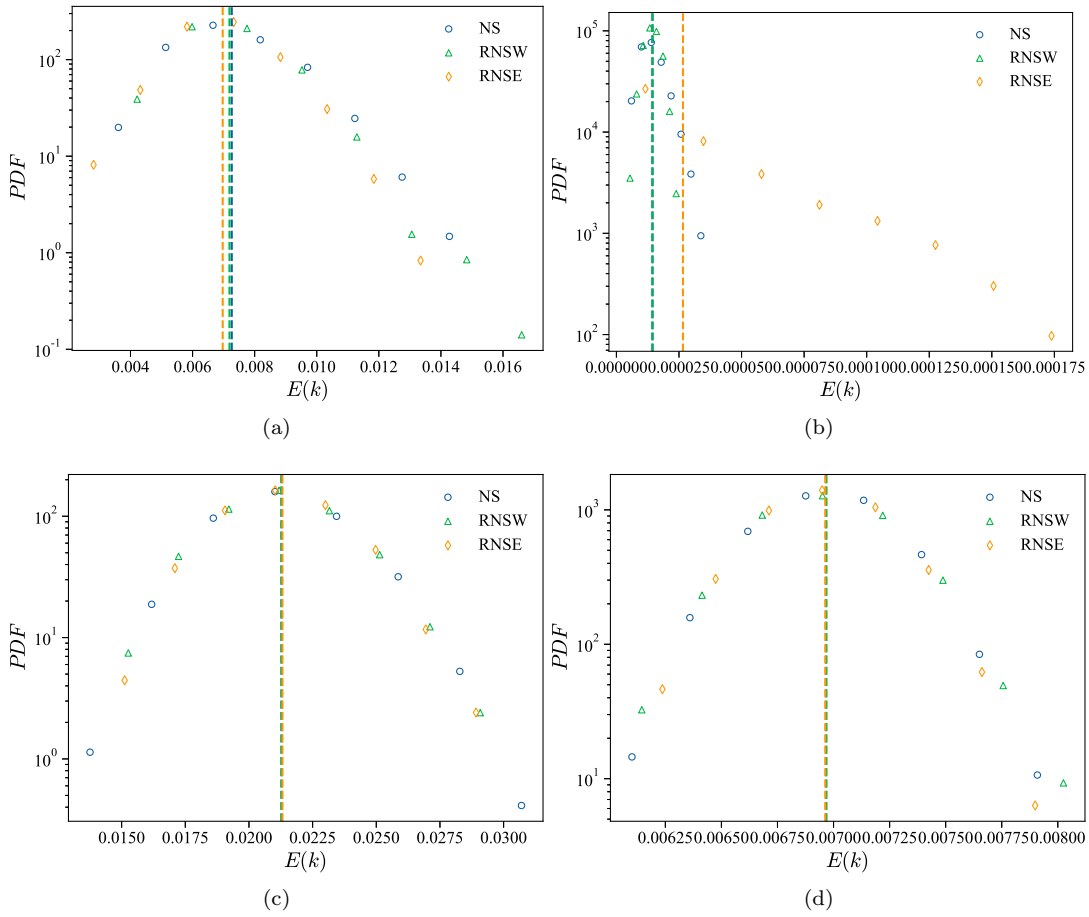


FIG. 13: **Energy PDF** Results are obtained for different values of $k_s$ and $\nu$, with $N = 8^3$. (13a & 13b) $\nu = 10^{-4}$, $k_s \approx 16.5$, $k_s \approx 182.6$ ; (13c & 13d) $\nu = 10^{-7}$, $k_s \approx 16.5$, $k_s \approx 182.6$. Dashed lines represent the mean values of the PDF.

In the conserved enstrophy case the analysis is straightforward. We show in Fig. 14 the evolution of the score $\mathcal{S}_\Omega(E)$ at various resolutions. At lower resolution, $\mathcal{S}_\Omega(E)$ drops quickly (Fig. 14, blue dots) highlighting the absence of equivalence between the reversible and irreversible ensemble. By increasing N, we obtain scores closer to 1 on intervals up to $K_\nu$, defined as the value of k such that $\forall k > K_\nu, \mathcal{S}_\mathcal{G}(\mathcal{O}) < 0.9$. We also observe that for low values of viscosity, the scores are similar for $N = 12^3$ and $N = 16^3$, supporting the second conjecture, in the conserved enstrophy case. For $k > K_\nu$, scores start to "oscillate", this is associated to the fact that the reversible moments fluctuate around the irreversible ones and sometimes lies in confidence interval, leading to artificially higher scores.

In the conserved energy case, the analysis is complicated by the phase transition, as detailed below. According to the *Conjecture 2*, one expects to observe scores $\mathcal{S}_\mathcal{G}(E) > 0.9$ on bigger and bigger domains as $\nu \to 0$. Fig. 15 shows the scores, in the case of conserved energy $E$, for various viscosities and $N = 12^3$ (Fig. 15a) or $N = 16^3$ (Fig. 15b). Our results indeed highlight a dependency of $K_\nu$ on $\nu$ (Fig. 14 & 15). Note that the red diamonds in Fig. 15a are associated with a crossover regime where thermalization at small scales starts to occur, leading to results similar to *Conjecture 1* (Fig. 12a) but with a slight drop.

Fig. 16 shows the extracted thresholds divided by the Kolmogorov scale for both conservation schemes, at different resolutions and different viscosities. Unlike in [3], $c_\nu$ is no longer a constant but depends on the value of $\nu$ and does not grow as fast as the Kolmogorov scale $k_\eta$ (Fig. 16).

Note that for $\nu = 10^{-7}$, the $N = 12^3$ are under-resolved, leading to an upper-bound $K = k_{\max}$ for the threshold, that can not grow anymore as $\nu$ decreases. Such phenomenon explains the difference between the two first points of Fig. 16b.

In the thermodynamic limit of the conserved energy case, the equivalence is best achieved for $\mathcal{R}_\mathrm{r} \to \mathcal{R}_\mathrm{r}^*(N)$. As mentioned before, such properties make the comparison between resolutions difficult, as the value of $\mathcal{R}_\mathrm{r}$ at which the transition between warm and hydrodynamical regimes occurs also depends on $N$. Nevertheless, Fig. 16a gathers the results for the conserved energy case, confirming the validity of *Conjecture 2*, on smaller domains with respect to

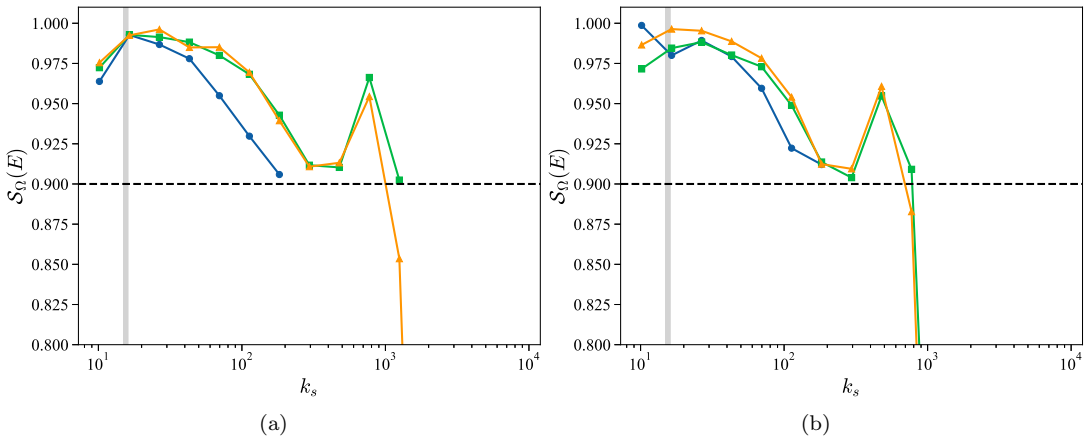


FIG. 14: **Score $\mathcal{S}(E)$ of the energy in each shell for $\mathcal{G} = \Omega$.** (14a) $\nu = 5 \cdot 10^{-6}$; (14b) $\nu = 10^{-5}$. Blue dots, green squares and orange triangles correspond to $N = 8^3$, $12^3$, $16^3$, respectively. Black dashed lines correspond to a score of 0.9.

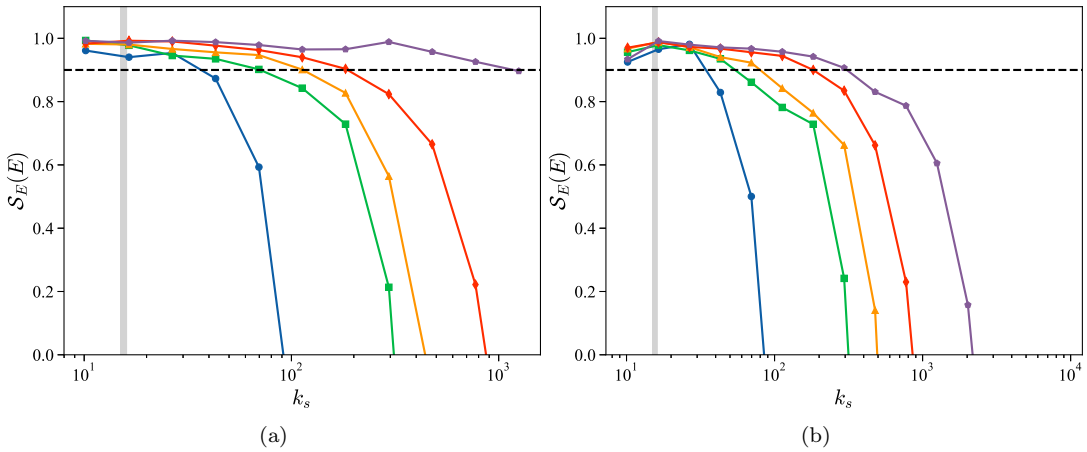


FIG. 15: **Score $\mathcal{S}(E)$ of the energy in each shell for $\mathcal{G} = E$.** (15a) $N = 12^3$; (15b) $N = 16^3$. Blue dots, green squares, orange triangles, red diamonds, and purple pentagons correspond to $\nu = 10^{-4}$, $\nu = 10^{-5}$, $5 \cdot 10^{-6}, 10^{-6}$, $10^{-7}$, respectively. Note that in (15a), the purple pentagons are associated with a quasi-thermalized state, being a crossover region between the two conjectures. Black dashed lines correspond to a score of 0.9.

those observed in the conserved enstrophy case.

## IV. CONCLUSION

We have shown that LLRNS models are able to reproduce features previously observed in DNS while allowing us to better probe the transition by reaching scales much lower than usual DNS. We found that the LLRNS system with conserved energy indeed exhibits a second order phase transition, with $\sqrt{\Omega}$ as an order parameter, sharing interesting features with the Reversible Leith model; a simple non-linear diffusion model. The phase transition separates two phases, the first characterized by the coexistence between a hydrodynamical regime and an equipartition of energy at small scale (named "warm" phase), and the second characterized by an over-damped regime with very large viscosity (named over-damped phase). In between, we have a turbulent hydrodynamical regime, with properties resembling that of solutions of the Navier-Stokes equations.

We have not observed a divergence of fluctuations in the LLRNS model with enstrophy conservation, nor in models with fixed viscosity. This may be due to the fact that the enstrophy conserving scheme is associated with more regular solutions than the energy conserving scheme. In particular, it rules out a spontaneous reversal symmetry breaking mediated by dissipating singularities as conjectured by Onsager [4]. More work is therefore needed to understand the

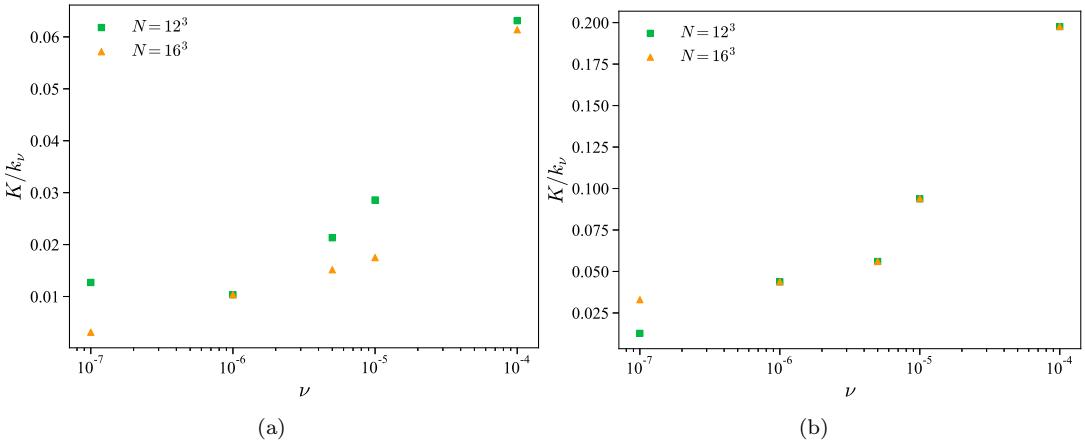


FIG. 16: **Ratio $K/k_\nu$ in the context of Conjecture 2** (16a) corresponds to conserved total kinetic energy while (16b) corresponds to conserved enstrophy. The thresholds $K$ were extracted directly from the score at the considered k. The thresholds were not extracted for $N = 8^3$ since the resolution is insufficient as most simulations lie on the thermalized branch (Fig. 6a, colored circles).

difference between the two conservation schemes from the point of view of the emergence of dissipative weak solutions. This is the subject of an ongoing work.

We also studied the finite-size corrections of the scalings induced by the finite resolution and found good agreement with tendencies predicted by the Leith model. Such a study would have been impossible to perform on present DNS. Finally, we studied the influence of reversibility on scalings of the ansatz of the structure functions. They were found to obey self-similar scaling in all phases, with an exponent ranging from 0.36 in the warm (reversible) phase, to 0.42 in the hydrodynamical (irreversible) phase. We did not find any intermittency corrections in either phase. It is an open question whether choosing other step sizes on the logarithmic grid, for instance allowing more interactions, will result in intermittency in either of the two phases.

We also tested the adaptation of two conjectures by Gallavotti ([1]), regarding the equivalence of the reversible models and the irreversible model. We find that the properties of the quasi-thermalized regime of the reversible and irreversible models are equivalent both for conserved enstrophy or conserved energy. This equivalence also holds in the hydrodynamical regime for local observables located at $k < K_\nu$, both for conserved enstrophy and conserved energy. This result is therefore an extension of the equivalence found by [3]) in DNS of RNS with conserved enstrophy. In addition, we find that equivalence between irreversible LL-Navier-Stokes models and LLRNS models with conserved energy, in fully developed turbulence (*Conjecture 2*) holds best in the limit $N \to \infty$, $\mathcal{R}_\mathrm{r} \xrightarrow{>} \mathcal{R}_r^*$. This feature was discussed but not proven by [2] in the DNS case. We showed that, unlike in DNS ([3]), the value of $c_\nu = K/k_\nu$ is not a constant but depends on $\nu$. Altogether, our results show that ensemble equivalence holds for LLRNS models in the average sense, since conserved enstrophy and conserved energy model display similar means for all observables studied in this paper.

These results show the interest of the models based on projecting fluid dynamics on log-lattice. Being 3-dimensional, and respecting most symmetries of the original equation, they may be used to explore fundamental issues of the original system, albeit at a moderate computational cost and without any adjustable parameters. By construction, they of course lack many interactions present in the original equations, and it is not clear how well many of the results presented here can be extended to real fluids. Nonetheless, it will likely take some time before direct numerical simulations can reach the parameter values explored here, so this interesting question is left for the future.

## Acknowledgments

This work received funding through the PhD fellowship programs of the Ecole Polytechnique and Ecole Normale Superieure Paris-Saclay, and through the ANR, via the grants ANR TILT grant agreement no. ANR-20-CE30-0035 and ANR BANG grant agreement no. ANR-22-CE30-0025.

## Appendix A: Viscous splitting

In our study, we propose to first solve the inviscid Navier-Stokes equation (12), then we compute the reversible viscosity, according to the quantity that must be conserved. Finally, we take into account the viscosity by rescaling the velocity fields. One could wonder if this method gives proper results in the reversible case.

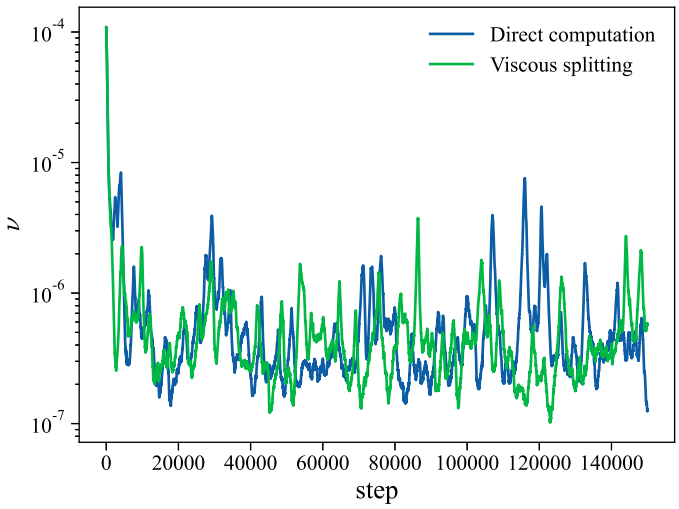


FIG. 17: **Evolution of the reversible viscosity $\nu_r$ at each step.** Both simulations are performed for $\lambda = \phi \approx 1.618$, $N = 12^3$, $f_0 = 0.27$. The green curve is obtained using the viscous splitting method while the blue curve is obtained by directly solving the RNS equation, where the reversible viscosity is computed using Eq. 3.

Both methods lead to similar behavior of the viscosity (Fig. 17), with mean values $\nu_{r,\text{Splitting}} \approx 4.9 \cdot 10^{-7}$ and $\nu_{r,\text{Direct}} \approx 5.9 \cdot 10^{-7}$. It is expected to find a slight difference as the number of time step is still relatively small. Moreover, the direct computation is performed using the analytical expression of the reversible viscosity and therefore leads to deviation from $E_0$.

Still, both methods give similar results (Fig. 17). However, the "viscous splitting" method allows us to "perfectly" (with floating-point accuracy) conserve a chosen quantity (here the total kinetic energy) without deviation.

## Appendix B: Enstrophy renormalization

The case of $\mathcal{R}_\text{r} \to 0$, is associated to a vanishing energy injection and therefore, in order to keep the total energy constant, to a vanishing viscosity. The system thus behaves as a truncated Euler equation and should exhibit an equipartition of energy. In our model, this equipartition is characterized by an energy spectrum developing a power law $k^{-1}$ that we will be using in order to compute the total enstrophy $\Omega_\text{max}$.

We start by assuming that the kinetic energy in a shell can be written as $E_k = \frac{A}{k}$, where A is a constant obtained through the total kinetic energy $E_0$:

$$E_0 = \sum_k E(k)\Delta\mu_k = A\sum_k \frac{1}{k}(\lambda k - k) = AN(\lambda - 1).$$

Where $\Delta\mu_k$ is the measure of the space, which is $(\lambda k - k)$ for the 1D shells here. This leads to $A = \frac{E_0}{N(\lambda-1)}$, where $N$ is the number of modes used on the grid.

We then compute the total enstrophy $\Omega_\text{max}$.

$$\begin{aligned}\Omega_\text{max} &= \sum_k k^2 E(k)(\lambda k - k) = \frac{E_0}{N}\sum_k k^2, \\ &= \frac{E_0 k_0^2}{N}\sum_{p=0}^{N-1}\lambda^{2p} \simeq \frac{E_0\lambda^2 k_\text{max}^2}{N(\lambda^2-1)}.\end{aligned}$$

We can now define the renormalized enstrophy:

$$\widetilde{\Omega} = \frac{\Omega}{\Omega_{\max}}. \tag{B1}$$

TABLE V: **Ratio of various quantities for constant energy.** $\mathcal{W}$ stands for the work of the forcing term.

| $N$ | $\nu$ | $\langle E_\mathcal{R}\rangle / \langle E_\mathcal{I}\rangle$ | $\langle \Omega_\mathcal{R}\rangle / \langle \Omega_\mathcal{I}\rangle$ | $\langle W_\mathcal{R}\rangle / \langle W_\mathcal{I}\rangle$ |
|---|---|---|---|---|
| $8^3$ | $10^{-4}$ | 100.0% | 125.6% | 99.9% |
| | $10^{-5}$ | 100.0% | 102.1% | 99.7% |
| | $5.10^{-6}$ | 100.0% | 98.2% | 98.6% |
| | $10^{-6}$ | 100.0% | 100.0% | 99.9% |
| | $10^{-7}$ | 100.0% | 100.0% | 97.3% |
| $12^3$ | $10^{-4}$ | 100.0% | 135.4% | 99.6% |
| | $10^{-5}$ | 100.0% | 160.0% | 99.3% |
| | $5.10^{-6}$ | 100.0% | 164.6% | 99.1% |
| | $10^{-6}$ | 100.0% | 132.3% | 99.7% |
| | $10^{-7}$ | 100.0% | 100.4% | 99.8% |
| $16^3$ | $10^{-4}$ | 100.0% | 142.9% | 97.5% |
| | $10^{-5}$ | 100.0% | 156.1% | 98.4% |
| | $5.10^{-6}$ | 100.0% | 145.1% | 98.9% |
| | $10^{-6}$ | 100.0% | 315.2% | 98.8% |
| | $10^{-7}$ | 100.0% | 313.4% | 97.9% |

TABLE VI: **Ratio of various quantities for constant enstrophy.** $\mathcal{W}$ stands for the work of the forcing term.

| $N$ | $\nu$ | $\langle E_\mathcal{R}\rangle / \langle E_\mathcal{I}\rangle$ | $\langle \Omega_\mathcal{R}\rangle / \langle \Omega_\mathcal{I}\rangle$ | $\langle W_\mathcal{R}\rangle / \langle W_\mathcal{I}\rangle$ |
|---|---|---|---|---|
| $8^3$ | $10^{-4}$ | 98.2% | 100.0% | 98.5% |
| | $10^{-5}$ | 99.8% | 100.0% | 99.9% |
| | $5.10^{-6}$ | 98.9% | 100.0% | 98.3% |
| | $10^{-6}$ | 99.8% | 100.0% | 99.4% |
| | $10^{-7}$ | 100.0% | 100.0% | 96.3% |
| $12^3$ | $10^{-4}$ | 98.5% | 100.0% | 98.1% |
| | $10^{-5}$ | 99.0% | 100.0% | 98.9% |
| | $5.10^{-6}$ | 98.8% | 100.0% | 98.6% |
| | $10^{-6}$ | 98.6% | 100.0% | 98.9% |
| | $10^{-7}$ | 100.0% | 100.0% | 99.7% |
| $16^3$ | $10^{-4}$ | 98.8% | 100.0% | 98.0% |
| | $10^{-5}$ | 99.6% | 100.0% | 99.3% |
| | $5.10^{-6}$ | 99.7% | 100.0% | 99.8 % |
| | $10^{-6}$ | 99.5% | 100.0% | 99.8% |
| | $10^{-7}$ | 98.7% | 100.0% | 98.5% |


[1] G. Gallavotti, Physics Letters A **223**, 91 (1996).
[2] V. Shukla, B. Dubrulle, S. Nazarenko, G. Krstulovic, and S. Thalabard, Physical Review E **100**, 043104 (2019).
[3] G. Margazoglou, L. Biferale, M. Cencini, G. Gallavotti, and V. Lucarini, arXiv preprint arXiv:2201.00530 (2022).
[4] L. Onsager, Il Nuovo Cimento (1943-1954) **6**, 279 (1949).
[5] B. Dubrulle, Journal of Fluid Mechanics **867** (2019).

[6] L. Kadanoff, D. Lohse, J. Wang, and R. Benzi, Physics of fluids **7**, 617 (1995).
[7] C. S. Campolina and A. A. Mailybaev, Nonlinearity **34**, 4684 (2021).
[8] C. Campolina, Master's thesis, IMPA (2019).
[9] P. Constantin, Bulletin of the American Mathematical Society **44**, 603 (2007).
[10] C. Connaughton and S. Nazarenko, Physical review letters **92**, 044501 (2004).
[11] D. Bandak, N. Goldenfeld, A. A. Mailybaev, and G. Eyink, Physical Review E **105**, 065113 (2022).
[12] L. Biferale, Annual review of fluid mechanics **35**, 441 (2003).
[13] T. Bohr, M. H. Jensen, G. Paladin, and A. Vulpiani, *Dynamical systems approach to turbulence* (1998).
[14] M. Jensen, G. Paladin, and A. Vulpiani, Physical Review A **43**, 798 (1991).
[15] M. De Pietro, L. Biferale, G. Boffetta, and M. Cencini, The European Physical Journal E **41**, 1 (2018).
[16] R. Benzi, S. Ciliberto, R. Tripiccione, C. Baudet, F. Massaioli, and S. Succi, Physical review E **48**, R29 (1993).
[17] S. Grossmann, D. Lohse, V. L'vov, and I. Procaccia, Phys. Rev. Lett. **73**, 432 (1994), URL `https://link.aps.org/doi/10.1103/PhysRevLett.73.432`.
[18] U. Frisch, A. Pomyalov, I. Procaccia, and S. S. Ray, Phys. Rev. Lett. **108**, 074501 (2012), URL `https://link.aps.org/doi/10.1103/PhysRevLett.108.074501`.
[19] A. S. Lanotte, R. Benzi, S. K. Malapaka, F. Toschi, and L. Biferale, Phys. Rev. Lett. **115**, 264502 (2015), URL `https://link.aps.org/doi/10.1103/PhysRevLett.115.264502`.
[20] V. S. L'vov, E. Podivilov, A. Pomyalov, I. Procaccia, and D. Vandembroucq, Physical Review E **58**, 1811 (1998).
[21] L. Biferale, A. Lambert, R. Lima, and G. Paladin, Physica D: Nonlinear Phenomena **80**, 105 (1995).
[22] C. S. Campolina and A. A. Mailybaev, Physical review letters **121**, 064501 (2018).
[23] Q.Pikeroen, A.Barral, G.Costa, C.Campolina, A.Mailybaev, and B.Dubrulle, to be published (2023).
[24] G. Gallavotti, The European Physical Journal Special Topics **227**, 217 (2018).

# Part IV

# Conclusions and perspectives

## 5.4 Overview of findings and objectives

### 5.4.1 Development of a comprehensive numerical framework

The primary objective of this research was met through the development of a versatile numerical framework for log-lattices. This framework serves two main purposes. Firstly, it caters to the needs of physicists, providing an optimized and user-friendly environment for simulating equations on log-lattices. While a proof-of-concept numerical framework existed before [Cam20], it was not suitable for long and numerous simulations using log-lattices. The new framework significantly enhances the speed and ease of performing and analyzing numerical simulations. Secondly, the development of this framework led to the introduction of several novel features, both in terms of numerical techniques and physical representations. These enhancements include more efficient and robust numerical solvers and schemes, the incorporation of $k_i = 0$ modes, and rectified representations of energy spectra.

This framework was successfully used with collaborators to investigate the Reversible Navier-Stokes equation [CBD23], and singularities in 1D viscous and non-viscous Burgers, 3D Euler and 3D Navier-Stokes equations [Pik+23].

### 5.4.2 Application to specific geophysical turbulence scenarios

Using this framework, we investigated geophysical turbulence scenarios of interest. Through the homogeneous Rayleigh-Bénard equations, we studied the influence of temperature. We recovered the asymptotic ultimate regime of homogeneous Rayleigh-Bénard convection predicted by GL theory[GL00], and at very high Rayleigh numbers found a transition from a stable to an intermittent regime. We then studied the influence of rotation, first through the 2D beta-plane quasi-geostrophic equations, where we were unable to observe the formation of zonal jets. In 3D homogeneous rotating turbulence, we recovered expected scaling laws from [Ale15].

### 5.4.3 Identifying advantages and limitations

We started this work knowing very little about the capabilities and practical weaknesses of log-lattices. By simulating the different scenarios outlined above, we gained a better understanding of their advantages and limitations, and on some directions of research that would be very beneficial for their wider adoption.

#### 5.4.3.1 Physical Perspective

Although the order of magnitude of the observables (such as Nu in the HRB case) can widely differ from that of DNS, log-lattices have overall proved successful in recovering known or expected scaling laws (up to prefactors) across a wide range of scales, as seen in buoyant and rotating turbulence and in blowup scenarios. The RNS study further indicates that the global behavior of the system, including phase transitions, is well described by log-lattice simulations. This is coherent with the boundary flow results of [Mar22].

It is difficult to draw precise conclusions of the failure of our 2D QG simulations, owing to the large number of possible explanations. The most telling cause is the lack of Rossby wave resonance, owing to the strict geometric structure of the lattice. Investigating other causes requires a better understanding of how log-lattice simulations behave in 2D and to which extent the inverse cascade is recovered; how the inclusion of the $k_i = 0$ modes, which add long-range

global interactions, affects the flow; and to which extent the lack of fine resolution around the Rhines scale is responsible for the missing zonal jets.

Part of the difficulty in interpreting log-lattice results is a lack of understanding "what the fields on the log-lattice correspond to" from a physical point of view. This question is directly linked to the ability to perform inverse Fourier transforms on log-lattices. We have made some progress in establishing this correspondence, and have identified challenges using sparse and non-sparse Fourier lattices as a representation, but further work is needed.

#### 5.4.3.2 Numerical Perspective

Common numerical frameworks and theories are not well suited for log-lattice simulations. Most state-of-the-art solvers use a mixture of absolute and relative precision to determine the accuracy of a simulation, which assumes that the observables are all more-or-less of the same order of magnitude. However, the sheer number of scales spanned by log-lattices imply widely diverging orders of magnitude of the simulated fields, which can easily reach values comparable to the lowest representable floating point number[2]. As a result, common criterions such as the Courant–Friedrichs–Lewy condition are of no use on log-lattices, and it is very unclear how "well-resolved" small scales are, even in a statistical sense. Luckily, using "DNS" solvers gives (up to some tweaks) satisfying results, but as log-lattices are very recent, there is to date no proper numerical study of what adapting those solvers and conditions to log-lattices would look like, and as such there is an inherent numerical uncertainty on the log-lattice results. If log-lattices are to be used in conjunction with DNS, it is crucial to investigate this further, and have quantitative estimates on the numerical error and stability induced by the time-stepping scheme on log-lattices.

## 5.5 Future prospects and research directions

This work started in 2019, shortly after the first log-lattice publication. Given how little we knew at the time, and the lack of a proper tool to perform simulations, it focused on simple use cases. The success of our log-lattice simulations has led us to expand our research team, which are actively working in several directions: more complex geophysical flows (combined rotation and temperature, humidity and rain, salinity), new ways of handling boundary conditions, enhanced solvers (stochastic, non-diagonal linear terms, preconditioning). This work has identified several other aspects where our lack of understanding hinders our progress: 2D turbulence, $k_i = 0$ modes, a proper understanding of physical representation of log-lattices (linked to inverse Fourier transforms on log-lattices), a proper numerical understanding of convergence on log-lattices.

Solving those questions would enable longer-term goals such as proper comparisons with DNS results, and interfacing between DNS and log-lattice simulations. This could be especially useful in climate simulations for LES, where dubious closure conditions could be replaced by log-lattice results, and would most likely be a prerequisite for a greater adoption of log-lattice methods by the scientific community.

## 5.6 Final remarks

This study demonstrates significant achievements in establishing log-lattices as a viable mathematical method for numerical turbulence. The developed numerical framework, along with the

[2] while still making physical sense ! This is not numerical noise.

insights gained from applying log-lattices to geophysical equations, lays a strong foundation for further research and real-world applications.

However, it is important to note that log-lattices represent one among several possibilities in the realm of turbulence modeling. While they demonstrate remarkable potential, they are not intended to be the sole solution for all scenarios, nor to replace DNS. Rather, log-lattices are a valuable addition to the repertoire of turbulence modeling techniques. As we move forward, it is essential to bear in mind their context-specific strengths and limitations.

# Part V

# Appendix

# Appendix A

# Technical details on the numerical Framework

*The content of this chapter moved to the online documentation, available here.*

# Appendix B

# Synthèse en Français

*L'école doctorale impose un résumé de 5 pages en Français pour les thèses rédigées en anglais. Vous trouverez donc ci-dessous un résumé autogénéré et traduit par IA.*

## Introduction

En 2019, Campolina a présenté un nouveau cadre mathématique appelé "log-lattices" pour simuler et explorer les équations de la dynamique des fluides avec un nombre réduit de modes. Ces équations, en particulier les équations de Navier-Stokes incompressibles, décrivent le comportement des fluides. La principale motivation de Campolina était d'étudier l'explosion potentielle des équations d'Euler, un aspect clé de la turbulence. Dans cette limite, connue sous le nom de dissipation anormale, la dissipation d'énergie ne s'évanouit pas lorsque le nombre de Reynolds s'approche de l'infini. On pense que ce phénomène résulte de solutions singulières des équations d'Euler.

Pour relever les défis de la simulation de ces scénarios, les grilles logarithmiques ont été introduits comme une nouvelle approche. Ces log-lattices sont construits sur la base d'une grille discrète dans l'espace de Fourier avec des points de grille espacés de façon exponentielle, ce qui permet des simulations avec moins de degrés de liberté. Il existe trois familles de valeurs admissibles pour le facteur d'espacement, chacune ayant un niveau de complexité différent : $\lambda = 2$, $\lambda$ valeurs entraînant des interactions triadiques de $z = 6$, et $\lambda = \sigma$ (le "nombre plastique") entraînant des interactions triadiques de $z = 12$.

Les recherches menées par Campolina et ses collègues ont révélé que les grilles logarithmiques peuvent simuler l'explosion des équations d'Euler en 3D, ce qui constitue un défi pour les simulations traditionnelles. Ils ont observé un attracteur chaotique dans l'explosion des équations d'Euler en 3D, ce qui donne des indications précieuses sur le comportement des turbulences. Leurs résultats sont cohérents pour différentes tailles de grille.

# Framework

## Mathématique

Les grilles logarithmiques, également connus sous le nom de log-grids, présentent un nouveau cadre mathématique pour l'examen des équations sur une grille spatiale fortement décimée et exponentiellement espacée. Ce cadre s'avère très avantageux lorsqu'il s'agit d'étudier des scénarios pour lesquels les simulations traditionnelles ne peuvent pas gérer efficacement la charge de calcul. Les grilles logarithmiques possèdent une véritable multidimensionnalité, contrairement aux modèles à coquille, et conservent la plupart des symétries trouvées dans les équations originales sans aucun paramètre supplémentaire.

Le paramètre d'espacement $\lambda$ peut prendre trois valeurs principales $\lambda = 2$, $\lambda = \phi \approx 1.6$ et $\lambda = \sigma \approx 1.3$. Ces valeurs sont classées par ordre croissant du nombre d'interactions.

Nous déconseillons l'utilisation de $\lambda = 2$ pour les simulations incompressibles.

## Numérique

Ce travail de doctorat s'est concentré sur le développement d'un cadre numérique pour des simulations efficaces sur des grilles logarithmiques. Le cadre, créé à partir de zéro en utilisant Python 3.11 avec quelques sections optimisées en Cython et C, est open-source, contrairement au cadre Matlab original. Il est conçu pour être convivial pour les physiciens, avec un code lisible et divers outils pour l'analyse des grilles logarithmiques. Le cadre comporte un dimensionnement adaptatif de la grille, ce qui le rend économe en ressources pour les flux intermittents. Il est bien documenté, testé en profondeur et comprend une documentation en ligne, une documentation en ligne (bien qu'incomplète) et des indications sur les types.

Le cadre combine la facilité d'utilisation de Python avec les performances et la rapidité du langage C. Il est flexible, ce qui permet de personnaliser l'utilisation du cadre. Il est flexible, permettant des modifications personnalisées et l'ajout de nouveaux composants sans altérer la structure existante. Les principales optimisations de performance en Cython et en C améliorent considérablement la vitesse de simulation. Le cadre est adapté au traitement par lots et aux sessions à distance, garantissant la sécurité en cas d'échec, l'interruptibilité et la reprise tout en gérant efficacement l'utilisation de l'unité centrale.

Plusieurs nouvelles fonctionnalités de la grille logarithmique, comme les modes avec $k_i = 0$ et les spectres rectifiés, ont été ajoutées. L'installation est facilitée par des scripts automatisés et la virtualisation, ce qui garantit une installation sans problème qui n'interfère pas avec les cadres existants. Actuellement, le code est hébergé sur le GitLab du CEA, mais l'objectif est de le rendre accessible à un public plus large dans un avenir proche.

# Rayleigh-Bénard Homogène

Dans ce chapitre, les auteurs étudient un phénomène appelé "Asymptotic Ultimate regime of Rayleigh-Bénard convection" en utilisant un cadre mathématique connu sous le nom de grilles logarithmiques. Ils introduisent un terme de friction à grande échelle pour atténuer les instabilités exponentielles qui peuvent affecter les simulations, même dans les simulations numériques directes (DNS). Ils retrouvent des relations d'échelle pour divers paramètres, notamment Nu (nombre de Nusselt), Re (nombre de Reynolds) et la dissipation en fonction de Ra (nombre de Rayleigh) et Pr (nombre de Prandtl), comme prévu par Grossman & Lohse. Ils observent une transition d'un régime "stable" à un régime "intermittent" avec des statistiques mal définies à Re très élevé. Dans l'ensemble, ce chapitre explore la convection, un processus qui influence le transport de chaleur et le mélange dans divers systèmes, et étudie le comportement de la convection de Rayleigh-Bénard dans différents régimes, en mettant en lumière ses lois d'échelle et sa stabilité. Le système présente initialement un régime stable avec un comportement prévisible, mais subit une transition abrupte vers un régime intermittent avec des fluctuations plus importantes à $Ra \approx 10^{11}$. Cette transition s'accompagne d'un comportement particulier dans les spectres d'énergie, avec l'apparition d'un pic singulier. L'emplacement de ce pic s'échelonne avec Ra, plus précisément $k_{peak} \propto Ra^{1/4}$, ressemblant au nombre d'ondes critique $k_c$ pour une instabilité. Cependant, la nature exacte de cette instabilité reste incertaine. Le régime intermittent est difficile à comprendre car il est associé à un point d'instabilité localisé dans le domaine de simulation, et les raisons de cette localisation ne sont pas encore claires. Malgré cette transition, les simulations continuent de présenter une échelle de régime ultime de $Nu \sim Ra^{0,5}$, ce qui suggère que la dynamique des fluides est toujours cohérente avec le comportement attendu. Ce développement fournit une direction intrigante pour la recherche future, et des recherches supplémentaires sont nécessaires pour comprendre la physique sous-jacente de ce nouveau régime et ses implications.

# Ecoulements en rotation

## Ecoulements beta-plans

Nous n'avons pas réussi à reproduire la dynamique des écoulements quasi-géostrophiques dans le plan bêta (QGBP) sur des grilles logarithmiques. Les équations brutes du QGBP à 2 couches posent des problèmes mathématiques lorsqu'elles sont traitées sur des grilles de Fourier. Les QGBP à une couche ne posent pas de tels problèmes. Cependant, l'émergence de jets zonaux, malgré le comportement apparemment satisfaisant des ondes de Rossby, n'est pas visible.

Cela pourrait être dû à l'impossibilité d'observer la résonance exacte des ondes de Rossby sur les grilles logarithmiques en raison de contraintes géométriques. Des recherches supplémentaires sont nécessaires pour déterminer si cela pourrait également être dû à des problèmes avec la cascade inverse dans les grilles logarithmiques 2D, l'absence d'interactions non locales, la nature éparse des interactions locales, ou l'implémentation mathématique des modes $k_i = 0$.

### Turbulence homogène en rotation

Nous simulons ensuite le NSE en rotation 3D, sans modes $k_i = 0$, ce qui empêche la condensation vers un écoulement quasi2D. Nous retrouvons les mêmes lois d'échelle que dans DNS [Ale15] pour tous les régimes qui n'impliquent pas de condensation.

### Autres contributions

J'expose ici les articles scientifiques auxquels j'ai contribué en tant que collaborateur, mais pas en tant qu'auteur principal.

Les articles présentés dans cette section sont le résultat d'un travail de collaboration avec des étudiants en doctorat qui ont rejoint notre groupe de recherche sur la grille logarithmique un ou deux ans après que j'ai commencé mes propres recherches. Bien que je n'aie pas assumé le rôle d'auteur principal, j'ai participé activement à la définition de l'orientation de la recherche, à l'amélioration du cadre numérique pour répondre à leurs besoins spécifiques et à l'engagement dans des discussions intellectuelles au sein des groupes de recherche respectifs.

Le premier article, intitulé "Grilles logarithmiques pour les écoulements atmosphériques", étudiee les écoulements soumis à des gradients de rotation et de température.

Le second article, intitulé "Tracking complex singularities of fluids on log-lattices", s'appuie sur les travaux de [CM21]. Il étudie les signatures des singularités dans les équations de Burgers visqueuses et non visqueuses 1D, les équations d'Euler 3D et les équations de Navier-Stokes 3D, avec une hyper-, une normale et une hypo-viscosité, en utilisant la méthode de la bande de singularité.

Le troisième article, intitulé "Équation de Navier-Stokes réversible sur des grilles logarithmiques", se concentre sur les transitions de phase dans l'équation de Navier-Stokes réversible.

## Conclusions

La recherche a atteint son objectif principal en créant un cadre numérique polyvalent pour les grilles logarithmiques. Ce cadre profite aux physiciens en fournissant un environnement optimisé et convivial pour simuler des équations sur des grilles logarithmiques. Le nouveau cadre améliore la vitesse et l'efficacité des simulations numériques et introduit de nouvelles caractéristiques telles que des solveurs numériques améliorés et l'incorporation des modes $k_i = 0$. Il a également été appliqué à l'étude de diverses équations, notamment l'équation de Navier-Stokes réversible et des scénarios de turbulence 1D et 3D.

En utilisant le cadre numérique, la recherche s'est penchée sur des scénarios de turbulence géophysique, y compris les équations de Rayleigh-Bénard, les équations quasi-géostrophiques du plan bêta en 2D et la turbulence rotative homogène en 3D. L'étude a exploré l'influence de facteurs tels que la température et la rotation dans ces scénarios, en retrouvant les lois d'échelle attendues.

La recherche a mis en évidence les avantages des grilles logarithmiques dans la récupération des lois d'échelle connues à travers différentes échelles dans les simulations de turbulence. Cependant, des défis et des limites ont également été identifiés, tels que les difficultés d'interprétation des résultats, en particulier dans les simulations 2D, et la nécessité d'une meilleure compréhension de la représentation physique des grilles logarithmiques.

Les solveurs numériques courants se sont révélés moins adaptés aux simulations de grilles logarithmiques en raison de la vaste gamme d'échelles concernées. Il a été noté que des recherches supplémentaires sont nécessaires pour adapter les solveurs aux grilles logarithmiques et quantifier l'erreur numérique et la stabilité introduites par les schémas à pas de temps.

La recherche se termine par une discussion sur les orientations futures de la recherche, y compris des écoulements géophysiques plus complexes, des conditions aux limites, des solveurs améliorés, et une meilleure compréhension de la turbulence 2D, des modes $k_i = 0$, et de la convergence numérique sur les grilles logarithmiques. Ces avancées sont considérées comme cruciales pour une adoption et une intégration plus larges des méthodes de grille logarithmique dans les simulations scientifiques.

L'étude reconnaît les progrès significatifs réalisés dans l'établissement des grilles logarithmiques en tant que méthode viable pour la modélisation numérique de la turbulence. Elle souligne que les grilles logarithmiques constituent un ajout précieux au répertoire des techniques de modélisation de la turbulence, mais qu'elles ne sont pas destinées à remplacer les méthodes traditionnelles telles que la simulation numérique directe (DNS). L'importance de comprendre les forces et les limites des grilles logarithmiques en fonction du contexte est soulignée à mesure que la recherche progresse.

# Bibliography


[AGL09] Guenter Ahlers, Siegfried Grossmann, and Detlef Lohse. "Heat transfer and large scale dynamics in turbulent Rayleigh-Bénard convection". In: *Rev. Mod. Phys.* 81 (2 Apr. 2009), pp. 503–537. DOI: 10.1103/RevModPhys.81.503.

[Ale15] Alexandros Alexakis. "Rotating Taylor-Green Flow". en. In: *Journal of Fluid Mechanics* 769 (Apr. 2015). arXiv:1409.5642 [physics], pp. 46–78. ISSN: 0022-1120, 1469-7645. DOI: 10.1017/jfm.2015.82.

[Bah17] Hajer Bahouri. "La Théorie de Littlewood-Paley: fil conducteur de nombreux travaux en analyse non linéaire". In: *Gazette des Mathématiciens* (2017). URL: https://hal.science/hal-02352900.

[Bah19] Hajer Bahouri. "The Littlewood–Paley Theory: A Common Thread of Many Works in Nonlinear Analysis". In: *European Mathematical Society Magazine* 112 (2019), pp. 15–23. URL: https://ems.press/content/serial-issue-files/12526#page=17.

[BD23] Amaury Barral and Berengere Dubrulle. "Asymptotic ultimate regime of homogeneous Rayleigh–Bénard convection on logarithmic lattices". In: *Journal of Fluid Mechanics* 962 (2023), A2. DOI: 10.1017/jfm.2023.204.

[Bif03] Luca Biferale. "Shell models of energy cascade in turbulence". In: *Annual Review of Fluid Mechanics* 35 (2003), pp. 441–468. DOI: 10.1146/annurev.fluid.35.101101.161122.

[BO97] Vadim Borue and Steven A Orszag. "Turbulent convection driven by a constant temperature gradient". In: *Journal of Scientific computing* 12.3 (1997), pp. 305–351. DOI: 10.1023/A:1025653628522.

[Bou+19] Vincent Bouillaut et al. "Transition to the ultimate regime in a radiatively driven convection experiment". In: *Journal of Fluid Mechanics* 861 (2019), R5. DOI: 10.1017/jfm.2018.972.

[Cal+05] Enrico Calzavarini et al. "Rayleigh and Prandtl number scaling in the bulk of Rayleigh–Bénard turbulence". In: *Physics of Fluids* 17.5 (2005), p. 055107. DOI: 10.1063/1.1884165.

[Cal+06] E. Calzavarini et al. "Exponentially growing solutions in homogeneous Rayleigh-Bénard convection". In: *Phys. Rev. E* 73 (3 Mar. 2006), p. 035301. DOI: 10.1103/PhysRevE.73.035301.

[Cam20] Ciro S Campolina. "LogLatt: A computational library for the calculus and flows on logarithmic lattices". In: *arXiv preprint arXiv:2006.00047* (2020). DOI: 10.48550/arXiv.2006.00047.

[Cas+17] B. Castaing et al. "Turbulent heat transport regimes in a channel". In: *Phys. Rev. Fluids* 2 (6 June 2017), p. 062801. DOI: 10.1103/PhysRevFluids.2.062801.

[CBD23] Guillaume Costa, Amaury Barral, and Bérengère Dubrulle. “Reversible Navier-Stokes equation on logarithmic lattices”. In: *Physical Review E* (June 2023). DOI: 10.1103/PhysRevE.107.065106.

[Cha+97] X. Chavanne et al. “Observation of the Ultimate Regime in Rayleigh-Bénard Convection”. In: *Phys. Rev. Lett.* 79 (19 Nov. 1997), pp. 3648–3651. DOI: 10.1103/PhysRevLett.79.3648.

[Che+96] Alexei Chekhlov et al. “The effect of small-scale forcing on large-scale structures in two-dimensional flows”. en. In: *Physica D: Nonlinear Phenomena* 98.2-4 (Nov. 1996), pp. 321–334. ISSN: 01672789. DOI: 10.1016/0167-2789(96)00102-9.

[CK08] Emily S. C. Ching and T. C. Ko. “Ultimate-state scaling in a shell model for homogeneous turbulent convection”. In: *Phys. Rev. E* 78 (3 Sept. 2008), p. 036309. DOI: 10.1103/PhysRevE.78.036309.

[CL99] S. Ciliberto and C. Laroche. “Random Roughness of Boundary Increases the Turbulent Convection Scaling Exponent”. In: *Phys. Rev. Lett.* 82 (20 May 1999), pp. 3998–4001. DOI: 10.1103/PhysRevLett.82.3998.

[CLT07] E. Calzavarini, D. Lohse, and F. Toschi. “Homogeneous Rayleigh-Bénard Convection”. In: *Progress in Turbulence II*. Berlin, Heidelberg: Springer Berlin Heidelberg, 2007, pp. 181–184. ISBN: 978-3-540-32603-8. DOI: 10.1007/978-3-540-32603-8.

[CM18] Ciro S. Campolina and Alexei A. Mailybaev. “Chaotic Blowup in the 3D Incompressible Euler Equations on a Logarithmic Lattice”. In: *Phys. Rev. Lett.* 121 (6 Aug. 2018), p. 064501. DOI: 10.1103/PhysRevLett.121.064501.

[CM21] Ciro S Campolina and Alexei A Mailybaev. “Fluid dynamics on logarithmic lattices”. In: *Nonlinearity* 34.7 (June 2021), pp. 4684–4715. DOI: 10.1088/1361-6544/abef73.

[CRG04] C Cambon, R Rubinstein, and FS Godeferd. “Advances in wave turbulence: rapidly rotating flows”. In: *New Journal of Physics* 6.1 (2004), p. 73. DOI: 10.1088/1367-2630/6/1/073.

[DC96] Charles R. Doering and Peter Constantin. “Variational bounds on energy dissipation in incompressible flows. III. Convection”. In: *Phys. Rev. E* 53 (6 June 1996), pp. 5957–5981. DOI: 10.1103/PhysRevE.53.5957.

[DG02] Sergey Danilov and David Gurarie. “Rhines scale and spectra of the $\beta$-plane turbulence with bottom drag”. en. In: *Physical Review E* 65.6 (June 2002), p. 067301. ISSN: 1063-651X, 1095-3787. DOI: 10.1103/PhysRevE.65.067301.

[EG91] Jens Eggers and Siegfried Grossman. “Anomalous turbulent velocity scaling from the Navier-Stokes equation”. In: *Physics Letters A* 156.7-8 (1991), pp. 444–449. DOI: 10.1016/0375-9601(91)90725-N.

[ES06] Gregory L Eyink and Katepalli R Sreenivasan. “Onsager and the theory of hydrodynamic turbulence”. In: *Reviews of modern physics* 78.1 (2006), p. 87. DOI: 10.1103/RevModPhys.78.87.

[For15] Najmeh Foroozani. “Numerical Study of Turbulent Rayleigh-Benard Convection with Cubic confinement”. en. In: *PhD thesis* (2015). URL: http://hdl.handle.net/10077/11115.

[Fri+12] Uriel Frisch et al. “Turbulence in Noninteger Dimensions by Fractal Fourier Decimation”. In: *Phys. Rev. Lett.* 108 (7 Feb. 2012), p. 074501. DOI: 10.1103/PhysRevLett.108.074501.

[Gal03] Sébastien Galtier. “Weak inertial-wave turbulence theory”. In: *Physical Review E* 68.1 (2003), p. 015301. DOI: 10.1103/PhysRevE.68.015301.

[GHS93] D Goldstein, R Handler, and L Sirovich. “Modeling a no-slip flow boundary with an external force field”. In: *Journal of computational physics* 105.2 (1993), pp. 354–366. DOI: 10.1006/jcph.1993.1081.

[Gib+06] M. Gibert et al. “High-Rayleigh-Number Convection in a Vertical Channel”. en. In: *Physical Review Letters* 96.8 (2006). ISSN: 0031-9007, 1079-7114. DOI: 10/fmjvd8.

[Gib08] John D Gibbon. “The three-dimensional Euler equations: Where do we stand?” In: *Physica D: Nonlinear Phenomena* 237.14-17 (2008), pp. 1894–1904. DOI: https://doi.org/10.1016/j.physd.2007.10.014.

[GL00] Siegfried Grossmann and Detlef Lohse. “Scaling in thermal convection: a unifying theory”. In: *Journal of Fluid Mechanics* 407 (2000), pp. 27–56. DOI: 10.1017/S0022112099007545.

[GL01] Siegfried Grossmann and Detlef Lohse. “Thermal convection for large Prandtl numbers”. en. In: *Physical Review Letters* 86.15 (Apr. 2001). arXiv:nlin/0011015, pp. 3316–3319. ISSN: 0031-9007, 1079-7114. DOI: 10.1103/PhysRevLett.86.3316.

[GL11] Siegfried Grossmann and Detlef Lohse. “Multiple scaling in the ultimate regime of thermal convection”. In: *Physics of Fluids* 23.4 (2011), p. 045108. DOI: 10.1063/1.3582362.

[GL92] Siegfried Grossmann and Detlef Lohse. “Intermittency in the Navier-Stokes dynamics”. In: *Zeitschrift für Physik B Condensed Matter* 89.1 (1992), pp. 11–19. DOI: 10.1007/BF01320823.

[GL94] Siegfried Grossmann and Detlef Lohse. “Scale resolved intermittency in turbulence”. In: *Physics of fluids* 6.2 (1994), pp. 611–617. DOI: 10.1063/1.868357.

[Glo+85] C. Gloaguen et al. “A scalar model for MHD turbulence”. In: *Physica D: Nonlinear Phenomena* 17.2 (1985), pp. 154–182. ISSN: 0167-2789. DOI: https://doi.org/10.1016/0167-2789(85)90002-8.

[GMG98] Rainer Grauer, Christiane Marliani, and Kai Germaschewski. “Adaptive mesh refinement for singular solutions of the incompressible Euler equations”. In: *Physical review letters* 80.19 (1998), p. 4177. DOI: 10.1103/PhysRevLett.80.4177.

[Gra+08] Tobias Grafke et al. “Numerical simulations of possible finite time singularities in the incompressible Euler equations: comparison of numerical methods”. In: *Physica D: Nonlinear Phenomena* 237.14-17 (2008), pp. 1932–1936. DOI: 10.1016/j.physd.2007.11.006.

[Gro+94] Siegfried Grossmann et al. “Finite size corrections to scaling in high Reynolds number turbulence”. In: *Phys. Rev. Lett.* 73 (3 July 1994), pp. 432–435. DOI: 10.1103/PhysRevLett.73.432.

[HL07] Thomas Y Hou and Ruo Li. “Computing nearly singular solutions using pseudo-spectral methods”. In: *Journal of Computational Physics* 226.1 (2007), pp. 379–397. DOI: 10.1016/j.jcp.2007.04.014.

[Hou09] Thomas Y Hou. "Blow-up or no blow-up? A unified computational and analytic approach to 3D incompressible Euler and Navier–Stokes equations". In: *Acta Numerica* 18 (2009), pp. 277–346. DOI: 10.1017/S0962492906420018.

[Jia+22] Hechuan Jiang et al. "Experimental Evidence for the Existence of the Ultimate Regime in Rapidly Rotating Turbulent Thermal Convection". In: *Phys. Rev. Lett.* 129 (20 Nov. 2022), p. 204502. DOI: 10.1103/PhysRevLett.129.204502.

[Kaw+21] Koki Kawano et al. "Ultimate heat transfer in 'wall-bounded' convective turbulence". In: *Journal of Fluid Mechanics* 914 (2021), A13. DOI: 10.1017/jfm.2020.867.

[Ker93] Robert M Kerr. "Evidence for a singularity of the three-dimensional, incompressible Euler equations". In: *Physics of Fluids A: Fluid Dynamics* 5.7 (1993), pp. 1725–1746. DOI: 10.1063/1.858849.

[Kra62] Robert H. Kraichnan. "Turbulent Thermal Convection at Arbitrary Prandtl Number". In: *The Physics of Fluids* 5.11 (1962), pp. 1374–1389. DOI: 10.1063/1.1706533.

[LAG18] Simon Lepot, Sébastien Aumaître, and Basile Gallet. "Radiative heating achieves the ultimate regime of thermal convection". In: *Proceedings of the National Academy of Sciences* 115.36 (2018), pp. 8937–8941. DOI: 10.1073/pnas.1806823115.

[Lan+15] Alessandra S. Lanotte et al. "Turbulence on a Fractal Fourier Set". In: *Phys. Rev. Lett.* 115 (26 Dec. 2015), p. 264502. DOI: 10.1103/PhysRevLett.115.264502.

[LB15] Jason Laurie and Freddy Bouchet. "Computation of rare transitions in the barotropic quasi-geostrophic equations". en. In: *New Journal of Physics* 17.1 (Jan. 2015). arXiv:1409.3219 [cond-mat, physics:physics], p. 015009. ISSN: 1367-2630. DOI: 10.1088/1367-2630/17/1/015009.

[LFB21] Daphné Lemasquerier, Benjamin Favier, and Michael Le Bars. "Zonal jets at the laboratory scale: hysteresis and Rossby waves resonance". en. In: *Journal of Fluid Mechanics* 910 (Mar. 2021). arXiv: 2008.10304, A18. ISSN: 0022-1120, 1469-7645. DOI: 10.1017/jfm.2020.1000.

[LT03] Detlef Lohse and Federico Toschi. "Ultimate State of Thermal Convection". In: *Phys. Rev. Lett.* 90 (3 Jan. 2003), p. 034502. DOI: 10.1103/PhysRevLett.90.034502.

[Mai12] Alexei A Mailybaev. "Renormalization and universality of blowup in hydrodynamic flows". In: *Physical Review E* 85.6 (2012), p. 066317. DOI: 10.1103/PhysRevE.85.066317.

[Mal89] Stephane G Mallat. "A theory for multiresolution signal decomposition: the wavelet representation". In: *IEEE transactions on pattern analysis and machine intelligence* 11.7 (1989), pp. 674–693. DOI: 10.1109/34.192463.

[Mar19] Ciro Sobrinho Campolina Martins. "Fluid Dynamics on Logarithmic Lattices and Singularities of Euler Flow". en. In: *Master's thesis* (2019). URL: https://impa.br/wp-content/uploads/2019/08/dissertacao_mest_Ciro-Sobrinho.pdf.

[Mar22] Ciro Sobrinho Campolina Martins. "Fluid Flows and Boundaries on Logarithmic Lattices". en. In: *PhD thesis* (2022).

[MC54] W. V. R. Malkus and Subrahmanyan Chandrasekhar. “The heat transport and spectrum of thermal turbulence”. In: *Proceedings of the Royal Society of London. Series A. Mathematical and Physical Sciences* 225.1161 (1954), pp. 196–212. DOI: 10.1098/rspa.1954.0197.

[MKS22] Shingo Motoki, Genta Kawahara, and Masaki Shimizu. “Steady thermal convection representing the ultimate scaling”. In: *Philosophical Transactions of the Royal Society A: Mathematical, Physical and Engineering Sciences* 380.2225 (2022), p. 20210037. DOI: 10.1098/rsta.2021.0037.

[Ons49] L Onsager. “Statistical hydrodynamics”. In: *Il Nuovo Cimento* 6 (1949), pp. 279–287.

[PA16] Shashikant S. Pawar and Jaywant H. Arakeri. “Two regimes of flux scaling in axially homogeneous turbulent convection in vertical tube”. In: *Phys. Rev. Fluids* 1 (4 Aug. 2016), p. 042401. DOI: 10.1103/PhysRevFluids.1.042401.

[Ped13] Joseph Pedlosky. *Geophysical fluid dynamics*. Springer Science & Business Media, 2013.

[Pik+23] Quentin Pikeroen et al. “Tracking complex singularities of fluids on log-lattices”. In: *submitted to Nonlinearity* (2023).

[PS92] Alain Pumir and Eric D Siggia. “Finite-time singularities in the axisymmetric three-dimension Euler equations”. In: *Physical review letters* 68.10 (1992), p. 1511. DOI: 10.1103/PhysRevLett.68.1511.

[PS95] Alain Pumir and Boris I. Shraiman. “Persistent Small Scale Anisotropy in Homogeneous Shear Flows”. In: *Phys. Rev. Lett.* 75 (17 Oct. 1995), pp. 3114–3117. DOI: 10.1103/PhysRevLett.75.3114.

[Roc20] Philippe-E Roche. “The ultimate state of convection: a unifying picture of very high Rayleigh numbers experiments”. In: *New Journal of Physics* 22.7 (2020), p. 073056. DOI: 10.1088/1367-2630/ab9449.

[Rus+18] E. Rusaouën et al. “Thermal transfer in Rayleigh–Bénard cell with smooth or rough boundaries”. In: *Journal of Fluid Mechanics* 837 (2018), pp. 443–460. DOI: 10.1017/jfm.2017.852.

[Sch+12] Laura E. Schmidt et al. “Axially homogeneous Rayleigh–Bénard convection in a cylindrical cell”. In: *Journal of Fluid Mechanics* 691 (2012), pp. 52–68. DOI: 10.1017/jfm.2011.440.

[SDG07] Semion Sukoriansky, Nadejda Dikovskaya, and Boris Galperin. “On the Arrest of Inverse Energy Cascade and the Rhines Scale”. en. In: *Journal of the Atmospheric Sciences* 64.9 (Sept. 2007), pp. 3312–3327. ISSN: 1520-0469, 0022-4928. DOI: 10.1175/JAS4013.1.

[SGC99] Semion Sukoriansky, Boris Galperin, and Alexei Chekhlov. “Large scale drag representation in simulations of two-dimensional turbulence”. In: *Physics of Fluids* 11.10 (1999), pp. 3043–3053. DOI: 10.1063/1.870163.

[Spi63] Edward A Spiegel. “A Generalization of the Mixing-Length Theory of Turbulent Convection”. In: *The Astrophysical Journal* 138 (1963), p. 216.

[SRB21] Eric Simonnet, Joran Rolland, and Freddy Bouchet. “Multistability and rare spontaneous transitions in barotropic $\beta$-plane turbulence”. en. In: *Journal of the Atmospheric Sciences* (Apr. 2021). arXiv: 2009.09913. ISSN: 0022-4928, 1520-0469. DOI: 10.1175/JAS-D-20-0279.1.

[Ste+02] Bjorn Stevens et al. “Entrainment, Rayleigh Friction, and Boundary Layer Winds over the Tropical Pacific”. In: *Journal of Climate* 15.1 (2002), pp. 30–44. DOI: 10.1175/1520-0442(2002)015<0030:ERFABL>2.0.CO;2.

[UE97] Ch Uhlig and J Eggers. “Singularities in cascade models of the Euler equation”. In: *Zeitschrift für Physik B Condensed Matter* 103 (1997), pp. 69–78. DOI: 10.1007/s002570050337.

[Urb+19] P. Urban et al. “Elusive transition to the ultimate regime of turbulent Rayleigh-Bénard convection”. In: *Phys. Rev. E* 99 (1 Jan. 2019), p. 011101. DOI: 10.1103/PhysRevE.99.011101.

[YSP18] P. K. Yeung, K. R. Sreenivasan, and S. B. Pope. “Effects of finite spatial and temporal resolution in direct numerical simulations of incompressible isotropic turbulence”. In: *Phys. Rev. Fluids* 3 (6 June 2018), p. 064603. DOI: 10.1103/PhysRevFluids.3.064603.

[YT17] Naoto Yokoyama and Masanori Takaoka. “Hysteretic transitions between quasi-two-dimensional flow and three-dimensional flow in forced rotating turbulence”. en. In: *Physical Review Fluids* 2.9 (Sept. 2017), p. 092602. ISSN: 2469-990X. DOI: 10.1103/PhysRevFluids.2.092602.

[Zhu+18] Xiaojue Zhu et al. “Transition to the Ultimate Regime in Two-Dimensional Rayleigh-Bénard Convection”. In: *Phys. Rev. Lett.* 120 (14 Apr. 2018), p. 144502. DOI: 10.1103/PhysRevLett.120.144502.

[Zhu+19a] Xiaojue Zhu et al. “$Nu \sim Ra^{1/2}$ scaling enabled by multiscale wall roughness in Rayleigh-Bénard turbulence”. In: *Journal of Fluid Mechanics* 869 (2019), R4. DOI: 10.1017/jfm.2019.228.

[Zhu+19b] Xiaojue Zhu et al. “Reply to ”Absence of Evidence for the Ultimate Regime in Two-Dimensional Rayleigh-Benard Convection””. In: *Physical Review Letters* 123.25 (2019), p. 259402.

[ZY21] Shufan Zou and Yantao Yang. “Realizing the ultimate scaling in convection turbulence by spatially decoupling the thermal and viscous boundary layers”. In: *Journal of Fluid Mechanics* 919 (2021), R3. DOI: 10.1017/jfm.2021.393.